

Volume 14 No. 2 2014

ISSN 1473-6691 (print)

ISSN 1472-3422 (online)

Journal of the ICRU

ICRU REPORT 91

Prescribing, Recording, and Reporting of Stereotactic Treatments with Small Photon Beams

OXFORD
UNIVERSITY PRESS



OXFORD UNIVERSITY PRESS

INTERNATIONAL COMMISSION ON
RADIATION UNITS AND
MEASUREMENTS

Journal of the ICRU

Commission Membership

H.-G. Menzel (Chairman)
P. M. DeLuca (Vice Chairman)
T. R. Mackie (Secretary)
J. M. Boone
M.-E. Brandan
D. T. Burns
A. Chiti
E. Fantuzzi
V. Gregoire
R. W. Howell
P. Olko
B. O'Sullivan
D. W. O. Rogers
A. Allisy (Honorary Chairman)
A. Wambersie (Honorary Chairman)

G. Whitmore (Emeritus Member)
H. G. Paretzke (Emeritus Member)

Executive Secretary
D. A. Schauer

Assistant Executive Secretary
L. J. Atwell

Scientific Editors: Journal of the ICRU
S. M. Seltzer

Managing Editor: ICRU Website and ICRU News
H.-G. Menzel

Honorary Counsel
W. R. Ney

Reports are available for purchase as single issues. Please see the Journal homepage: <https://academic.oup.com/jicru>, and go to 'Purchase back reports of the ICRU'.

Full prepayment, in the correct currency, is required for all orders. Orders are regarded as firm and payments are not refundable. Subscriptions are accepted and entered on a complete volume basis. Claims cannot be considered more than FOUR months after publication or date of order, whichever is later. All subscriptions in Canada are subject to GST. Subscriptions in the EU may be subject to European VAT. If registered, please supply details to avoid unnecessary charges. For subscriptions that include online versions, a proportion of the subscription price may be subject to UKVAT. Personal rate subscriptions are only available if payment is made by personal cheque or credit card and delivery is to a private address.

Visit <https://academic.oup.com/jicru> for complete listing of previous reports available from Oxford University Press.

For further information, please contact: Journals Customer Service Department, Oxford University Press, Great Clarendon Street, Oxford OX2 6DP, UK. Email: jnls.cust.serv@oup.com. Tel (and answerphone outside normal working hours): +44 (0)1865 353907. Fax: +44 (0)1865 353485. **In the US, please contact:** Journals Customer Service Department, Oxford University Press, 2001 Evans Road, Cary, NC 27513, USA. Email: jnlorders@oup.com. Tel (and answerphone outside normal working hours): 800 852 7323 (toll-free in USA/Canada). Fax: 919 677 1714. **In Japan, please contact:** Journals Customer Services, Oxford University Press, 1-1-17-5F, Mukogaoka, Bunkyo-ku, Tokyo, 113-0023, Japan. Email: okudaoup@po.ijinet.or.jp. Tel: (03) 3813 1461. Fax: (03) 3818 1522.

Methods of payment. Payment should be made: by cheque (to Oxford University Press, Cashiers' Office, Great Clarendon Street, Oxford, OX2 6DP, UK); by bank transfer [to Barclays Bank Plc, Oxford Office, Oxford (bank sort code 20-65-18) (UK); overseas only Swift code BARC GB22 (GB£ Sterling Account no. 70299332, IBAN GB89BARC20651870299332; US\$ Dollars Account no. 66014600, IBAN GB27BARC20651866014600; EU€EURO Account no. 78923655, IBAN GB16BARC20651878923655]; or by credit card (Mastercard, Visa, Switch or American Express).

Journal of the ICRU is published twice a year, June and December, by Oxford University Press, Oxford, UK. Annual subscription price is £205/\$389/€307. Journal of the ICRU is distributed by Air Business Ltd, c/o Worldnet Shipping Inc., 156-15, 146th Avenue, 2nd Floor, Jamaica, NY 11434, USA.

US Postmaster: send address changes to Journal of the ICRU, Air Business Ltd, c/o Worldnet Shipping Inc., 156-15, 146th Avenue, 2nd Floor, Jamaica, NY 11434, USA.

Permissions

For information on how to request permissions to reproduce articles/information from this journal, please visit https://academic.oup.com/journals/pages/access_purchase/rights_and_permissions.

Dosage disclaimer

The mention of trade names, commercial products or organizations, and the inclusion of advertisements in the journal does not imply endorsement by the ICRU, the editors, the editorial board, Oxford University Press or the organization to which the authors are affiliated. The editors and publishers have taken all reasonable precautions to verify dosage, the results of experimental work and clinical findings published in the journal. The ultimate responsibility for the use and dosage of drugs mentioned in the Journal and in interpretation of published material lies with the medical practitioner, and the editors and publishers cannot accept liability for damages arising from any errors or omissions in the journal. Please inform the editors of any errors.

Legal Notice

This report was prepared by the International Commission on Radiation Units and Measurements, Inc. (ICRU). The Commission strives to provide accurate, complete and useful information in its reports. However, neither the ICRU, the members of the ICRU, Oxford University Press, other persons contributing to or assisting in the preparation of this report, nor any person acting on behalf of any of these parties: (a) makes any warranty or representation, express or implied, with respect to the accuracy, completeness or usefulness of the information contained in this report, or that the use of any information, method or process disclosed in this report may not infringe on privately owned rights; or (b) assumes any liability with respect to the use of, or for damages resulting from the use of any information, method or process disclosed in this report.

© International Commission on Radiation Units and Measurements 2017

All rights reserved; no part of this publication may be reproduced, stored in a retrieval system, or transmitted in any form or by any means, electronic, mechanical, photocopying, recording, or otherwise without prior written permission of the Publishers, or a licence permitting restricted copying issued in the UK by the Copyright Licensing Agency Ltd, 90 Tottenham Court Road, London W1P 9HE, or in the USA by the Copyright Clearance Center, 222 Rosewood Drive, Danvers, MA 01923. For those in the USA or Canada not registered with CCC, articles can be obtained by fax in 48 hours by calling: WISE for MedicineTM1-800-667-WISE.

Typeset by MPS Limited, Chennai, India
Printed by Bell & Bain, Glasgow, UK

**PRESCRIBING, RECORDING, AND
REPORTING OF STEREOTACTIC
TREATMENTS WITH SMALL
PHOTON BEAMS**

**THE INTERNATIONAL COMMISSION ON
RADIATION UNITS AND
MEASUREMENTS
(Published July, 2017)**

Journal of the ICRU Volume 14 No 2 2014
Published by Oxford University Press

PRESCRIBING, RECORDING, AND REPORTING OF STEREOTACTIC TREATMENTS WITH SMALL PHOTON BEAMS

Report Committee

J. Seuntjens (Co-Chair), McGill University Health Centre, Montreal, Canada

E. F. Lartigau (Co-Chair), Centre Oscar Lambret, Lille, France

S. Cora, San Bartolo Hospital, Vicenza, Italy

G. X. Ding, Vanderbilt - Ingram Cancer Center, Nashville, USA

S. Goetsch, San Diego Medical Physics, Inc., La Jolla, California, USA

J. Nuyttens, The Erasmus MC-Daniel den Hoed Cancer Center, Rotterdam, Netherlands

D. Roberge, CHUM - Hôpital Notre-Dame, Montreal, Canada

Commission Sponsors

D. T. Burns, Bureau International des Poids et Mesures, Sèvres, France

V. Grégoire, Université Catholique de Louvain, Brussels, Belgium

P M DeLuca, University of Wisconsin, Madison, USA

Consultant to the Report Committee

I. El Naqa, McGill University Health Centre, Montreal, Canada

The Commission wishes to express its appreciation to the individuals involved in the preparation of this Report for the time and efforts that they devoted to this task and to express its appreciation to the organizations with which they are affiliated.

All rights reserved. No part of this book may be reproduced, stored in retrieval systems or transmitted in any form by any means, electronic, electrostatic, magnetic, mechanical photocopying, recording, or otherwise, without the permission in writing from the publishers.

British Library Cataloguing in Publication Data. A Catalogue record of this book is available at the British Library.

International Commission on Radiation Units and Measurements

Introduction

The International Commission on Radiation Units and Measurements (ICRU), since its inception in 1925, has had as its principal objective the development of internationally acceptable recommendations regarding:

- (1) quantities and units of ionizing radiation and radioactivity,
- (2) procedures suitable for the measurement and application of these quantities in clinical radiology and radiobiology, and
- (3) physical data needed in the application of these procedures, the use of which tends to assure uniformity in reporting.

The Commission also considers and makes similar types of recommendations for the radiation protection field. In this connection, its work is performed in cooperation with the International Commission on Radiological Protection (ICRP).

Policy

ICRU endeavors to collect and evaluate the latest data and information pertinent to the problems of radiation measurement and dosimetry and to recommend the most acceptable numerical values for physical reference data and techniques for current use.

The Commission's recommendations are kept under continual review in order to keep abreast of the rapidly expanding uses of radiation.

ICRU feels that it is the responsibility of national organizations to introduce their own detailed technical procedures for the development and maintenance of standards. However, it urges that all countries adhere as closely as possible to the internationally recommended basic concepts of radiation quantities and units.

The Commission maintains and develops a system of quantities and units and concepts (e.g., for radiation therapy) and guidance for measurement procedures and techniques having the widest possible range of applicability. Situations can arise from time

to time for which an expedient solution of a current problem is required.

ICRU invites and welcomes constructive comments and suggestions regarding its recommendations and reports. These may be transmitted to the Chairman.

Current Program

The Commission recognizes its obligation to provide guidance and recommendations in the areas of radiation therapy, radiation protection, and the compilation of data important to these fields, and to scientific research and industrial applications of radiation. Increasingly, the Commission is focusing on the problems of protection of the patient and evaluation of image quality in diagnostic radiology and radiation oncology. These activities do not diminish the ICRU's commitment to the provision of a rigorously defined set of quantities and units useful in a very broad range of scientific endeavors.

The Commission is currently engaged in the formulation of ICRU Reports treating the following subjects:

Bioeffect Modeling and Biologically Equivalent Dose Concepts in Radiation Therapy
Monitoring and Assessment of Radiation Releases to the Environment
Operational Radiation Protection Quantities for External Radiation
Prescribing, Recording, and Reporting Ion-Beam Therapy
Retrospective Assessment of Individual Doses for Acute Exposures to Ionizing Radiation

The Commission continually reviews progress in radiation science with the aim of identifying areas in which the development of guidance and recommendations can make an important contribution.

ICRU's Relationship with Other Organizations

In addition to its close relationship with the ICRP, ICRU has developed relationships with national and

PRESCRIBING, RECORDING, AND REPORTING SMALL BEAM SRT

international agencies and organizations. In these relationships, ICRU is looked to for primary guidance in matters relating to quantities, units, and measurements for ionizing radiation, and their applications in the radiological sciences. In 1960, through a special liaison agreement, ICRU entered into consultative status with the International Atomic Energy Agency (IAEA). The Commission has a formal relationship with the United Nations Scientific Committee on the Effects of Atomic Radiation (UNSCEAR), whereby ICRU observers are invited to attend annual UNSCEAR meetings. The Commission and the International Organization for Standardization (ISO) informally exchange notifications of meetings, and ICRU is formally designated for liaison with two of the ISO technical committees. ICRU is a member of Consultative Committee for Units (CCU) – BIPM and Consultative Committee for Ionizing Radiation (CCRI(I) – BIPM and Observer to CCRI(II) and CCRI (III)). ICRU also enjoys a strong relationship with its sister organization, the National Council on Radiation Protection and Measurements (NCRP). In essence, ICRU and NCRP were founded concurrently by the same individuals. Presently, this long-standing relationship is formally acknowledged by a special liaison agreement. ICRU also exchanges reports with the following organizations:

Bureau International des Poids et Mesures
European Commission
International Council for Science
International Electrotechnical Commission
International Labour Office
International Organization for Medical Physics
International Radiation Protection Association
International Union of Pure and Applied Physics
United Nations Educational, Scientific and Cultural Organization

The Commission has found its relationship with all of these organizations fruitful and of substantial benefit to the ICRU program.

Operating Funds

Financial support has been received from the following organizations:

Accuray Incorporated
American Association of Physicists in Medicine
Belgian Nuclear Research Centre
Canadian Nuclear Safety Commission
Federal Office Public Health, Switzerland
Helmholtz Zentrum München Hitachi, Ltd.
International Atomic Energy Agency
International Radiation Protection Association
International Society of Radiology
Ion Beam Applications, S.A.
Japanese Society of Radiological Technology
MDS Nordin
Nederlandse Vereniging voor Radiologie
Philips Medical Systems, Incorporated
Radiological Society of North America
Siemens Medical Solutions
U.S. Environmental Protection Agency
U.S. Nuclear Regulatory Commission
Varian Medical Systems

In addition to the direct monetary support provided by these organizations, many organizations provide indirect support for the Commission's program. This support is provided in many forms, including, among others, subsidies for (1) the time of individuals participating in ICRU activities, (2) travel costs involved in ICRU meetings, and (3) meeting facilities and services.

In recognition of the fact that its work is made possible by the generous support provided by all of the organizations supporting its program, the Commission expresses its deep appreciation.

Hans-Georg Menzel
Chairman, ICRU
Heidelberg, Germany

Prescribing, Recording, and Reporting of Stereotactic Treatments with Small Photon Beams

Preface	1
Glossary	3
Abstract.....	5
Executive Summary.....	7
1. Introduction	11
1.1 Definition and Scope.....	11
1.2 Aim of Report	11
1.3 History of SRS and SRT.....	12
1.4 Overview of Small-Field Radiation Therapy Equipment	15
1.4.1 Dedicated Devices	15
1.4.1.1 Cobalt radiosurgery devices.....	15
1.4.1.2 Robotic non-isocentric linear accelerators.....	15
1.4.1.3 Dedicated gantry-based isocentric linear accelerators.....	16
1.4.1.4 Dedicated ring-based linacs	16
1.4.2 Non-Dedicated Stereotactic Radiosurgery and Radiotherapy Accelerators.....	17
1.5 Similarities and Differences Between 3D-CRT, IMRT, and SRT	18
1.5.1 Inverse Optimization.....	18
1.5.2 Imaging and 4D Adaptive Treatment	18
1.5.3 Volume Definition.....	19
1.5.4 Dose–Volume Histograms in SRT	20
1.5.5 Radiation Biology of Small Field Radiation Therapy	20
1.5.5.1 Effect of physical variables on biological response	21
1.5.5.2 Effect of biological variables on biological response	21
1.5.5.3 New radiation biology concepts or not?.....	22
1.5.5.4 Clinical prescriptions and dose tolerances for hypofractionation	22
1.6 Clinical Experience With Small Field Radiation Therapy	24
1.6.1 Intracranial Tumors	24
1.6.1.1 Brain metastases	24
1.6.1.2 Primary brain tumors	24
1.6.2 Functional Disorders.....	25
1.6.2.1 Trigeminal neuralgia	26
1.6.2.2 Arteriovenous malformations	26
1.6.3 Extracranial Metastatic Tumors.....	26
1.6.3.1 Liver metastases	26
1.6.3.2 Lung metastases	27
1.6.3.3 Spinal metastases	27
1.6.3.4 Other oligometastatic tumors.....	27

1.6.4 Primary Extracranial Tumors	28
1.6.4.1 Stereotactic radiotherapy as curative treatment	28
1.6.4.2 Stereotactic radiotherapy as a boost treatment	29
1.6.5 Recurrent Tumors	29
1.6.5.1 Head and neck cancer	29
1.7 Summary of Contents of the Report	30
2. Small Field Dosimetry	31
2.1 Defining Characteristics of Small Radiation Therapy Beams	32
2.1.1 Lateral Charged Particle Disequilibrium	32
2.1.2 Partial Source Occlusion	33
2.1.3 Detector Size Relative to Field Size	34
2.2 Fluence Spectrum Changes in Small Fields	34
2.3 Theoretical Framework for In-Phantom Reference Dosimetry	36
2.4 Stopping-Power Ratios in Small Fields	38
2.5 Ionization Chamber Detector Response in Small Fields	39
2.6 Specification of the Radiation Quality of the Beam in Small Fields	40
2.7 Suitability of Detectors for Measurements in Small Field Conditions	42
2.8 Formalism for Small Field Clinical Reference Dosimetry	44
2.9 Machine Specific Reference Fields and Beam Quality Correction Factors	45
2.10 Output Factors	47
2.11 Practical Aspects in Output Factors Measurements	49
2.12 Relative Dosimetry for Radiotherapy Using Small Fields	50
2.12.1 General Aspects	50
2.12.2 Percentage Depth Dose	50
2.12.3 Conversion of PDD to TPR	51
2.12.4 Dose Profile Measurements	52
2.12.5 Manufacturer-Provided Relative Dosimetry	53
3. Definition of Volumes	55
3.1 Volume Definitions in Radiation Therapy Using Small Fields	55
3.2 Gross Tumor Volume	55
3.3 Clinical Target Volume	57
3.4 Internal Target Volume	57
3.5 Planning Target Volume	58
3.6 Organ At Risk	59
3.6.1 Types of OAR	59
3.6.2 Implied OAR of Cranial Radiosurgery	60
3.7 Planning Organ At Risk Volume	60
3.8 Remaining Volume at Risk	61
3.9 Imaging for GTV Definition	61
3.9.1 Liver	61
3.9.2 Head and Neck	61
3.9.3 Brain Tumors	61
3.9.4 Vascular Lesions of the Brain	62
3.9.5 Lung	62
3.9.6 Pancreas	62
3.9.7 Bone	63
3.9.8 Prostate	63
4. Treatment Planning Algorithms	65
4.1 Introduction	65

4.2	Classification of Algorithms	65
4.2.1	Factor-Based Algorithms	65
4.2.2	Model-Based Algorithms.....	66
4.3	Beam Model, Source Parameters, and Collimation System	67
4.3.1	Beam Model	67
4.3.2	Source Parameters and Collimation System.....	67
4.4	Dose Calculation Algorithms	68
4.5	Small Field Implications of Dose Calculation Algorithms.....	69
4.6	Considerations for Clinical Prescription Using Type-b Dose Calculation Algorithms in Small Fields	71
4.7	Implementation Considerations	73
4.8	Measurement Aspects of Treatment Planning Algorithm Commissioning.....	75
5.	Image-Guided Beam Delivery.....	77
5.1	Introduction	77
5.2	Purpose of IGRT in SRT.....	77
5.3	IGRT Technology.....	78
5.3.1	Immobilization Systems	78
5.3.2	Overview of Current IGRT Technologies.....	79
5.3.2.1	Planar systems.....	79
5.3.2.2	Volumetric systems.....	79
5.3.2.3	Nonradiographic systems	82
5.4	Radiation Dose from Image Guidance and Tracking.....	83
5.5	IGRT and Management of Respiratory Motion	83
5.5.1	Management of Respiratory Motion	84
5.5.1.1	Motion-encompassing methods	84
5.5.1.2	Breath-hold and forced shallow-breathing techniques	84
5.5.1.3	Respiratory-gating techniques.....	85
5.5.1.4	Respiration-synchronized free-breathing techniques	85
5.5.2	Image Guidance with Respiratory Motion.....	85
5.5.2.1	Image-guided techniques	86
5.5.2.2	Optical tracking systems.....	86
5.5.2.3	Hybrid systems.....	86
5.5.2.4	Delivery adaptation based on acquired information	86
5.6	Uncertainties in Image Guidance of Radiation Therapy Using Small Fields.....	87
5.6.1	Examples of IGRT Accuracy and Uncertainties	87
5.6.1.1	Intra-observer variability	87
5.6.1.2	Image-registration uncertainties	88
5.6.1.3	Inadequacy of surrogates for tumor position.....	89
5.6.2	Evaluation of the Total System Accuracy and Uncertainty.....	89
5.7	Quality Assurance for Image Guidance for SRT	91
6.	Quality Assurance	93
6.1	Introduction	93
6.2	QA of SRT Machines	94
6.2.1	QA of Linear Accelerators Adapted for SRT	94
6.2.2	QA of Gamma Stereotactic Radiosurgery System	94
6.2.3	QA of the Tomotherapy System.....	96
6.2.3.1	Laser localization	96
6.2.3.2	Geometric distortions.....	96
6.2.3.3	Imaging/treatment/laser coordinate coincidence	97
6.2.4	QA of CyberKnife®	97
6.2.5	QA for Dedicated SRT Accelerators.....	99
6.3	Uncertainties	99

7. Prescribing, Recording, and Reporting	101
7.1 ICRU Reporting Levels	101
7.2 Dose Prescription in SRT	102
7.2.1 Recommendation for Prescription in SRT	102
7.3 Reporting in SRT	103
7.3.1 Recommendation for Reporting at Level 2	104
7.3.2 Discussion and Rationale of Level 2 Reporting	105
7.3.2.1 Dose-volume specification	105
7.3.2.2 Dose-volume reporting specific to OAR and PRV	106
7.3.2.3 Dose homogeneity	106
7.3.2.4 Dose conformity	107
7.3.3 Reporting at Level 3	109
7.3.3.1 Reporting integral dose	109
7.3.3.2 Biology-based evaluation metrics	109
7.4 Reporting of Software Versions for Treatment Planning and Delivery	109
7.5 Reporting of Confidence Intervals	109
Appendix A: Clinical Examples	111
A.1 Lung Cancer	111
A.1.1 Patient History	111
A.1.2 Treatment Intent	111
A.1.3 Simulation	111
A.1.4 Target volume and OAR selection and Delineation	111
A.1.5 Planning Aims and DVH Constraints	111
A.1.6 Description of Treatment Planning System	111
A.1.7 Prescription	111
A.1.8 Patient-specific QA	111
A.1.9 Delivery	112
A.1.10 Dose Reporting	112
A.2 Prostate	112
A.2.1 Patient History	112
A.2.2 Treatment Intent	112
A.2.3 Simulation	112
A.2.4 Target Volume and OAR Selection and Delineation	113
A.2.5 Planning Aims and DVH Constraints	113
A.2.6 Description of Treatment Planning System	113
A.2.7 Prescription	113
A.2.8 Patient-specific QA	113
A.2.9 Delivery	113
A.2.10 Dose Reporting	113
A.3 Reirradiation with Stereotactic Radiotherapy	114
A.3.1 Patient History	114
A.3.2 Treatment Intent	114
A.3.3 Simulation	114
A.3.4 Target Volume and OAR Selection and Delineation	114
A.3.5 Planning Aims and DVH Constraints	114
A.3.6 Description of Treatment Planning System	114
A.3.7 Prescription	115
A.3.8 Patient-specific QA	115
A.3.9 Delivery	115
A.3.10 Dose Reporting	115
A.4 Spine Case using Helical TomoTherapy	115
A.4.1 Patient History	115
A.4.2 Treatment Intent	116

A.4.3	Simulation	116
A.4.4	Target Volume and OAR Selection and Delineation	116
A.4.5	Planning Aims and DVH Constraints	116
A.4.6	Description of Treatment Planning System	116
A.4.7	Prescription	116
A.4.8	Patient-specific QA	116
A.4.9	Delivery	116
A.4.10	Dose Reporting.....	116
A.5	Spine Case with CyberKnife	116
A.5.1	Patient History.....	116
A.5.2	Treatment Intent	116
A.5.3	Simulation	116
A.5.4	Target Volume and OAR Selection and Delineation	116
A.5.5	Planning Aims and DVH Constraints	117
A.5.6	Description of Treatment Planning System	117
A.5.7	Prescription	117
A.5.8	Patient Specific QA	117
A.5.9	Delivery	117
A.5.10	Dose Reporting.....	117
A.6	Brain Metastasis	118
A.6.1	Patient History.....	118
A.6.2	Treatment Intent	118
A.6.3	Simulation	118
A.6.4	Target Volume and OAR Selection and Delineation	118
A.6.5	Planning Aims and DVH Constraints	118
A.6.6	Description of Treatment Planning System	118
A.6.7	Prescription	118
A.6.8	Patient-specific QA	118
A.6.9	Delivery	118
A.6.10	Dose Reporting.....	118
A.7	Acoustic Neuroma.....	118
A.7.1	Patient History.....	118
A.7.2	Treatment Intent	118
A.7.3	Simulation	118
A.7.4	Target Volume and OAR Selection and Delineation	119
A.7.5	Planning Aims and DVH Constraints	119
A.7.6	Description of Treatment Planning System	119
A.7.7	Prescription	119
A.7.8	Patient-specific QA	119
A.7.9	Delivery	119
A.7.10	Dose Reporting.....	119
A.8	Hepatocarcinoma	119
A.8.1	Patient History.....	119
A.8.2	Treatment Intent	121
A.8.3	Simulation	121
A.8.4	Target Volume and OAR Selection and Delineation	121
A.8.5	Planning Aims and DVH Constraints	121
A.8.6	Description of Treatment Planning System	121
A.8.7	Prescription	121
A.8.8	Patient-specific QA	121
A.8.9	Delivery	121
A.8.10	Dose Reporting.....	121
	References	123

Preface

Stereotactic radiosurgery (SRS) was developed decades ago to obliterate malignant and non-malignant structures in the cranial vault. Obviously these were small in size often a few mm^3 and were treated in a few fractions. Conventional fractionated radiobiology was not employed. Even during these early times, treatment was characterized by small radiation fields, often less than 100 mm^2 , steep absorbed dose gradients, and simplistic definitions of radiated volumes. These features of course dramatically increased the process of measuring and establishing treatment absorbed dose values. Since this therapeutic approach preceded high-resolution CT to say nothing of MR, volume definitions were two dimensional and, at best, limited in scope. Finally, considerable development of beam delivery apparatus was needed and concentrated on spherically symmetric distributions of medium energy photon sources such as ^{60}Co . Despite these extraordinary limitations, significant success was achieved and utilization grew.

Presently, this therapeutic approach has significantly matured. In fact, advancements in diagnostic techniques and fidelity have and will lead to earlier and earlier tumor identification further increasing the use of SRS. Beam delivery techniques have expanded to include fixed spherically symmetric distributions of photon sources with variable field sizes and the ability to radiate the cranial vault. IMRT devices using axially symmetric rotation can deliver small fields in almost arbitrary geometry and to arbitrary locations in the body. Robotically position-controlled linacs can provide similar radiation fields outside of axial symmetry in similar sized radiation fields. In short, these devices can produce small three dimensional radiated volumes using exquisite image guidance. Absorbed dose to the treated volume is uniform and exhibits steep absorbed dose fall-off and normal tissue dose avoidance. Finally, these instruments have led to routine

treatments outside the cranial vault using hypofractionated schedules.

These advances have created a pressing need to provide guidance as appropriate in dosimetric techniques, volume definitions, radiobiological considerations, and needed image guidance for treatment planning. Dosimetric accuracy is always complicated and easily compromised when the range of directly ionizing particles, in this case electrons, exceeds the dimensions of the radiated volumes producing situations of electronic disequilibrium. Absorbed dose measurements which generally demand particle equilibrium for accuracy are compromised and require the application of various correction factors. The state of disequilibrium, steep gradients, and small volumes also perturbs the usual volume definitions such as PTV, GTV, and OAR's. Stereotactic Radiation Therapy (SRT) requires special care in prescribing, recording, reporting treatments to fully utilize the world-wide use of this technique. As absorbed dose gradients become steeper, radiated volumes become smaller and better delineated, and tumor treatment approaches ablation, conventional radiation biology is less useful. While linear-quadratic cell response functions allow a confident adjustment to fraction dose and time, hypofractionation with dose escalation changes the underlying biology in as yet unknown ways.

All of these phenomena require even greater attention to the specifics of treatment prescribing, recording, and reporting. The ICRU has always stressed such activities and the present Report is consistent with prior ICRU Reports in the radiation therapeutic area. These include ICRU Reports 50 (ICRU, 1993), 62 (ICRU, 1999), and 83 (ICRU, 2010). We anticipate the ever increasing utilization of SRT as an advanced treatment modality.

Paul M. DeLuca, Jr.

Glossary

3D	three-dimensional (imaging or radiation therapy)
4D	four-dimensional (imaging or radiation therapy)
4D-CT	four dimensional CT imaging
4D-PET/CT	four dimensional integrated positron-emission tomography and CT imaging
AAA	anisotropic analytical algorithm
ABC	active breathing control
AVM	arteriovenous malformation
AXB	Accuros® XB algorithm
BED	biologically effective dose
BHCT	breath-hold computed tomography imaging
CBCT	cone-beam computed tomography
CISS	constructive interference in steady state sequence (MRI)
CPDE	charged-particle disequilibrium
CPE	charged-particle equilibrium
CT	computed tomography
CTV	clinical-target volume
CVD	synthetic-diamond detector
DCE-MRI	digital-contrast enhanced MRI
DRIVE	driven-equilibrium fast-spin echo sequence (MRI)
DRR	digitally reconstructed radiograph
DSA	digital-subtraction angiography imaging
DSB	double-strand (DNA) break
EFD	electron-field diode
EPID	electronic portal-imaging device
EPR	electron paramagnetic resonance
EQD _{2,n}	equi effective dose in 2 Gy fractions (index n is the α/β ratio used)
FB	free-breathing
FFF	flattening-filter free (x-ray beams from linear accelerators)
FIESTA	fast imaging employing steady-state acquisition sequence (MRI)
Five R's	(attributed to Withers): repair of sublethal damage; reassortment and redistribution of cells in the cell cycle; reoxygenation over the course of therapy; and cellular repopulation and division over the course of therapy
FLAIR	fluid-attenuated inversion-recovery sequence (MRI)
FSB	forced shallow breathing
FWHM	full width at half maximum
GI	gastrointestinal system
GSR	gamma stereotactic radiosurgery
GTV	gross tumor volume
HDR-BT	high dose-rate brachytherapy
HRS	hyper radiosensitivity
IGRT	image-guided radiotherapy
IMRT	intensity-modulated radiation therapy
IR-LEDs	infrared-light-emitting diodes
ITV	internal target volume
$k_{Q,Q0}$	beam-quality correction factor (also known as k_Q)

PRESCRIBING, RECORDING, AND REPORTING SMALL BEAM SRT

LCPDE	lateral charged-particle disequilibrium
LCPE	lateral charged-particle equilibrium
LET	linear energy transfer
LQ	linear-quadratic equation (radiation biology model)
LQC	linear-quadratic-cubic model
LQL	linear-quadratic linear model
MC	Monte Carlo (context of calculation technique or treatment planning algorithm)
mDIBH	moderate deep-inspiration breath hold
MLQ	modified linear-quadratic model
MOSFET	metal-oxide semiconductor field-effect-transistor dosimeter
MRI	magnetic-resonance imaging
MRS	proton magnetic-resonance spectroscopy imaging / analysis
<i>msr</i>	machine-specific reference field
MU	monitor unit
NTCP	normal-tissue-complication probability
OAR	organ at risk
OAR	off-axis ratio
OER	oxygen-enhancement ratio
OSLD	optically stimulated luminescent dosimeter
PET/CT	positron-emission tomography combined with CT imaging
PFD	photon-field diode
PPP	pancreatic parenchymal phase imaging
PRV	planning organ at risk volume
PSD	plastic scintillation dosimeter
PTV	planning target volume
PVP	portal-venous-phase imaging
QUANTEC	quantitative analysis of normal-tissue effects in the clinic
RBE	relative biological effectiveness
r_{LCPE}	range of lateral charged-particle equilibrium
RTTT	real-time tumor tracking
SABR	stereotactic ablative radiation therapy
SBRT	stereotactic body radiotherapy
SDD	source-detector distance (sometimes used in context of source-isocenter distance)
SF	surviving fraction
SFD	small-field diodes (or stereotactic field diodes)
SLD	sublethal cellular damage
SRS	stereotactic radiosurgery
SRT	stereotactic radiotherapy (overall term that covers SRS, SBRT, and SABR)
SSB	single-strand (DNA) break
SSD	source-surface distance
T1	T1-weighted sequence (MRI)
T2	T2-weighted sequence (MRI)
TCP	tumor-control probability
TCPE	transient charged-particle equilibrium
TE	total effect
TERMA	total energy released per unit mass
TLD	thermoluminescent dosimeter
TMR	tissue-maximum ratio
TPR	tissue-phantom ratio
TPS	treatment-planning system
USC	universal survival curve
WFF	with flattening filter (x-ray beams from linear accelerators)

Abstract

Rapid developments in imaging and radiation-delivery technology have fueled the application of small photon beams in stereotactic radiation therapy (SRT). Historically, stereotaxy referred to the use of a three-dimensional coordinate system to localize intracranial targets and has been more recently extensively developed in extracranial clinical situations. SRT involves stereotactic localization techniques combined with the delivery of multiple small photon fields in a few high-dose fractions. In SRT, the therapeutic ratio is optimized through delivery of highly conformal absorbed dose distributions with steep dose fall-off ensuring optimal absorbed dose in the target volume combined with minimal normal-tissue irradiation. Consistent with previous ICRU Reports 50 (ICRU, 1993), 62, (ICRU, 1999), and 83, (ICRU, 2010), this Report recommends a strict definition of target volumes (GTV, CTV) by reviewing imaging modalities used in clinical practice. This Report covers fundamentals of small-field dosimetry, treatment-planning algorithms, commissioning, and quality assurance for the existing delivery systems, as well as the role of image guidance during delivery. Finally, it recommends a framework for prescribing, recording, and reporting stereotactic radiotherapy, and covers most of the pathologies eligible for stereotactic delivery (malignant and non-malignant).

Executive Summary

In the context of this Report, stereotactic radiotherapy (SRT) encompasses stereotactic radiosurgery (SRS), stereotactic body radiation therapy (SBRT), and stereotactic ablative body radiation therapy (SABR). SRT involves stereotactic localization techniques (*i.e.*, use of a three-dimensional coordinate system to localize the target) combined with the delivery of multiple small photon fields in a few high-dose fractions.

There is wide diversity in the clinical prescriptions for SRS and SBRT, some of which are based on pre-clinical studies, some based on modeling using the linear-quadratic (LQ) model, and others that result from trial-and-error experiences. The limitations of the LQ model in scenarios of SRS/SBRT might suggest the possible existence of new cell-death mechanisms related to stem cells, vascular damage, bystander effects, and immune-mediated effects, or combinations of these. Therefore, there is a need to develop a better rationale for current practice and future hypofractionation clinical trials by incorporating classical and new radiobiology and appropriately upgrading the modeling schemes for high doses to reflect new evidence-based understanding of tumor control and normal-tissue tolerances at higher doses per fraction. The understanding of the radiobiology of hypofractionation has been the subject of renewed intense interest driven by clinical successes and socio-economical benefits of shortened treatment times and potentially improved outcomes.

The role of clinical medical physics in radiation therapy is to ensure that the prescription is delivered accurately. Comprehensive quality assurance encompasses all aspects of radiation medicine ranging from SRT device acceptance, commissioning, image guidance, and delivery. Recent incidents in radiation therapy using small fields have indicated that the dosimetry of small fields is complex and prone to errors. The requirements in terms of accurate beam calibration, treatment planning, accuracy of delivery, and quality assurance are more stringent than in other areas of radiation therapy. The active collaboration among all professions in the SRT program is critical for treatment quality and patient safety.

Three main features dominate the dosimetry of small beams from accelerators. Firstly, absorbed-dose distributions formed by small beams are characterized by a lack of charged-particle equilibrium over a much greater fraction of the treatment volume than for conventional radiotherapies. This has implications in dose measurements as well as treatment-planning dose calculations, especially in the vicinity of tissue heterogeneities. Secondly, in small beams, part of the source is often occluded by the collimation system, leading to beam-penumbra overlap and a drastic reduction in output fluence rate. Overlap of penumbra leads to effective-beam broadening in small beams compared to the geometric beam definition. Thirdly, the measurement of absorbed dose from small beams is highly dependent on the size and construction details of the detector used. Conventional calibration techniques applicable to standard $10\text{ cm}^2 \times 10\text{ cm}^2$ radiation beams cannot be applied to small beams without modification and supplementary detector-correction factors must be accurately known. These features have cast considerable dosimetric uncertainty in small-field dosimetry.

Three basic criteria, mostly related to the material in the sensitive region of the detector, dictate the suitability of a particular detector for a small-field absorbed-dose measurement: (1) the sensitive region of the detector is water equivalent in terms of radiation-absorption characteristics; (2) the mass density of the sensitive region is the same as or close to the mass density of water; and (3) the size of the sensitive region can be made small compared to the field size. Physical phenomena that strongly affect detector response in small fields are the effects of volume averaging and fluence perturbation. The latter may be due to the use of materials with a density significantly different from water such as the gas cavity in gas-filled ionization chambers or metals in the wiring of diode detectors. None of the detectors currently available are ideal for small-field dosimetry.

In the formalism for reference dosimetry for SRT, a machine-specific reference field (*msr*) is introduced to account for the fact that modern small-field

radiation-therapy equipment cannot usually establish the conventional $10\text{ cm}^2 \times 10\text{ cm}^2$ field and that the *msr* is usually free of a flattening-filter. An ionization chamber-specific correction factor, $k_{Q_{msr},Q}^{f_{msr},f_{ref}}$, is applied because the calibration coefficient for the air-filled ionization chamber in the conventional field must be modified to account for these conditions.

The present Report recommends that different detectors be used to determine relative output factors and that the measured data are corrected with the type-specific $k_{Q_{clin},Q_{msr}}^{f_{clin},f_{msr}}$, correction factor values. Relative output factors measured in this manner should be cross-compared with those obtained by other centers on the same radiation equipment.

In SRT, the therapeutic ratio is optimized through delivery of highly conformal dose distributions with steep dose fall-off ensuring optimal dose in the target volume combined with minimal normal-tissue irradiation. Stereotactic radiotherapy delivers a high dose to the target while relying heavily on tight margins and steep dose gradients to reduce the effect on organs at risk. As introduced in ICRU reports 50 (ICRU, 1993), 62 (ICRU, 1999), 71 (ICRU, 2004), and 78 (ICRU, 2007), several volumes related to both tumor and normal tissues have been defined for use in the treatment planning and reporting processes. Delineation of these volumes is a mandatory step in the planning process, as dose cannot be prescribed, recorded, and reported without specification of target volumes and volumes of normal tissue at risk. In order to compare and reproduce clinical results, it is important that the definitions of the target and the organs at risk be as clear and as reproducible as possible. The GTV, CTV, and OAR correspond, respectively, to volumes of known (GTV), and/or suspected (CTV) tumor infiltration, and volumes of normal tissues that might be irradiated and affect the treatment prescription (OAR). The GTV and CTV have an anatomical/physiological basis, in contrast to the ITV, PTV and PRV, which are concepts introduced to ensure that the absorbed dose delivered to the respective CTV and OAR is clinically acceptable. There is no unique definition of these volumes for small-field radiation, but there are peculiarities in how these volumes are designed and used. In SRT, there may be cases for where there is no GTV or the GTV is not explicitly defined, but where the PTV is based directly on a CTV (e.g., a surgical cavity following the resection of a brain metastasis). In the treatment of targets that are not tumors (benign or malignant), the concept of the CTV might be less applicable - such is the case for the treatment of tremor, trigeminal neuralgia, or arterio-venous malformations. The use of an expansion from the GTV to the CTV is routinely outside of the cranial vault, hence, as a clinical choice, it could be decided to have

GTV and CTV represent identical volumes. When this is the case, the CTV should still be defined.

According to techniques and equipment used for SRT, image acquisition can vary. Formal written protocols must be available in any department, precisely describing the imaging process considered for volume definition, image thickness, timing of acquisition, *etc*. Although small-field treatments tend to be delivered over fewer sessions and are thus less forgiving to random error, the immobilization and image-guidance protocols tend to be more stringent and thus permit tight PTV margins. In cranial radiosurgery, the total geometric uncertainties are usually quite small, typically less than 1 mm. Even if the absorbed dose will be prescribed directly to the GTV, it is recommended to report it to a PTV. It is then possible to compare and evaluate clinical studies.

Dose-volume constraints for OARs are mainly derived from retrospective clinical observations of treatment with “conventional fractionation.” As small-field radiotherapy is typically applied in larger individual fractions, knowledge from cohorts treated at 1.8 Gy – 2 Gy per day are not directly applicable and tolerances will have to be re-learned from new clinical experience. This Report recommends an internal policy to record and evaluate observed toxicity within the treatment schedule, and strongly recommends implementing or joining prospective multicenter studies.

In SRT, the accurate modeling of lateral electron scattering in heterogeneous regions with mass densities that differ significantly from water is critical. The impact of lateral electron scattering increases with increasing energy as the lateral range of the secondary electrons increases. Therefore, for treatment planning in SRT, advanced model based absorbed-dose-calculation algorithms such as Monte Carlo, or deterministic algorithms should be used to ensure that dose in tissue of heterogeneous density is accurately calculated. To this end, accurate knowledge and modeling of the collimation devices [*i.e.*, collimators and multileaf collimator (MLC)] and their leakage, combined with accurate knowledge of the relative location, shape and size of the source spot, play a key role in the accurate beam-model representation and ultimately in the accurate calculation of absorbed dose. A common consequence of Monte Carlo treatment planning is statistical noise in the calculated absorbed-dose distributions. Dose reporting, dose uncertainty, grid-size effects, and dose calculations in small volumes, need to be carefully considered. For small-field planning-system commissioning, the suitability of the detector used in the data acquisition is essential. The commissioning and validation process should include tests that verify the performance of the algorithm in the presence of tissue heterogeneities.

Executive Summary

The use of image guidance is critical in the application of SRT. To minimize daily treatment variations, image-guided radiation-therapy (IGRT) technology has been widely adopted to provide real-time geometric and anatomic information with the patient in treatment position. In SRT treatments, these daily variations have a greater impact on the absorbed-dose distribution compared to conformal radiation therapy, due to the high gradients present in the absorbed-dose distribution delivered with small fields. Furthermore, a hypo-fractionated scheme is usually employed in SRT and, therefore, daily correction to match the original plan is required instead of averaging the dose delivery over many fractions. This involves accounting for both shifts of the target prior to delivery and the changes in the target volume or internal-organ variations during delivery. SRT is based on precision in addition to accuracy of the absorbed dose delivered to the target. This precision is essential in the delivery of high doses per fraction in few fractions. Therefore, the verification of target location in all treatment positions during all fractions for the entire procedure should ideally be achieved at sub-millimeter precision.

In order to take advantage of the steep dose gradients obtained with SRT, selection of the CTV-to-PTV margin is critical. Continuing evaluation and management of intra-fraction target location is important since organ motion can affect the consistency between delivered dose and the planned dose in the PTV and PRVs. The likelihood of missing moving targets during the treatment could dramatically increase without IGRT.

An institution embarking on radiation medicine using small beams should establish a comprehensive quality-assurance (QA) program. A QA program for radiation therapy using small beams consists of procedures that ensure that the prescribed absorbed-dose distribution is faithfully delivered to the intended target, and its success requires the involvement of the entire radiation-therapy professional team. For SRT treatments, execution of this mandate requires an extraordinary amount of vigilance. For such a complex and delicate procedure it is advisable to establish a specialized and dedicated team. In general, QA procedures will be specific to the particular equipment and to the implemented technology. It is important that the institution that starts a new small-beam therapy program has access to dosimetric data of users of the same equipment in other established institutions, obtains independent checks from another

institution, and preferably, performs end-to-end checks through an independent external audit. Other important aspects in patient-specific QA are related to the type of phantoms and detectors currently available on the market that are not always suitable to measure the steep gradients present in SRT treatment plans. It is beneficial to develop a checklist to be used for each SRT treatment before a patient is treated.

The process of developing a treatment plan consists of three major components:

- (1) The definition and description of the “planning aims” using image-based information from which all of the volumes of interest are delineated and the desired absorbed-dose levels are specified (physician);
- (2) A complex beam delivery “optimization” process to achieve and, if needed, modify the initial “planning aims” (physicist); and
- (3) A complete set of finally accepted values, which becomes the “prescription” and, together with the required “technical data,” represent the “accepted treatment plan. The treating physician(s) and involved physicist(s) hold shared responsibility for this process.

For dose reporting, this Report recommends the following metrics:

- (1) $D_{50\%}$, PTV median absorbed dose. As this Report recommends a CTV be defined for each case, the $D_{50\%}$ can be also reported for the CTV. In the specific case of peripheral lung lesions, for which the absorbed-dose distribution is strongly affected by tissue-density variations, a dose to a target that does not include uninvolved lung parenchyma, $D_{50\%}$ (GTV / CTV) should be systematically reported.
- (2) The SRT near-maximum dose, $D_{near-max}$. For PTV V larger or equal than 2 cm^3 the $near-max$ volume represents 2 % of the PTV, as recommended in ICRU Report 83 (ICRU, 2010) ($D_{2\%}$). For a PTV V of less than 2 cm^3 , $near-max$ is an absolute volume of 35 mm^3 , in which case $D_{35\text{mm}^3}$ is reported.
- (3) The SRT near-minimum dose, $D_{near-min}$. For PTV V larger or equal than 2 cm^3 the $near-min$ volume represents 2 % of the PTV, as recommended in ICRU Report 83 (ICRU, 2010) ($D_{98\%}$). For PTV V of less than 2 cm^3 , $near-min$ is an absolute volume of 35 mm^3 , in which case $D_{V-35\text{mm}^3}$ is reported.

1. Introduction

1.1 Definition and Scope

A small photon field is usually characterized by the following limitations to accurate dosimetry: (1) lack of lateral electron equilibrium; (2) obscuring of the primary photon source by the collimation system; and (3) the limitations of conventional broad-field detectors to accurately measure absorbed dose under small-field conditions. Small photon fields are used both for intensity-modulated radiation therapy (IMRT) (ICRU, 2010) and for stereotactic radiation therapy (SRT), which is discussed in the present report.

Stereotaxy historically refers to the use of a 3-dimensional (3D) coordinate system to localize intracranial targets. As of the time of publication of this report the concept of stereotactic treatment has been expanded to refer to the accurate and reproducible localization of the clinical target in space (*i.e.*, at the mm level) and in time.

SRT involves stereotactic localization techniques combined with delivery of multiple small photon fields in a few high-dose fractions, leading to a highly conformal dose delivery with steep dose gradients. Stereotactic localization techniques may include the use of relocatable rigid frames, image-guidance techniques, and other positioning tools. Stereotactic radiosurgery (SRS) is intracranial SRT delivered in a single fraction. Stereotactic body radiation therapy (SBRT) is the use of SRT for extracranial treatments. Other nomenclature such as SABR, which stands for stereotactic ablative (body) radiotherapy, is also used, but is not recommended by ICRU.

In SRT techniques, a high dose per fraction is a prescribed absorbed dose to the target per treatment fraction. The dose is higher than what would be delivered using conventional radiation therapy in a similar situation. A “few fractions” refers to a number of fractions that is significantly lower than the number of fractions that would be delivered using conventional radiation therapy in the identical clinical situation (*i.e.*, typically 25 fractions or more) in a non-palliative scenario. Fractionation protocols can range from a single fraction of over 180 Gy (Kooshkabadi *et al.*, 2013) for functional indications to 12 fractions of 4.3 Gy (Ritter *et al.*,

2009) in early prostate cancer. The therapeutic ratio is enhanced through delivery of highly conformal dose distributions with steep dose fall-off ensuring optimal dose in the target volume with minimal normal tissue irradiation.

The scope of this report is to discuss spatially small photon beam delivery, including dosimetry, commissioning, and quality assurance as well as to recommend a framework for prescribing, recording, and reporting stereotactic radiotherapy. This report covers all pathologies eligible for stereotactic delivery (malignant and non-malignant). Note that other radiation therapy techniques may deliver a high dose per fraction in a well-defined target volume, such as, intra-operative radiation therapy or high dose rate brachytherapy (HDR-BT). These techniques are not discussed.

1.2 Aim of Report

ICRU has been involved in a continuous effort to improve uniformity in defining terms and concepts and in specifying doses for reporting in radiation therapy.

ICRU Report 29, “Dose Specification for Reporting External Beam Therapy with Photons and Electrons”, was published in 1978 (ICRU, 1978) and ICRU Report 50, “Prescribing, Recording, and Reporting Photon Beam Therapy”, was published in 1993 (ICRU, 1993). A supplement to Report 50 (ICRU Report 62) was later published (ICRU, 1999) that included 3D conformal radiation therapy (3D-CRT). ICRU Report 83 on IMRT was published in 2010 (ICRU, 2010). ICRU Report 71 on electron-beam therapy (ICRU, 2004) and ICRU Report 78 on proton-beam therapy (ICRU, 2007) have also been published. As a general rule, the recommendations for prescribing, recording, and reporting special techniques in external photon beam therapy such as stereotactic treatments must be consistent with the previous ICRU recommendations. In particular, the same definitions of terms and concepts should be used where applicable. However, account must be taken of the clinical and technical uniqueness of each treatment approach.

The present report is based on concepts and definitions previously introduced in ICRU Reports 50, 62, and 83 (ICRU, 1993; 1999; 2010). It is a complementary report to ICRU Report 83 (ICRU, 2010) but covers a different field. The principles of optimized inverse planning, target definition, imaging, and 4D adaptation are very similar but dose volume prescription and reporting are different and require specific considerations.

The aims of the present Report are to provide a review of the physics and dosimetry of radiation therapy with small beams, quality assurance of stereotactic treatments with small beams and to provide a framework for consistency in prescribing, recording, and reporting treatment of patients with different technologies. Finally, clinical examples are provided for the main SRT indications.

1.3 History of SRS and SRT

Stereotaxis (stereo from the Greek root word for solid body and *taxis* from the Greek word for arrangement or order) relies on a detailed knowledge of human anatomy as well as highly precise radiological imaging techniques. Human brain mapping was developed in detail from the early 20th century and reliable brain atlases existed at the time that stereotactic techniques were first developed (Schaltenbrand *et al.*, 1977). The British scientist Robert H. Clarke and surgeon Sir Victor Horsley created the first recognized stereotactic frame to study the intact cerebellum of primates in 1906 (Clarke and Horsley, 1906). The Horsley–Clarke stereotactic frame relied on external anatomical landmarks such as the external auditory canal and orbital rims to guide a probe to structures inside the brain and was the first device to use a Cartesian coordinate system for locating brain structures. American neurophysiologist Ernest Spiegel and surgeon Henry Wycis created a stereotactic frame for human patients based on the earlier Horsley–Clarke frame (Spiegel *et al.*, 1947). This frame relied on x-ray pneumoencephalograms (requiring injection of contrast agent through a lumbar puncture) to locate an anatomical target for an invasive surgical probe.

SRS was first described in 1951 by Swedish neurosurgeon Lars Leksell (Leksell, 1951). Leksell used a stereotactic frame of his own design coupled with a 200 kV x-ray-therapy machine to treat patients for trigeminal neuralgia (a condition characterized by persistent episodes of intense facial pain). Leksell's strategy of precise stereotactic localization of a target and then irradiating the target with a focused beam of x rays was the first example of a minimally invasive procedure called radiosurgery, which has proliferated extensively since then. Leksell abandoned low-energy x rays and moved to the utilization

of protons at Uppsala University from 1957 to about 1967 (Larsson *et al.*, 1958). This work led Leksell and physicist Borje Larsson to the invention of a dedicated radiosurgery treatment device, the Leksell Gamma Knife (Leksell, 1968). This device contained 179 high-intensity ^{60}Co sealed radiation sources, distributed in an approximately hemispherical pattern and directed with extremely high precision to spherical volumes of 4 mm, 8 mm, or 14 mm in diameter. The radiation sources were housed in a massive 20 000 kg steel body (Fig. 1.1).

The Leksell Gamma Knife, first tested in 1967, was used only for treatment of functional diseases, since intracranial imaging at that time could not reveal brain tumors. All patients had the Leksell stereotactic frame affixed to their head (Fig. 1.1) and were then subjected to a painful pneumoencephalographic x-ray examination, where air was injected into the cerebrospinal column to displace cerebrospinal fluid from the brain ventricles. An anterior-posterior radiograph, paired with an orthogonal lateral radiograph, allowed Leksell to deduce the location of the ventricles, from which he could calculate, using brain atlases, the displacement to targets of interest such as the left or right globus pallidus of patients with Parkinson's disease. Leksell discontinued the use of the first unit, which was located at Sophiahemmet Hospital and had a new unit built for installation at the Karolinska Hospital in Stockholm in 1974, where it was used for many years. Two other units were custom built for neurosurgeons in



Figure 1.1. Leksell and Lindstrom with a patient being prepared for intracranial radiosurgery.

Introduction

Buenos Aires, Argentina and Sheffield, England and installed in 1984 and 1985, respectively (Bunge *et al.*, 1987; Walton *et al.*, 1987). Ultimately Leksell's invention was taken over by the Elekta Corporation, which delivered the first commercial Gamma Knife Model U to the University of Pittsburgh in 1987 (Wu *et al.*, 1990). The Gamma Knife Model U was specified to deliver an absorbed dose rate of 3 Gy min^{-1} at the isocenter of the treatment volume with the newly developed helmet, and was stated to have a mechanical precision of 0.5 mm or less, as verified by a radiographic test.

Radiosurgery with orthovoltage x rays, protons, and gamma rays, led to the development of similar systems with megavoltage x rays and ^{60}Co teletherapy units utilizing specialized collimators and stereotactic positioning frames. Barcia-Salorio *et al.* (1982) reported use of a special collimator with a ^{60}Co teletherapy unit in Vicenza, Italy. Betti and Derechinsky (1982) reported in that same year use of a photon beam from a 10 MV linear accelerator with the patient sitting in a movable chair (Fig. 1.2) while wearing the Talarach head frame to perform stereotactic radiosurgery in Buenos Aires.

Whereas gamma-ray stereotactic radiosurgery devices were dedicated to a single purpose, linear accelerators used for stereotactic radiosurgery and stereotactic radiotherapy began as conventional radiation therapy devices that were adapted for special procedures by the addition of specialized collimators and other devices. Colombo *et al.* (1985) used a photon beam from a 4 MV linear accelerator to produce up to 11 converging non-coplanar arcs. During a period of rapid development, other groups around the world reported on other linear accelerator

stereotactic radiosurgery techniques (Hartmann *et al.*, 1985; Houdek *et al.*, 1985). An example of a successful pioneering in-house implementation of linac-based radiosurgery was the McGill dynamic arc radiosurgery technique (Podgorsak *et al.*, 1987), which combined small field delivery with arc delivery in a coupled arc-couch motion (Fig. 1.3).

A seminal paper from the Joint Center for Radiation Therapy in Boston by Winston and Lutz led to the proliferation of commercial devices in the USA (Winston and Lutz, 1988). Prior to this time, all linear accelerator radiosurgery devices were custom made for each clinical facility. Another innovation at the University of Florida Medical Center was the introduction of a floor stand with two high precision ball bearings to support the small radiosurgical collimators and mitigate the inherent imprecision of the rotation of linear accelerator gantries of that era (Friedman and Bova, 1989).

An increase in linear accelerator based treatments began when the Gill-Thomas-Cosman frame was introduced at the Royal Marsden Hospital in London, England in 1991 (Gill *et al.*, 1991). This stereotactic frame was non-invasive (*i.e.*, no skin penetration) and could subsequently be repositioned within $<1.0 \text{ mm}$ (3D displacement). The frame was so successful that it was commercially manufactured (Radionics, Inc.) and used initially on a series of pediatric patients at the Joint Center for Radiation Therapy in Boston (Kooy *et al.*, 1994). The development of other relocatable frames followed rapidly.

The capability of locating, removing, and relocating a stereotactic frame led to the concept of stereotactic radiotherapy, where a course of between 3 and 25 fractions were used to administer radiation

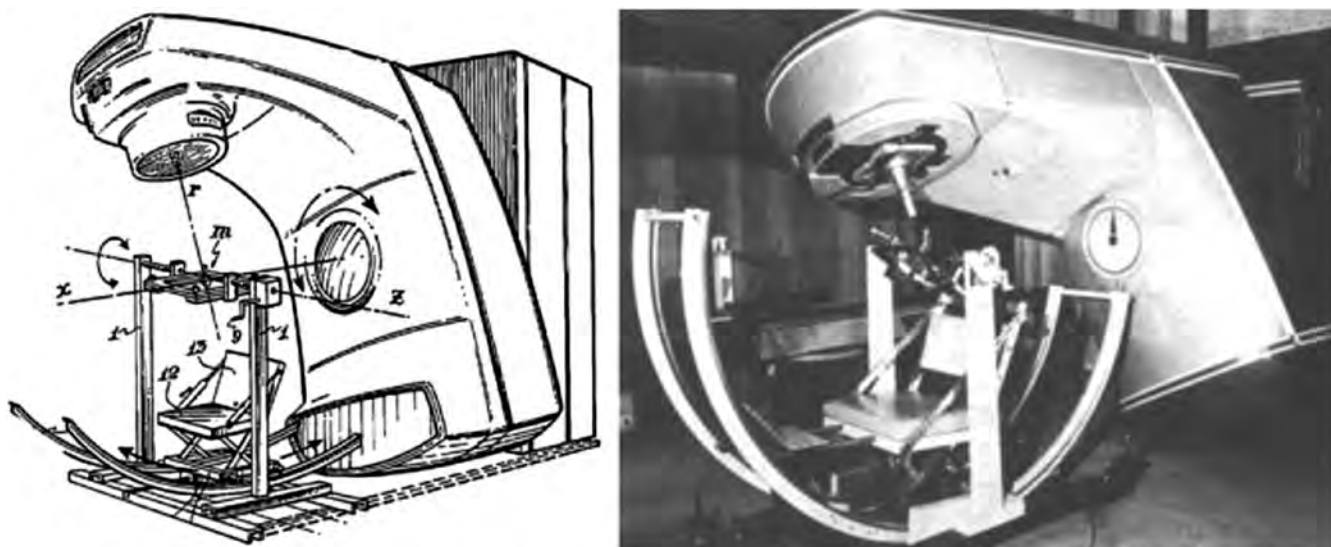


Figure 1.2. Drawing from patent and a photograph of the original "Betti chair," installed in Buenos Aires, Argentina (Derechinsky and Betti, 1986).

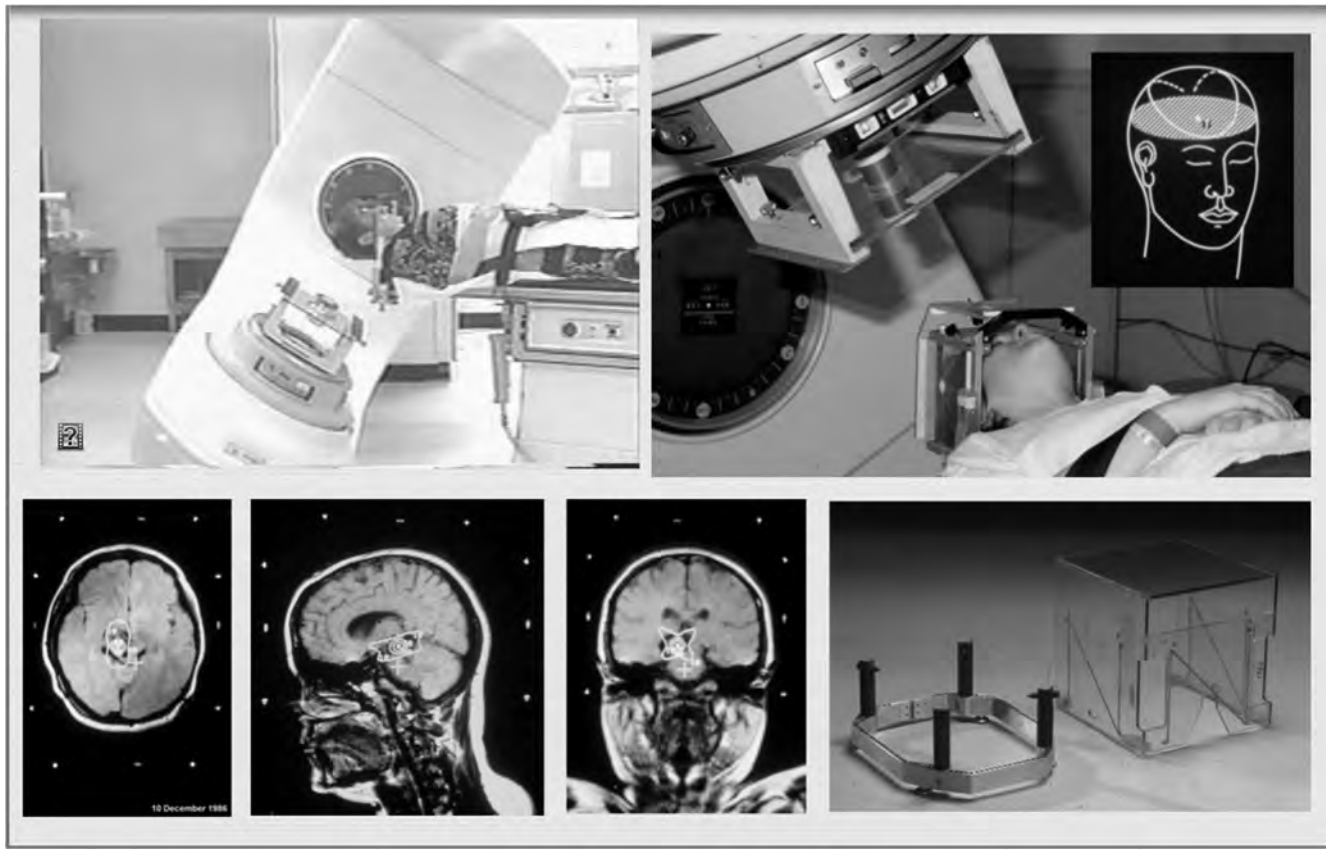


Figure 1.3. In-house developed McGill University stereotactic dynamic arc system for the delivery of SRT (Podgorsak *et al.*, 1987). *Upper panel*: Clinac 18® (Varian) accelerator and patient on couch performing a coupled gantry-couch motion, describing entry patterns as shown in the inset, top right. *Bottom panel*: from left to right: isodose distribution in three orthogonal sections and stereotactic localization box.

to a precisely defined intracranial volume (Schlegel *et al.*, 1993; Shrieve *et al.*, 1994; Souhami *et al.*, 1991). The American Association of Physicists in Medicine published a report on intracranial stereotactic positioning systems (Lightstone *et al.*, 2005). The radiobiological effects of fractionated *versus* single-dose irradiation for metastatic brain tumors was discussed by Manning (Manning *et al.*, 2000).

A new linear accelerator first installed at the University of California—Los Angeles Medical Center in 1997 was designed to be capable of both SRS and SRT treatments with little or no modification (Solberg *et al.*, 2001). The device, the Novalis system, employed both additional circular collimators attached to an accessory tray and a multileaf collimator (MLC) with leaves as narrow as 3 mm. The device also delivered what at the time was an exceptionally high dose rate (up to 8 Gy min^{-1}) with a beam-positioning accuracy of 0.4 mm. The multileaf collimator was conceived many years earlier as a flexible means of field shaping that did not rely on custom-made heavy metal blocks, especially in particle-beam therapy (Brahme, 1988; Ishigaki *et al.*, 1988; Sofia, 1979). The Novalis device

provided both circular collimators from 5 mm to 60 mm in diameter as well as a micro-MLC with 26 pairs of leaves varying in thickness from 0.30 cm for the central 14 pairs of leaves, to 0.45 cm for the adjacent 6 pairs of leaves, to 0.55 cm for the outer 6 pairs of leaves and a maximum field size of $10 \text{ cm} \times 10 \text{ cm}$ at isocenter. Another unique dedicated SRS and SRT linear accelerator, was first devised and tested at Stanford University Medical Center (Fig. 1.4), featuring a compact, x-band linear accelerator mounted on an industrial robotic arm (Adler *et al.*, 1999).

This device is now distributed by Accuray® Corporation under the trade name CyberKnife®. Both the Novalis device (and similar linear accelerator devices) and the robotic CyberKnife® device benefit from imaging including electronic portal imaging or kV or MV cone-beam imaging (Mosleh-Shirazi *et al.*, 1998). The imaging tools help in patient localization, they ensure high positioning accuracy (mean vector deviation of 1.0 mm) in repeated stereotactic radiotherapy treatments (Solberg *et al.*, 2008), have therefore gradually replaced the need for hard patient fixtures and led to reduced invasiveness and pain.



Figure 1.4. Prototype robotic radiosurgery system termed Neurotron 1000 ready for treating a patient. Dr. J. Adler is on the left.

1.4 Overview of Small-Field Radiation Therapy Equipment

Small-field stereotactic intracranial and extracranial photon treatments are delivered using a variety of multipurpose or dedicated treatment units. As described above, although stereotactic treatments were originally undertaken using convergent kilovoltage x-ray beams, photon treatments are now all delivered with megavoltage beams—either gamma rays from ^{60}Co sources or x-rays from linear accelerators. Treatments are delivered on dedicated devices or modified conventional radiotherapy units. Some examples of radiotherapy units are given below.

1.4.1 Dedicated Devices

1.4.1.1 Cobalt radiosurgery devices. The first dedicated radiosurgery device was the Leksell Gamma Knife. First introduced in 1968, the Gamma Knife was launched internationally in 1986–1987. The unit has evolved through multiple revisions but until the latest Perfexion redesign, the basic principle remained constant. In earlier units, multiple ^{60}Co sources (201) are permanently focused on a single point in space. Secondary collimation is provided by means of interchangeable “helmets” with small circular collimators for each ^{60}Co source, producing almost spherical dose distributions with diameters of 4 mm, 8 mm, 14 mm, and 18 mm. Immobilization and localization is provided by an invasive frame. Treatment planning involves packing spheres (delivery of spherical dose distributions to different isocenters) of varied diameters covering the target volume

(Wu and Bourland, 1999). Plan optimization can involve blocking individual beams by manually replacing circular collimators with “plugs”. On the Gamma Knife Perfexion model, the circular collimators are built into the device (now with three diameters: 4 mm, 8 mm, and 16 mm) and the device is designed to extend the treatment range into the upper cervical spine. Eight sectors of 24 sources (total 192 sources) can move independently to block the sources or position them in front of one of three sets of apertures. While non-spherical “shots” (single irradiation at a given stereotactic isocenter) can thus be produced, the basic planning principle remains the overlapping of multiple treatment isocenters within the target. The Perfexion device (Fig. 1.5), through the use of an optional relocatable frame system called EXTEND, also allows the possibility of fractionated treatments.

As an alternative to having a hemispherical distribution of fixed sources, rotational gamma-ray radiosurgery devices rotate a single sector of higher activity sources. In the case of the American Radiosurgery Vertex360 device (now known as the GammaART-6000, Cancer Care International, Shenzhen, China), 30 sources are used. Secondary collimation is achieved through a rotating inner shell which can block the sources or align them with apertures producing radiation spheres of 4 mm, 8 mm, 14 mm, or 18 mm. Invasive immobilization is used and plan optimization is again through sphere packing.

In extending the concept of multiple-focused cobalt beams beyond the cranial vault, multiple-ring-based, and C-arm-rotational systems have been developed. For example, the GyroKnife (GammaStar Inc., Shanghai, China) utilizes a single ring-mounted high-activity source that is triple-focused with three axes of rotation. This produces irradiated volumes with large isocenter-to-skin-dose ratios (>500:1). As with the intracranial ^{60}Co radiosurgery devices, plan optimization relies on sphere packing. Currently target localization relies on various forms of rigid or semi-rigid immobilization. Using instead 42 double-focused C-arm mounted ^{60}Co sources, the Orbiter (or Luna) (American Radiosurgery) packs non-spherical shots at its isocenter. The cobalt sources are shaped using interchangeable fixed collimators with apertures for beams of $6\text{ mm}^2 \times 6\text{ mm}^2$, $8\text{ mm}^2 \times 8\text{ mm}^2$, $14\text{ mm}^2 \times 14\text{ mm}^2$, $14\text{ mm}^2 \times 40\text{ mm}^2$, or $14\text{ mm}^2 \times 60\text{ mm}^2$.

1.4.1.2 Robotic non-isocentric linear accelerators. Developed at Stanford University Medical Center, the CyberKnife® (originally the Neurotron 1000, Fig. 1.4) consists of a 6 MV x-band linear accelerator mounted on an industrial robotic arm. A purely image-guided device, the CyberKnife® relies

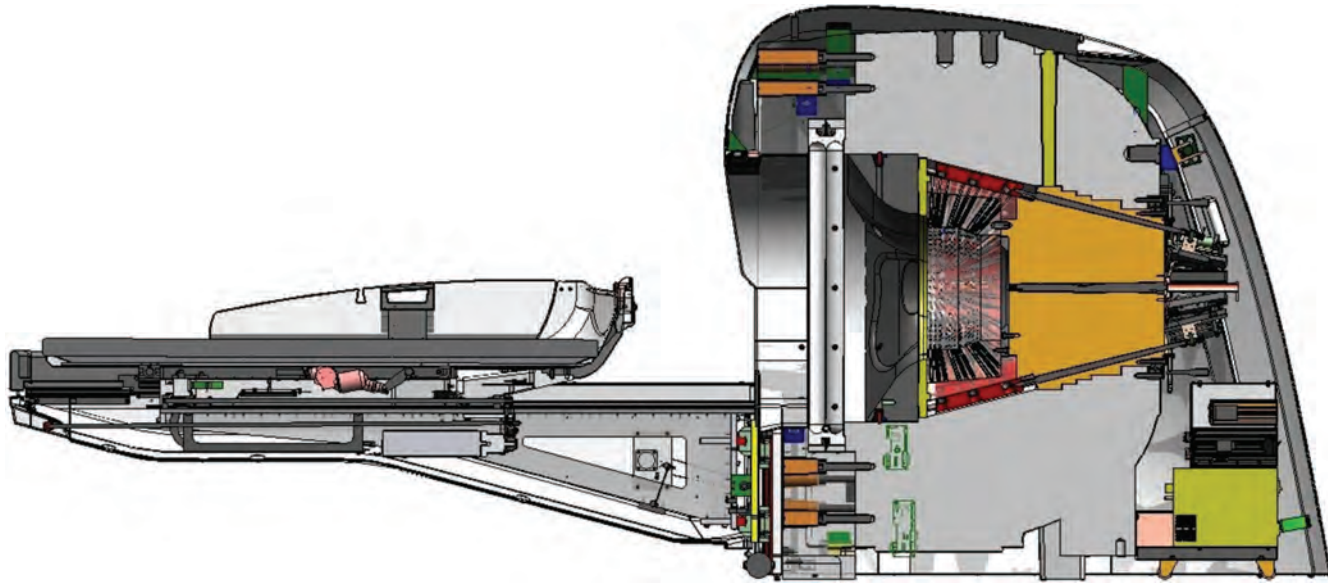


Figure 1.5. Cut away view of the Gamma Knife Perfexion (Elekta, Stockholm).

on stereoscopic planar imaging to direct multiple non-coplanar, non-isocentric beams onto fixed or moving targets inside or outside the head. The CyberKnife® uses either fixed conical collimators, a variable collimator called IRIS™ (two superposed banks of six tungsten segments) or InCise® MLC (CyberKnife® M6; Fig. 1.6). Respiratory motion management relies on predictive tumor tracking through correlation of external chest wall markers and either implanted x-ray fiducials or direct recognition of well-defined pulmonary tumors on planar images.



Figure 1.6. CyberKnife® system, Model M6, with the RoboCouch (Accuray, Sunnyvale, CA).

1.4.1.3 Dedicated gantry-based isocentric linear accelerators. With the increased use of stereotactic irradiation, various modifications to gantry-based linacs have been made to turn them into dedicated stereotactic devices. Depending on the manufacturer and version of the product, the differences between these dedicated devices and multipurpose modified linacs can be substantial or mainly cosmetic. A stereotactic linac is characterized by the availability of features such as:

- High-intensity photon beams (often achieved through reduced beam flattening)
- Integrated image-guidance system
- Integrated MLC with reduced leaf width
- Add-on conical collimators
- Improved precision of the mechanical isocenter
- Bundled motion management systems
- Bundled radiosurgery planning software
- Bundled 6D “robotic” couch tabletop

The typical tradeoffs when compared to standard radiotherapy accelerators are a reduced maximum field size and an increased purchase cost. Typical examples are the Varian Novalis® TX (with ExacTrac®, Brainlab), Varian TrueBeam STX® with Novalis, Varian EDGE® (Fig. 1.7) or Elekta Axesse® and VersaHD®.

1.4.1.4 Dedicated ring-based linacs. The helical tomotherapy unit was brought to the market by TomoTherapy Inc. and was designated the TomoTherapy Hi-Art® system. Tomotherapy is now marketed by Accuray, Inc. and the current version is the TomoTherapy HD® or HDA® system. An S-band 6 MV linear accelerator is mounted on a CT ring that rotates as the couch translates. During treatment, small beamlets are delivered through a binary MLC.

Introduction

Although recent modifications allow for delivery of non-rotational 3D conformal therapy; the Hi-Art system was primarily designed for inverse-planned intensity-modulated beam delivery and is now known as the HD (or HDA) system (Accuray, SunnyVale, CA) (Fig. 1.8). Although frame-based treatments are possible, helical tomotherapy devices are designed specifically for image-guided treatment. Pretreatment helical MVCT scans are acquired using a reduced-energy beam from the therapy linac. Treatments are essentially coplanar and there is currently no commercially available motion management system (e.g., tracking and gating).

With increased clinical use, dedicated SRT devices are being designed from scratch. One of these is the MHI-TM2000 or Brainlab Vero system (discontinued in 2015). The Vero system uses a gimbal-mounted C-band 6 MV linac on a ring (Fig. 1.9). A 15 cm × 15 cm field is defined by a 60-leaf MLC. In contrast to helical tomotherapy devices, the couch does not

translate during treatment but can rotate $\pm 60^\circ$ for non-coplanar treatments or what are referred to as “dynamic wave” treatments analogous to dynamic stereotactic radiosurgery where couch and gantry move synchronously to produce a unique non-coplanar beam path (Podgorsak *et al.*, 1987). The couch can provide pitch and tilt corrections while rotational corrections are possible through the main linac ring. Imaging is made possible by two coplanar flat-panel imagers capable of performing stereoscopy, fluoroscopy, and cone-beam CT. Tumor tracking would be possible through the use of the gimbal.

1.4.2 Non-Dedicated Stereotactic Radiosurgery and Radiotherapy Accelerators

Since the mid 1980s, conventional isocentric linear accelerators have been modified for the delivery of radiosurgery. Early modifications aimed at improving the mechanical accuracy of the couch and gantry used mechanical subsystems that supported the patients’ head and sometimes the conical collimators (Podgorsak *et al.*, 1987). Current systems rely on the improved mechanics of modern linacs and focus on beam collimation (*i.e.*, shaping small fields with conical collimators or micro-MLCs). Minor modifications to the couch to block movement during treatment delivery and allow an adjustable interface with cranial immobilization systems are implemented. In addition, dedicated radiosurgery treatment-planning software is provided. Motion management can be accomplished through various modular systems and can include



Figure 1.7. Varian Edge® accelerator (Varian, Palo Alto, CA).



Figure 1.8. TomoTherapy HD unit (Accuray, Sunnyvale, CA).

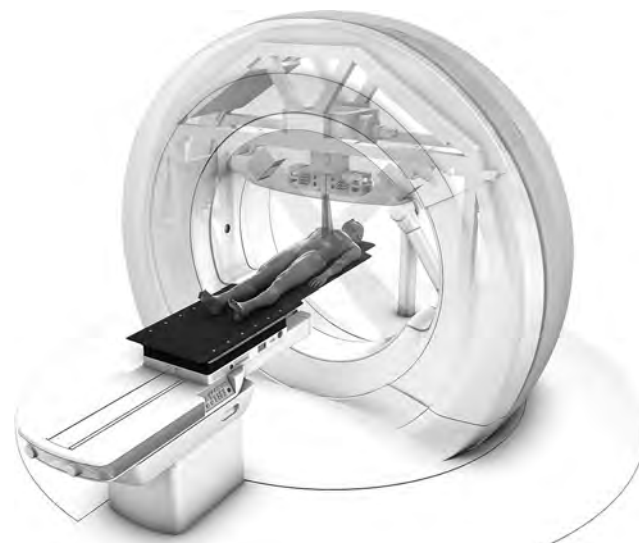


Figure 1.9. Brainlab Vero treatment unit with internal workings schematically exposed (Brainlab AG and Mitsubishi Heavy Industries Ltd.).

breathing suppression, gating, or so-called adaptive gating (where internal fiducials are tracked along with external fiducials), “active breathing control” or customized margins. Now that it is possible to implement volumetric imaging, stereoscopic imaging, and couch robotics on “conventional” accelerators, the dividing line between dedicated and modified accelerators has been significantly blurred.

Serial tomotherapy (Curran, 2003) has been used for stereotactic radiation. Intensity-modulated coplanar or non-coplanar “slices” are stacked through indexing of the treatment couch. An add-on device can aid this couch indexing. Treatment arcs from a standard gantry-based linear accelerator (this can also, in principle, be a gantry-based cobalt unit) are modulated through an add-on binary collimator. By their nature the treatments are inverse-planned. With cranial targets these treatments have typically relied on rigid immobilization, although in serial tomotherapy localization/image-guidance is independent of beam delivery (Young *et al.*, 2010).

1.5 Similarities and Differences Between 3D-CRT, IMRT, and SRT

The concept of SRT started with the need to deliver a high dose in a single fraction to intracranial targets. This was both biologically and clinically possible because of limited treated volumes and lack of organ motion. This concept of ablative treatment mimicked surgical removal of arteriovenous malformations, small neuromas, or small (*i.e.*, <3 cm maximum diameter) single metastases. The proof of concept obtained in two decades of experience has driven research in the field of extracranial treatments covering larger volumes and moving targets (stereotactic body radiotherapy: SBRT).

1.5.1 Inverse Optimization

Dose delivery in SRT has a different nature than dose delivery in IMRT. For IMRT it was shown that a set of intensity-modulated beams from multiple directions could be designed to produce dose homogeneity similar to conventional radiotherapy within the tumor but with superior conformality, especially for concave or other complex shaped target volumes, thereby sparing nearby normal tissues (ICRU, 2010). Rather than using relatively uniform-intensity distributions across each incident field, IMRT attempts to achieve more optimal dose distributions by varying the beam intensity (fluence) across each incident beam, usually by subdividing the beam into many smaller segments and modulating the dose in each segment. In SRT, the conformity is obtained through the use of multiple small beams that can be non-

coplanar and/or non-isocentric. Current techniques may combine the principle of IMRT (varying the fluence) and SRT (the use of arcs, the use of multiple small beams, *etc.*).

Similar to IMRT, SRT can be planned on the principle of “inverse treatment planning”. The word “inverse” was used in reference to the established body of mathematical inverse problem solving techniques, which start at the final or desired result and work backwards to establish the solution. So-called inverse treatment planning starts from a desired solution (*i.e.*, a series of descriptors characterizing the desired dose distribution within the tumor with additional descriptors designed to spare normal tissues). The inverse planning process works iteratively to help determine beam shapes and fluence patterns to achieve an optimal or acceptable dose distribution. An optimization procedure, which is an iterative search for the solution that minimizes the cost or maximizes the goodness, is guided by an objective function. The objective function is a mathematical function that specifies, with a single number, the value or merit (also called, cost or goodness) of the plan. The values of the descriptors may need to change at different stages of the process in order to achieve a compromise between different competing goals. Because of the iterative nature of finding the solution and the need to change values of the treatment descriptors, the term “optimized planning” will be adopted in the rest of this document to describe the treatment planning process for SRT as it was used for IMRT (ICRU, 2010).

Many advances and emerging concerns in radiation therapy in the past decade are not unique to SRT but also impact 3D-CRT and IMRT. Nevertheless, issues such as image guidance are more significant for SRT and differences in biological effects due to high dose per fraction used with small fields are unknown.

1.5.2 Imaging and 4D Adaptive Treatment

Selecting and delineating regions of interest is one of the most technically and intellectually challenging and time-consuming aspects of modern radiotherapy. SRT, 3D-CRT, and IMRT increase the need for accurate anatomic delineation and require an adequate description of the tumor location. In SRT, as in IMRT, the optimization process has no ability to constrain the dose to tissue structures that are not delineated. Consequently tissues containing tumor cells that are not delineated are unlikely to be adequately treated and sensitive structures not delineated may receive an unacceptably high dose. 3D imaging systems are the key to the determination of the tumor and normal tissue volumes. Modern image-acquisition systems are

increasing the sensitivity and specificity of tumor detection.

The typical SRT target is different than that of 3D-CRT/IMRT, e.g., prophylactic nodal radiation is uncommon and non-malignant targets frequent. As SRT uses steep gradients, high doses, and few fractions, the impact of setup errors is more significant than in conventional radiotherapy. Because of this, greater care must be exercised to reduce residual setup uncertainties—often at the cost of increased resource utilization or treatment time. The resulting planning target volumes (PTVs) margins can therefore be limited to a few millimeters or less.

Modern CT scanners have rotational periods of <1 s. Adequate image reconstruction only requires a gantry rotation of slightly more than 180° . This fast data acquisition speed enables multiple images to be acquired to characterize the motion during typical breathing cycles. These advances may make it possible to dynamically define the position and extent of the gross tumor volume (GTV) and clinical target volume (CTV) during a treatment fraction (e.g., the availability of 4D anatomic data improves the treatment of lung cancer because of lung motion evaluation) (Mageras *et al.*, 2004).

However, it has been recognized that delineation of the tumors and/or normal tissues in SRT has limitations, as target morphology and position may change not only during treatment, but also between fractions due to tumor response and/or patient weight loss. The ability to track these changes leads to adaptive treatment, which is also called 4D-adaptive treatment (Ramsey *et al.*, 2006). Real-time imaging tools are being developed to produce multiple 3D views of the patient immediately before and/or during treatment delivery—the ultimate goal being adaptation of the treatment plan before and/or during each treatment fraction.

Image guidance systems themselves have uncertainties and deformation of the patient's anatomy cannot be eliminated although its extent can be estimated with deformable registration techniques (Lu *et al.*, 2004). Beam delivery can perhaps be modified (Mohan *et al.*, 2005) to reduce these errors. Imaging at the time of treatment can be used to better define the pattern of errors or reduce the uncertainty of setup. Image-guidance can be used to define the margins for a specific protocol or treatment machine or to adjust a patient-specific margin using repeated imaging procedures. Yan *et al.* (1999) showed that such repeated imaging procedures can greatly reduce the systematic uncertainty in positioning with respect to the original planning image. When delineating a PTV, the different types of uncertainties and variations identified above should be estimated and combined. Even if the

setup uncertainty were to be completely eliminated there would still be uncertainty due to organ motion and to changes in the anatomy of the patient due to weight loss or tumor shrinkage (or growth). This contribution to the margin can be reduced with gating or tracking techniques or replanning (adaptive treatment) but the uncertainty cannot be eliminated completely. Adaptation is typically limited to adjustments in patient setup and occasional replanning between fractions (Fallone *et al.*, 2009).

The PTV (see Section 4) includes the CTV and a margin to take into account uncertainty of positioning, motion, and anatomical changes. The 4D information can be used in lung SRT to more accurately determine the optimal breathing phase to gate the beam and to determine how much of the breathing cycle can be safely used for irradiation when the treatment is gated (Mageras *et al.*, 2004; Seppenwoolde *et al.*, 2002).

1.5.3 Volume Definition

The concepts of GTV, CTV, and PTV were described in ICRU Reports 50, 62, 71, 78, and 83. Volume definitions for SRT will be detailed in Section 3. Historically, numerous SRT studies have been published without a strict definition of volume or margin. Contouring was performed with limited imaging and the concepts of GTV, CTV, and PTV were not used. These concepts have been progressively implemented as SRT became more extracranial and moved from single dose radiosurgery toward fractionated stereotactic radiotherapy. However, as with IMRT, and even with the best image guidance systems, variations, and errors cannot be totally eliminated and can be a significant factor if extracranial moving targets are treated.

Systematic errors may arise from artifacts and distortion in the planning CT (and in other image modalities, like CT-PET or MRI) and in the delineation of the target and organs at risk (OAR), due to blurred images or images that do not contain enough information (*i.e.*, morphological *versus* functional imaging). Other uncertainties arise from the inter and intra-observer variability in target delineation of GTV and CTV during planning (Keall *et al.*, 2002; Rietzel *et al.*, 2005; Steenbakkers *et al.*, 2006).

The margin defining the PTV is principally used to maintain the dose at or near the prescription value in the CTV. Historically, there have been limited means to make isodose surfaces conform to the PTV, but recently the degree of control over conformity has greatly improved with the use of inverse planning software and beam delivery hardware.

In radiation therapy, several approaches to quantify the CTV-to-PTV margin requirements have

been published (Austin-Seymour *et al.*, 1995; Balter *et al.*, 1996; Goitein and Schultheiss, 1985; Roeske *et al.*, 1995; Stroom *et al.*, 1999; van Herk *et al.*, 2000). Variations in the required margins can result from a variety of reasons. One example is the systematic error that arises if the planning CT image is not appropriately representative of the patient throughout the course of therapy. For example, if on the day of CT planning the patient's rectum is distended by bowel gas, the position of the prostate will be offset and perhaps rotated from its average position. A random variation about the average position can occur daily. Every investigation has concluded that systematic variations are more important than random variations. Daily CT guidance using an in-room CT system is becoming common practice to reduce systematic and random position variations (Forrest *et al.*, 2004; Ma and Paskalev, 2006). However, in SRT, because of the low number of fractions and the limited margins involved, it is critical to limit the systematic and/or random errors.

Margins allowing for positioning, motion, and anatomical changes are also required for OAR. The need to quantify margin requirements is of increasing relevance for SRT. Having realistic margins for both the tumor volume and any organ at risk volume allows the planning process to be a better compromise between an adequate dose to the PTV and a safe dose to normal tissue. Factors affecting margin requirements to define the PTV include:

- patient-related factors such as organ movement, organ deformation, patient motion;
- mechanical properties of the delivery device such as gantry sag, robot position accuracy, couch motion uncertainties;
- treatment plan issues such as the number of fractions, the dose gradient;
- human factors such as contouring uncertainties; and
- imaging and informatics issues such as image distortion and image registration uncertainties

Patient position and setup issues include reproducibility of placement of relocatable frames, flexing of frames, laser alignment, imaging to radiation field alignment, registration uncertainties for stereoscopic images, variations in the relationship between implanted fiducials, and the target.

These factors will vary from center to center and, within a given center, from machine to machine and from patient to patient. The use of patient immobilization devices, the application of quality-assurance programs, and the skill and experience of the radiographers/radiotherapists are also important

and must be taken into account. Also, the use of different image-guidance systems or other uncertainty-reduction techniques may significantly alter the size of the required margins. Standardized methods for determining the margins must be established and followed to ensure that the margins are sufficient but not excessive.

1.5.4 Dose–Volume Histograms in SRT

The evaluation of PTV coverage is quantified by the use of dose–volume histograms (DVHs). The DVH has become a critical tool to evaluate complex 3D dose distributions (Drzymala *et al.*, 1991).

Cumulative DVHs are histograms of the volume elements that receive at least a given absorbed dose, and they are usually expressed as either the absolute volume or the volume relative to the total structure volume, receiving at least an absorbed dose, D . DVHs can be used to determine values such as minimum dose, maximum dose, or median dose. The median dose $D_{50\%}$ divides the dose distribution into two equal volumes, with 50 % receiving more than $D_{50\%}$ and 50 % receiving less. The median dose is often a good choice for a representative absorbed-dose value for the PTV even though it does not provide information about where in the volume the median absorbed dose might occur and is thus less useful if the absorbed-dose distribution in the structure is highly heterogeneous.

Dose heterogeneity is a consequence of overlapping isocenters and can be otherwise employed to achieve steep dose gradients at the PTV margin and/or an increased mean target dose. Dose heterogeneity will be reflected in the DVH where there will often be a larger disparity between minimum and maximum PTV dose. As the absolute target volumes may be very small, relative target volumes may fall below the volume of a single voxel of the image set used for treatment planning. Maximum and minimum doses will thus be statistically and clinically unreliable. When the areas of high dose are located with GTV, they should not be harmful (as they can be when they are located in normal tissue which comprises the GTV to PTV margin). Whether dose heterogeneity is desirable when homogeneity with sufficient dose conformity can be achieved remains a matter of clinical debate.

1.5.5 Radiation Biology of Small Field Radiation Therapy

The understanding of radiation biology of hypofractionation in SRT has been the subject of renewed interest driven by recent clinical successes as well as the socioeconomic benefits of shortened treatment times and potentially improved

outcomes. Hypofractionation with significant dose escalation can be accomplished as a result of improved geometric localization thereby allowing higher target doses with minimal increases in normal tissue damage. With increasing dose per fraction, a process similar to macroscopic ablation is gradually replacing the conventional damage/repair biologic response. The transition from deliveries involving larger volumes irradiated under conditions of more uncertain geometric localization and significant normal tissue exposure into deliveries that are highly localized and ablative includes biologic responses from both scenarios. Available clinical data generally support the application of the standard linear quadratic (LQ) model in the range of 1 Gy to 5 Gy per fraction (Steel, 1993). Beyond this dose the validity of the standard LQ model to predict response to SRS and SBRT/SABR, (in regimens of >5 Gy dose per fraction) is a matter of debate (Brown *et al.*, 2014; Kirkpatrick *et al.*, 2008; Orton, 2012; Sheu *et al.*, 2013; Song *et al.*, 2013). The background of this debate is briefly summarized below preceded by a discussion of the main physical and biological variables contributing to response.

1.5.5.1 Effect of physical variables on biological response

Geometrical window of opportunity. The development of advanced image-guided delivery systems including the use of particle therapy allows for considerable geometrical sparing of normal tissues. This creates a so-called “window of opportunity,” which allows for the safer eradication of the tumor with higher dose per fraction, reduced margins and higher gradients outside the target leading to lower risk of normal tissue toxicity compared to a decade ago (Brown *et al.*, 2014; Orton, 2012).

Treatment duration. Time plays a delicate role in achieving an optimal therapeutic gain [*i.e.*, the difference in tumor control probability (TCP) to normal tissue complication probability at an accepted maximum tolerance level] and can be divided into intra-fraction (*i.e.*, delivery) time, inter-fraction time (*i.e.*, period between fractions), and the overall treatment time. Increasing the intra-fraction time as experienced in hypofractionation treatments (*e.g.*, SRS or SBRT) allows for sublethal damage repair in both the tumor and normal tissue and since repair half times for tumors are generally shorter than for normal tissue, particularly for early damage, increasing the intra-fraction time reduces the therapeutic gain. It is suggested that a fraction delivery that lasts more than half an

hour might lead to a significant loss of cell sterilizing effect and hence a reduction in tumor biologically effective dose BED is defined as $BED = nd(1 + d/(\alpha/\beta)) - \ln(T - T_k)/\alpha T_p$ with n the fractions of d Gy given in an overall time of T days and tumor repopulation does not start until day T_k with k for kick-off, or onset, of the delayed repopulation during fractionated irradiation (Fowler *et al.*, 2004). Increases in the time between fractions, or the whole treatment period, will result in a reduction in BED due to proliferation and radiation-induced repopulation. Mechanisms that govern repopulation are summarized by the 3As: *asymmetry loss*; *acceleration of stem-cell divisions*; and *abortive divisions* (Dorr, 1997). It is also recognized that sufficient inter-fraction time (about 24 h) allows for reoxygenation and improved cell killing as discussed below. It has been reported that prolonged treatment periods have little sparing effect on late responding tissues compared to early responding tissue as noted in some hyper-fractionation trials (Hall and Giaccia, 2006).

Dose rate. To first order, as the dose rate is decreased and the exposure time is protracted, the BED is reduced as discussed above. However, an inverse effect takes place when the dose rate falls below a critical value (*e.g.*, 0.4 Gy h⁻¹ in HeLa cells), in which an increase in cell radiosensitivity is observed with decreasing dose rate below 1 cGy min⁻¹ because cells fall into a so-called low-dose hyper-radiosensitivity (HRS) range (Mitchell *et al.*, 2002).

Dose heterogeneities. The obvious effect of dose heterogeneity is the potential lack of appropriate coverage of the tumor causing hot and cold spots, which may compromise tumor response by not delivering the curative dose. At the same time, the delivered dose may lead to some normal tissue being irradiated with lower doses that would fall within the HRS range mentioned above. The potentially higher cell kill would be underestimated using the standard LQ model (Joiner *et al.*, 2001).

1.5.5.2 Effect of biological variables on biological response.

There are currently two main interpretations for the current clinical success of SRS/SBRT treatments. One interpretation suggests that conventional radiation biology principles (5Rs) and the LQ model are adequate to explain the effects of large dose per fraction and the currently observed advantages are mainly attributed to the Geometrical Window of Opportunity (Section 1.5.5.1) that is expanded by advancements in

image-guidance and treatment delivery techniques (Brenner, 2008; Brown *et al.*, 2014; Orton, 2012). The other interpretation highlights some of the conflicting issues of the conventional radiobiology principles and the limitations of the LQ model in scenarios of SRS/SBRT suggesting the possible existence of new radiation biology that may involve mechanisms related to stem cells, vascular damage, abscopal, and immune-mediated effects or a combination of these (Demaria *et al.*, 2015; Kirkpatrick *et al.*, 2008; McMahon *et al.*, 2015; Song *et al.*, 2013).

1.5.5.3 New radiation biology concepts or not? Proponents of new radiation biology concepts cite that under certain SRS and SBRT regimens conventional radiobiology fails to explain outcomes, for instance SRS or SBRT delivery is relatively longer than conventional fractionation allowing for higher rates of SLD repair as mentioned before, where a fraction delivery in excess of 30 minutes may lead to loss of BED (Fowler *et al.*, 2004). Moreover, at large doses (e.g., >10 Gy/fraction), significant vascular damage occurs, leading to a tumor microenvironment of hypoxia and acidification, both of which prevent reoxygenation. High doses prevent cell cycle progression and cells undergo interphase death in the cell cycle phases where they are irradiated rather than being redistributed. Repopulation during the shortened 1 weeks to 2 weeks period may be negligible as well. Furthermore, they assert that the LQ model may not be appropriate at the high doses per fraction encountered in SRS/SBRT because it was derived largely from *in vitro*, rather than *in vivo* data, and thus does not consider the impact of ionizing radiation on the supporting tissues nor does it consider the impact of the subpopulation of radioresistant clonogens (*i.e.*, cancer stem cell) or vascular damage (Kirkpatrick *et al.*, 2008; Song *et al.*, 2013).

On the other hand, opponents of the need for new radiobiological concepts, argue that the 5Rs and the LQ model are supported by available preclinical and clinical data and there is little evidence to suggest otherwise (Brenner, 2008; Brown *et al.*, 2014). For instance, in the case of lung cancer, Brown *et al.* showed that dose escalation (BED > 100), rather than new radiobiology concepts can explain the efficacy of SBRT with early stage non-small cell lung cancer (NSCLC) as shown in Fig. 1.10 (Brown *et al.*, 2013). This issue is still a subject of ongoing debate in the literature given the uncertainties in the presented data.

1.5.5.4 Clinical prescriptions and dose tolerances for hypofractionation. There is wide diversity in the clinical prescriptions for SRS

and SBRT treatments, some of which are based on preclinical studies, some based on modeling using the LQ, and others are trial and error experiences. Therefore, a better rationale for current practice and future hypofractionation clinical trials must be developed by incorporating classical and new radiation biology concepts and appropriately upgrading modeling schemes for high doses to reflect evidence-based new understanding of tumor control and normal tissue tolerances at higher doses per fraction. A number of areas of improvement are summarized below.

LQ limitations and alternative models. As discussed, the validity of the LQ model for doses above 5 Gy has been the subject of intense debate in the literature (Brenner, 2008; Brown *et al.*, 2014; Kirkpatrick *et al.*, 2008; Song *et al.*, 2013). Regardless, it is recognized that the LQ model is an approximation to more sophisticated models (Curtis, 1986). Therefore, several modifications have been introduced to the LQ model to allow better fit to high doses per fraction. These modifications to the LQ model effectively aim to straighten the survival curve at high doses, where it fails. This could be achieved by simply having higher α/β values in cases of rapidly proliferating and hypoxic tumors (Brown *et al.*, 2014; Fowler, 2006) or by developing alternates to the standard LQ model such as the modified LQ (MLQ), the linear-quadratic-linear (LQL) (Guerrero and Carlone, 2010; Guerrero and Li, 2004), linear-quadratic-cubic (LQC) (Joiner and Kogel, 2009), the universal survival curve (USC) (Park *et al.*, 2008), and the generalized LQ (gLQ) (Wang *et al.*, 2010) among others. It should be noted that caution should be used when interpreting and applying these models to clinical data and comparing their performances in terms of the parameters setup, dose prescription, isodose lines, and the size of irradiated volume.

Following advances in informatics and biotechnology, an alternative promising approach to modifications to the LQ model is to explore systems-based solutions that are able to integrate a wealth of information ranging from clinical, biological in addition to dosimetric and timing data into a more robust evidence-based advanced computational model. Using these system approaches, intra-radiotherapy changes and post-radiotherapy treatment outcomes could be optimized through using top-down approaches based on complex systems analyses (*e.g.*, machine learning methods) (El Naqa, 2013) or bottom-up approaches based on first principles of radiation physics and biology to model cellular damage temporally and spatially (*e.g.*, multiscale-modeling with Monte Carlo techniques) (El Naqa *et al.*, 2012).

Introduction

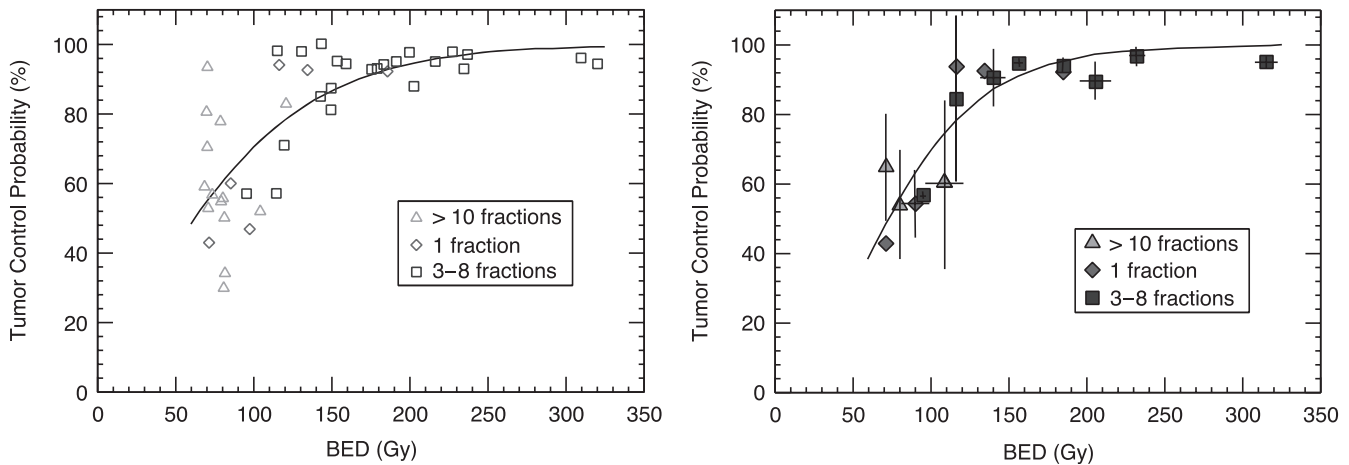


Figure 1.10. Tumor control probability (TCP) as a function of biological effective dose (BED) for stage I non-small cell lung cancer. *Left:* Raw local control rates (≥ 2 years) with different symbols distinguishing regimens of 3-dimensional conformal radiation therapy (3D-CRT) and stereotactic body radiation therapy (SBRT). *Right:* Number of patients-weighted mean TCP probabilities calculated from the same data; to compensate for the different numbers of patients in each study. Solid lines are TCP predictions for a linear-quadratic-based fit to the available data (adapted from Brown *et al.*, 2013).

Need for new normal tissue tolerances. Most of the effort in hypofractionation has been directed towards achieving higher tumor control at acceptable risk level. However, normal tissue toxicities remain the major limiting factor to dose escalation and treatment success despite the fact that most SRS or SBRT regimens have been limited to small volumes. To date, current normal tissue tolerances are based on previous experiences in conventional fractionation using the Emami tables (Emami *et al.*, 1991) or the more recent updated QUANTEC data (Marks *et al.*, 2010), however, no reliable data on hypofractionation are currently available. A review summary of the different constraints used clinically for SRS / SBRT can be found in Grimm *et al.* (2011). However, these data merely reflect treatment planning practices rather than evidence-based recommendations. An AAPM working group is engaged in a QUANTEC-like effort for SRS/SBRT hypofractionation to address this problem (Working Group on Biological Effects of Hypofractionated Radiotherapy/SBRT of the American Association of Physicists in Medicine, WGSBRT).

Site-specific response. In the following, to illustrate the complexity of radiation biology in this regimen, example data from different extra- and intracranial cancer sites are presented; this is not intended to be comprehensive but rather representative.

Among extracranial sites, NSCLC has been the subject of intense investigation. Pooled data analysis from 42 studies by Mehta *et al.* suggested that $TCP \geq 90\%$ at 2-year could be achieved with BED (with an $\alpha/\beta = 8.6$) ≥ 159 Gy and 124 Gy according to the LQ and USC models, respectively (Mehta *et al.*, 2012). The findings are consistent with other

clinical studies (McGarry *et al.*, 2005; Onishi *et al.*, 2004). These data have been used as part of the argument that dose escalation and not new radiation biology understanding would be credited with SBRT success as discussed earlier. However, a possibly more appropriate choice is to use $\alpha/\beta > 10$ Gy for the prediction of dose response in lung SBRT (Chi *et al.*, 2013). On the other hand, no dose-effect relationship for pulmonary function changes has been reported (Guckenberger *et al.*, 2013; Stanic *et al.*, 2014). In abdominal cancers such as pancreatic cancer, Moraru *et al.* used a modified LQ model to fit clinical tumor response and survival data of chemo-radiation treatments from 20 institutions. The parameters of the model were extracted from data fits and suggested a $TCP \geq 50\%$ at 1 year could be achieved with BED (with an $\alpha/\beta = 10$) ≥ 80 (Moraru *et al.*, 2014). In colorectal liver metastases, assuming an $\alpha/\beta = 10$, Chang *et al.* (2011), showed that the estimated doses required for a 90 % local control at 1 year are 48, 117, and 33 Gy when expressed as single-fraction equivalent dose (SFED, is the dose delivered in 1 fraction that would cause the same biological effect as the dose fractionation scheme in question), BED, or LQ model-based single-fraction dose, respectively.

In intracranial cancers, arteriovenous malformation (AVM) dose response to SRS has been substantially investigated (Flickinger *et al.*, 1996; Lawrence *et al.*, 2010). Qi *et al.* (2007) analyzed data from eight clinical series and estimated that AVM has an $\alpha/\beta = 2.2$ suggesting that the therapeutic gain from fractionation is low compared to single dose such as 15 Gy to achieve a $TCP \geq 50\%$. In contrast, when analyzing brain metastasis from 11 studies,

Wiggenraad *et al.* estimated that to achieve TCP \geq 70 % at 1 year, a BED \geq 40 Gy using the LQC model would be needed using $\alpha/\beta = 12$. This is equivalent to single fraction of 20 Gy, 2 fractions of 11.6 Gy, or 3 fractions of 8.5 Gy (Wiggenraad *et al.*, 2011).

The role of conventional *versus* new radiation biology seems to vary by site. There is evidence to support both schools of thought in radiation biology that is site specific and may still benefit from the classical 5Rs while acknowledging recent discoveries related to vascular damage, cancer stem cells, and immune-mediated effects that may take place at such higher doses per fraction. However, issues related to increased intra-fraction delivery times, varying dose prescriptions and irradiated volumes must be carefully monitored and reported. Radiation response assessment and modeling can also benefit from advances in bioinformatics and computational modeling to go beyond simplified dosimetric models into more advanced systems-based approaches in radiobiology.

1.6 Clinical Experience With Small Field Radiation Therapy

The clinical use of stereotactic radiotherapy has its origins in the treatment of intracranial tumors. Subsequently, precise, high dose treatments have been delivered with reduced fractionation to extracranial targets such as metastatic tumors in the liver, lung, and later the spine. Recently, several reports have described the treatment of primary tumors in the lung, liver, prostate, kidney, and pancreas. Inside and outside the cranial vault, stereotactic treatments have been applied as boosts following wider field radiation (*e.g.*, in the case of head and neck, gynecological, or breast tumors) or salvage treatment of recurrences following prior radiation (*e.g.*, for recurrent head and neck malignancies).

Despite the long clinical history of SRT for intracranial lesions, at the time of writing of this report, around 14 000 clinical manuscripts on stereotactic radiotherapy have been reported in PubMed with Phase III studies only in brain metastases. Prescribing, reporting, and recording are performed in different ways at different institutions which emphasizes the need for the present Report to standardize the process. The design of large-scale clinical randomized or comparative studies (lung, liver, prostate, other sites) that use standardized processes is therefore encouraged. Intracranial indications such as AVMs and metastases have been treated in the last 30 years. More recently, acoustic neuromas, meningiomas, and functional indications have been treated. With the development of new technology allowing tracking of moving targets, techniques for treating extracranial indications have been implemented such as for lung, liver, *etc.* A non-exhaustive overview of

current treatment sites with the reported doses is summarized in the following sections.

1.6.1 Intracranial Tumors

1.6.1.1 Brain metastases. Brain metastases represent the most common intracranial target for radiosurgery. They are treated along three main paradigms: with radiosurgery as a single modality, combined with whole-brain radiation, or more recently combined with surgery. The purpose of the treatment can be improved local control leading, in some cases, to improved patient survival or decreased toxicity (through avoidance of whole-brain radiation). As brain metastases tend to have well-defined borders, they are well suited to the steep dose gradients of radiosurgery. Control of these tumors, especially when small (<2 cm) is good and compares favorably to surgical removal.

The treatment of newly diagnosed brain metastases is the domain of radiosurgery most investigated with prospective comparative trials (Aoyama *et al.*, 2006; Linskey *et al.*, 2010; Steinmann *et al.*, 2013). These trials have typically included patients with up to three or four brain metastases and have demonstrated improved survival in some cases (*e.g.*, patients with one metastasis) and decreased toxicity in others, such as, for example, better short-term memory when radiosurgery is used *in lieu* of whole-brain radiotherapy (Lassman *et al.*, 2011). Outside of clinical trials, the total number of brain metastases that should be treated with radiosurgery at one time, is the subject of some controversy and will depend on factors including physician bias, delivery device, and clinical situation.

Although total number of lesions, tumor location, prior radiation, and nature of the primary tumor can all factor into dose selection, target size is typically the most important factor. Single-fraction treatments have a poor therapeutic ratio for metastases larger than 3 cm in maximal diameter. More work remains to be done in defining the role of fractionated treatments for large tumors where currently local control is suboptimal. In the meantime, large tumors are often extirpated surgically. Following surgery local recurrences are common. An ongoing randomized trial should clarify if radiosurgery to the surgical margin can provide local control similar to adjuvant whole-brain radiotherapy whilst sparing cognitive toxicity (Roberge *et al.*, 2012).

1.6.1.2 Primary brain tumors. Radiosurgery has been used in the management of most intracranial tumors. Malignant tumors, because of their high alpha/beta ratios and infiltrative nature, are poorly suited to highly focused hypofractionated

Introduction

radiation as a single treatment modality. There may be selected cases of astrocytic tumors, oligodendroglial tumors, oligoastrocytic tumors, atypical meningioma, malignant meningioma, high-grade ependymoma, medulloblastoma; primitive neuroectodermal tumors; pineoblastoma, lymphoma, or germ-cell tumors where radiosurgery is appropriate as intensification of up-front treatment or palliation of localized recurrences. However, the application of radiosurgery to infiltrative “benign” astrocytic tumors, oligodendroglial tumors, and oligoastrocytic brain tumors is uncommon.

Where the value of radiosurgery has been best documented is in the non-invasive management of the more common base of skull tumors: meningioma, vestibular schwannoma, or pituitary adenoma. Retrospective series also report favorable outcomes for selected cases of hemangioblastoma, pineocytoma, glomus jugulare, and other rare benign tumors. For chordoma, chondrasarcoma and craniopharyngiomas, focused radiation is standard but the fractionation can be a source of controversy with conventional fractionation more commonly applied *versus* single fraction radiosurgery.

Treatment planning of primary brain tumors differs somewhat from that of brain metastases. The nature of the tumor has a greater influence on dose planning. As the doses are often lower, volume has a lower impact on dose selection. There are more often explicit OAR to be avoided: cochlea, optic nerve, or optic chiasm as examples. The optimal fractionation can be controversial. For example, case series can be found of acoustic neuromas treated with almost every fractionation imaginable between 1 and 30 fractions (the optimal fractionation is still unclear). As the target volume can contain functional normal tissue, the argument can be made for more homogeneous treatment plans.

As meningiomas and gliomas are the most common benign and malignant primary brain tumors, respectively, a short discussion is included for each.

Benign (grade I) meningiomas. SRS is useful for treating meningiomas at locations where surgical intervention might threaten neurovascular integrity, such as the cavernous sinus or posterior parasagittal region. In cases where SRS can be applied safely, the outcomes appear similar to fractionated SRT, thus radiosurgery is often preferred because of the shorter treatment (Loeffler *et al.*, 2003). In cases for which SRS is contraindicated, such as those which arise within or near the optic apparatus, fractionated SRT offers a favorable therapeutic ratio. This is the case for optic nerve sheath meningiomas, where few other alternatives are appropriate (Elia *et al.*, 2007).

Retrospective studies have suggested that single doses generally between 12 and 18 Gy (14 Gy is a common prescription) are sufficient to provide excellent tumor control with acceptable toxicity. An example is Kollova *et al.*, 2007 reporting on the Gamma Knife treatment of 325 benign intracranial meningiomas between 1992 and 1999. After a median follow-up of 60 months, the 5-year local control was excellent at 97.9 %. Improvement in neurological symptoms (e.g., imbalance, oculomotor palsy, trigeminal neuralgia, seizure, hemiparesis, and vertigo) occurred in 61.9 %. Permanent toxicity occurred in 5.7 % of patients and included seizures, trigeminal symptoms, hemiparesis, oculomotor palsy, vertigo, cognitive changes, and hearing loss.

Malignant gliomas. Glioblastoma multiforme, the most common glioma and most common primary brain tumor, is notoriously difficult to control. Although these are rapidly dividing infiltrative tumors, selected cases have been treated up-front with radiosurgery boosts or with stereotactic re-irradiation at the time of recurrence. The disappointing results of the only randomized trial examining up-front radiosurgery boost appears to confirm previous suspicion that prior favorable results were mainly the result of selection bias. When 203 patients were randomized to external beam radiotherapy and bischloroethylnitrosurea with or without up-front radiosurgery boost to the region of contrast enhancement (<4 cm in diameter), no advantage was detected in terms of survival, quality of life, or patterns of failure (Souhami *et al.*, 2004).

Although the use of radiosurgery up-front has declined, radiosurgery and hypofractionated re-irradiation continues to be used in selected cases of recurrent glioblastoma multiforme. Current evidence is mainly retrospective and re-treatment essentially palliative (Hazard *et al.*, 2005). Dose and fractionation schemes are variable—single dose schemes being more commonly volume-based. Future trials should help clarify the benefit of re-irradiation and novel drugs may improve the therapeutic ratio by limiting symptomatic necrosis.

1.6.2 Functional Disorders

A wide range of functional and vascular disorders have been treated with radiosurgery (Leveque *et al.*, 2013; Sedrak *et al.*, 2013). The conditions treated can be broadly categorized into: seizure disorders, psychiatric conditions, pain syndromes, movement disorders, and vascular malformation. In most cases, high doses of radiation cause lesioning of the brain in the form of a small necrotic lesion. For vascular disorders, lower doses lead to slow fibrosis and obliteration of the aberrant vessels. For

some indications, such as Parkinson's disease, the use of radiosurgery has essentially been abandoned. For other indications, such as essential tremor, the use is concentrated in a few institutions. For most indications, such as obsessive-compulsive disorder, the evidence is anecdotal or retrospective. Efforts to scientifically document the role of radiosurgery in functional disorders have been sparse but a prospective trial has been initiated comparing radiosurgery to open surgery for temporal lobe epilepsy (Rolston *et al.*, 2011). Widest acceptance and use is seen for trigeminal neuralgia and arteriovenous malformations.

1.6.2.1 Trigeminal neuralgia. Trigeminal neuralgia is a syndrome characterized by severe, often stabbing, facial pain. Most cases are thought to be due to an abnormal vascular loop compressing the trigeminal nerve root. Other cases are associated with multiple sclerosis or a tumor abutting the nerve. For idiopathic neuralgia several treatment options exist (e.g., drug treatment, surgical decompression of the nerve root, or various forms of percutaneous rhizotomy). First line treatment is drug therapy. When this fails, radiosurgery is commonly proposed to patients unfit or unwilling to undergo surgery.

Radiosurgery targets a short segment of the trigeminal nerve between the brainstem and Meckel's cave. The dose is typically reported as a maximum point dose, which ranges from 50 Gy to 90 Gy. In a typical case series, Sheehan and Steiner (2005) reported the results in 151 cases with a median follow up of 19 months. The 2- and 3-year pain free outcome was 45 % and 34 %, respectively. The mean time to relief of pain was 24 days (range 1 days to 180 days). Overall, 90 %, 77 %, and 70 % of patients experienced some improvement in pain at the 1-, 2-, and 3-year follow up, respectively. And 33 (27 %) of 122 patients with initial improvement subsequently experienced pain recurrence a median of 12 months (range 2 months to 34 months) post-Gamma-Knife radiosurgery. The most common toxicity is facial numbness, which is rarely painful (anesthesia dolorosa).

1.6.2.2 Arteriovenous malformations.

Although arteriovenous malformations (AVMs) can present with a variety of symptoms including seizures and headaches, they are most often treated following hemorrhage in order to prevent repeat bleeding. Higher early rates of death or stroke have been reported for the intervention arm in a randomized trial of medical management with or without intervention for unruptured malformations (Mohr *et al.*, 2014). This recent report has increased the controversy as to whether or not most unruptured

malformations benefit from ablative treatment, including radiosurgery.

AVMs are typically treated with peripheral dose of 16 Gy to 25 Gy. Complete obliteration following radiosurgery generally takes 1 years to 3 years and the risk of hemorrhage during this latency period remains essentially unchanged from untreated patients. Obliteration rates following radiosurgery range from 54 % to 92 % (Starke *et al.*, 2008), but depend on dose, AVM volume, the number of prior treatments, timing of follow-up, and follow-up imaging technique. Complications associated with radiosurgery include seizures, headache, neurological deficits, and radiation-induced cerebral injuries such as oedema, necrosis, and cyst formation. Postoperative morbidity leading to permanent deficits is observed in 0.4 % to 20.6 % of patients in the current literature. Two factors have been shown to be predictive of permanent injury: AVM location and the volume of tissue receiving radiation in excess of 12 Gy (Flickinger *et al.*, 2000).

Large AVMs pose a therapeutic challenge. When the entire malformation cannot be safely treated to a dose of 15 Gy or more, it has been proposed to "stage" the radiosurgery (Kano *et al.*, 2012). The AVM volume is thus broken up into two or more subvolumes, which are treated during separate procedures separated by days, weeks, or months. Such a paradigm poses the additional planning challenge of dose summation and the need to reduce unnecessary dose to normal tissue.

1.6.3 Extracranial Metastatic Tumors

The rationale for the treatment of extracranial metastatic tumors varies depending on the site. In the case of lung and liver, treating metastatic tumors has led to long-term disease control, whereas in spine, the treatment rationale is pain control or local control.

1.6.3.1 Liver metastases. So far, surgery has been the treatment of choice. However, patients who are unfit to be operated on or have metastases too close to the large blood vessels are excellent candidates for a stereotactic treatment. Several authors reported retrospectively on good to excellent local control varying from 57 % to 100 %, however, usually with a short follow-up of 18 months. Several dose escalation studies have been done: dose-escalation with a single fraction of 14 Gy to 26 Gy was safe and no incidents of dose-limiting toxicity or radiation-induced liver disease were reported (Herfarth *et al.*, 2001). A phase I dose-escalating study with risk adaptive schedules and doses ranging from 27.7 Gy to 60 Gy in 6 fractions (Lee, 2009) resulted in a 1

year local control rate of 71 % without dose-limiting toxic events. Another phase I trial escalated the dose from 36 Gy (in 3 fractions) up to 60 Gy also without dose limiting toxicity. The 1-year local control was 95 % (Rusthoven *et al.*, 2009a). Besides these three studies there are many retrospective studies with a local control of 78 % to 94 % (Dewas *et al.*, 2012; Mendez Romero *et al.*, 2006; Rusthoven *et al.*, 2009a; Wulf *et al.*, 2001).

Stereotactic radiotherapy to the liver can safely be given. However, it is currently not clear what the maximum allowable dose to the OAR such as bowel is and whether a single fraction, 3 fractions, or 6 fractions result in better outcome. There is also significant variation in the prescription with some authors prescribing to the isocenter, others to the 65 % or 80 % isodose line covering the whole PTV, or the isodose line that covers the whole PTV.

1.6.3.2 Lung metastases. Patients with metastatic disease to the lung who are referred for stereotactic radiotherapy are, for a number of reasons, a very different group compared to surgical candidates: they often have centrally located lesions, may have one or more lesions in each lung, have previously undergone a lobectomy or pneumonectomy, or are bad surgical candidates due to their medical condition. Retrospective studies with 3 to 5 fractions did report a good to excellent local control of 78 % to 89 % after 1 year (Collins *et al.*, 2007; Hof *et al.*, 2007; Okunieff *et al.*, 2006), and maybe also a better overall survival (Dhakal *et al.*, 2012). Okunieff *et al.* (2006) reported results on 125 metastatic lung lesions. In their study, metastatic disease had to be confined to the thorax and a maximum of five metastases were treated with curative intent. Excellent local control of 91 % at three years was reported with delivery of 50 Gy to 55 Gy in 5 Gy fractions. Nagata *et al.* (2005) suggested a dose escalation to 3 Gy \times 20 Gy in pulmonary metastases larger than 3 cm after treating metastases with 4 \times 10–12 Gy because they found three recurrences in nine metastatic lesions. Rusthoven (2009b) and Alongi *et al.* (2012) reported a local control at 2 years to 3 years from 70 % to 100 % but overall survival was generally much lower, typically due to progression outside the treated region. For example, a phase I/II study in which 48 Gy to 60 Gy was delivered in 3 fractions, obtained local control of 96 % at 2 years while median survival was only 19 months (Rusthoven *et al.*, 2009b). Many different treatment schedules are still used, but it is still not clear what the best schedule is. Also single high dose SBRT reported an increased local control with

increasing radiation dose. In a series by Wulf *et al.* (2005) including both lung metastases ($n = 56$) and primary lung tumors ($n = 36$), 24 patients receiving 3 Gy \times 10 Gy, 22 patients receiving 3 Gy \times 12.5 Gy, and 31 patients receiving 1 Gy \times 26 Gy, had 2 year local control rates of 71 %, 92 %, and 100 %, respectively. These dose escalation data are also supported by Hara *et al.* (2006), who treated 48 patients with lung metastases and 11 patients with early-stage NSCLC. The two-year local control rate for patients receiving a single fraction of 30 Gy or more was 83 % compared to 52 % in those treated with a single fraction <30 Gy. Several studies reported a trend towards better results for smaller tumor volumes. Hof *et al.* (2007) reported that tumors with volumes of <10 cm³, and treated with doses exceeding 26 Gy ($n = 11$), had local control of 100 % at year 1 compared to 85.7 % at 1 year found in the rest of the tumors ($P = 0.11$). The survival of the patients is varying on the inclusion criteria [e.g., Rusthoven *et al.* (2009b)] reported a median survival of 19 months while Nuyttens *et al.* (2015) reported a 4-year overall survival of 38 %. We can conclude from this and other studies that the identification of “oligometastatic” patients, who can benefit from long-term disease control, requires additional investigation.

1.6.3.3 Spinal metastases. Stereotactic radiotherapy is an excellent palliative treatment with a primary goal of long-term pain reduction. Excellent local control in retrospective studies has been reported in the treatment of spinal metastasis (Cox *et al.*, 2012; Heron *et al.*, 2012; Lo *et al.*, 2009; Sahgal *et al.*, 2009). The doses vary, but are delivered in a single fraction of 16 Gy to 20 Gy or in 3 fractions to 27 Gy to 30 Gy (Wang *et al.*, 2012) or 5 fractions in 30 Gy (Zelefsky *et al.*, 2012). A concern remains about the rate of vertebral fracture after SBRT, which can be as high as 20 % with the amount of risk related to the patient age, pre-existing fracture, and local pain (Boehling *et al.*, 2012).

1.6.3.4 Other oligometastatic tumors. Stereotactic radiotherapy has been used in the treatment of pelvic or paraaortic lymph node recurrences (Jereczek-Fossa *et al.*, 2014; Nuyttens *et al.*, 2007), but also to metastases in adrenal glands, or metastases in the renal bed (Svedman *et al.*, 2006). Due to the proximity of critical structures like bowel, kidney, and spinal cord, 3 to 6 fractions are used to a total dose of 30 Gy to 48 Gy. Also in these series, an excellent local control is reported, combined with an excellent overall survival (60 % to 100 %). However, caution must be taken when bowel or stomach

receive high doses as strictures and ulcers can appear as late radiation toxicity (Jereczek-Fossa *et al.*, 2014; Wersäll *et al.*, 2005).

1.6.4 Primary Extracranial Tumors

1.6.4.1 Stereotactic radiotherapy as curative treatment

Early stage lung cancer. Stereotactic radiotherapy to the tumors in the lung are classified into two groups: patients with peripheral tumors and patients with central tumors. Although there are several definitions, central tumors are tumors located <2 cm from the trachea, main stem bronchus, main bronchi or esophagus, but also tumors located close to the heart and tumors located in the mediastinum.

SBRT to peripheral tumors resulted in high local tumor control rates exceeding 90 % at 1 year for early-stage NSCLC patients with 3 to 5 fractions to a total dose of 45 Gy to 60 Gy (Lagerwaard *et al.*, 2008; Ng *et al.*, 2008; Nyman *et al.*, 2006). As will be discussed in Section 5, the application of stereotactic radiotherapy to tumors in the lung requires respiratory motion management. Also the use of a single fraction resulted in excellent local control: 83 % at 2 years for patients treated with a single fraction of 30 Gy or more, compared to 52 % for those treated with <30 Gy (Hara *et al.*, 2006). Recently, a randomized trial comparing a single fraction of 30 with 34 Gy did not reveal a significant difference in local control (Videtic *et al.*, 2014). The achievement of excellent local control with stereotactic radiotherapy is reported with a low level of late toxicity in 3 % to 10 % of patients (Lagerwaard *et al.*, 2008; van der Voort van Zyp *et al.*, 2009), and excellent quality of life (Lagerwaard *et al.*, 2012; van der Voort van Zyp *et al.*, 2010a).

Central tumors cannot be treated safely with common SBRT dose schedules, such as, for example, 3 fractions of 20 Gy, due to the proximity of trachea, main stem bronchus, esophagus, or heart (Timmerman *et al.*, 2006). By increasing the number of fractions and reducing the fractional dose, some groups have reported successful treatment of central lung tumors with minimal complications (Chi *et al.*, 2010; Nuyttens and van de Pol, 2012). However, other authors reported grade 5 toxicity related to the stereotactic radiotherapy treatment (Bral *et al.*, 2011; Fakiris *et al.*, 2009; Onimaru *et al.*, 2003).

Liver cancer. Most studies report on mixed populations of primary liver cancer and liver metastasis. The treatment and techniques are quite similar to those used in the treatment of liver metastases. Small tumors can be treated with 3 fractions. However, most authors use 5 to 6

fractions. Published papers report on small series with short follow up and caution should be taken for patients with Child–Pugh class B cirrhosis because toxicity is higher (Mendez Romero *et al.*, 2006; Vautravers-Dewas *et al.*, 2011). Tse *et al.* (2008) used a dose of 24 Gy to 54 Gy (median 36 Gy) delivered in 6 fractions. No radiation-induced liver disease or treatment related grade 4 or 5 toxic effects were seen within the 3 months after SBRT (Tse *et al.*, 2008). There is strong consideration of liver stereotactic radiotherapy as an alternative to other local treatments and as a bridge technique before liver transplant (O'Connor *et al.*, 2012).

Prostate cancer. Stereotactic radiotherapy was performed on 304 patients with clinically localized prostate cancer (Katz *et al.*, 2010): 50 received 5 fractions of 7 Gy (total dose 35 Gy) and 254 received 5 fractions of 7.25 Gy (total dose 36.25 Gy). At a median 30-month (26 months to 37 months, range) follow-up there were no biochemical failures for the 35-Gy dose level. Acute Grade II urinary and rectal toxicities occurred in 4 % of patients with no higher Grade acute toxicities. One Grade II late urinary toxicity occurred with no other Grade II or higher late toxicities. At a 17-month median (8 months to 27 months, range) follow-up the 36.25 Gy dose level had 2 low- and 2 high-risk patients who failed biochemically (biopsy showed 2 low- and 1 high-risk patients were disease-free in the gland). Acute Grade II urinary and rectal toxicities occurred in 4.7 % (12/253) and 3.6 % (9/253) of patients, respectively. For those patients with a minimum of 12 months follow-up, 5.8 % (12/206) had late Grade II urinary toxicity and 2.9 % (6/206) had late Grade II rectal toxicities. One late Grade III urinary toxicity occurred while no Grade IV toxicities were observed. For both dose levels at 17 months, bowel, and urinary quality of life (QOL) returned to baseline values. The sexual QOL decreased by 10 % (Katz *et al.*, 2010). Bolzicco *et al.* (2010) and King *et al.* (2009) reported similar results with 35 Gy and 36.25 Gy in 5 fractions in patients with low- and intermediate prostate cancer, respectively. Aluwini *et al.* (2010) reported their early results with the stereotactic treatment of 38 Gy in 4 daily fractions of 9.5 Gy in 10 patients. The International Prostate Symptom Scores after 3 months were stable compared with the pretreatment scores. Urinary and bowel Radiation Therapy Oncology Group symptoms were mild and within the expected levels. Randomized studies comparing surgery with stereotactic radiotherapy are ongoing (PACE, 2013) (Tree *et al.*, 2013).

Renal-cell cancer. A few articles report on an excellent local control for renal tumors and a few

treatment related toxic effects have been reported (Lo *et al.*, 2010; Svedman *et al.*, 2008; Teh *et al.*, 2010). In a phase II study of SBRT for primary or metastatic renal cell carcinoma, 30 patients with 82 lesions were treated with SBRT with dose regimens of 32 Gy in 4 fractions, 40 Gy in 4 fractions, 30 Gy in 2 fractions or 45 Gy in 3 fractions. With a median follow up of 52 months, the local control rate was 98 %, with a complete response seen in 21 % of patients. The most common adverse effects were cough, fatigue, skin rash and local pain, which were grades 1 to 2 in 90 % of cases. The median overall survival was 32 months (Ponsky and Vricella, 2012).

1.6.4.2 Stereotactic radiotherapy as a boost treatment

Breast cancer. In primary breast cancer, stereotactic radiotherapy has not been used often. Only a few studies reported the use of stereotactic radiotherapy: one study reported the use of stereotactic radiotherapy as an upfront boost after neoadjuvant chemotherapy. A dose escalation of 19.5 Gy or 22.5 Gy delivered in 3 fractions did not show skin toxicity, suggesting the dose could be increased to higher levels. After the neoadjuvant chemoradiotherapy patients were operated upon using breast-conserving surgery and post-operative conventional radiotherapy. The conventional radiotherapy was delivered without toxicity (Bondiau *et al.*, 2013). Another study used stereotactic radiotherapy for partial breast irradiation after conservative surgery (Vermeulen *et al.*, 2011). The patients received a total dose of 30 Gy in 5 fractions or 34 Gy in 10 fractions. However, both studies reported on small patient groups, so more studies are needed to determine the suitability of stereotactic radiotherapy of the breast.

One planning study reported on the use of preoperative accelerated partial breast stereotactic irradiation (15 Gy in a single fraction). This study revealed a substantial reduction in ipsilateral breast tissue dose compared with postoperative partial breast irradiation. The skin dose appeared reasonable, given the small volumes of the PTV (Palta *et al.*, 2012).

Gynecological cancer. In some locally advanced tumors, BT boost is challenging and may not cover all tumor extensions. Stereotactic radiotherapy could be an alternative for tumors with lateral parametrial infiltration. Jorcano *et al.* (2010) reported the toxicity and outcome in patients with gynecological tumors treated with a final boost using stereotactic radiotherapy with a linac-based micro-MLC technique as an alternative to HDR-BT. Overall, 26 patients with either endometrial ($n = 17$) or cervical ($n = 9$) cancer were treated according

to this protocol: 45 Gy to 50.4 Gy external radiotherapy to the pelvic \pm paraaortic regions followed by a final stereotactic boost of 2 Gy \times 7 Gy to the vaginal vault. The 3-year loco-regional failure-free and overall survival rates were 96 and 95 %, respectively. No severe ($>$ grade 3) acute urinary or low-gastrointestinal (GI) toxicity was observed during treatment and up to 3 months after treatment completion. Moderate (grade \leq 3) acute urinary or low-GI toxicity was observed in 23 % and 35 % of patients, respectively. After a median follow-up of 47 months (4 to 77, range), late urinary, low-GI, and sexual \geq grade 2 (worst score) has been reported in 4 %, 12 %, and 29.4 % of patients, respectively (Jorcano *et al.*, 2010).

1.6.5 Recurrent Tumors

1.6.5.1 Head and neck cancer. Most of the results have been published on previously irradiated patient populations. Stereotactic radiotherapy was used as salvage re-irradiation. Outcome of small patient groups (22 to 46 patients) are reported by several authors (Cengiz *et al.*, 2011; Kawaguchi *et al.*, 2010; Roh *et al.*, 2009) and were mostly treated with a total dose of 18–40 Gy in 3 to 5 fractions. Local disease control (complete response, partial response) and stable disease was achieved in 79 % to 89 % of the patients. However, Cengiz *et al.* (2011) reported a 1-year overall survival of 46 % and Kawaguchi *et al.* (2010) a 2-year overall survival of 78 % in node negative patients and 12 % in node positive patients. Grade II or greater long-term complications were observed in 13.3 % of the patients (Cengiz *et al.*, 2011). On follow-up, 17.3 % of the patients had carotid blow-out syndrome, and 15.2 % of the patients died of bleeding from carotid arteries (Cengiz *et al.*, 2011). Roh *et al.* (2009) reported grade III acute complications in 36 % of the patients. Late complications were observed in three patients (1 bone necrosis, 2 soft tissue necrosis) during follow-up. Wu *et al.* (2007) treated 90 patients with persistent (Group 1: $n = 34$, relapse within 6 months of RT) or recurrent (Group 2: $n = 56$, relapse beyond 6 months) nasopharyngeal carcinoma and used multiple non-coplanar arcs of 8 MV photons to the target to a median dose of 18 Gy in 3 fractions (Group 1) or 48 Gy in 6 fractions (Group 2). Complete response rate was 66 % for Group 1 and 63 % for Group 2. With a median follow-up of 20.3 months, the 2-year disease-specific survival and progression-free survival rates for all patients were 74.8 % and 60.4 %, respectively. Multivariate analysis showed that recurrent disease and large tumor volume were independent factors that predicted poorer disease-specific survival and progression-free survival. A total of 17

patients (19 %) developed late complications, including two with fatal hemorrhage (Wu *et al.*, 2007).

Heron *et al.* (2011) compared two groups of patients with head and neck cancer treated over a 6-year period with stereotactic body radiation therapy alone ($n = 35$) or with weekly cetuximab infusion during stereotactic body radiation therapy ($n = 35$), and reported an overall survival advantage (24.5 *versus* 14.8 months) when treated with stereotactic radiotherapy and cetuximab compared to the stereotactic body radiation therapy alone arm, without a significant increase in grade 3/4 toxicities. This survival advantage was also observed in the subgroup that had received cetuximab therapy during their prior therapeutic regimen (Rwigema *et al.*, 2010; Vargo *et al.*, 2012). Comparable results have been reported with a 6 Gy \times 6 Gy regimen (Comet *et al.*, 2012).

Gynecological cancer. Guckenberger *et al.* (2010) reported on 19 patients treated for a locally recurrent cervical ($n = 12$) or endometrial ($n = 7$) cancer after initial surgery. The whole pelvis was irradiated with 50 Gy conventionally fractionated radiotherapy ($n = 16$). Because of the large size of the recurrent cancer (median 45 cm³) and the peripheral location ($n = 12$), stereotactic body radiotherapy was used for

local dose escalation instead of ($n = 16$) or combined with ($n = 3$) vaginal BT. A median total dose of 15 Gy in 3 fractions was given. After median follow-up of 22 months, the 3-year overall survival was 34 %. Three local recurrences resulted in a local control rate of 81 % at 3 years. No correlation between survival, systemic, or local control and any patient or treatment characteristic was observed. The rate of late toxicity above grade 2 was 25 % at 3 years: two patients developed a grade 4 intestino-vaginal fistula and one patient suffered from a grade 4 small bowel ileus (Guckenberger *et al.*, 2010).

1.7 Summary of Contents of the Report

Section 2 outlines the dosimetry aspects of small fields including reference dosimetry, relative dosimetry, and output factors. Section 3 reviews the definitions of dose reporting volumes for SRT. Section 4 discusses aspects of treatment planning algorithms, specific to SRT whereas Section 5 deals with the image guidance aspects specific to SRT and Section 6 deals with quality assurance aspects, specific to SRT. Section 7 is devoted to prescribing, recording, and reporting of SRT. Appendix A contains examples of prescribing, reporting, and recording of SRT according to the recommendations in this report.

2. Small Field Dosimetry

The role of clinical medical physics in radiation therapy is to ensure that the prescription is delivered accurately. This means that there is a need for a comprehensive quality assurance program, which encompasses all aspects of radiation medicine ranging from therapy machine acceptance, commissioning and calibration, image guidance and delivery, and that all procedures and workflows are in place to deliver the prescription accurately. The dosimetric portion of the quality assurance program starts with accurate calibration of the beam and the measurement of output factors and other dosimetric functions. In this context, the requirements in terms of accurate beam calibration, treatment planning, delivery, and quality assurance of stereotactic radiation therapy are as stringent, if not more stringent, as in conventional radiation therapy (Thwaites, 2013). Recent incidents in radiation therapy (Ford and Evans, 2014; IAEA, 2014) using small fields have indicated that dosimetry of small fields is complex and prone to errors. In general, absorbed dose determination in small fields requires multiple levels of redundancy including the use of different detectors with appropriate detector-dependent correction factors for the measurements, a critical analysis of measured data on equipment of the same type in comparison with peer centers, corroboration of data with manufacturer “golden beam data” (*i.e.*, reference data), *etc.* As will be clear from the present section, simple pooling of relative reading data from different detector types is not the same as the relative dose in small fields; accurate depth and field-size dependent correction factors are required to ensure that the detector signal is faithfully converted into absorbed dose. In addition, the execution of an independent third-party dosimetry end-to-end review (*e.g.*, Imaging and Radiation Oncology Core, IROC, MD Anderson Houston) is strongly suggested. Because of this complexity, an institution starting a new small-field radiation therapy program should consider training programs for physicists, radiation therapy planning personnel and radiation oncologists that includes a review of the basis of small field dosimetry. The active collaboration between all professions in the

SRT program is critical for treatment quality and patient safety.

In 3D conformal radiation therapy, higher energies (defined for the purpose of this discussion as photon beams created from accelerating potentials of larger than 10 MV) are regularly used to improve coverage in the case of deep-seated tumors. The secondary electron path for a 15 MV beam may be of the order of 3 cm or more thereby significantly affecting penumbra width. This leads to problems in the application of SRT using higher energies especially for small targets in regions involving lower density, such as lung. In these conditions, the accuracy requirements imposed on the dose calculation algorithm used for treatment planning are more difficult to meet for higher energies (>10 MV). Secondly, collimation systems, such as MLCs, typically block 6 MV photons better than they block 15 MV or higher energies. This and other effects lead to a more significant dose beyond the penumbra in higher (>10 MV) compared to lower (\leq 10 MV) photon energies, ultimately affecting off-axis ratios (OAR) sparing. Finally, higher-energy (>10 MV) photon beams give rise to neutron production through the (γ , n) reaction. At 18 MV, the cross-section for neutron production by collimation is two orders of magnitude greater than for 10 MV photons (Maglieri *et al.*, 2015). This may lead to activation of linac components as well as unwanted out-of-field patient exposure although the dosimetric impact of this needs further investigation (Horst *et al.*, 2015). For all of these reasons, the present Report recommends the use of lower-energy photon beams (\leq 10 MV) for the clinical implementation of SRT programs. This recommendation is consistent with ICRU Report 83, which states that the use of higher-energy beams is not justified for IMRT (ICRU, 2010).

In the present section, the specific physics aspects of dosimetry in small beam radiation therapy are summarized. The nomenclature introduced covers small beams, for which defining conditions will be presented. For the discussion of reference dosimetry and output factors, this section follows the recommendations of the IAEA-AAPM code of practice

(IAEA-AAPM, 2017), the formalism for which was introduced by Alfonso *et al.* (2008).

2.1 Defining Characteristics of Small Radiation Therapy Beams

Dosimetry of broad fields in conventional radiation therapy is helped by the fact that a significant part of the dose distribution contains regions of transient charged particle equilibrium (TCPE). This brings about the simplification that, past the build-up region, collision kerma, and absorbed dose are related by a slowly varying function. Measurements for calibration or relative dosimetry in regions of TCPE are well-conditioned and well-studied correction factors and conversion factors are involved in the formalisms. In radiation therapy, charged particle disequilibrium occurs in regions of build-up, everywhere in electron beams, in the penumbra area, or inside small fields. In broad photon beams, there is not only TCPE in the longitudinal direction but also in the lateral direction; charged particles set in motion from regions lateral of the central axis in a broad beam may enter the central axis region and compensate for charged particles set in motion along the central axis and leaving the central axis region. One will find in the literature that this latter effect is often termed “lateral charged particle equilibrium” (LCPE), which, strictly speaking, is transient. However, there is no clear way to distinguish the lateral component from the longitudinal component. Lateral charged particle disequilibrium occurs in narrow photon fields when the beam radius becomes small in comparison to the maximum range of secondary electrons. Since the electron range increases with energy, the beam radius at which this becomes significant increases as the beam energy increases. In the absence of LCPE both the shape of the transverse beam profile as well as the absorbed dose on the central axis are affected. In addition, the average energy of the electrons increases at the central axis of the field when the distance to the field boundary is less than the range of secondary electrons as lower-energy electrons are under-represented there (Section 2.2). Central axis LCPE will be well-approximated when both the measurement depth and the diameter of the radiation beam are greater than the maximum range of the secondary electrons (Attix, 1986; Wu *et al.*, 1993). There is no generally accepted definition of when a radiation field can be considered small. The designation of a small field can be based on a few characteristics as well as on pragmatic clinical physics considerations. Three conditions, however, have been considered to contribute to small field conditions.

2.1.1 Lateral Charged Particle Disequilibrium

The first condition defining small field conditions is formulated in terms of a size parameter r_{LCPE} , which is a measure of the range of laterally scattered electrons, and which represents the smallest field dimension for which, past the build-up region, the absorbed dose and collision kerma become proportional as a function of field radius.

The field aperture is often defined by the field diameter at isocenter and can be quantified by determining the full-width at half maximum (FWHM) of the dose profile in a phantom at isocenter, which, for broad beams, is equal to the collimation aperture projected to isocenter. For reasons that will be discussed below, in small fields, the FWHM exceeds the collimation aperture projected to isocenter.

To define conditions for small fields, the minimum beam diameter for which TCPE is reached can be accepted as a lower limit to the diameter for which a beam can be considered broad. As the energy reduces, the diameter of the beam for which one can assume a beam to be broad narrows because of the reduction in charged particle range. The relation between the breakdown of charged particle equilibrium and energy of interest in radiation applications can be visualized by considering the ratio of absorbed dose to water to collision kerma in water, $D_w/K_{w,\text{coll}}$, beyond depth of maximum dose for parallel beams of increasing beam radii (Fig. 2.1). The values shown in Fig. 2.1 are normalized on the equilibrium value of $D_w/K_{w,\text{coll}}$ obtained at large beam radii. If the radius of the field is smaller than r_{LCPE} , the penumbrae of the field

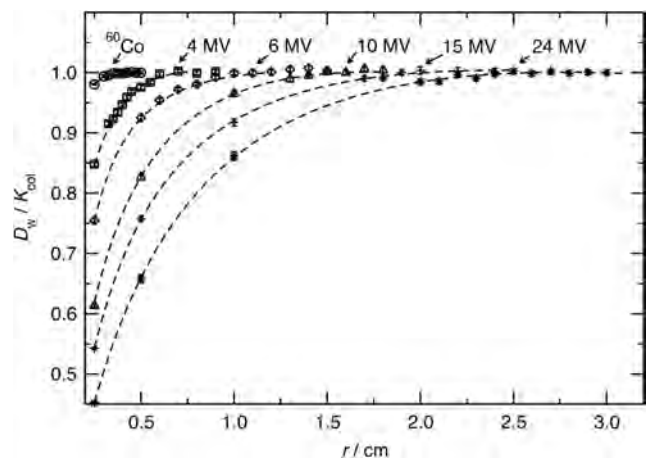


Figure 2.1. Ratio of $D_w/K_{w,\text{coll}}$ for parallel beams of varying beam diameter and beam energy normalized to the equilibrium value for large radius. Depth of $D_w/K_{w,\text{coll}}$ evaluation in this figure is 5.25 cm for a point source collimated to radius, r . (Adapted with permission from IAEA-AAPM 2017.)

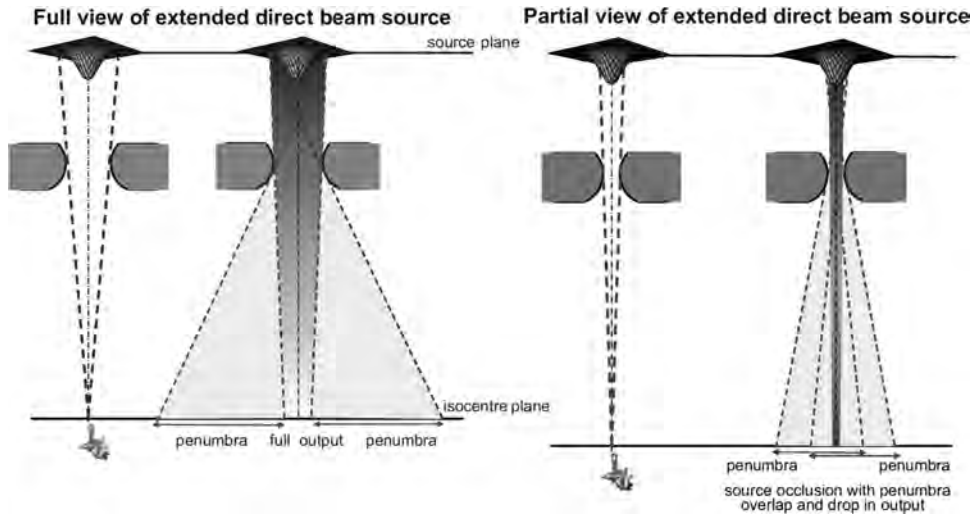


Figure 2.2. Schematic illustration of source occlusion. *Left*: the full, extended source can be “viewed” by an observer on the central axis. *Right*: only partial view of the source is possible by an observer on the central axis. (Adapted from IPEM Report 103 (Aspradakis *et al.* (2010).)

overlap with the detector, resulting in a characteristically sharp reduction in machine output when the field size decreases further. As indicated in Fig. 2.1, this effect is energy dependent as the ranges of the secondary electrons are affected by the photon energy, *e.g.*, r_{LCPE} is <0.4 cm in water for a ^{60}Co gamma ray beam and \approx 1.1 cm in water for a 6 MV high-energy x-ray beam. Li *et al.* (1995) showed that there is a linear relationship between the beam quality specifier (*e.g.*, $TPR_{20,10}$, or $\%dd(10)_x$) and the minimum field radius required to achieve LCPE. The IAEA-AAPM (2017) protocol provides this relation as follows:¹

$$r_{LCPE}(\text{in cm}) = 8.369 \cdot TPR_{20,10} - 4.382 \text{ or}$$

$$r_{LCPE}(\text{in cm}) = 0.07797 \cdot \%dd(10)_x - 4.112 \quad (2.1)$$

The LCPE characteristic is a natural, energy dependent lower bound on when a field can be considered small regardless of how the field is created and regardless of the detector involved in measuring it. The difficulties of working with small fields in radiation dosimetry and radiation therapy due to this characteristic may manifest themselves in, *e.g.*, a treatment planning dose calculation algorithm that is incapable of correctly calculating dose when using small fields because of the simplified

modeling of the lateral electron scattering. The result of this is that dose calculations will be wrong and this will manifest itself more prominently in heterogeneous situations involving low-density regions such as lung.

2.1.2 Partial Source Occlusion

There are issues related to the generation of narrow fields in modern external beam radiation therapy that have an impact on the ability to measure the dose in the field. In medical accelerators, small fields are obtained by collimation jaws, MLCs, iris collimators and/or special collimators with small apertures. The second characteristic for obtaining small field conditions is related to the parameters of the primary photon source at the exit plane of the bremsstrahlung target for x-rays (also known as the focal spot size), which has finite dimensions, and, relative to that, the state of the downstream collimation system. As illustrated in Fig. 2.2, there will always be a size of a field (created by the collimators) below which part of the direct focal spot viewed from the measurement point is occluded by the collimators.

This results in the direct photon penumbrae overlapping, with the consequence that the output is reduced when the field size further decreases. For a given source-to-detector distance this effect is dependent on the source-to-collimator distance. For modern accelerators where the spot size is typically smaller than 5 mm, direct source occlusion usually occurs at field sizes smaller than those where lateral electron disequilibrium starts, making this a less restrictive criterion than the first criterion. An

¹The tissue-phantom ratio, $TPR_{20,10}$, represents the dose ratio at 20 and 10 cm depth with a constant source to detector distance of 100 cm, for a field size of $10 \times 10 \text{ cm}^2$ at isocenter. The percentage depth dose, $\%dd(10)_x$, represents the photon component of the dose at a depth of 10 cm in water normalized to the dose at depth of maximum dose times 100, in a $10 \times 10 \text{ cm}^2$ field at 100 cm SSD.

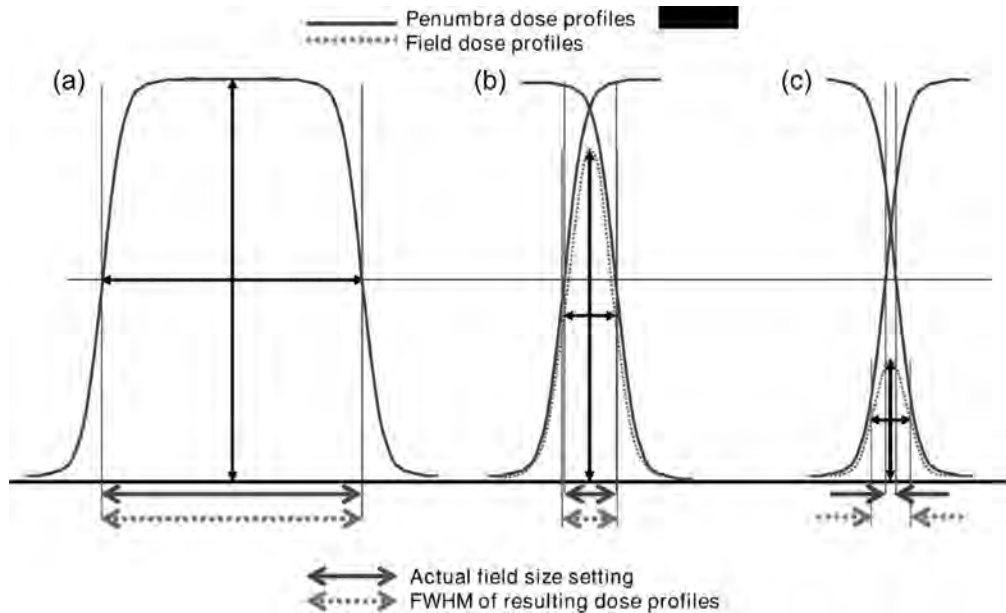


Figure 2.3. Apparent profile widening associated with small fields. *Full lines*: profiles and penumbra shapes of individual beam modifying devices. *Dotted lines*: resulting profile widening (right) and profile maximum (output) reduction. (Adapted with modifications from Das *et al.* (2008b).)

additional effect is the increase in the width of the beam profile (*i.e.*, an increase in FWHM) to a value that does not concord with the nominal collimator setting. The extent of this widening depends on the lateral electron ranges and potentially leads to complications in the definition of field sizes of small fields in treatment planning systems (TPSs) (Fig. 2.3). For this reason, dosimetric data for small fields should generally be specified as a function of the FWHM of the small field profile at the depth of measurement and not as a function of nominal collimator-set field size.

Since partial source occlusion affects the energy and angular fluence distribution in a medium, it affects the response of detectors in small fields. In contrast to the lateral disequilibrium effect discussed above, partial source occlusion is not an effect that is independent of the manner in which the beam is generated nor is it independent of the detector used to determine the dose. In principle, the coupling of the detector response in small fields to the source spot size leads to complications in the application of detector correction factors in small fields. Partial occlusion of the source is the main reason the output factors decrease so rapidly as the field dimension reduces.

2.1.3 Detector Size Relative to Field Size

A third criterion for defining small field conditions is related to the size of the detector used to characterize the field. This is a “relative” criterion

(in the sense that it is dependent on the measurement device) but important since the detector volume averaging effect, which is dependent on detector size, plays a central role in the ability to measure small field dose. A practical criterion could be that a field is called small if the conventional ionization chamber type used for standard reference dosimetry becomes too large to give reliable results. This could be quantitatively specified as fields for which any lateral edge of the detector is less than r_{LCPE} away from the edge of the field. The relative nature of the latter condition for small fields is the reason why some recent guidelines for small field dosimetry have opted to choose a single size, *e.g.*, 3 cm (diameter or side of the field) as the condition for defining a field as small [*see, e.g.*, IPEM Report 103, (Aspradakis *et al.*, 2010)]. The combination of rapid decrease in output as the field size reduces and the under-measurement of this falloff with detectors with a large volume is one of the largest errors that occur in SRS with errors of up to 50 % in the dose delivered reported (Ford and Evans, 2014).

2.2 Fluence Spectrum Changes in Small Fields

Changes in the energy spectrum of the photon fluence for small fields fundamentally arise from two different sources. There are spectrum changes induced by the changes in the treatment head when shaping small fields, and there are spectrum

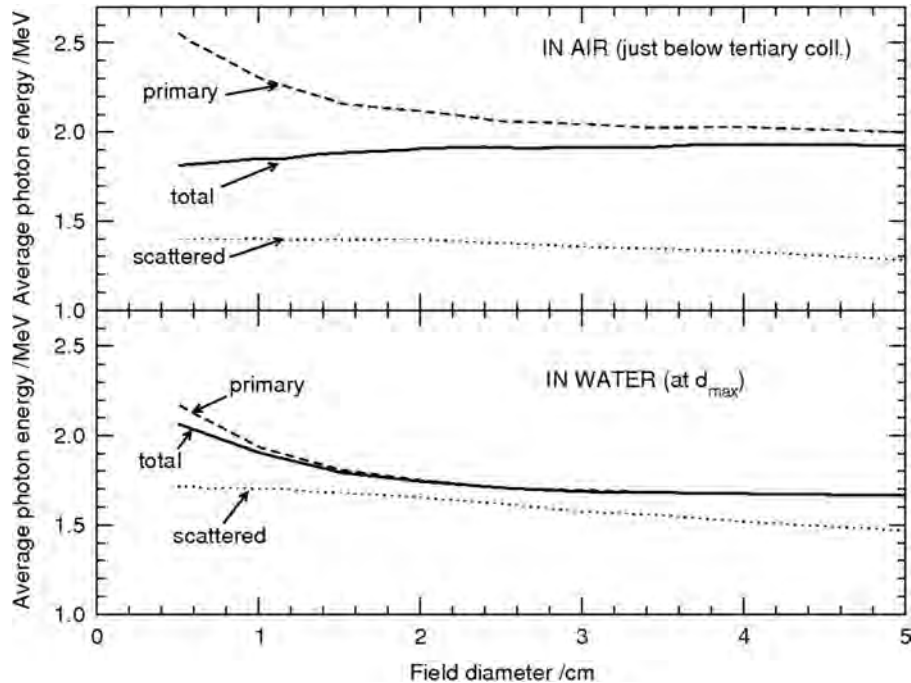


Figure 2.4. Average energy of the photon fluence versus field diameter for a 6 MV Varian accelerator with flattening filter. *Upper panel:* in air, just below the tertiary conic applicator. The contribution of scattered photons in the total fluence decreases with increasing radius and amounts to 64 and 9 % of the total for the 0.5 and the 5 cm field, respectively. *Lower panel:* in water, at depth of maximum dose on the beam central axis. [Data from Verhaegen *et al.* (1998).]

changes in the phantom (or patient) when field size is reduced.

The spectrum changes resulting from the treatment head are in general situation-specific. They depend on the beam head design (primary collimator, flattening filter, shape of the jaws/MLC collimator system, and distance of the collimator from the source). An example from a Monte Carlo study is given in Fig. 2.4, where the dependence of the average photon energy in a Varian 6 MV beam on field diameter both in air, at the accelerator exit and in-phantom on the central axis, at depth of maximum dose, z_{\max} are given. The beam is from a Varian stereotactic accelerator where ultimate collimation is done using a tertiary conic applicator. In the figure, three components are illustrated, the primary fluence, the scattered fluence, and the total fluence for an in-air beam and an in-phantom beam. The primary fluence is that resulting directly from the target/flattening filter without further scattering on any collimators or phantom. An immediate observation from Fig. 2.4 is that the changes in average photon energy between 5 mm and 5 cm diameter fields are not large.

The upper panel shows the average energy of the in-air fluence just below the conic applicator. The average energy of the primary fluence decreases as collimation opens since, on-axis, the flattening filter

provides more beam hardening. The scattered photons are relatively constant in average energy as a function of radius, but their contribution to the total fluence decreases with increasing radius (64 and 9 % for the 0.5 and the 5 cm field, respectively). The total fluence therefore increases in average energy with field diameter (Verhaegen *et al.*, 1998).

The in-phantom data (lower panel, Fig. 2.4) show an increase in average energy as the field diameter decreases as the phantom scatter contribution on the central axis is reduced compared to larger fields. That is because photons scattering out of the small field are compensated by photons scattering into the field, which leads to a spectrum hardening in small fields. In broad beams, from a certain depth onwards, the phantom scatter will be larger than the scatter from the collimation system, especially for flattening filter-free setups. Hence, the reduced phantom scatter will usually be the more important source of beam hardening in small fields. Figure 2.5 shows the depth dependence of the average photon energy; whereas in large fields spectrum hardening with depth is counteracted by increased scattering, this is not the case in small fields, and the average photon energy increases with depth in small fields.

Figure 2.4 provides information for small fields about only the photon fluence. What is also important

in detector dosimetry is the impact on the secondary charged particle spectra. To first order, the secondary electron fluence distribution will follow the trend of the photon energy distribution with the consequence that the average electron energy will modestly increase for smaller field sizes. Compounded with this is that in the case that the field is so small that there is no LCPE on the central axis, there will be an excess of high-energy electrons created nearby the central axis not balanced by incoming, lower-energy electrons that would have been created farther away. All this will lead to increased average electron energy as the field size decreases as seen in Fig. 2.5.

Away from the central axis it is not clear, *a priori*, if the net effect will be beam hardening or beam softening. The deficit of high-energy electrons off-axis due to the lack of LCPE will counteract the result of beam hardening on the electron spectrum and thus absorbed dose. Due to this complexity, it is impossible to establish simple generic models for energy spectra and for energy dependent correction factors for dosimeters. Even for different radiation therapy units of the same type this also results in output factors being different. Monte Carlo simulations of the specific situation are usually required to provide an accurate description.

2.3 Theoretical Framework for In-Phantom Reference Dosimetry

In this section some basic concepts of absorbed dose determination in a radiation field are reviewed. This determination is performed using a radiation detector under standard reference conditions, defined by the radiation source and geometry

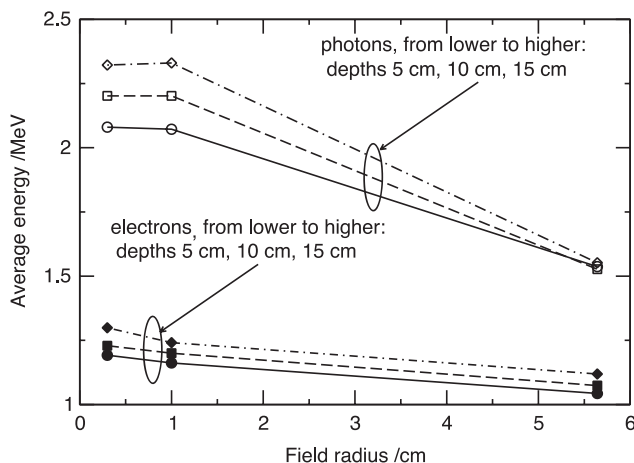


Figure 2.5. Average energy of photon and electron fluence spectra at different depths (5 cm—circles, 10 cm—squares, 15 cm—diamonds) in water for different field sizes ($10 \times 10 \text{ cm}^2$, 1 cm diameter circular field, 3 mm circular field). Data are for a 6 MV accelerator with flattening filter (Sanchez-Doblado *et al.*, 2003)

of interest. By performing a measurement of the detector reading or signal under these conditions, the desired quantity can be obtained by converting the detector signal, induced by a physical process specific to the device, to absorbed dose to the medium at the reference point. It is assumed in what follows that all appropriate corrections have been applied to the detector signal, M_{det} , namely (1) normalization to standard reference conditions (*e.g.*, environmental conditions in ionization chambers) and (2) correction for effects that influence the measurement of the physical process itself (*e.g.*, ionization chamber recombination and polarity effects).

The detector signal is first converted to absorbed dose in the sensitive volume of the detector, called the detector cavity. For a given detector signal M_{det} , the absorbed dose in the detector cavity, denoted D_{det} , can be expressed as follows:

$$D_{\text{det}} = C_Q M_{\text{det}}, \quad (2.2)$$

where C_Q is a conversion factor from detector signal to absorbed dose in the detector cavity for a specific beam quality, Q . This factor depends on the physical detection mechanism and includes the so-called intrinsic energy dependence of the detector (Rogers, 2009), its linearity and its dose rate dependence.²

Typical detectors intended for “point dose” measurements consist of a cavity containing a homogeneous detection material, as well as other structural components, sometimes referred to as non-sensitive components, designed to both assure the physical integrity of the detector as well as to assure basic operation. As the radiation field interacts with these components, the resulting reading is specific to the detector geometry and materials (to the extent that the materials of these components are different from the medium in which the detector is embedded). Therefore, since the measured cavity response differs from what would be measured without these components present, the dose to the detector D_{det} , in Eq. (2.2) is perturbed. This ensemble of phenomena can be termed the component-specific perturbation effects (Bouchard and Seuntjens, 2013).

²Note that C_Q can also be expressed as the product of a series of factors, each individually compensating for specific effects (*e.g.*, Rogers, 2009). The intrinsic energy dependence can only be determined indirectly, by calibration against a standard and after removing the absorbed dose energy dependence as calculated by MC methods. Theoretical determination of the intrinsic energy dependence requires models of the physical or chemical behavior of the mechanism that links the observed reading to the absorbed dose to the sensitive volume.

For a detection cavity “free” of non-sensitive components, there still is some remaining perturbation effect during radiation detection, since the cavity itself usually contains a material different from the medium. As physical properties such as mass density, atomic number, and I -value affect it, the energy fluence in the cavity differs from that at the point of measurement without the detector present. This phenomenon is referred to as the detector replacement perturbation effect. As for the component-specific perturbation effect, the replacement perturbation effect depends on the cavity size and shape, the nature of the material constituting the cavity, as well as the irradiation conditions.

Figure 2.6 shows a schematic representation of the different components of the perturbation effects. In essence, component-specific perturbation effects and replacement perturbation effects can be estimated by taking the ratio of calculated absorbed doses in a series of detector geometries, only differing in their components or in the composition of the cavity. In this manner, perturbation correction factors can be evaluated as a ratio of doses scored in geometries connected to each other by a chain of correlated geometries. The chain of correlated geometries can consist of a fully modeled chamber that has components that are gradually removed from it to represent the effect of a specific perturbation. The ratio of absorbed doses for a successive pair of geometries corresponds to a perturbation factor related to the differences between the two geometries (including differences in composition). For example, the ratio between the calculated absorbed doses to the chamber without wall and the fully modeled chamber is, by definition, the wall perturbation factor. It is evident that the manner by which a given perturbation correction factor is defined, affects the definition of the remaining corrections, *i.e.*, the factors are coupled and the method must be applied consistently in order to avoid double-counting (or not accounting for) certain

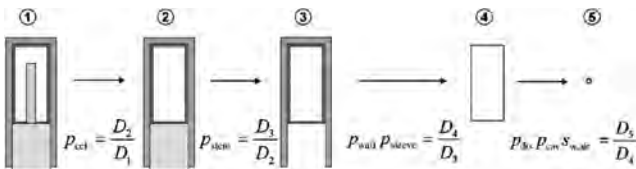


Figure 2.6. Illustration of a possible implementation of the chain technique with the perturbation correction factors calculated in the order defined by Wulff *et al.* (2008). The various perturbation factors are given by the dose ratios from one step to another in the ionization chambers’ cavity (1–4) and the dose to a small volume of water (5). The step from models 3 and 4 could be further subdivided into separate calculation of p_{wall} and p_{sleeve} . Effects of radial non-uniformity are also incorporated in the final step (steps 4 and 5).

effects. This method represents a clear path to disentangle the component-specific perturbation correction factors from the product of replacement correction and stopping-power ratio.

The product of replacement correction factor³ and stopping-power ratio cannot be easily disentangled. The reason is that the replacement perturbation corrects for assumptions embedded in the calculation of the Spencer–Attix stopping-power ratio. Historically, radiation dosimetry was based on Bragg–Gray principles and Fano’s theorem (Fano, 1954), which implies that there is no replacement perturbation effect under charged particle equilibrium (CPE) conditions (in essence, it is assumed that the detector cavity does not perturb the electron fluence). For practical situations, Fano’s theorem is not strictly applicable (Bjarnegard and Kase, 1985; Bouchard *et al.*, 2012), and therefore, a replacement perturbation effect is always present, especially for low energies, where the electron scattering power is high.

The absorbed dose energy dependence of a detector, denoted, f , can be defined as follows:

$$D_{\text{med}} = f \cdot D_{\text{det}}, \quad (2.3)$$

where D_{med} is the absorbed dose to the medium at a well-defined effective point of measurement. D_{det} is the average dose to the detector sensitive volume. f is a factor representing the overall absorbed-dose energy dependence of the detector. The factor f incorporates the perturbation effects as well as the absorbed-dose energy dependence of the detection sensitive material as conventionally quantified by the stopping-power ratio.

The absorbed dose detector response (sometimes termed absorbed dose detector sensitivity) can be defined as the ratio of its reading, M_{det} , to the quantity of interest (which could be air kerma or dose to a medium). For example, the detector absorbed dose response, is defined as follows:

$$R_D = \frac{M_{\text{det}}}{D_{\text{med}}}, \quad (2.4)$$

where, M_{det} is the reading of the detector placed in the medium med and D_{med} the absorbed dose at the effective point of measurement in the medium med . By combining Eqs. (2.2) and (2.3) and (2.4), the absorbed dose response can be written as follows:

³The effect of replacement of the cavity is subdivided in the effect of changing the material or cavity fluence perturbation, referred to as p_{cav} , and a gradient or displacement effect, referred to as p_{dis} .

$$R_D = \frac{1}{f \cdot C_Q}. \quad (2.5)$$

Monte Carlo simulations of detector response are used to determine f either as a direct ratio of doses, according to the definition in Eq. (2.3), or with sub-specification of the individual perturbation correction factors using the chain approach of Fig. 2.6. The function C_Q and the factor f , defined in Eqs. (2.2) and (2.3), respectively, depend on the nature of the detector (its detection mechanism) and the beam quality.

While this formalism is valid for any detector, it was historically developed for ionization chambers, the gold standard most commonly used in clinical reference dosimetry. For these detectors, it is instructive to explicitly discuss the role played by the different quantities defined above. The conversion function of detector signal to absorbed dose to the detector is, for air-filled ionization chambers, equal to:

$$C_Q = N_{D,\text{air}}, \quad (2.6)$$

where $N_{D,\text{air}}$ is a signal-to-dose calibration coefficient defined in the IAEA TRS-277 (IAEA, 1987) protocol [or called N_{gas} in the AAPM's TG-21 protocol (AAPM, 1983)], and can be expressed as follows:

$$N_{D,\text{air}} = \frac{(W/e)_{\text{air}}}{m_{\text{air}}} \quad (2.7)$$

Here $(W/e)_{\text{air}}$ is the mean energy per unit charge in the chamber (*i.e.*, 33.97 J/C^{-1} for dry air, (Burns, 2012; Burns *et al.*, 2014)) and m_{air} is the mass of air in the sensitive volume of the chamber. The absorbed-dose energy dependence factor f , used to convert detector dose to dose to medium is expressed (for measurements in water) as follows:

$$f = s_{w,\text{air}} p_{\text{dis}} p_{\text{cav}} p_{\text{wall}} p_{\text{cel}} p_{\text{stem}}, \quad (2.8)$$

where $s_{w,\text{air}}$ is the water-to-air Spencer-Attix stopping-power ratio, representing the absorbed-dose energy dependence of the detection material, $p_{\text{dis}} p_{\text{cav}}$ is the replacement perturbation factor (consisting of gradient and fluence perturbation components), and p_{wall} , p_{cel} , and p_{stem} are the wall, central electrode and stem perturbation factors, respectively. It should be noted that in the application of Eq. (2.3) a humidity correction factor k_h is involved in the product of f and the detector reading, correcting for variation in stopping-power ratios and W_{air}/e as a function of relative humidity.

This formalism can be generalized to any detector. While the approach to convert detector

signal to absorbed dose is linear for ionization chambers, it can be specific to the detection mechanism. As for the absorbed-dose energy dependence factor given by Eq. (2.8), the component-specific perturbation factors (*i.e.*, p_{wall} , p_{cel} , and p_{stem}) are clearly defined by the presence of these components. Generally, there could be a series of perturbation factors required to account for all non-sensitive components constituting the detector. That is, one can define the following for a more general context:

$$f = s_{w,\text{air}} p_{\text{dis}} p_{\text{cav}} \cdot \prod_i p_i, \quad (2.9)$$

where p_i are the component-specific perturbation correction factors of the detector and the product $s_{w,\text{air}} p_{\text{dis}} p_{\text{cav}}$ establishes the conversion of the average dose to the detector material to the point dose in water.

Eq. (2.9) delineates the factors contributing to absorbed dose energy dependence and it is in these that the detector physics of small fields differs greatly from that in large fields.

2.4 Stopping-Power Ratios in Small Fields

Stopping-power ratios are essential components in measurement dosimetry as they are a core component of the process of converting absorbed dose in the sensitive region of the dosimeter into absorbed dose to the medium in the absence of the dosimeter. Established conventional large-field absorbed dose dosimetry protocols are based on stopping-power ratios, water to air, calculated for open fields of typically $10 \times 10 \text{ cm}^2$.⁴ Table 2.1 shows a summary of some literature data obtained using Monte Carlo simulations and analytical modeling for 6 MV beams of different field sizes, at different depths on the central axis as well as off axis.

It is clear that the variations in stopping-power ratio water-to-air with field size are 0.6 % or less, on the central axis at 10 cm depth and 1.2 %, at 2 cm outside of the field at a depth of 10 cm. On the central axis there is generally a decreasing trend in the stopping-power ratio with depth due to spectrum hardening. Table 2.1 does not present data at depths shallower than 1.5 cm. It is known that the stopping-power ratio can vary more significantly in the build-up region but a complete prediction of its

⁴It should be noted that although the Addendum to AAPM's TG-51 (McEwen *et al.*, 2014) directly makes use of Monte Carlo calculated beam quality correction factors and not stopping-power ratios combined with detector-dependent correction factors, there still is significant pedagogical value in considering the variations in stopping-power ratio as a means to study detector response in small fields.

Table 2.1. Spencer-Attix stopping-power ratios water-to-air, $s_{w,air}$ ($\Delta = 10$ keV), for different field sizes and depths in water (data from Eklund and öö, 2008). The data off-axis are at 2 cm outside of the field, all fields are centered. The uncertainties on these values are typically below 0.1 %

Field size (cm^2)	Central axis		Off axis, 2 cm outside field	
	Depth		Depth	
	5 cm	10 cm	1.5 cm	10 cm
10 × 10	1.118	1.118	1.120	1.127
1 × 1	1.117	1.115	1.113	1.116
0.5 × 0.5	1.115	1.114	1.112	1.115
0.3 × 0.3	1.114	1.112	1.112	1.115

behavior depends on the details of the treatment head such as, collimators, flattening filter, *etc.*, which affect electron contamination.

2.5 Ionization Chamber Detector Response in Small Fields

The ideal detector for measurement dosimetry would be a point detector that is energy independent and requires only a single calibration that is valid for all possible energies and irradiation scenarios. Because of the minor variation in stopping-power ratio, water-to-air observed in Table 2.1 under different conditions, it might appear that measurement dosimetry for air-filled ionization chambers should not be significantly more challenging in small fields than it is in a $10 \times 10 \text{ cm}^2$ field. As discussed in Section 2.6, however, the absorbed dose energy dependence contains, in addition, a contribution from perturbation correction factors. The magnitude of these correction factors in small fields can be large compared to broad fields, as seen in Fig. 2.7 which presents the Monte Carlo calculated ratio of absorbed dose to water to absorbed dose to air averaged over a 1.5 mm diameter volume corresponding to the size of the cavity of an Exradin A14P chamber. The Exradin A14P is a miniature parallel plate ionization chamber. A 1.5 mm diameter circular 10 MV SRS beam is incident on axis on the front face of the phantom and the chamber is initially positioned on-axis at 3 cm depth in the water and is moved off-axis to different positions as shown in the plot. Also indicated are the stopping-power ratios water-to-air for a $10 \times 10 \text{ cm}^2$ and a 3 mm field. It should be noted that the dose to water in this calculation represents the absorbed dose averaged over the chamber volume; the overall ratio, that would correctly convert to absorbed dose to a point rather than over a volume on-axis, is even larger. This figure demonstrates that the

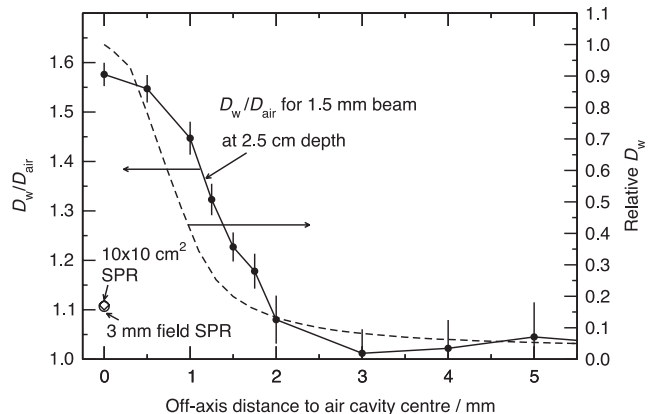


Figure 2.7. Ratio D_w/D_{air} where D_w is the dose to water averaged over the sensitive volume of a 1.5 mm diameter, 1 mm thick disc-shaped cavity (representing the cavity of the Exradin A14P parallel plate ionization chamber) and D_{air} is the dose to air in the cavity of the chamber. The details of the chamber were not modeled. The ratios are calculated for a 1.5 mm SRS field created by collimation of a 10 MV accelerator photon beam using cone. Data are plotted as a function of off-axis distance. (Data from Paskalev *et al.* (2003).)

stopping-power ratio in this very small field is underestimating the real dose conversion on-axis of cavity signal to dose to water by over 40 %. If the chamber were to be used in a $10 \times 10 \text{ cm}^2$ field, the overall perturbation effect would only be of the order of 1.5 %.

The data in Fig. 2.7 are calculated in the absence of any chamber components, thereby excluding ionization chamber wall, stem, and central electrode effects. It illustrates the main point that the component-independent perturbation effect of placing a cavity in a narrow beam can potentially be very large and vastly different from its value in broad field conditions. Physically this is an expression of the fact that, in narrow fields, large fluence perturbation effects as well as large gradient effects play a dominant role. More recent studies confirm the Paskalev *et al.* (2003) observations and report values of fluence perturbation and gradient effects in small fields using realistic ionization chamber Monte Carlo calculations. An example of this is the study by Crop *et al.* (2008), which is illustrated in Fig. 2.8 for a $8 \text{ mm} \times 8 \text{ mm}$ field. Scanning with the ionization chamber is done along the direction that represents the best geometrical resolution (*i.e.*, along the detector's smallest dimension). From this figure it is clear that the two dominating effects on the perturbation (and, the dose conversion) in small fields are the displacement (or gradient) effect and the cavity perturbation (or fluence perturbation) effect. The component-dependent corrections are comparatively small. Note that the perturbation effects are a function of the focal spot size used in

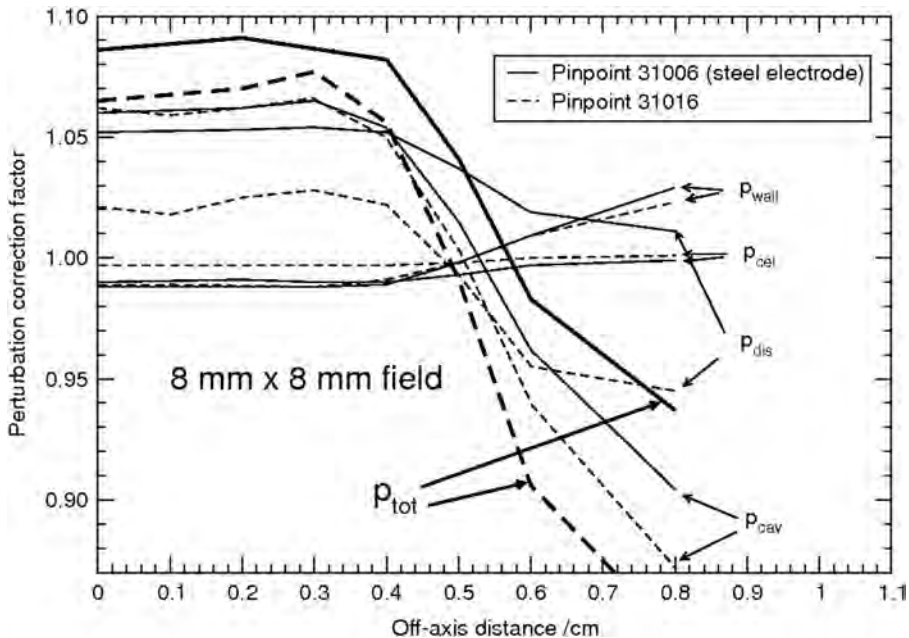


Figure 2.8. Perturbation correction factors for PTW Pinpoint chamber types (31006 steel electrode, 31016 Al electrode) in a small 8 mm \times 8 mm field. The outer diameter of the thimble of the 31006 and the 31016 chamber are 3.4 and 4.3 mm, respectively. The off-axis dimension is specified to the detector axis. The detector is scanning with its axis perpendicular to the axis of motion (optimal resolution). Individual components of perturbation correction factors, p_{wall} , p_{cel} , p_{dis} , p_{cav} , and p_{tot} are wall correction factor, central electrode correction factor, displacement correction factor, fluence perturbation correction factor and total perturbation correction factor, respectively. (Data from Crop *et al.* (2008).)

the simulations (*i.e.*, there is a coupling of the detector perturbation effects with the focal spot size of the photon source). The results presented in Fig. 2.8 are valid for a spot size of 2 mm.

Detector response for air-filled ionization chambers is thus strongly affected by the fact that the air cavity suffers from perturbation effects. Compared to large fields, these perturbation effects for small fields are no longer a second order effect in relation to stopping-power ratios.

Practically, these effects play out in relative as well as reference dosimetry measurements. Since air-filled ionization chambers are widely used in clinical measurements, accurate correction factors for these radiation beams are very important. A general formalism for dosimetry of small fields is presented in Section 2.8.

2.6 Specification of the Radiation Quality of the Beam in Small Fields

A beam quality specifier is, ideally, a unique measurable surrogate for a beam energy fluence spectrum, such that a calibration coefficient for a detector can be accurately specified. In conventional large-field reference dosimetry, a simple beam quality specifier is defined that is sufficiently representative and characteristic for the energy spectrum and, hence the stopping-power ratio $s_{\text{w},\text{air}}$. This is

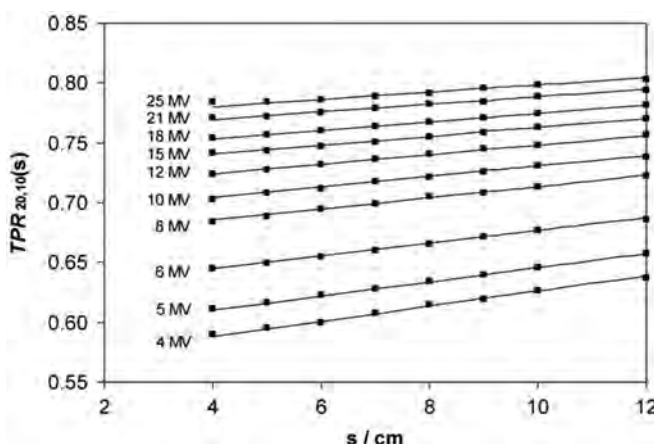
the determining quantity for the detector calibration coefficient in large fields. For heavily filtered photon beams, as used in conventional radiation therapy beams (henceforth denoted as WFF beams, standing for “With Flattening Filter”), it has been demonstrated that the tissue phantom ratio $\text{TPR}_{20,10}$, or the photon component of the percent depth dose at a depth of 10 cm, $\%dd(10)_x$ are well-correlated with the water-to-air mass collision stopping-power ratio, $s_{\text{w},\text{air}}$ (Andreo, 2000; Kosunen and Rogers, 1993; Kalach and Rogers, 2003). For flattening-filter-free photon beams (henceforth denoted as FFF beams), the relation between $s_{\text{w},\text{air}}$ and either $\text{TPR}_{20,10}$ or $\%dd(10)_x$ are different, and Xiong and Rogers (2008) showed that adequate beam quality specification of FFF beams is possible using $\%dd(10)_x$. A good correlation is also possible for modalities such as CyberKnife, TomoTherapy or Varian Truebeam that do not use flattening filters (IAEA-AAPM, 2017). It is important for small field dosimetry, that it is either proven that the beam quality of a large field in the same beam is sufficiently representative or that an alternative beam quality measurement is introduced that can account for any deviation from the large-field dosimetric parameters. As discussed in Section 2.4, Monte Carlo simulations suggest that the influence of field size on $s_{\text{w},\text{air}}$ is limited to 0.3–0.5 % at the reference depth of 5 cm in a 6 MV photon beam from 10 cm \times

10 cm reference fields down to 0.3 cm \times 0.3 cm square fields and 0.3 cm diameter circular fields. Even over a range of depths from the dose maximum to 30 cm, the variation is not larger than 1 %. Small fields are therefore well-specified by beam quality specifiers measured in larger fields and no separate measurement of a dedicated “small field beam quality specifier” is needed.

A practical concern is that in some units, large (reference) field conditions cannot be established so it is impossible to measure the beam quality in a conventional way for those systems. A machine-specific reference field, abbreviated *msr*, in which the beam quality specifier can be measured, will be defined in Section 2.8. Sauer (2009) proposed to use a measurement of tissue-phantom ratio in a small field defined at 100 cm, s , denoted by $TPR_{20,10}^{(s)}$, and correct it for field size dependence based on tabulated data from BJR Supplement 25 report (BIR, 1996). Palmans (2012) produced more practical fits to the BJR data and proposed a linear approximation for field sizes, s , limited to between 4 cm and 12 cm. This is illustrated in Fig. 2.9 for energies between 4 and 25 MV. For a radiation therapy unit with energy between 4 and 12 MV for which the largest field size that can be realized is $s \times s$ cm² (with 4 cm $< s <$ 12 cm), $TPR_{20,10}(s = 10\text{ cm})$ at field size equivalent to 10 cm \times 10 cm can be derived from $TPR_{20,10}(s)$ measured at field size, s , using the following equation:

$$TPR_{20,10}(10) = \frac{TPR_{20,10}(s) + 0.01615 \cdot (10 - s)}{1 + 0.01615 \cdot (10 - s)} \quad (2.10)$$

For the AAPM TG-51 (Almond *et al.*, 1999) beam quality specifier, $\%dd(10, s = 10)_X$, the linear approximation yields (Palmans, 2012):



$$\%dd(10, 10) = \frac{\%dd(10, s) + 4.2712 \cdot (10 - s)}{1 + 0.05339 \cdot (10 - s)} \quad (2.11)$$

Consistent with AAPM’s addendum to TG-51 (McEwen *et al.*, 2014), for beams with flattening filter (WFF beams) with energies below 10 MV ($\%dd(10,10) \leq 75\%$), $\%dd(10,10)$ is the beam quality specifier $\%dd(10,10)_X$. For beams with energies of 10 MV and higher and for FFF beams of any energy, it is recommended to introduce a 1 mm lead foil in the beam to eliminate the potential effect of accelerator-produced electron contamination and obtain $\%dd(10,10)_{\text{Pb}}$. The beam quality specifier $\%dd(10,10)_X$ can then be obtained from $\%dd(10,10)_{\text{Pb}}$ using the relations in AAPM’s TG-51 protocol (Almond *et al.*, 1999).

In Eq. (2.10), s is defined at the depth of measurement with $SDD = 100$ cm whereas in Eq. (2.11), s is defined at the phantom surface with $SSD = 100$ cm. Eqs. (2.10) and (2.11) have been proven to work reasonably well but for FFF beams (e.g., TomoTherapy and Cyberknife) it is necessary to account for an effective field size that produces the same amount of phantom scatter given the conical lateral beam profile. In the IAEA-AAPM protocol (IAEA-AAPM, 2017) methods are recommended that allow a user to determine for a nonstandard field, the side s of the equivalent square field. These methods are based on equating the scatter contribution in *msr* field and equivalent square field (BIR, 1996) for beams with flattening filter (WFF) as well as for FFF beams (IAEA-AAPM, 2017).

In addition, for units like Cyberknife and TomoTherapy where the isocentric distance is <100 cm, a correction to account for the deviation from the reference distance is required. The approach taken to quantify the TomoTherapy

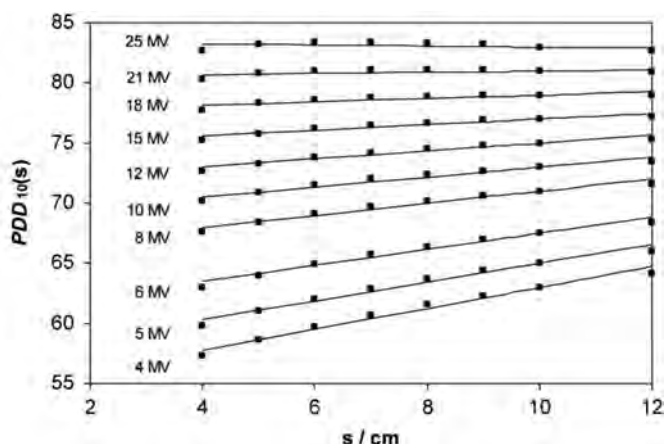


Figure 2.9. Dependence of $TPR_{20,10}$ (left panel) and of PDD (right panel) on field size, as per data from BJR Suppl 25 (BIR, 1996). Lines are linear fits, see text for discussion. [Adapted with permission from Palmans (2012).]

beam quality index is as follows. A specific beam quality index $\%dd(10)_{x,[HT\ Ref]}$ was defined as the percentage depth dose of the photon component at 10 cm depth at an SSD of 85 cm and a field size of $10 \times 5 \text{ cm}^2$ at the phantom surface. k_Q factors for the Exradin A1SL type ionization chamber and $\%dd(10)_{x,[HT\ Ref]}$ were calculated for a range of mean electron energies incident on a bremsstrahlung target and for each of these, the TG-51 (Almond *et al.*, 1999) beam quality $\%dd(10)_x$ for a conventional reference field that results in the same k_Q was then called $\%dd(10)_{x,[HT\ TG51]}$. This led to a functional relation that can be used to obtain $\%dd(10)_x$ for the lookup of k_Q factors and was adopted in the AAPM TG148 report (Langen *et al.*, 2010; Thomas *et al.*, 2005).

In summary, a beam quality specifier is a measurable parameter that specifies, ideally uniquely, the detector calibration coefficient under reference conditions. In principle, beam quality affects the ability of a detector to accurately measure absorbed dose in small field conditions. Specification of beam quality is thus needed for two reasons: (1) to describe the calibration coefficient of the detector in the machine-specific reference field and (2) to account for the changes between machine-specific reference conditions and small field conditions, where it might affect the measurement of output factors. In case (1), for external beam radiation therapy machine specific reference (*msr*) fields, large-field beam quality specifiers can be applied with some minor, practical adjustments. More details on reference calibration fields are discussed in the context of the calibration protocol, see Section 2.9. In case (2), for correction of measured output factors, beam quality specifiers are insufficient to describe the detector response in non-equilibrium conditions and details of spot size, field size and detector dimensions and composition need to be taken into consideration to describe the detector response appropriately. More practical details are given in Section 2.10.

2.7 Suitability of Detectors for Measurements in Small Field Conditions

An ideal detector would determine dose at a point, its response per unit dose would be energy independent and it would require only a single calibration valid for all possible energies and irradiation scenarios of interest. The lower limit on the volume of air-filled ionization chambers size is governed by the signal to noise ratio, which for therapeutic dose levels requires a volume of about at least 0.01 cm^3 to achieve a signal to noise ratio of around 1000 for a well-behaved chamber. For such

small chambers radiation-induced stem currents and cable currents can become very large compared to the signal. Currently, no alternative detector fulfills all of the above requirements but there are detectors that do better than air-filled ionization chambers when it comes to energy dependence and the magnitude of perturbation effects in small fields. However, these advantages often come with a price in terms of reproducibility or ease of operation.

There are three characteristics that would make a detector more suitable than air-filled ionization chambers for small field dosimetry:

- (1) the sensitive region of the detector is close to water equivalent in terms of radiation absorption characteristics;
- (2) the density of the sensitive region is close to the density of water; and
- (3) the size of the sensitive region can be made small compared to the field size while keeping noise levels under control.

Currently, detectors classes that fulfill these requirements to a greater or lesser extent are:

- (1) calorimeters made of materials that are approximately water equivalent;
- (2) detectors based on ionization in solids or liquids, or based on scintillation in materials with density close to water; and
- (3) aqueous chemical dosimeters.

Table 2.2 summarizes general characteristics and issues with these detector types. Water calorimeters are the most water-equivalent instruments and their responses have no known energy dependence or dose-rate dependence, except indirectly, as a result of heat loss and chemical heat defect (Seuntjens and Duane, 2009). However, it is an insensitive technique and due to the time needed to accumulate a sufficient signal combined with the heat diffusion properties of water, the measured signal represents a water volume that grows with time. To some extent, this issue can be handled through detailed heat loss modeling but so far the smallest field size that has been used with a water calorimeter is $3 \text{ cm} \times 3 \text{ cm}$. In graphite calorimeters this issue can be overcome since the volume over which the average dose is measured is thermally isolated from the surrounding material by one or more insulating gaps. Extension to smaller fields is then a matter of miniaturization of the device (Renaud *et al.*, 2013). This miniaturization will not have the consequence that signal is lost because of the calorimetric principle,

Small Field Dosimetry

Table 2.2. Detector classes and types and their performance for small field dosimetry

Detector class	Detector type	Mechanism of detection and detection medium	Advantages	Disadvantages in small fields
1. Calorimeters				
	Water	Temperature rise in water	Dose at a point in water	Magnitude of signal and reproducibility, heat loss
	Graphite	Temperature rise in graphite	Reproducibility, electrical calibration	Dose conversion to water
2. Solid state detectors				
	TLD, OSLD	Ionization in LiF or aluminum oxide	Small size	High density, non-trivial protocol for processing
	Diode	Ionization in silicon	Small size, ease of use	Energy dependence, perturbations caused by the substrate
	MOSFET	Ionization in silicon	Small size	Energy dependence, perturbations caused by the substrate
	Diamond	Ionization in diamond	Small size, tissue equivalent	Dose rate dependence
3. Liquid detectors				
	Liquid ionization chamber	Ionization in liquid	Small collection volume, small perturbation correction factors, energy independent	Recombination effects (dose rate dependent), temperature dependence
4. Scintillating detectors				
	Scintillating fibers	Luminescence	Small detector, water equivalent, small perturbations	Cerenkov correction, LET dependence
5. Chemical detectors				
	Fricke dosimeter	Change in optical density due to change in Fe^{3+} concentration	Energy independent, high reproducibility	Low sensitivity, volume averaging, involved process, volume averaging
	Gel dosimeter	Change in light transmission or proton composition due to chemical reactions	3D dosimeter	Non-trivial protocol for processing, involved instrumentation, reproducibility for point type measurements
	Radiochromic film (EBT TM , EBT2 TM , EBT3 TM)	Change in optical density due to chemical reactions	Nearly energy independent, density of detection material close to unity, high resolution, 2D dosimeter	Measurement protocol is involved; non-linear response, reproducibility for low doses is limited
	Alanine	Radicals resulting from chemical reactions	Nearly energy independent, density of detection material close to unity	Volume averaging, sensitivity

although the effectiveness of the insulating gaps will decrease as they become smaller, and other field dependent corrections might be required. At present, calorimetry is not yet a practical technique for small field dosimetry although it is very suitable for absorbed dose determination in machine-specific reference fields.

Solid-state detectors can be made small while remaining sufficiently sensitive. Their main shortcomings are energy dependence and dose-rate dependence. Diodes are important detectors used in clinical relative dosimetry, *e.g.*, to measure the beam profile, but cannot be used to calibrate the output of the beam. Inherently, the diode over-responds to low-energy photons interacting in the relatively high-Z sensitive material (Si). This comes into play in large fields where diodes that are not shielded (unshielded diodes) over-respond due to the low-energy scattered photon component.

“Photon” diodes (also known as PFDs) are diodes that include a high-Z layer downstream from the active layer that shields it from backscattered low-energy photons. However, removing low-energy photons by shielding causes perturbations in small fields. In the context of small field dosimetry, unshielded diodes (SFD: small field or stereotactic field diodes) can be used to measure in fields smaller than 3 cm × 3 cm through cross-calibration against an air-filled ionization chamber at 3 cm × 3 cm and provided the appropriate correction factors are applied (Section 2.10). The sensitivity of diodes changes with time as they are slowly damaged by radiation exposure.

A number of more specialized detectors with potentially interesting characteristics are available. Natural diamond detectors have favorable energy dependence (Vatnitsky *et al.*, 1993). However, there is significant dose-rate dependence due to ionic

recombination and their availability is limited. More recently, the single crystal diamond detectors operated as diodes (Buttar *et al.*, 1997; Larraga-Gutierrez *et al.*, 2015; Papaconstadopoulos *et al.*, 2014) have become available with promising dosimetric characteristics. Thermoluminescent detectors (TLDS) (DeWerd and Bartol, 2009) and optically stimulated luminescence detectors (OSLDs) (Cygler and Yukihara, 2009) are very useful dosimeters but involved protocols are required for their analysis. Fiber-based scintillators (Archambault *et al.*, 2007; Beddar and Briere, 2009; Letourneau *et al.*, 1999) are very promising devices as they are water equivalent (in terms of radiation interactions), have density close to water and can be made very small. A correction for Cerenkov generated signal in the connecting fibers is required (Archambault *et al.*, 2006) and is now part of a practical measurement technique. These detectors have a definite role in relative dosimetry.

Liquid ion chambers are close to water-equivalent, the detector material has a density close to water and they are small but they suffer from substantial general recombination (Chung *et al.*, 2013; Wagner *et al.*, 2013a); furthermore their response is temperature dependent and long-term stability of the device has been an issue. Aqueous chemical dosimeters such as the Fricke dosimeter (Klassen *et al.*, 1999; McEwen and Ross, 2009) are water equivalent and highly precise but require an extensive setup and specialized handling to maintain a sub-percent reproducibility. Radiochromic film has probably the highest intrinsic resolution of detectors which are relatively water equivalent (Devic, 2011; Soares *et al.*, 2009). However, film requires elaborate protocols to obtain acceptable accuracy for reference dosimetry. Alanine is close to water equivalent (McEwen and Ross, 2009) and its readout is relatively standardized but involves expensive equipment and the pellets with which reference dosimetry is performed are usually quite large (e.g., typically 5 mm diameter and 2.5 mm thick) and therefore suffer from substantial volume averaging. Another problem with alanine dosimetry is its comparatively low sensitivity.

Recent work has elucidated component-specific perturbations involved in the measurement of output factors or dose profiles using small field detectors (Cranmer-Sargison *et al.*, 2012; Wagner *et al.*, 2013b) and allow the determination of the most important components of a detector that lead to significant perturbations. This knowledge can be used as a guide for designing future detectors, which ideally would require no correction. Examples of such studies are those by Underwood *et al.* (2013) and Charles *et al.* (2013) who suggested modifications of the mass of

the material surrounding the active volume of diamond and diode detectors to arrive at reduced perturbations. Alternatively, Papaconstadopoulos *et al.* (2014) suggested compensating the perturbation effect from a Si substrate and wall in a D1V diode (Standard Imaging, Madison) by increasing the volume averaging effect, that is, by increasing the radius of the sensitive volume. Although these compensation scenarios are situation-specific and cannot be generalized, they are not foreign to modern detector dosimetry and have been used traditionally, e.g., to improve the energy response of detectors.

To summarize, three basic criteria mostly related to the material in and around the detector sensitive region dictate the suitability of a detector for a small field dose measurement:

- (1) the degree to which the sensitive region of the detector is water equivalent in terms of radiation absorption characteristics;
- (2) the degree to which the density of the sensitive region and surrounding materials is the same as that of water; and
- (3) the degree to which the size of the sensitive region can be made small compared to the field size.

None of the detectors currently available are perfect for small field dosimetry although there are very promising detectors for small fields of basically two classes:

- (1) Detectors that attempt to fulfill the three criteria, for example, the scintillation detectors, the liquid ionization chamber and the single crystal diamond diodes.
- (2) Detectors that take advantage of compensating effects: the over-response caused by perturbations of surrounding materials is compensated by under-response caused by volume averaging but it must be remembered that the compensation technique is situation-specific and cannot be generalized.

2.8 Formalism for Small Field Clinical Reference Dosimetry

Suitable formalisms for reference dosimetry in small fields usually have the following ingredients:

- (1) they provide a link between the use of detectors calibrated in a conventional large field for a reference beam quality and the dose determination in a small field in the users beam;
- (2) they give a recommendation on how to specify the beam quality in a small field; and

(3) they provide guidance on the use of detectors for the determination of output factors in small fields. The formalism proposed by Alfonso *et al.* (2008), also followed in the IAEA-AAPM protocol (IAEA-AAPM, 2017), introduced the concept of a machine-specific reference field (*msr* field). The *msr* field is the largest possible field, or at most 10 cm × 10 cm, that can be realized on the treatment unit involved in small field radiation therapy. The *msr* field is an intermediate reference field.

The formalism starts from the basic absorbed dose equation as in the TRS-398 (IAEA, 2000a) or TG-51 (Almond *et al.*, 1999) approach but applied to a measurement with a suitable detector in an *msr* field, and introduces an additional correction factor, $k_{Q_{msr},Q}^{f_{msr},f_{ref}}$ to account for the difference between the conditions for a conventional large reference field Q and those in the *msr* field Q_{msr} . The dose in the *msr* field is determined using the following equation:

$$D_{w,Q_{msr}}^{f_{msr}} = M_{Q_{msr}}^{f_{msr}} N_{D,w,Q_0} k_{Q,Q_0} k_{Q_{msr},Q}^{f_{msr},f_{ref}}, \quad (2.11)$$

where $M_{Q_{msr}}^{f_{msr}}$ is the detector reading in the *msr* field corrected for influence quantities, N_{D,w,Q_0} the absorbed dose to water calibration coefficient at beam quality, Q_0 (usually ^{60}Co), and k_{Q,Q_0} is the usual beam quality correction factor for the difference in beam quality between the users large field reference Q and the calibration beam Q_0 . For most of the external beam radiation therapy devices that cannot realize 10 cm × 10 cm beams, the *msr* is an open field with size well above that would be classified as a “small field”. In case the accelerator cannot realize a 10 cm × 10 cm field size, the procedure discussed in Section 2.6 is followed to determine the corresponding beam quality Q . Thus, in general the *msr* field differs from the conventional 10 cm × 10 cm field in both (1) field size and (2) beam quality (Fig. 2.9).

2.9 Machine Specific Reference Fields and Beam Quality Correction Factors

Table 2.3. summarizes examples of the *msr* fields for some standard and nonstandard devices as well as commonly used reference conditions for the measurement of the beam quality of *msr* fields.

Until recently, the Cyberknife® Robotic Radiosurgery System (Accuray Inc., Sunnyvale, CA), could realize a 6 cm calibration field and lacks a flattening filter. This leads to a lower-energy beam spectrum than that of a conventional linac with the same nominal energy. In addition, until recently, the 6 cm profile for the largest field available, which is used as the *msr* field, is not flat. Xiong and Rogers (2008) showed that there is a difference of 0.4–1 % between the water-to-air restricted stopping-power ratios in FFF beams compared to WFF beams at the same nominal energy. They suggested that in this case the value of k_{Q,Q_0} derived from the IAEA TRS-398 code of practice (IAEA, 2000a) should be decreased by about 0.5 %. If one adopts the TG-51 protocol for reference dosimetry (Almond *et al.*, 1999), in which the photon component of the percent absorbed dose at 10 cm (%dd $_{10}$) is used as beam quality specifier, the relationship between %dd $_{10}$ and restricted stopping-power ratio, water-air is retained.

Several papers have been published (Francescon *et al.*, 2012; Kawachi *et al.*, 2008; Pantelis *et al.*, 2010; Sauer, 2009) that provide methods to obtain the machine specific correction factor $k_{Q_{msr},Q}^{f_{msr},f_{ref}}$ or the overall correction factor $k_{Q,Q_0} k_{Q_{msr},Q}^{f_{msr},f_{ref}}$. The method can be analytical (Sauer, 2009) or experimental (Pantelis *et al.*, 2010). In the analytical method, the beam quality index TPR $_{20,10}$ measured in the *msr* field is converted to that in a hypothetical 10 × 10 cm 2 field with the same nominal energy using equations discussed in Section 2.6. The beam quality correction factor for the latter beam quality index is then extracted from the protocol. A correction is applied to account for the non-uniformity of

Table 2.3. Examples of machine-specific reference fields and reference conditions for the measurement of beam quality

Device	Machine-specific reference field	Reference conditions for beam quality specifier determination	
		Field size	SSD or SDD
Helical tomotherapy	10 cm × 5 cm	10 cm × 5 cm	85 cm
Cyberknife	6 cm diameter	6 cm diameter	80 cm if using TPR $_{20,10}$ 100 cm if using %dd $_{10}(\text{s})$
FFF SRS accelerator	10 × 10 cm 2	10 × 10 cm 2	100 cm
Gamma Knife (4C and Perfexion)	All sources open Field diameter of individual beam ports is 1.6 or 1.8 cm for Perfexion and 4C, respectively	Beam quality not measured	

the profile in the FFF beam over the area of the chamber. Corrections of the order of 1 % in the case of typical Farmer type chambers are found due to the large dose gradients within the cavity volume (Francescon *et al.*, 2012; Kawachi *et al.*, 2008; Pantelis *et al.*, 2010).

Direct Monte Carlo methods have also been applied to determine the overall correction factor $k_{Q,Q_0} k_{Q_{msr},Q}^{f_{msr}f_{ref}}$ by Araki (2006), Francescon *et al.* (2012), and Kawachi *et al.* (2008). For the Cyberknife machine, correction factors for reference dosimetry have been calculated for a variety of ionization chamber types, from the standard Farmer-like chambers typically used in reference clinical dosimetry, to micro-chambers with small cavity lengths. As an illustration, Table 2.4 shows the Monte Carlo values of $k_{Q_{msr},Q_0} = k_{Q,Q_0} k_{Q_{msr},Q}^{f_{msr}f_{ref}}$ in comparison with k_{Q,Q_0} from TRS-398 (IAEA, 2000a) from the paper by Francescon *et al.* (2012). The overall correction factor k_{Q_{msr},Q_0} generated by a precise Monte Carlo model (Francescon *et al.*, 2012) is within 1 % of the k_{Q,Q_0} extracted from TRS-398 (IAEA, 2000a). As discussed above, for Farmer-like chambers the difference of around +0.7 to +0.9 % in the result is due to the effect of profile non-uniformity on the volume averaging (a correction of 1.4 % to the IAEA, 2000a data) and the difference in stopping-power ratio between the FFF beam of the Cyberknife and the WFF beams assumed in the TRS-398 data. If these effects are taken into consideration, the agreement is within 0.5 % for all chambers (Francescon *et al.*, 2012).

Uncertainties on measured k_{Q_{msr},Q_0} can be as large as 1.6 % depending on the accuracy of the reference detector (Pantelis *et al.*, 2010). Krauss and Kapsch (2007) measured the beam quality correction factors with reference to water calorimetry with a combined standard uncertainty of 0.3 %. Most of the present day numerical values for k_{Q_{msr},Q_0} , however, come from Monte Carlo studies where the overall standard uncertainty is

Table 2.4. Example of Monte Carlo calculated values of $k_{Q_{msr},Q_0} = k_{Q,Q_0} k_{Q_{msr},Q}^{f_{msr}f_{ref}}$ for several detectors in the 6 cm 6 MV beam of the CyberKnife. Comparison is made with values of k_{Q,Q_0} from TRS-398 (IAEA, 2000a) where TPR_{20,10} in a hypothetical $10 \times 10 \text{ cm}^2$ is obtained using the method of Sauer (2009) from the measured TPR_{20,10} in the 6 cm circular field size. Data from Francescon *et al.* (2012)

Chamber type	k_{Q_{msr},Q_0}	k_{Q,Q_0}	Difference (%)
PTW 30006 Farmer	1.000	0.993	+0.7 %
PTW 31014 Pinpoint	0.990	0.995	-0.5 %
Exradin A12 Farmer	1.006	0.997	+0.9 %
NE 2571 Farmer	1.003	0.995	+0.8 %
PTW 31010 Semiflex	0.990	–	–

estimated to be 0.5 % or less (Francescon *et al.*, 2012; Muir *et al.*, 2011; Wulff *et al.*, 2010). Table 2.5 shows examples of k_{Q_{msr},Q_0} factors obtained by Monte Carlo for the Tomotherapy calibration field for seven distinct detectors (Sterpin *et al.*, 2012) for the Tomotherapy nominal beam quality. IAEA-AAPM (2017) can be consulted for a complete dataset of beam quality correction factors for Tomotherapy and CyberKnife.

The *msr* field is essentially a large field for all current SRT devices, except for the Gamma Knife. The Gamma Knife cannot generate individual fields with diameter larger than 16 or 18 mm for the Perfexion and 4C model, respectively. Not all air-filled ionization chambers are suitable for measurement in these fields because of the size of the collection volume and remembering that r_{LCPE} is ~4 mm. It is thus important to choose a chamber with a volume small enough to be covered in the field to within r_{LCPE} . For practical reasons, one chooses to open all Gamma Knife sources to realize a multi-angle exposure of the ionization chamber in the center of a spherical phantom, which defines the *msr* in a Gamma Knife field. Reference dosimetry of Gamma Knife is commonly performed in spherical plastic phantoms such as ABS (Acrylonitrile Butadiene Styrene) and Solid Water (RMI 457) and only exceptionally in water and beam quality correction factors account for the special beam arrangement and for the difference in radiation absorption characteristics between plastic and water. The IAEA-AAPM code of practice (IAEA-AAPM, 2017) lists beam quality correction factors that differ from unity by –0.2 to +1.7 % for a water phantom and between +0.7 and +3.0 % for an ABS phantom. For more details on values of beam quality correction factors for Gamma Knife and specific phantom types IAEA-AAPM (2017) can be consulted.

If a correction factor for a specific chamber is not available, the method to obtain the quality beam

Table 2.5. TomoTherapy *msr* overall beam quality correction factors, k_{Q_{msr},Q_0} (data from Sterpin *et al.*, 2012). The Type A uncertainty ($k = 1$) on these calculations was specified as below 0.2 %; the type B uncertainty ranging between 0.3 and 1.0 % depending on the source of uncertainty taken into consideration

Chamber type	k_{Q_{msr},Q_0}
Exradin A1SL	0.997
Exradin A12 Farmer	1.000
PTW 30006 Farmer	0.996
PTW 31010 Semiflex	0.995
PTW 31014 Pinpoint	0.993
PTW 31018 microLion	0.993
NE 2571 Farmer	0.997

correction factor is to convert the quality index Q measured under the msr conditions to standard reference conditions using the method described in Palmans (2012) (see Eqs. 2.10 and 2.11 and the IAEA-AAPM (2017) report for more details). A correction for volume averaging should be applied (e.g., Pantelis *et al.*, 2010) which adds a modest component to the uncertainty compared to standard reference dosimetry. In this case, the uncertainty in the calibration of the output of the machine in the msr field, consistent with the TG-51 addendum (McEwen *et al.*, 2014), should be considered to be in the range from 1 to 2.5 %, for a Farmer-like chamber.

Small volume ionization chambers have the advantage of a lower volume-averaging effect. Nevertheless, a study performed on several micro-chambers (Le Roy *et al.*, 2011; McEwen *et al.*, 2008) has shown that not all types of micro-chambers are suitable for reference dosimetry, since significant recombination and polarity effects have been observed. AAPM's addendum to TG-51 (McEwen *et al.*, 2014) as well as IAEA-AAPM (2017) rule out the use of micro-chambers for conventional and machine-specific reference fields, respectively and adopt the requirements for reference class ionization chambers developed by McEwen (2010).

2.10 Output Factors

Calibration of a unit in the msr fields only partially addresses the needs for measurements in small fields as the msr fields, except for the Gamma Knife, are still defining conditions that are significantly different from small field conditions. The Alfonso *et al.* (2008) formalism also provides guidelines on the measurement of relative output factors in small fields. Different nomenclature for relative output factor exists in the literature, such as simply “output factor”, “field factor”, or “total scatter factor”. For clarity, in the present Report, the term “output factor” is used.

Output factors are the ratio of absorbed doses to water per accelerator monitor unit (MU) in the small (clinical) field of interest and in the msr field. The measurement is performed at a user specified depth and SSD. Usually a depth of 5 or 10 cm is suggested in order to avoid electron contamination from the treatment head at shallow depths. To distinguish between the actual output factor [*i.e.*, the ratio of absorbed doses in water per accelerator MU, and the ratio of the detector readings, the symbols Ω and $OF(\text{det})$ will be used, respectively]. These quantities are related through:

$$\Omega_{Q_{\text{clin}}, Q_{\text{msr}}}^{f_{\text{clin}}, f_{\text{msr}}} = OF_{Q_{\text{clin}}, Q_{\text{msr}}}^{f_{\text{clin}}, f_{\text{msr}}}(\text{det}) \cdot k_{Q_{\text{clin}}, Q_{\text{msr}}}^{f_{\text{clin}}, f_{\text{msr}}}, \quad (2.12)$$

where $OF_{Q_{\text{clin}}, Q_{\text{msr}}}^{f_{\text{clin}}, f_{\text{msr}}}(\text{det})$ is the ratio of the detector readings given by the following equation:

$$OF_{Q_{\text{clin}}, Q_{\text{msr}}}^{f_{\text{clin}}, f_{\text{msr}}}(\text{det}) = \frac{M_{Q_{\text{clin}}}^{f_{\text{clin}}}}{M_{Q_{\text{msr}}}^{f_{\text{msr}}}}, \quad (2.13)$$

where $M_{Q_{\text{clin}}}^{f_{\text{clin}}}$ and $M_{Q_{\text{msr}}}^{f_{\text{msr}}}$ are the detector readings in the clinical and msr field, respectively. The output correction factor $k_{Q_{\text{clin}}, Q_{\text{msr}}}^{f_{\text{clin}}, f_{\text{msr}}}$ is given by the following equation:

$$k_{Q_{\text{clin}}, Q_{\text{msr}}}^{f_{\text{clin}}, f_{\text{msr}}} = \left[\frac{D_{w, Q_{\text{clin}}}^{f_{\text{clin}}} / M_{Q_{\text{clin}}}^{f_{\text{clin}}}}{D_{w, Q_{\text{msr}}}^{f_{\text{msr}}} / M_{Q_{\text{msr}}}^{f_{\text{msr}}}} \right], \quad (2.14)$$

where $D_{w, Q_{\text{clin}}}^{f_{\text{clin}}}$ and $D_{w, Q_{\text{msr}}}^{f_{\text{msr}}}$ are the absorbed doses to water in the clinical small field (*clin*) and in the msr field, respectively. $M_{w, Q_{\text{clin}}}^{f_{\text{clin}}}$ and $M_{w, Q_{\text{msr}}}^{f_{\text{msr}}}$ are the detector readings in the clinical small field (*clin*) and the msr field, respectively. The determination of the factor $k_{Q_{\text{clin}}, Q_{\text{msr}}}^{f_{\text{clin}}, f_{\text{msr}}}$ can involve a measurement with a suitable reference dose detector, capable of measuring absorbed dose in the small field of interest. Note that a suitable detector in small fields can become unsuitable in larger fields and of course the reverse is also true. An example of the former scenario is the unshielded diode, while an example of the latter is a Farmer-type ionization chamber.

However, the preferred method is using $k_{Q_{\text{clin}}, Q_{\text{msr}}}^{f_{\text{clin}}, f_{\text{msr}}}$ factors determined from Monte Carlo calculations that include detailed modeling of the detector and the external beam for the clinical small field. As discussed previously, the deviation of the correction factor from unity depends not only on the size of the detector and on its sensitive volume, but also on the materials in the sensitive volume as well as surrounding it. This should be taken into account when selecting a dosimeter for output factor measurements in small fields. Since the formalism published by Alfonso *et al.* (2008), there has been a surge in the literature on correction factor studies for small field dosimetry. Experimental and combined experimental—Monte Carlo studies on diodes, ionization chambers and plastic scintillators have been made by Bassinet *et al.* (2013); Cranmer-Sargison *et al.* (2013); Czarnecki and Zink (2013); Francescon *et al.* (2011); Klein *et al.* (2010); Wang and Beddar (2011) among others. Ralston *et al.* (2012) used an experimental technique to determine diode correction factors. While such measurements are useful to confirm correction factors determined by other means, it has to be noted that these measurements require a great deal of care and effort to arrive at an acceptable accuracy and experimental uncertainty.

Because of the perturbation effects involved in the $k_{Q_{\text{clin}}, Q_{\text{msr}}}^{f_{\text{clin}}, f_{\text{msr}}}$ factors it is expected that the values will depend on the details of the source (*i.e.*, focal spot, collimation system). It turns out that the correction factors for most detectors investigated so far depend much less on these details than the output factors themselves. Francescon *et al.* (2011), *e.g.*, published correction factors based on Monte Carlo simulations with incorporation of Type B uncertainties that take into account the effect of the spot size, variation in primary electron energy, variation in distance between exit window and target as well as calculations for two different accelerator types. The largest combined uncertainty, 1.8 %, was for the (completely inappropriate) Farmer type chamber in the smallest field (5 mm) studied. Benmakhlof *et al.* (2014) studied the correction factors for two air-filled ionization chambers, five diode types and a liquid ionization chamber. They compared their data with literature values and extracted combined standard uncertainties on the resulting average correction factor data. The results are shown for illustration in Fig. 2.10.

These data indicate the over-response of the diode detectors (PTW T60016, PTW T60017, IBA PFD, IBA EFD, IBA SFD) at small fields (5 mm \times 5 mm) whereas the air-filled ionization chambers (PTW T31016, IBA CC01) under respond in small fields by as much as 10.3 % for the 0.016 cm³

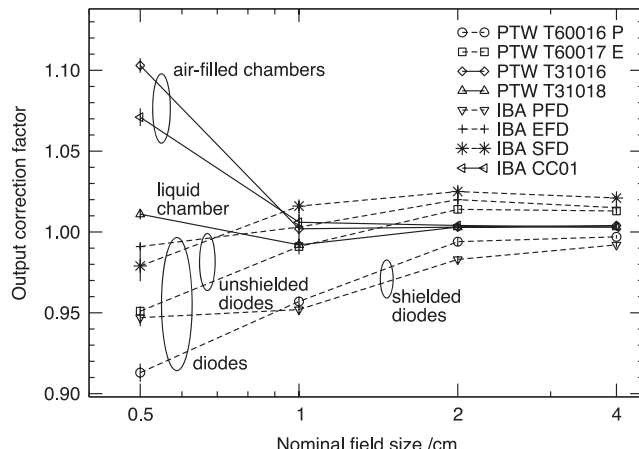


Figure 2.10. Output correction factors, $k_{Q_{\text{clin}}, Q_{\text{msr}}}^{f_{\text{clin}}, f_{\text{msr}}}$, for eight detector types in small fields from the Varian IX series for 5 mm, 1, 2, and 4 cm field openings normalized to a 10 \times 10 cm² field size. Three types of detectors are involved: air-filled ionization chambers (PTW T31016, IBA CC01), liquid ionization chamber (PTW T31018), and diodes (PTW T60016, PTW T60017; IBA PFD, IBA EFD, IBA SFD). The diode data is shown in two classes (*unshielded*: under-response in intermediate field sizes 2–4 cm and over-response in small fields; *shielded*: over-response in fields 4 cm and smaller). The field size is specified as the nominal side of a square field. The data is an average of several studies Monte Carlo and measurements. (Benmakhlof *et al.*, 2014) and references therein.

Pinpoint chamber (PTW T31016), when normalized to a 10 cm \times 10 cm field. Figure 2.10 illustrates an important difference between shielded and unshielded diodes. Whereas all diodes over-respond in the smallest field (5 mm) due to the density perturbation effect, unshielded diodes under-respond in intermediate field sizes (2–4 cm) relative to the reference field of 10 cm. This behavior is due to the reduction in average photon energy and its effect on the mass-energy absorption coefficient ratio Si-to-water as the field size becomes larger. For shielded diodes, where low-energy photons are absorbed in the detector shielding, this relative under-response is eliminated (Sauer and Wilbert, 2007).

In the smallest field none of the detectors shown in Fig. 2.10 exhibit negligible correction factors, the MicroLion liquid chamber (PTW T31018) being the closest to unity. Note that the Monte Carlo simulations cannot include other effects involved in the measurement in small fields (*e.g.*, polarity effects, recombination effects) which might be important for detectors, such as diamond detectors and liquid ionization chambers.

It should also be noted that the MC computed correction factors for the PTW liquid ionization chamber were found to be more sensitive to the parameters chosen for the treatment head simulation (*i.e.*, spot size, collimation settings) compared to diodes (Francescon *et al.*, 2011). The dependence of the correction factors on the type of treatment unit for the same nominal energy and on other dosimetric parameters such as depth of measurement and source detector distance (SDD) has also been studied (Francescon *et al.*, 2011, 2012; Pantelis *et al.*, 2012). It has been shown that diodes are not only field size dependent, for units with a different treatment head design but with the same nominal energy (Francescon *et al.*, 2011). In addition, their correction factors are uncorrelated with changes in SDD (Pantelis *et al.*, 2012). In contrast, correction factors for both liquid and air filled micro-chambers, are dependent on the model of the treatment unit (Francescon *et al.*, 2011) and they also vary with SDD (Pantelis *et al.*, 2012). The degree of variation with SDD for the type of micro-chamber analyzed (PTW 31014) is of the order of 13 % for the smallest 5 mm diameter collimator of the CyberKnife. Such dependencies should be considered when choosing a detector.

Output correction factors $k_{Q_{\text{clin}}, Q_{\text{msr}}}^{f_{\text{clin}}, f_{\text{msr}}}$ must be reported as a function of FWHM of the small field profile at the point of measurement and FWHM in both in- and cross-plane directions (*i.e.*, FWHM_x and FWHM_y) are, in general, not identical. The IAEA-AAPM (IAEA-AAPM, 2017) code of practice defines the small field equivalent field size s as the

geometric mean of FWHM_x and FWHM_y , *i.e.*, $s = \sqrt{\text{FWHM}_x \cdot \text{FWHM}_y}$. This is based on the observation that the output correction factor $k_{Q_{\text{clin}}, Q_{\text{msr}}}^{f_{\text{clin}}, f_{\text{msr}}}$ for small fields collimated with different methods, is well-specified using the geometric mean (Cranmer-Sargison *et al.*, 2012).

Output factors for the Gamma Knife and other gamma-ray stereotactic radiosurgery devices have been reported in the literature. The relative output of the 4 mm diameter fields remains one of the most challenging problems in small field measurements (Goetsch, 2002a; Nizin, 1998). The original measurement of the output ratio between the 18 mm helmet for the Elekta Gamma Knife (largest available field size) and the smallest helmet (4 mm nominal diameter) was determined by the manufacturer to be 0.80 (history summarized in Arndt 1999). The manufacturer recommended a change to 0.87 (9 % increase) based on measurements with a liquid ionization chamber (Wickman and Holmstrom, 1992) and Monte Carlo calculations (Cheung *et al.*, 1999). A number of researchers attempted to measure the output factor of the 4 mm Gamma Knife helmet (Kurjewicz and Berndt, 2007; Mack *et al.*, 2002; Perks *et al.*, 2005; Somigliana *et al.*, 1999) using a wide variety of techniques including miniature ionization chambers, liquid ionization chambers, radiochromic films, diodes, MOSFETs, diamond detectors, glass rods, thermoluminescent microcube dosimeters, and alanine EPR detectors. In the end, most investigators converged on an estimate for 4 mm helmet output factors close to that provided by the manufacturer (*i.e.*, 0.87). Historically it has been difficult for clinical Gamma Knife users to verify the manufacturers suggested helmet output factors for 8 and 4 mm helmets. A novel technique involving double exposures on a single piece of radiochromic EBTTM film was published (Ma *et al.*, 2009). This technique is simple and requires no complex analytical equipment, only a 16-bit film scanner.

The IAEA-AAPM (2017) code of practice lists output correction factors $k_{Q_{\text{clin}}, Q_{\text{msr}}}^{f_{\text{clin}}, f_{\text{msr}}}$ for a number of ionization chambers, diode detectors and diamond detectors in 8 and 4 mm fields relative to the *msr* field (16 mm) thereby enabling verification of the manufacturer recommended output factors.

To summarize, the determination of output factor $\Omega_{Q_{\text{clin}}, Q_{\text{msr}}}^{f_{\text{clin}}, f_{\text{msr}}}$ involves the output correction factor $k_{Q_{\text{clin}}, Q_{\text{msr}}}^{f_{\text{clin}}, f_{\text{msr}}}$, which in general depends on detector type, field size and linac model. Recent literature has provided output correction factors, $k_{Q_{\text{clin}}, Q_{\text{msr}}}^{f_{\text{clin}}, f_{\text{msr}}}$, and uncertainty estimates for an extensive set of chambers. These are available in the IAEA-AAPM (2017) code of practice. A user in the clinic should compare

output factors determined using two or more distinct detectors, appropriately corrected using these detector-dependent $k_{Q_{\text{clin}}, Q_{\text{msr}}}^{f_{\text{clin}}, f_{\text{msr}}}$ values. Obtaining consistency in the determination of output factors and absorbed dose by using different detectors, after accounting for their corrections, is the best approach to ensuring accuracy in the measurement of small fields. Corroborating output factors determined in one institution with data from another institution with comparable irradiation equipment should be considered as a second check.

2.11 Practical Aspects in Output Factors Measurements

As discussed in Section 2.1.1, when lateral electronic equilibrium is not established in small fields, absorbed dose changes rapidly with beam size and, for a given beam size absorbed dose per unit detector reading as the detector moves through the penumbra. Therefore, measurements are subject to systematic uncertainties, which can have a more severe impact on dosimetric accuracy and precision as the field size decreases. The sources of uncertainty are:

- (1) detector position and orientation, and
- (2) accuracy of collimation system settings.

In small fields, output factor determination is typically performed by orienting the detector with its longest axis parallel to the beam axis. To avoid leakage, particular care must be taken to reduce as much as possible parts of the cable within the radiation field. The main challenge in output factor determination is the accurate alignment of the center of the detector with the beam axis. Since the measurement is performed at a fixed depth along the beam/z axis, centering of the detector by scanning in two perpendicular dimensions, *x* and *y*, is sufficient, one along the *x*-axis and the other along the *y*-axis. This allows the user to determine the *x*- and *y*-offsets of the detector, initially positioned at the origin of the coordinate system of the water phantom, with respect to the central axis, as determined from the measured dose profiles in the two orthogonal dimensions. Potential scanning system hysteresis effects must be verified. To achieve an accurate positioning, a very small field should be used, such as a $5 \times 5 \text{ mm}^2$. Once the appropriate shift to properly align the detector with the central axis (CAX) is made, beam profiles should be scanned again in both orthogonal directions to confirm the alignment of the detector with the CAX. In general the detector can be centered with the CAX to within a fraction of a millimeter.

Another common problem is the collimator setting: the output of small fields is very sensitive to small variations in the aperture of the field, which might be determined by a MLC, by a variable collimator like the IRIS™ in the Cyberknife system, or by fixed cones mounted to the treatment head. A small variation of ± 0.1 mm on a field of 5 mm size can have an effect up to ± 5 % in the measured $OF(\text{det})$. This is a combination of the phenomenon of source occlusion (discussed in Section 2.1.2) with the reduction in electron fluence received by the detector due to absence of photons near the edge of the field. Fixed cones have the advantage that their dimension does not change, but there can be a difference between the nominal diameter and the actual diameter, and therefore the actual dimension of the collimator must be measured if field size-dependent correction factors are to be applied. This applies even more to variable or MLC, for which the reproducibility of the positioning of the leaves (or of the leaf banks) is limited by the mechanical tolerances of the collimation system. Therefore, the measurement of an output factor must be always accompanied by a measurement of the actual profile of the field.

2.12 Relative Dosimetry for Radiotherapy Using Small Fields

2.12.1 General Aspects

Aside from the output factor discussed in the two preceding sections, the basic dosimetry parameters for relative dosimetry are the depth-dose distribution (represented by Percentage Depth Dose, PDD), Tissue Maximum Ratio (TMR), or Tissue Phantom ratio (TPR), and OAR.

As in the discussion of output factor, the same precautions in terms of dosimeters and their performance apply to the measurement of dosimetric parameters such as PDD, TPR and OAR. For the fundamental reasons discussed in the previous sections, the assumption that the detector correction factors are independent of field size is not valid (Francescon *et al.*, 2008, 2011). By choice of nomenclature it was made clear in Section 2.10 that the output factor $\Omega_{Q_{\text{clin}}, Q_{\text{msr}}}^{f_{\text{clin}}, f_{\text{msr}}}$ is a ratio of absorbed doses at a given depth in two different fields (the clinical field and the reference (*msr*) field) and when the clinical field is “small” compared to the reference field the ratio of absorbed doses cannot simply be calculated as a ratio of dosimeter readings. Similarly, PDD, which is the ratio between the absorbed dose to water at any given depth to the absorbed dose at the depth of maximum dose might require the application of field size and depth dependent correction factors in small fields.

The essence of suitability of detectors for small field dosimetry has been discussed in Section 2.7. Studies (Francescon *et al.*, 2014; Papaconstadopoulos *et al.*, 2014) provide data on the correction factor required to convert relative detector readings to relative absorbed doses. In general, in the context of relative measurements, the choice of the detector for small fields dosimetry should be based on:

- (1) the size of its sensitive volume;
- (2) the intrinsic characteristics of the detector (response independent from energy, dose rate, reproducibility); and
- (3) the water equivalence of the materials surrounding the sensitive volume.

The lack of scattered low-energy photons in small fields might have an impact on measurement results when a detector’s energy response is not constant. It is very important that the measurements be performed with appropriate detectors in order to acquire accurate data for small fields. To reiterate, both detector size and detector materials (e.g., shielding layer in a diode detector) can have a significant impact on the measured data especially for the smallest fields. Other problems to take into account in small beam relative dosimetry are: (1) error in detector positioning and (2) setting of the collimation system. These two last issues have been discussed in detail in the AAPM TG 106 (Das *et al.*, 2008a) and the IPEM report 103 (Aspradakis *et al.*, 2010) reports.

It is possible to use Monte Carlo methods to help obtain accurate dosimetric data under extreme, but increasingly common treatment conditions where measurements are difficult or impossible, and to serve as a guide to reconciling data measured with different detectors, when their results disagree. Sometimes the Monte Carlo calculations can provide an independent quality assurance tool to prevent beam-commissioning errors. The combination of measurements using different detectors and Monte Carlo calculations can significantly reduce the dosimetry uncertainties.

2.12.2 Percentage Depth Dose

From the perspective of the measurement of the PDD in small beams, an ideal detector should also be energy-independent. The field size and, as discussed in Section 2.2, the energy spectrum changes with depth. In small fields the photon spectrum becomes harder with depth (Fig. 2.5). This is different from the behavior in larger fields where the beam hardening effect is offset by an increasing amount of scattered radiation, which, depending on

the field size, might lead to the photon spectrum effectively becoming softer with depth. Thus, detectors that have a strong energy-dependent response are not well suited for PDD measurements in small fields. Diodes, which have a high atomic number are more sensitive to energy variations than micro-chambers, especially when they are unshielded. Also, in small beams as a function of depth they tend to under-predict the dose relative to that at z_{\max} , thereby producing depth dose curves characteristic of a softer beam. On the other hand, micro-chambers suffer from volume averaging effect, which leads to a field size dependent correction factor. Since field size changes with depth, the PDD for very small fields taken with micro-chambers will suffer from significant measurement uncertainties.

Moreover, the effective point of measurement for micro-chambers is generally not well-known (Tessier and Kawrakow, 2010). This problem is even more serious when they are used with their stem parallel to the beam axis because the cavity length is generally larger than the radius. In particular, micro-chambers with high-Z electrodes show a more pronounced depth dependent effect (Tessier and Kawrakow, 2010). The determination of the effective point of measurement is not trivial. The only correct way to determine the effective point of measurement is by comparison of a Monte Carlo simulation of PDD curves of the actual detector with the Monte Carlo-calculated depth absorbed dose in water. This leads to shifts that can be expressed as a fraction of the chamber radius and that depend on the details of the chamber materials and construction. It is important to underline that the effective point of measurement changes with field size, because the fluence perturbation of the beam within the sensitive volume of the detector changes with field size: the smaller the field, the larger is the perturbation of the detector.

Many of the details of the types of errors that are encountered in measurements of depth-dose curves in small beam dosimetry have been reported by Li *et al.* (2004) and in AAPM TG 106 (Das *et al.*, 2008a). Briefly they are:

- the determination of the effective point of measurement;
- positioning errors (the proper mounting of the detector; the alignment of the detector axis with the central axis of the beam, which must be kept when the dosimeter is measuring at different depths during the vertical scan); and
- effect of collimator jaw setting on PDD.

With regard to positioning, the detector should be mounted with its axis parallel to the beam axis

(*i.e.*, vertical mounting) so that the perturbation of the field with depth is constant. A misalignment of the detector axis with the beam central axis results in a change in the PDD of a few percent (Cheng *et al.*, 2007); a deviation from the central axis along the scan depth can result in an even higher difference in PDD (Cheng *et al.*, 2007; Li *et al.*, 2006). Methods to minimize the positioning errors should be applied, as shown in the literature (Li *et al.*, 2006). The effect of the collimator jaw setting on the conversion of percent depth ionization into PDD was analyzed by Cheng *et al.* (2007). The effect of a ± 2 mm collimator setting uncertainty was found to have a negligible influence on the stopping-power ratio water to air, consistent with an only modest field size dependence of the quantity as a function of field size, whereas the effect on the overall correction factor was not investigated. The Cheng *et al.* (2007) study also reported a maximum of 2 % measured variation in the extrapolated zero-field PDD for a field size change of ± 2 mm applied to all fields in the range $1 \times 1 \text{ cm}^2$ – $10 \times 10 \text{ cm}^2$.

2.12.3 Conversion of PDD to TPR

Some TPSs require the measurement of a TPR (or TMR) instead of PDD. TPR data, acquired by changing the water level while keeping the detector fixed, are also often used for independent MU checks. The motivation for measuring TPR instead of PDD is that a TPR measurement is potentially more accurate than a PDD measurement because the detector positioning on the beam axis is performed only once and the requirement for an absolutely perfect alignment between the beam axis and the scanning path is not needed. In addition, due to the fact that the field size at the detector does not change, corrections due to the volume averaging effect might cancel. Despite this, TPR measurements are seldom performed because regular scanning tanks do not have a TPR data acquisition mode or the accurate determination of the water level is challenging (McEwen *et al.*, 2008), which may adversely affect the accuracy of the measurements in the build-up region. It is worth noting that a TPR measurement does not avoid issues related to the change in beam spectrum as the amount of attenuating material in front of the detector changes. In clinical applications users generally measure PDD and convert to TPRs. This process introduces its own uncertainties (Cheng *et al.*, 2007; Li *et al.*, 2004; Thomas *et al.*, 2014), as the conversion between PDD and TPR is not so well established for small fields as it is for the standard field sizes found in conventional radiotherapy (Aspradakis *et al.*, 2010). The standard conversion

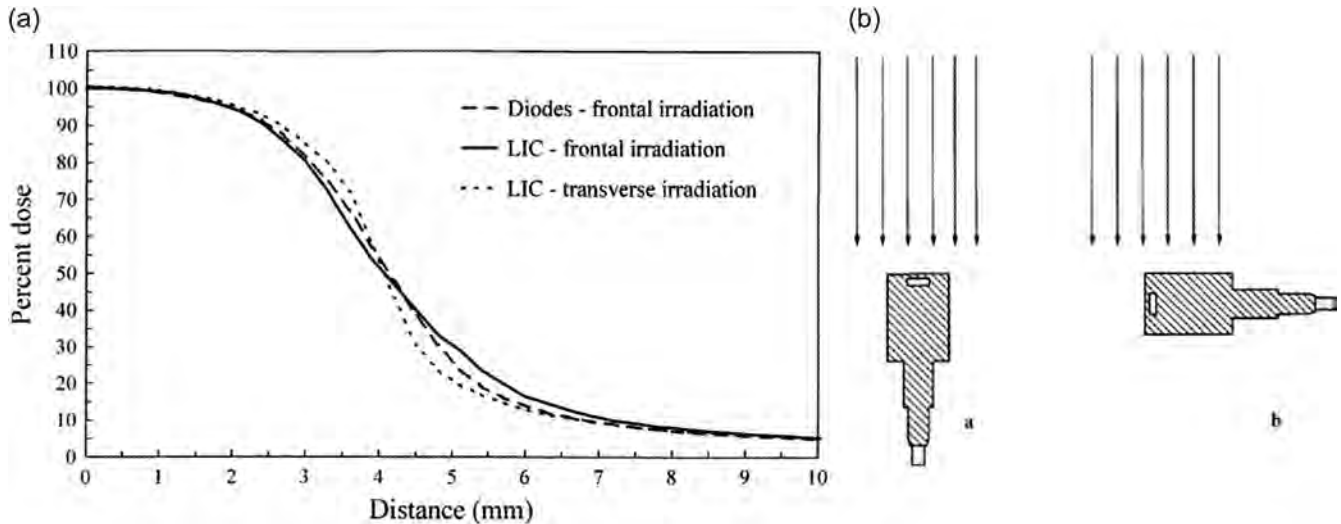


Figure 2.11. (a) Profile curves in two directions for an 8 mm diameter 6 MV photon beam measured with diode detectors (Scanditronics photon (shielded) diode and electron (unshielded) diode, frontally irradiated, lateral extent of the detection volume, 2.5 mm) and with a liquid ionization chamber (in-house developed Wickman design, sensitive volume 3 mm diameter laterally and 0.3 mm thickness). (b) Illustration of frontal and lateral irradiation orientation of the liquid ionization chamber. [Adapted from Dasu *et al.* (1998).]

of PDD to TPR in broad fields is given by the following equation:

$$TPR(z, s) = \frac{PDD(z, s \frac{SSD}{SSD+z})}{PDD(z_{ref}, s \frac{SSD}{SSD+z_{ref}})} \frac{PSF(s \frac{SSD}{SSD+z})}{PSF(s \frac{SSD}{SSD+z_{ref}})} \left(\frac{SSD + z}{SSD + z_{ref}} \right)^2 \quad (2.15)$$

where z is the depth, s the field size at isocentre (at the surface in an SSD setup), SSD the source-surface distance, and z_{ref} the reference depth. The quantity

$PDD(z, s \frac{SSD}{SSD+z})$ is the PDD at depth z for a field size at the surface that produces a field size s at depth z , and similarly for the other dosimetric functions in Eq. (2.15). PSF is the peak scatter factor, sometimes designated backscatter factor. Eq. (2.15) is usually used in simplified form, ignoring the difference between field size at the surface and at depth and ignoring the ratio of PSF for these minor field size differences:

$$TPR(z, s) = \frac{PDD(z, s)}{PDD(z_{ref}, s)} \left(\frac{SSD + z}{SSD + z_{ref}} \right)^2. \quad (2.16)$$

However, Eqs. (2.15) and (2.16) are inaccurate for small fields. Ding and Krauss (2013) evaluated an empirical correction to Eq. (2.16) for circular fields ranging between 0.4 and 3 cm. The correction was derived from realistic Monte Carlo simulations using field sizes ranging from 4 to 30 mm and depth ranging from 1.5 to 25 cm. They concluded that the conventional method of obtaining TPR from PDD Eq. (2.16) underestimated the

TPR by 3.4 and 0.6 % at a depth 1.5 cm for 4 and 30 mm fields, respectively. It also overestimated the TPR by 6.4 and 1.7 % at a depth of 25 cm for 4 and 30 mm diameter circular fields, respectively. The empirical correction reduced the difference between directly measured TPRs and converted TPRs from measured PDD curves to within 1 % for small fields. Other studies have been published (Bjarnegard *et al.*, 1996; Sauer, 2009; Thomas *et al.* 2005; Xiao *et al.*, 1998) on methods to convert from PDD to TMR/TPR, but there is not enough evidence of their suitability in small photon fields. Consequently, for situations in which the determination of TPR is necessary, the direct measurement of it is recommended unless reliable Monte Carlo data are available.

2.12.4 Dose Profile Measurements

The commissioning of a TPS involving small fields typically involves the acquisition of profiles in both directions (gun-target and left-right) at a variety of depths, for a variety of small fields down to 0.5 cm \times 0.5 cm. The photon spectrum at a given depth as a function of off-axis distance varies much less in small fields than it does in conventional large fields. Thus, for off-axis measurements a detector with a modest energy dependence can be still be used, unlike in the situation for PDD measurements and large beam profile measurements. Stereotactic field diodes (SFDs) provide a very high resolution and have also been shown to produce relative profile measurements practically identical to Monte Carlo dose to water profiles.

Thus, these unshielded diodes can be considered to be suitable detectors for relative profile measurements.

Much of the discussions above, regarding the necessity for correct mounting and precise alignment of the detector on the central axis of the beam at all depths, also apply to profile measurements. Use of a small-volume detector is extremely important for profile measurements to avoid significant penumbra blurring as the active volume of the detector moves through the steep lateral penumbra of the profile. For some of the high-resolution detectors (*e.g.*, diodes, liquid ionization chambers, and diamond detectors) the user should verify whether or not the reading depends on dose-rate changes provoked by changes with the distance from the central axis. If detectors with a directional asymmetry (*e.g.*, ionization chambers) are used, they can be mounted vertically in order to minimize the magnitude of penumbra blurring in both lateral and in-plane profiles. In general, the detector should be used in the orientation that optimizes its spatial resolution. However, the user should first verify the absence of any significant stem effect or polarity effect, which might occur as a result of asymmetric scanning. As an example, Fig. 2.11, adapted from Dasu *et al.* (1998), shows the effect on penumbra when a liquid ionization chamber is used in two orthogonal orientations.

Alternatively, radiochromic film can be used to measure dose profiles provided an accurate film data processing protocol has been developed and validated by comparison with conventional techniques in large fields (Devic, 2011). The potential penumbra blurring associated with the film scanner also needs to be taken into account. Finally, a recently available detector suitable for small field profile measurements is the plastic scintillation detector. A study by Morin *et al.* (2013) shows that profiles are in agreement with Monte Carlo results.

2.12.5 Manufacturer-Provided Relative Dosimetry

Some manufacturers may commission the relative dosimetry for their dedicated TPS at the factory and take responsibility for ensuring that service personnel restore the unit to its factory commissioned settings. While this relieves the supervising physicist of routine output factor, PDD, and profile measurements described here and eliminates the possibility of user-derived dosimetry mistakes, it does not relieve them from quality assurance methods that ensure that the commissioning is correct. Refer to company product guidelines and customer publications for suggestions on quality management. The physicist remains responsible for clinical reference dose calibration of the system.

3. Definition of Volumes

3.1 Volume Definitions in Radiation Therapy Using Small Fields

Stereotactic radiotherapy delivers a very high dose to the target while relying heavily on tight margins and steep dose gradients to reduce the impact on organs at risk. Stereotactic radiosurgery has historically been used as a neurosurgery technique but in this context volumes have not strictly been defined. As introduced in ICRU Reports 50, 62, 71, 78, and 83 several volumes related to both tumor and normal tissues have been defined for use in the treatment planning and reporting processes (ICRU, 1993; 1999; 2004; 2007; 2010). It has been practice in (*e.g.*, cranial radiosurgery) not to prescribe and, instead, to deliver spherical dose distributions. However, delineation of these volumes is a mandatory step in the planning process, as dose cannot be prescribed, recorded, and reported without specification of target volume and normal tissue at risk volume. In order to compare and reproduce clinical results, it is important that the definitions of the target and the organs at risk be as clear and as reproducible as possible. The volumes to be considered are:

- Gross Tumor Volume (GTV),
- Clinical Target Volume (CTV),
- Internal Target Volume (ITV),
- Planning Target Volume (PTV),
- Organs At Risk (OAR),
- Planning organ at Risk Volume (PRV),
- Treated Volume (TV),
- Remaining Volume at Risk (RVR).

The GTV, CTV, and OAR correspond, respectively, to volumes of known (GTV), and/or suspected (CTV) tumor infiltration, and volumes of normal tissues that might be irradiated and affect the treatment prescription (OAR). The GTV and CTV have an anatomical/physiological basis, in contrast to the ITV, PTV, and PRV, which are concepts introduced to ensure that the dose delivered to the respective CTV and OAR is clinically acceptable within the defined dose–volume constraints. Therefore, reference

to the imaging modalities used to define it, should be mentioned.

For small-field radiation, the definition of these volumes is fully maintained, but there are particularities as to how the volumes are designed and used. As an example, stereotactic radiation will not be used in the treatment of clinically uninvolved lymph nodes (*i.e.*, prophylactic treatment). Also, common formalisms used to calculate PTV margins may not be relevant to single fraction treatments with steep dose gradients.

The definitions of target volumes for conventional radiotherapy (GTV, CTV, and PTV) have traditionally reflected two underlying assumptions: (1) the pathology being treated is malignant and (2) the local control will be dependent on the sufficiency of dose delivered to the GTV/CTV. The need to avoid the treatment of uninvolved tissues and the concurrent need to target the local or regional extent of cancer are not debated. These needs may be met by means of improved imaging, training, guideline development, peer review, *etc.* More controversial are the choice of dose parameters that drive local control and the impact of intentionally over- or undertreated parts of the target. The application of these concepts to functional targets (*e.g.*, tremor, epilepsy, or neuralgia), although not always straightforward, is still useful.

One of the most important reasons to define volumes is to allow standardized prescribing and reporting of dose—most notably through the use of dose–volume histograms (DVHs), D_V (the absorbed dose received by a certain volume V of the target) and V_D (the volume of a target receiving a certain dose D) metrics. Dose reporting using these metrics is discussed in Section 7.3 of this Report.

3.2 Gross Tumor Volume

The GTV is the gross demonstrable extent and location of the “tumor”. In contrast to other forms of radiotherapy, small-field irradiation is not currently used to treat loco-regionally advanced cancers. In this respect, there will typically be no need to define

a primary and nodal GTV (primary tumor GTV or GTV-T and a separate nodal GTV or GTV-N). It will, however, be common to treat multiple metastatic deposits in a single plan. In this latter case, it will be useful to use a clear naming scheme to distinguish multiple targets (GTV1, GTV2, GTV3, or GTV-RT_FRONTAL, GTV-LT_PARIETAL, GTV-RT_CEREBELLUM, *etc.*). Whether areas that are clearly abnormal on imaging (*e.g.*, enhancement of surgical cavities, “tails” around meningiomas, small projections around a lung tumor), but not clearly part of the tumor are included in the GTV, is a matter of clinical evaluation of the likelihood that they represent tumor. There is no defined threshold beyond which the probability of a voxel containing tumor cells is high enough to assign it to the GTV. Areas very likely to be tumor will be GTV, areas less likely to be tumor may be considered CTV and some areas felt to be at low enough risk may be completely excluded from all target volumes. Such evaluations should be done with consistency from case to case and be reported in an informative way.

SRT is uncommon in the absence of a GTV. There will, however, be cases where there is no evidence of a GTV or the GTV cannot be explicitly defined but where the PTV is based directly on a CTV. Examples could be treatment of a surgical cavity following resection of a brain metastasis or treatment of UICC/AJCC T1cN0M0 prostate cancer. In any case, the concept of an anatomically defined target must be used.

For the treatment of nonmalignant or functional disease, the concepts of GTV–CTV can be more difficult to apply. For example, in radiosurgery for trigeminal neuralgia, treatment has commonly been described without delineation of a target volume. In these latter cases, there is no biological reason that a target could not be defined but rather the radiosurgery practice evolved as a result of the technical nature of the delivery device. Limitations stemming from such a lack of volume definition become evident in dose reporting and translation of past experience to new radiation delivery devices. It is unlikely that the benefits of radiosurgery in the treatment of trigeminal neuralgia are the result of one voxel of the trigeminal nerve receiving 80 Gy to 90 Gy. Rather, it is likely that the therapeutic benefit is linked to the treatment of a volume of the nerve to a lesser dose (30 Gy to 60 Gy). The delivery of a point dose to a specific coordinate is thus a surrogate for the treatment of a larger (albeit small) volume, consequently to a lower dose. The reporting of all radiation treatments in terms of dose to target volumes can only help in understanding and advancing current practice. This will require a change in culture that has already been imposed upon users

of some devices. Whereas constructing a sphere-packing⁵ plan prior to any target delineation may be a valid planning method for some nonmalignant or functional disease, a formal target volume should be defined in all cases. In the case of tumors, even benign, a GTV that includes any region intentionally undertreated should not be revised based on prescription isodose lines. Consistent and complete GTV definition is mandatory for proper data collection and reporting.

When reporting a GTV several items should be specified:

- The imaging modality and the time when the images were taken.
- The location and extent of the target, when appropriate according to the TNM/AJCC or UICC cancer staging systems and/or the WHO International Code for Disease (AJCC, 2010; Greene, 2002; Sabin *et al.*, 2010; WHO, 2000).
- The methods used to delineate the GTV. In small-field radiation therapy, rarely is physical examination used to define the GTV. Three-dimensional volumetric anatomical imaging [computed tomography (CT) and magnetic resonance imaging (MRI)] will form the basis for GTV delineation. Because of its limited spatial resolution, functional imaging [PET or magnetic resonance spectroscopy (MRS)] is rarely the principal means of defining the GTV. This does not mean that functional imaging cannot be of use for case selection (*e.g.*, to exclude lung cancer patients with regional or distant metastases), escalation of dose to biologically defined subvolumes of the GTV (Bentzen and Gregoire, 2011; Ling *et al.*, 2000) or in delineation of certain targets less well visualized on anatomic imaging (*e.g.*, in the presence of atelectasis). Planar imaging, which is excluded from 3D-CRT or IMRT planning, is still of occasional use in small-field radiation—specifically in the definition of vascular malformations. In certain circumstances, it may be useful to identify GTV volumes through the imaging modality used by subscripts (*e.g.*, GTV_{PET}, GTV_{DCE-MRI}, *etc.*). Within a radiotherapy department, a standardized and descriptive nomenclature should be used in these subscripts. Depending upon the techniques and equipment used for SRT, image acquisition may vary. It is good clinical practice to formalize and document these protocols, noting values such as image slice thickness, resolution, timing of contrast administration, type of contrast

⁵“Sphere packing” refers to the superposition of spherical dose distributions used in treatment planning of nonmalignant targets.

used, type of radiopharmaceutical used in the case of PET, imaging sequence used for MRI, etc.

Modern image-acquisition systems are increasing the sensitivity and specificity of tumor detection. Functional and molecular imaging are emerging and could provide new opportunities to understand the biology of both normal tissues and tumors (Bradbury and Hricak, 2005; Jager *et al.*, 2005). Each tumor site will have its own requirements for imaging based on normal tissue/tumor contrast, tumor motion and tumor biology. In many cases, GTV will be delineated with the help of an additional image set co-registered to a primary treatment-planning CT scan. The uncertainties related to this co-registration should be accounted for in the CTV to PTV margin (see Section 3.5).

3.3 Clinical Target Volume

The CTV is a volume of tissue that contains a demonstrable GTV and/or subclinical target tissue at a probability considered relevant for therapy. As described in previous ICRU reports, the notion of subclinical disease takes into account the microscopic tumor spread at the boundary of the primary tumor (GTV) as well as at a distance (typically regional lymph nodes).

The decisions as to what margin to add from GTV to CTV is a clinical judgment. This decision should be informed by knowledge of the risk of disease being present. Ideally, CTV margins should be informed by histopathological analyses and clinical experience with patterns of failure. As an example, although studies of operative specimens have suggested that margins of 0 mm to 26 mm were necessary to treat microscopic disease around primary nonsmall cell lung tumors, clinical experience shows a favorable local control with CTV margins of 0 mm to 5 mm. The expansion from GTV to CTV is not a geometric process and should take into account known patterns of spread and knowledge of anatomy including structures that are barriers to tissue infiltration (e.g., pleura, periosteum) (Chan *et al.*, 2001; Giraud *et al.*, 2000; Grills *et al.*, 2007; van Loon *et al.*, 2012).

In the treatment of targets that are not tumors, the concept of the CTV may seem less applicable—such is the case for the treatment of tremor, trigeminal neuralgia, or arterio-venous malformations.

For tumors, when CTV margins are used for small-field radiotherapy, they are typically no more than a few millimeters. In specific cases, these margins are often defined anatomically rather than by expansion. As examples, prostate CTV volumes typically include the entire organ, spine radiosurgery

CTV volumes typically encompass an anatomical segment of the vertebral body.

Whereas distinct definitions for GTV and CTV are routine outside of the cranial vault, it has been less common in cranial radiosurgery. Although many intracranial targets are well-defined on contrast MRI disease may still extend beyond what is seen on imaging. In fact, autopsy review suggests that it is not uncommon for apparently well-defined brain metastases to have microscopic infiltration 1 mm beyond the main tumor mass. As a clinical choice, it may be decided to have the CTV default to the GTV. Despite the fact that CTV expansions are often not used, the dose in the penumbra region may be enough to eradicate microscopic tumor infiltrates. Instead of assuming that the penumbra will cover an undefined CTV, it is recommended to formally assess the dose to the CTV. Two treatment plans, which deliver the same minimum dose to the GTV may deliver different doses to the CTV because of asymmetry in the penumbra. Knowledge of a low minimum dose to the CTV may then lead to plan modifications. It is possible that local control would be improved by specific targeting of a CTV. However, in small-field radiation therapy, adding even a small margin (e.g., from GTV to CTV) can increase the target volume substantially and is likely to increase the risk of complications. For example, a CTV created by adding a uniform 1 mm margin to a 1 cm spherical tumor will contain almost as much normal tissue as GTV.

It is of great importance in the reporting of clinical results to specify what GTV to CTV margin, if any, was used. If several CTVs are used (CTV1_HIGH_DOSE, CTV2_PROPHYLACTIC, etc.), it is recommended that an unambiguous terminology corresponding to the GTV denomination be used.

3.4 Internal Target Volume

In ICRU Report 62 (ICRU, 1999) and Report 83 (ICRU, 2010), the ITV was defined as an optional volume as the CTV plus an “internal margin” taking into account uncertainties in size, shape, and position of the CTV within the patient. It was implied that internal and setup (or “external”) margins should be added quadratically but in practice they are often added linearly.

The usefulness and application of the ITV will be dependent on the host organ and the treatment technique. The ITV concept was predicated on the notion that radiation treatments were setup to external or bony landmarks in relation to which internal motion occurred whereas many current treatments are guided by direct target imaging. As

an example, hypofractionated high-dose prostate treatments are always delivered with daily image-guidance. The treatments are setup to the prostate itself and not to pelvic bones or skin tattoos. It is therefore not necessary to add a margin for inter-fraction displacement due to variation in rectal and bladder filling. Whether or not a margin has to be considered for the tilting of the prostate caused by rectal gas would depend in part on whether or not rotational setup errors are corrected at the time of treatment. Whether or not intra-treatment prostate motion is important will depend on the immobilization used (e.g., the use of a rectal balloon), the duration of treatment and the intra-treatment monitoring used. In clinical practice, it is often reasonable to account for small potential errors due to organ deformation and internal motion within a single PTV margin (see Section 3.5).

In small primary lung tumors located in the lower lung, internal margin due to respiratory motion can overshadow the required setup margin due, for example, to uncertainties in coincidence between imaging and radiation isocenters (Section 3.5). When the patient breathes freely during treatment, tumor motion needs to be quantified for treatment planning. Various valid means can be used to determine an ITV for tumors associated with respiratory motion. Examples include contouring on co-registered prospectively binned inspiratory and expiratory three-dimensional CT (3D CT) scans or contouring on a maximum-intensity projection CT scan (from a retrospectively binned 4D-CT dataset). If the intent is to treat with breath hold or respiratory gating, then the internal margin will need to account for uncertainties in reproducibility of breath hold and residual motion. If the intent is to treat with direct tumor chasing or tumor tracking then the internal margin may need to account for variations in the correlation of internal and external fiducials or movement of the tumor in relation to implanted fiducials. Deformation and rotation of the tumor during the breathing cycle are part of the internal margin although these components may be quite minor.

Internal and setup (or “external”) margins are tools to ensure coverage of the CTV. It may be that for specific techniques, a single expansion of the CTV to a PTV (see Section 3.5) will be replaced by a set of PTV specific to phases of the breathing cycle—the MLCs could then adapt to these multiple PTVs as the patient breathes. New planning methodologies in the literature may also put into question the traditional view of the PTV (see Section 3.5) as a volume by directly including evaluation of the effect of geometrical uncertainties in the objectives and constraints (Baum *et al.*, 2006).

3.5 Planning Target Volume

The concept of PTV was introduced in ICRU Report 50 (ICRU, 1993) and restated in ICRU Reports 62, 71, 78, and 83 (ICRU, 1985; 1999; 2004; 2007; 2010).

The PTV concept is a tool to ensure with a clinically acceptable probability that the prescribed dose will be delivered to all parts of the CTV despite geometrical uncertainties such as organ motion and setup variations. It is also used for dose prescription and reporting. It surrounds the CTV typically with a margin, which takes into account both the internal and the setup (external) uncertainties.

The setup margin accounts specifically for uncertainties in patient positioning and alignment of the therapeutic beams during the treatment planning and through all treatment sessions. For SRT, this may be due to uncertainties in, for example, external fiducial alignment versus patient skull or, IGRT-related uncertainties, such as, for example, the physician/therapist not consistently identifying the prostate on the CBCT. Although small-field treatments tend to be delivered over fewer sessions and are thus less forgiving to random error, the immobilization and image-guidance protocols tend to be more stringent and thus still permit tight PTV margins.

The PTV is a geometric concept that does not respect anatomy and may encroach on neighboring OAR. Such areas of potential overlap pose a dilemma to the physician who must often make a clinical decision between reducing the probability of delivering the planned dose to the CTV or accepting a higher risk of normal tissue complications. In many cases, the choice will be to incompletely irradiate the PTV. To achieve a compromise treatment plan, one or more sub-volumes of the PTV may need to be created. No matter what PTV sub-volumes are created during the planning process, the dose should be reported to the entire, uncompromised PTV. Doing so ensures that reporting adequately reflects the lower probability of adequate dose coverage to the CTV.

In cranial radiosurgery, especially when dedicated devices are used, the total geometric uncertainties are usually quite small. In end-to-end testing, these can be less than 1 mm. In these cases, it is not uncommon for patients to be treated without any expansion from CTV to PTV (for that matter, any expansion from GTV to PTV). As with CTV, there may be rational reasons for which a 0.5 mm to 1 mm uncertainty is ignored in the planning process. However, even if the dose will be prescribed directly to the GTV, it is recommended to evaluate and report the dose to a PTV. It is then possible to

compare and evaluate clinical studies. As the penumbra region can be asymmetric, plans providing similar GTV/CTV coverage may variably irradiate the PTV. Knowledge of the minimum dose to the PTV can lead to plan modifications. As an illustration of this, we can consider the ratio of the prescription isodose volume to the target volume [PITV (Shaw *et al.*, 1993)] that is commonly used as an index to evaluate plan quality. Somewhat arbitrarily, a plan, which irradiates more normal tissue than PTV to the prescription dose, can be considered of poor quality.

Factors contributing to the setup uncertainty include methods of patient positioning/immobilization, mechanical uncertainty of the equipment (e.g., sagging of gantry, collimators, and couch), mechanical and software uncertainties in image-guidance (e.g., concordance of imaging and treatment isocenters, image co-registration algorithm uncertainties), dosimetric uncertainties (e.g., output factors, dose calculation algorithm uncertainties), planning image co-registration errors, CT localization errors, and human factors. The importance of these factors will vary from center to center and within a given center from machine to machine, protocol to protocol, and patient to patient.

As the mechanics and quality assurance of radiotherapy treatments improve, target contouring accounts for a larger proportion of the “setup” uncertainty. The impact can be great if significant normal tissue is misidentified as tumor or significant tumor is misidentified as normal tissue. Adding margins to account for all possible variations in target contouring is not a solution to this problem but peer-review and multi-disciplinary treatment planning may reduce mis-targeting. Intra- and inter-observer variations can be limited by well-defined imaging protocols for target definition and training (e.g., atlas, teaching courses). The more protocols that provide detail about the imaging technique, contrast agent (if any), display settings, contouring tools and contouring technique used, the more reproducible the contours should be.

External or setup margins are often derived, at least initially, from the published experience of others but this should not replace local quality assurance protocols including thorough end-to-end testing (see Section 7) and issues such as multi-modality localization and/or pre and post treatment imaging.

The PTV margin concept was not designed to specifically address the issue of interplay between organ motion and the small beamlets of intensity-modulated radiation. It was also not designed to account for the possible effects of tracking a tumor

with a field smaller than the CTV. When moving tumors are treated with sub-fields or beamlets smaller than the target volume, the possibility will arise that certain parts of the target or adjacent normal tissue will be under or overdosed (ICRU, 2010). These issues tend not to be solved by increasing the target volume and must be evaluated on a technique-specific basis. Upcoming developments in treatment planning software, such as multiple instance geometry approximation and robust optimization, may provide solutions (Chu *et al.*, 2005; Unkelbach and Oelfke, 2004).

3.6 Organ At Risk

The OAR are organs, when irradiated, that could result in significant morbidity, and thus influencing treatment planning.

Although any nontarget tissue could be considered an organ at risk, the tissues explicitly outlined as such will depend on the location of the PTV, the treatment technique and the prescribed dose. As an example, the brachial plexus may be meticulously outlined in planning a stereotactic treatment of a tumor of the pulmonary apex whereas it may not be specifically contoured in treating a lower lobe lesion. Another example, in treating a meningioma of the cranial vault with coplanar technique, the orbits may not need to be contoured but will be defined when noncoplanar nonisocentric radiosurgery is used. Third example, the main stem bronchus may not be contoured when delivering 50 Gy in 20 fractions but will be when planning 50 Gy in 5 fractions.

3.6.1 Types of OAR

From a modeling point of view, tissue organization has been divided into serial-like, parallel-like, or a combination of serial-like and parallel-like (ICRU, 1993; Withers *et al.*, 1988). Serial-like organs (e.g., spinal cord, brachial plexus, the esophagus) consist schematically of a chain of functional units, all of which need to be preserved to guarantee the functional integrity of the tissue. For instance, destruction of a short segment of spinal cord may result in loss of function distal to the point of injury. Parallel-like organs (e.g., liver, parotid) consist schematically of functional units acting independently of each other. Conceptualizing organs as serial-parallel or combined serial-like and parallel-like has not proven to be very useful. Rather, the serial-like and parallel-like components of organs have been teased apart to create new OARs—for instance, if one wants to consider the myocardium and the coronary arteries parallel and

serial subunits of the same heart, they can be contoured separately and accounted for individually in the treatment plan. The lung, long considered a prototypical parallel-like organ, is commonly divided into bronchi and parenchyma. This is required because very high doses of stereotactic radiation are toxic to the proximal bronchial tree with potential impact on a large volume of nonirradiated lung distal to the treatment site (Chang *et al.*, 2008).

As a general rule, high dose (to point, or preferably a small volume) will be more of a concern in serial-like organs whereas volume irradiated to a threshold dose, V_D , will be more of a concern in parallel-like organs. This is not to say that large volumes irradiated to low dose do not affect serial-like organs or that small regions irradiated to high doses do not affect parallel organs. The so-called bath and shower effect is seen in experimental models of rodent and swine spinal cord where irradiation of a longer segment to a low dose reduces the tolerance of a very short segment to a high dose (Medin *et al.*, 2013). In the lung and liver, smaller areas of high dose may (or may not) be significant as they contribute to the mean dose.

For serial-like organs, details of how contouring was performed is important since small variations in the contouring have a large effect on dose metrics. For parallel-like organs small variations in contouring have a lesser impact on dose–volume metrics (see Section 7.3.2). The protocol or method used should be specified. For example, the term “spinal cord” should not be used for the spinal canal, the spinal cord being more easily defined by CT myelography or MRI co-registration. Reporting of dose to a specified small absolute volume makes the issue of length of cord contoured unimportant.

The reporting of dose to parallel-like organs has traditionally been as dose to a percentage volume or mean dose. This holds true in small-field radiotherapy for lung and kidney irradiation (the dose levels considered tolerable will need to be specific to the number of fractions used). In the liver, the absolute volume above the threshold dose (or rather below it) is commonly used (this may gradually become more common for the lung and kidney). When the tumor is within the OAR, it has been commonplace to subtract the target volume from that organ in dose reporting. It is sensible to conclude that a tumor does not contribute to lung or liver function. On the other hand, subtracting the volume in the CTV and especially PTV margin would seem to make little biological sense. The means of OAR contouring (*i.e.*, the atlas or protocol used) should be reported and a note should highlight organs, which lie partially outside the

planning CT and/or calculation grid, (situations which should generally be avoided).

Dose–volume constraints for many OARs are mainly derived from retrospective clinical observations of treatment with “conventional fractionation”. As small-field radiotherapy is typically applied in larger individual fractions, knowledge from cohorts treated at 1.8 Gy to 2 Gy per day are not directly applicable and tolerances have to be re-learned from new clinical experience. For many less-studied organs (*e.g.*, vessels, peripheral nerves) tolerances will first be cautious extrapolations from standard fractionation and hypofractionated palliative treatments. For other more critical (*e.g.*, spinal cord) or better-studied (*e.g.*, lung) organs, clinical experience is already available from the nascent SRT literature. It is recommended that an internal policy be established in any department implementing SRT to record and evaluate observed toxicity within the treatment schedule. Implementing or joining prospective multicenter studies is also strongly recommended.

3.6.2 Implied OAR of Cranial Radiosurgery

In the case of intra-parenchymal brain lesions, it is common not to define explicit OARs, the implied OAR being the surrounding brain parenchyma. Specific regions could be outlined based on their function but in day-to-day practice, this may require advanced (functional) imaging. Although this has not yet proven itself of benefit in reducing toxicity, it may be advisable to delineate critical structures (*e.g.*, thalamus, optic chiasm, optic nerves, *etc.*). The conformity and gradient of the plan are calculated and reported (see Section 7) as a means of evaluating and reporting the dose to these implicit OARs.

3.7 Planning Organ At Risk Volume

As is the case with the Clinical Target Volume, uncertainties and variations in the position of the OAR during treatment must be considered to avoid serious complications. For this reason, the concept of adding a margin to an OAR, the PRV, was introduced in ICRU Report 62 (ICRU, 1999).

These PRV margins are of little use when evaluating a parallel organ where the percent or absolute volume irradiated (or spared) is of concern compared to serial structures in which a margin around an Organ at Risk is clinically relevant. As the PRV is a geometric concept that does not respect anatomical boundaries, PRV and PTV margins may overlap. The PRV margins should not be modified where they encroach on the PTV and, although

creating sub-regions may be helpful in the planning process, final dose reports should include the entire PRV. For reporting, as for the PTV, the means by which the OAR volumes were expanded to create the PRV volumes should be described.

Analogous to target volumes, uncertainties in OAR avoidance can be divided into systematic and random error, internal and external margins. Approaches to calculating these errors have been described and margins will be technique and protocol specific (McKenzie *et al.*, 2002). It must be noted, as for PTV margins, that literature from conventional radiotherapy may not be directly applicable in the context of the number of fractions and steep penumbra of small-field radiotherapy.

In clinical practice, PRV margins have been mainly used for structures of the nervous system (e.g., brainstem, spinal cord, optic chiasm, optic nerves). For serial organs with more substantive internal motion or deformation, approaches can vary. In the small bowel, a more liberal approach of contouring the peritoneal space may be reasonable rather than contouring individual bowel loops, adding a margin and then trimming it to the peritoneal cavity. It is important that the means of defining the OAR and/or PRV be documented adequately.

3.8 Remaining Volume at Risk

Ideally, when delineating the OAR, all normal tissues that could potentially be irradiated should be outlined. The imaged volume within the patient, excluding any delineated OAR and the CTVs, can be identified as the RVR. The RVR is operationally defined by the difference between the volume enclosed by the external contour of the patient and that of the CTVs and OARs on the slices that have been imaged. The RVR is of importance in evaluating plans as there can be unsuspected regions of high absorbed dose within the patient that would otherwise not be reported. In addition, the absorbed dose in the RVR might be useful in estimating the risk of certain late effects, such as cancer induction. Therefore, contouring the RVR is especially important for younger patients who can expect a long life span. In small-field radiation therapy, because of the high-dose gradients and the small target volumes, the amount of irradiated nontarget tissue is usually smaller than with IMRT and the concept of RVR may be of less clinical relevance. Looking for high-dose regions using a DVH of the RVR is, however, no substitute for a thorough analysis, on a slice-by-slice basis, to examine the absorbed-dose distribution for all beam paths (ICRU, 2010).

3.9 Imaging for GTV Definition

This Section discusses imaging modalities and techniques for the definition of the GTV in the context of small-field radiation therapy. It covers the sites liver, head & neck, malignant and non-malignant brain lesions, lung, pancreas, bone, and prostate.

3.9.1 Liver

Stereotactic body radiotherapy treatment of liver lesions is a viable treatment option for a growing proportion of patients with primary or metastatic liver tumors. The definition of GTV within the liver remains a challenge. A particular issue is the combination of liver motion with the importance of intravenous contrast timing. A hepatocellular carcinoma will typically enhance during a narrow arterial phase whilst a metastatic lesion will become more apparent in a later venous phase (Baron, 1994). Although (Beddar *et al.*, 2008) protocols have been described for 4D contrast imaging, two planning studies will often be acquired: a 4D study to evaluate liver motion and deformation and a 3D contrast study to define the GTV. An additional co-registration between CT and MRI will often be of use although care will be required to account for possible liver deformation.

3.9.2 Head and Neck

Stereotactic body radiotherapy is mostly used in head and neck cancer as retreatment or as a boost technique. Soft tissue lesions of the head and neck can be difficult to identify on contrast CT scans and thus co-registration of a contrast MRI (in treatment position, if feasible) will commonly be used. Even if there is evidence that PET/CT can improve contouring in conventional RT, few studies have looked at this issue in SBRT. In reported phase *VII* studies, PET use has typically been confined to staging.

3.9.3 Brain Tumors

Because of better parenchymal contrast, MRI will be the preferred imaging modality to define GTV of brain tumors. For enhancing lesions, a T1-weighted sequence will typically be the basis for contouring. A rapid sequence will allow timely acquisition of a large volume for identification of multiple targets, image registration or visualization of external fiducials when MRI is used as the primary imaging modality with an invasive frame. Nonenhancing tumors will more commonly be imaged with a T2 or FLAIR sequence. Specific situations will benefit from other sequences; this is the case for trigeminal neuralgia or cerebello-pontine tumors where clinicians will appreciate the cisternographic effect of

certain high-resolution T2 sequences (CISS, DRIVE, FIESTA).

Because of the high degree of geometric accuracy required in SRS or SRT, the issue of geometric accuracy of MR images is of concern. Distortions in MR images are caused by system-related effects, including main field inhomogeneities, gradient magnetic field nonlinearity, as well as patient-related effects including chemical shift and susceptibility artifacts. Despite the fact that the use of 1.5 T MRI has long been standard, recent studies have addressed the development of an accurate imaging protocol at 3 T and patient-induced susceptibility effects of geometric distortion on a 3 T scanner (Wang *et al.*, 2013; Zhang *et al.*, 2010). These latter studies concentrate on MR-based anatomic imaging applications in treatment planning. Continued clinical research and improved resolution may, in the future, lead to a greater adoption of functional imaging (*e.g.*, spectroscopy, perfusion)—for now these modalities are those of the researcher or diagnostician.

3.9.4 Vascular Lesions of the Brain

Target definition in arterio-venous malformation radiosurgery aims to define the abnormal vessels of the nidus as completely as possible while differentiating them from parenchymal enhancement, embolization material, feeding arteries, and draining veins. Stereoscopic 2D digital subtraction angiograms (DSA) have been the standard imaging modality for this purpose. The subtraction process can remove artifacts from surgical clips or embolization material and the high-resolution movies show sequential filling of the feeding arteries, nidus, and veins. In addition, selective catheterization can reduce the amount of normal vasculature seen on the angiography loops. In a typical SRS planning system, 2D physician contours from anterior–posterior and lateral DSA projections are transposed into the stereotactic space through the use of sets of radio-opaque fiducials on the proximal and distal walls of a target localizer “box”. When necessary, DSA image distortion can be corrected by software recognition of a distortion correction grid before localization. Each 2D contour can be converted to a conical volume on a 3D CT or MRI dataset. The intersection of the projected anterior–posterior volume with the lateral volume, define the DSA target.

The principal limitation of such a use of DSA imaging is that it provides limited definition of complex 3D shapes (concavities, for example, cannot be defined). It has thus become standard to modify the DSA volumes using a co-registered 3D CT angiogram and/or MRI angiogram. Computed tomography and MRI equipment and sequences are constantly evolving

but these 3D images typically lack the detailed hemodynamic information provided by these DSA movie loops. For selected small and/or well-defined AVMs, specialized 3D imaging (*i.e.*, high-resolution time of flight MRI and CT angiogram) may replace DSA. It has, however, yet to be shown that DSA can be eliminated for all patients. This presents a challenge for frameless radiosurgery systems, which has yet to be optimally resolved (Hristov *et al.*, 2011). One palliative measure has been to convert the “spin” rotational DSAs of modern angiography suites to a cone-beam CT image, which can be co-registered to other imaging studies using standard 3D registration algorithms.

3.9.5 Lung

Computed tomography is the standard imaging study for planning radiation therapy of lung tumors. It offers high contrast with lung parenchyma and good spatial and temporal resolution. Intravenous contrast will not be necessary for simple peripheral lesions but may help highlight normal vasculature for central tumors. Artifacts impacting the imaged tumor volume can be seen in conventional 3D CT scans for planning of lung cancer radiotherapy but can be reduced with the use of respiration-correlated imaging [*i.e.*, 4D-CT or breath-hold computed tomography (BHCT) scans (Persson *et al.*, 2011)]. Four-dimensional CT and multiphase 3D CT have the advantage to provide patient-specific tumor motion information, based on which appropriate margins can be designed to ensure daily target coverage (Wang *et al.*, 2009).

Positron-emission tomography combined with CT imaging has become a routinely performed imaging modality for the assessment of lung cancer patients (Silvestri *et al.*, 2007). Its main use will be in case selection and, in particular, the exclusion of patients with extra-pulmonary disease. Positron-emission tomography combined with CT imaging may, however, aid contouring in cases of atelectasis as long as one is aware of the uncertainties related to PET/CT thresholding and the issues related to the long acquisition times of what should ideally be scanned using 4D PET/CT.

3.9.6 Pancreas

Multislice CT is the established modality for diagnosis and staging of pancreatic cancer (Soriano *et al.*, 2004). A combination of pancreatic parenchymal phase (PPP) imaging and portal venous phase (PVP) imaging is sufficient for detection of pancreatic adenocarcinoma, because it provides maximal pancreatic parenchymal and peripancreatic vascular enhancement. The late or PVP imaging, performed with a scanning delay of 60–70 s, obtains a maximal

mesenteric and portal venous as well as hepatic parenchymal enhancement. A PPP imaging, with a scanning delay of 40 s to 70 s, results in superior pancreatic parenchymal enhancement compared with that achieved during the PVP (McNulty *et al.*, 2001). Positron-emission tomography combined with CT imaging can be of use for contouring selected cases provided that recurrent issues of thresholding and long acquisition times can be taken into account.

3.9.7 Bone

Current target volumes for spinal SBRT extend the GTV to create an anatomically based CTV. The bony anatomy can be imaged at high resolution with CT but MRI will allow better definition of the spinal cord, the tumor within the bone as well as possibly extra-osseous extension. In those patients where MRI is not possible, CT myelography allows precise definition of the spinal cord at the expense of an intrathecal contrast injection.

3.9.8 Prostate

Computed tomography has been used as standard for planning purposes in the treatment of prostate

cancer. During the last decade, however, MRI has become more commonly used in the planning of primary radiotherapy for prostate cancer. Compared with planning CT, it provides greater resolution of soft tissues and thereby allows more precise delineation of CTV and OAR (Khoo *et al.*, 1999; Roach *et al.*, 1996). Clear evidence has shown that in primary radiotherapy planning of the prostate, the CTV defined using MRI will be smaller than the CTV defined using planning CT (Rasch *et al.*, 1999; Roach *et al.*, 1996), leading to more effective sparing of the OAR, especially the rectum. The delineation variability has also been smaller using MRI, particularly in the area of the prostate apex and anterior rectal wall (Debois *et al.*, 1999; Roach *et al.*, 1996; Smith *et al.*, 2007). Co-registration between CT and MRI should thus be strongly advocated in prostate SRT.

Dynamic contrast enhanced T1-weighted magnetic resonance (MR) images (DCE-MRI) and ¹H MRS are helpful for a precise biopsy of the prostate. Until now it is unclear whether the parametric maps of DCE-MRI and MRS can be used for radiation treatment planning of the prostate (Schmoecking *et al.*, 2009).

4. Treatment Planning Algorithms

4.1 Introduction

An important limitation on the accuracy of the dose delivered to the patient in radiation therapy is determined by the accuracy of the treatment planning dose calculation algorithm. Existing recommendations for the commissioning and verification of treatment planning system (TPS) dose calculations are given by AAPM TG 53 (Fraass *et al.*, 1998), IAEA TRS 430 (IAEA, 2004), NCS Report 15 (Reynaert *et al.*, 2006). The American Association of Physicists in Medicine Task Group Report 67 described benchmark tests for the validation of dose calculation algorithms. These reports, however, are general and not sufficiently specific for small fields. This Section reviews some general features and addresses a few pertinent issues specific to dose calculation algorithms for small fields. An overview of historical and general aspects of treatment planning algorithms can be found in ICRU Report 83. This Section will concentrate on the details that should be considered when implementing these algorithms for small field stereotactic radiation therapy/stereotactic body radiotherapy (SRT/SBRT).

4.2 Classification of Algorithms

Dose calculation algorithms used for treatment planning are generally classified as factor-based algorithms or model-based algorithms.

4.2.1 Factor-Based Algorithms

In factor-based algorithms,⁶ the starting point is the measurement of the absorbed dose in a water phantom from a rectangular beam incident normally on the surface of the phantom. These data are parameterized into absorbed-dose distributions

⁶Factor-based algorithms are also known as “correction-based” algorithms. The nomenclature “factor-based” is preferred since the structure of the algorithm is a series of factors that move from the point in a geometry of interest to the reference point and geometry used for beam calibration (based on a reference dosimetry protocol). Some of the factors can be interpreted as corrections (*e.g.*, inhomogeneity corrections), but several, if not most, are just dose ratios between two different irradiation geometries in a chain of geometries making up for the factors.

as functions of the source–isocenter distance, field size, depth, and lateral position. Factors are then applied *a posteriori* to account for the difference between the phantom setup in the measurement and the patient-specific conditions, such as blocks, compensators as well as for the fact that the patient surface is not flat and tissues in the patient are not water. Although approximate, most of these factor-based algorithms consider the variation in absorbed dose caused by the difference in attenuation as a result of passage of the beam through heterogeneous tissues upstream of the absorbed-dose calculation point. In the context of small field RT applications for SRS/SRT of the brain where a limited range of auxiliary collimators is used to define the beams, TPSs have traditionally used factor-based algorithms. In those cases, the patient treatment irradiation conditions were deemed not significantly different from the measurement conditions used for commissioning or these were situations where heterogeneity corrections were deemed unimportant. The use of, for example, dynamic arc techniques in cranial SRS was considered to blur the importance of accurate modeling of the source size, the collimating device and lateral electron transport and decrease the influence of any tissue heterogeneities on the final dose distribution. Pike *et al.* (1987) presented a TMR-based calculation method to calculate 3D dose distributions from measured percentage depth dose curves for dynamic radiosurgery. The dose D_Q , at the point-of-interest Q for a given number of MU, is calculated using the following relationship:

$$D_Q(d, \Phi_Q) = \text{MU} \left(\frac{D_{\text{ref}}(d_i, \Phi_i)}{\text{MU}} \right) \cdot PDD \left(d, \Phi_i \frac{f_i - d_i + d}{f_i + d} \right) \cdot \left(\frac{f_i + d}{f_i + d_{\text{max}}} \right)^2 \left(\frac{f_i}{f_i - d_i + d} \right)^2 OAR(d, r_Q),$$

where $\frac{D_{\text{ref}}(d_i, \Phi_i)}{\text{MU}}$ is the reference dose at depth of maximum dose at the isocenter per MU (typically tuned to 1 Gy/100 MU), d is the depth of point Q , d_{max} the depth of maximum dose, d_i the isocenter depth, f_i the source–axis distance (SAD 100 cm), Φ_Q

the field diameter at point Q , Φ_i the field diameter at isocenter as defined by the collimator used, PDD the percentage depth dose value at depth d for SSD equal to f_i , and field size equal to $\left(\frac{f_i - d_i + d}{f_i + d}\right)\Phi_i$ and $OAR(d, r_Q)$ the off-axis ratio for point Q at depth d at a distance r_Q from the central axis. The dose contributions of beams at 10° gantry steps and 5° couch angle steps of the dynamic delivery were calculated and summed. Figure 4.1 shows an example of the dose fall-off obtained around the target volume for dynamic stereotactic radiosurgery delivery, as compared to a single-arc delivery (Pike *et al.*, 1987).

Factor-based models are inappropriate for use with very small fields when the irradiated medium deviates significantly from the homogeneous water medium in which the input basic dosimetric data were measured. Corrections that account for the lack of lateral charged particle equilibrium require non-trivial calculations for heterogeneous media. Simple factor methods can only be used in irradiation geometries and dose deposition conditions similar to those in which the input data to the models were measured. For example, these methods would be inappropriate for use in SBRT for lung cancer because it would create a false impression of dose homogeneity near the target volume due to tissue heterogeneities.

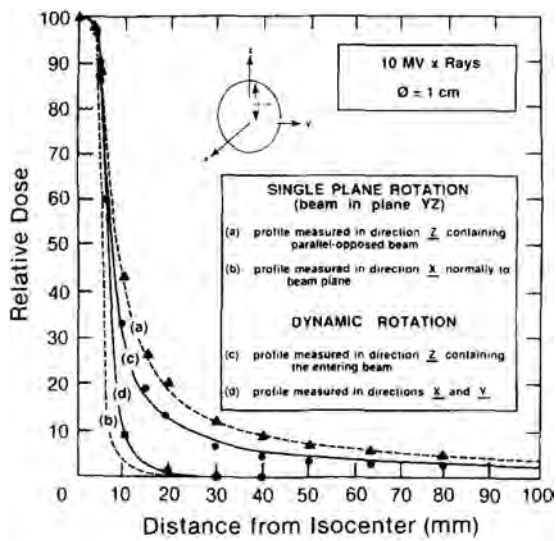


Figure 4.1. Application of TMR-based dose calculation for a 10 MV, 1 cm diameter field at isocenter, accelerator-based dynamic stereotactic radiosurgery technique in comparison with a single plane arc (Pike *et al.*, 1987). Dose profiles are shown in several directions through the center of a humanoid head phantom. Single plane rotation: curve (a) and (b), for the dynamic rotation: curves (c) and (d). Calculated profiles are shown as solid and dashed curves, measured profiles as data points. These dose calculations show more spatial homogeneity in the fall-off using the dynamic technique.

4.2.2 Model-Based Algorithms

Algorithms and TPSs for 3-dimensional (3D) treatment planning of conformal and fluence- ("intensity-") modulated radiation therapy (IMRT) were first used in the early 1990s. Limitations in the traditional approach to effectively account for absorbed-dose variations due to varying field geometries and tissue heterogeneities stimulated the introduction of newer model-based algorithms. These algorithms were based on convolution or superposition methods (Ahnesjö *et al.*, 1987; Aspradakis *et al.*, 2003; Boyer and Mok, 1985; Mackie *et al.*, 1985; Papanikolaou *et al.*, 1993) in which the transport kernels are generated by Monte Carlo simulation (Ahnesjö, 1989; Ahnesjö and Aspradakis, 1999; Mackie *et al.*, 1988) or direct Monte Carlo simulation of the particle transport (Deng *et al.*, 2004; Fippel *et al.*, 2003; Jeraj and Keall, 1999; Ma *et al.*, 1999). Rather than correcting absorbed-dose distributions measured for normally incident beams in a water phantom for the effects of patient-specific conditions such as beam modifiers, surface contour, or tissue heterogeneities, the model-based methods directly compute the absorbed dose per energy fluence in the patient (ICRU, 2010).

Model-based algorithms typically consist of two parts: (1) a part of the algorithm that models the beam, and provides a representation of the fluence distribution before the beam enters the patient and (2) a part that models the patient, usually based on a tomographic representation of the patient tissues. Part (2) calculates the dose at any point in the patient per incident fluence. The introduction of the reference dose calibration (measured absorbed dose at the reference point in water per MU) allows a system dose calibration linking fluence to MU necessary for the algorithm to provide MUs out directly out as a dose prescription for a plan.

Model-based algorithms have been further described as being of either two types or categories (Knoos *et al.*, 2006), type-a (or category 1) and type-b (category 2). Model-based algorithms of type-a are primarily based on equivalent path length scaling for inhomogeneity corrections. Changes in lateral transport of electrons are not modeled. Examples of algorithms in this class are Varian Eclipse with the Modified Batho correction (Batho, 1964), Varian Eclipse with Equivalent TAR correction, Oncentra MasterPlan with Pencil Beam convolution, PPLAN and XiO/Convolution. Model-based algorithms of type-b are those that, in a more or less approximate way consider changes in lateral electron transport. For the more approximate algorithms, electron modeling is not explicitly performed. The energy from both primary electrons and scattered photons,

which are scaled rectilinearly with electron density according to the theorem by O'Connor (O'Connor, 1957), is included in an approximate manner. Examples of the models in this group are Pinnacle/CC, Oncentra MasterPlan/CC, XiO/Super, and TomoTherapy. The more advanced type-b algorithms perform explicit lateral electron transport and include the Monte Carlo algorithms and the deterministic solvers (e.g., Varian Acuras). Some algorithms should be considered as an “intermediate” between type-a and type-b, where the core of the algorithm is pencil beam convolution with some elements borrowed from type-b algorithms (e.g., Varian Eclipse/AAA).

4.3 Beam Model, Source Parameters, and Collimation System

4.3.1 Beam Model

The beam model, in its most general form, provides a coupled angular—energy distribution of a representative set of particles in the beam (photons and contamination particles). In clinical model-based algorithms, the beam model is usually represented by energy fluence distributions normalized to the monitor signal (or unit). The monitor unit may consist of a contribution due to the direct beam and a contribution from back scattering. In small fields, the contribution from scattering from the flattening filter and of collimation devices is drastically reduced and the primary energy fluence is the main contributor to the energy fluence entering the patient plane. Whereas flattening filter scattering is mostly obscured in a small field it is not in a $10\text{ cm}^2 \times 10\text{ cm}^2$ calibration field and this reduced scattering must be taken into consideration in relative output calculation in small fields.

The primary energy fluence distribution is dictated by the shape and size of the direct beam source as viewed from the point-of-interest in the patient. Hence accurate knowledge and modeling of the collimation devices i.e., collimators and multi-leaf collimator (MLC) and leakage through these combined with an accurate knowledge of relative location, shape, and size of the source spot plays a key role in accurate beam model representation and ultimately accurate dose calculation.

4.3.2 Source Parameters and Collimation System

In the prediction of the dose in the patient, the parameters of the source spot as it emerges from the flattening filter (or, in the absence of the flattening filter, the target) play an essential role. The more important spot parameters are the spot size

and shape (or distribution). The source spot size can be determined experimentally from analysis of the penumbra of a dose profile, by performing measurements through a slit or by using a spot size camera (Jaffray *et al.*, 1993; Munro *et al.*, 1988). Literature suggests a wide variation in experimental results of spot sizes between accelerators but also for different energies of the same accelerator (Chen *et al.*, 2011; Sham *et al.*, 2008; Yeboah, 2011).

Figure 4.2 shows measured spot sizes for the Varian TrueBeam for different beams (Sawkey *et al.*, 2012). Typical values for spot sizes can range between less than 2.5 mm and 4.6 mm and the typical spot size is also not perfectly circular if the electron beam is bent by a bending magnet. Part of this variation may be attributed to different methods that are used in determining the spot size or simply the definition of spot size used in the individual investigation, but different spot sizes can be obtained by changes in linac settings such as the electron gun voltage. Manufacturers may choose a larger spot size in order to accommodate larger dose rates. A TPS may parameterize the source based on measurements in large fields but the accuracy in small fields will be compromised because of sensitivity of the end-points such as output factor on the source size. Hence, a treatment

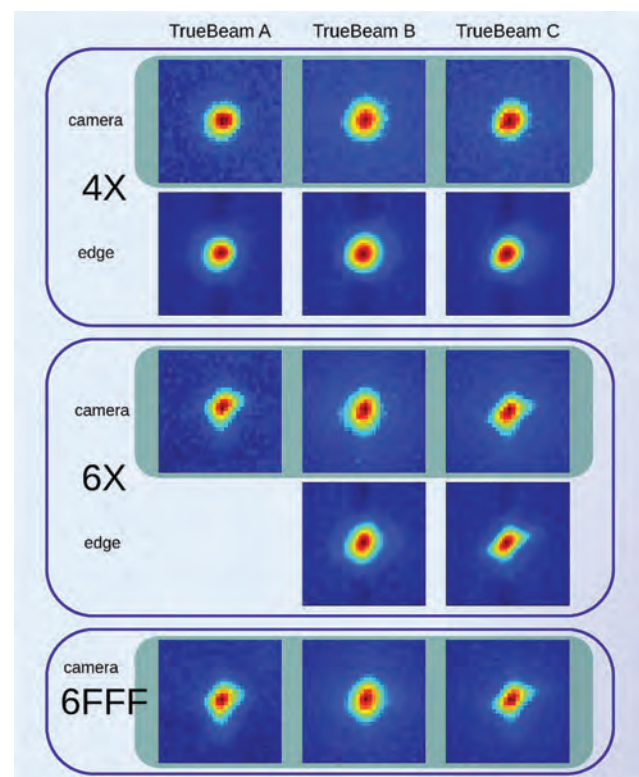


Figure 4.2. Example of measured spot sizes for the Varian TrueBeam for different beams. Data and figure from Sawkey *et al.* (2012). The dimension of one film square is 8 mm \times 8 mm.

planning algorithm commissioned primarily using large fields needs to undergo a separate additional verification in small fields by direct comparison of suitably measured output factors to values produced by the algorithm. In addition, lateral dose profiles and depth dose, which are affected by the details of the spot distribution (*e.g.*, actual shape, eccentricity, and intensity distribution) in fields with size inferior to $2\text{ cm}^2 \times 2\text{ cm}^2$.

The location of the collimation system (*i.e.*, MLC and possible backup collimation) with respect to the source spot intensity distribution affects the small field fluence profiles as the latter are strongly affected by source occlusion and leakage. This means that the representation of the collimation devices in the treatment planning algorithm needs to be accurately validated. This becomes even more pertinent if multiple collimation systems are used (*e.g.*, MLC collimation backed up by jaw collimation) and alignment of these with respect to each other strongly affects the resulting source occlusion and hence output factor and dose distribution. For this reason, in an SRT delivery use of single collimation (*i.e.*, backup collimation retracted to, *e.g.*, 1 cm from field edges) can reduce the effect of collimator alignment on small field dose delivery and improve the consistency between algorithm prediction and actual delivery conditions.

One of the effects of source occlusion in small fields is broadening of beam penumbra (Section 2). This effect increases when collimation is performed closer to the beam source. The broadening of the beam penumbra also gives rise to a difference in expected full-width at half maximum (FWHM) of the beam profile based on geometric collimator setting and the actual FWHM. For example, the error in dose for a 2 mm error in leaf position for leaf gaps of 2 cm or less easily exceeds 10 % (LoSasso *et al.*, 1998). It is thus imperative that collimator settings and integrity for small field shaping are independently verified.

As an overall test on beam model integrity, beam model fluence distributions for well-defined collimation conditions should be verified (*e.g.*, tongue and groove effects, interleaf leakage, and abutting leaf leakage).

4.4 Dose Calculation Algorithms

A dose calculation algorithm will calculate the absorbed dose distribution in a tomographic representation of the patient based on a model. It is important to be cognizant of the various approximations in the dose calculation model to understand possible shortcomings of their behavior in small fields.

A dose calculation algorithm will essentially present an approximation to the solution of the linear Boltzmann transport equation (LBTE), the governing equation that describes the macroscopic behavior of ionizing radiations (neutrons, gamma-rays, electrons, *etc.*) as they travel through and interact with matter.⁷ The most commonly used current algorithms are convolution-superposition as well as advanced algorithms such as Monte Carlo (Chetty *et al.*, 2007) and deterministic methods (Failla *et al.*, 2011; Vassiliev *et al.*, 2010). The latter two types of algorithms are considered the most accurate dose calculation methods available.

The convolution superposition method convolves the TERMA distribution with a dose kernel obtained through Monte Carlo methods (Ahnesjö, 1989; Ahnesjö *et al.*, 1987; Aspradakis *et al.*, 2003; Boyer and Mok, 1985; Mackie *et al.*, 1985, 1988; Papanikolaou *et al.*, 1993). The dose kernel incorporates the energy deposited by all secondary particles including electrons per energy released by the primary photons. This means that a reconstituted dose distribution is exact when calculated in the same large volume medium in which the kernel was generated (*i.e.*, water). In some implementations, to better describe effects from spectral changes, TERMA is split into K_{coll} and SCERMA components the latter being the energy that is diverted to scatter dose. Two different kernels, a primary dose kernel and a scatter dose kernel, are then being used onto these components, respectively, in the superposition operation (Ahnesjö and Aspradakis, 1999; Ahnesjö *et al.*, 2005).

The convolution-superposition based algorithms contain approximations to deal with tissue heterogeneities and these approximations perform to a variable level of accuracy depending on the implementation. The accuracy of the model has been reported in numerous publications to be acceptable when applied to situations with tissues with density close to water, provided, of course that the beam model is accurate (Papanikolaou *et al.*, 2004).

The Monte Carlo method is a statistical method for performing numerical integrations of, in this case, the LBTE. The method consists of using knowledge of the probability distributions governing the individual interactions of electrons and photons in materials to simulate the random trajectories of individual particles (*i.e.*, photons and electrons). One keeps track of physical quantities of interest for a large number of histories to provide

⁷Strictly, a solution to the Boltzmann equation provides fluence, not absorbed dose. Absorbed dose can be derived from fluence; most dose calculation algorithms, however, do not determine the fluence distributions in the patient explicitly.

the required information about the average quantities, such as absorbed dose or fluence (Andre, 1991; Rogers and Bielajew, 1990). Applied to treatment planning, the Monte Carlo technique has been instrumental in the development of accurate beam models used in conjunction with other dose calculation algorithms as well as for the patient dose calculation, *e.g.*, dose kernels in the convolution-superposition method are Monte Carlo calculated (Mackie *et al.*, 1985; Mohan *et al.*, 1986). Significant progress in accurate beam modeling came with the introduction of MC simulation systems that had the capability to model the entire accelerator head geometry based on available geometry and material information (Rogers *et al.*, 1995; Sempau *et al.*, 2001). This includes the fixed elements of the head (*i.e.*, targets or scattering foils, primary collimators, monitor chambers, flattening filters and the various beam shaping devices which are patient specific such as jaws, MLC, applicators, cutouts, wedges, and compensators) (Verhaegen and Seuntjens, 2003; Ma and Jiang, 1999). The patient-specific simulation includes transport of the particles through patient-specific beam modifiers and the patient CT dataset to arrive at detailed patient dose distributions. Monte Carlo techniques are now clinically available for direct treatment planning thanks to variance reduction techniques (Kawrakow and Fippel, 2000; Sempau *et al.*, 2000), progress in computational capabilities (Jia *et al.*, 2011) and some approximations in the implementation (Chetty *et al.*, 2007; Reynaert *et al.*, 2007). More recent work discusses applications of Monte Carlo dose calculations to patient-specific quality assurance based on machine treatment logs (Luo *et al.*, 2006; Teke *et al.*, 2010; Wijesooriya *et al.*, 2012), dynamic radiation therapy dose calculations with applications involving gating and dose accumulation (Heath and Seuntjens, 2006; Jensen *et al.*, 2012; Lobo and Popescu, 2010), dose estimations from patient imaging in IGRT, *e.g.*, Alaei *et al.* (2010), large scale retrospective treatment plan analyses (Kry *et al.*, 2013) and more specialized topics such as brachytherapy Monte Carlo dose calculations (Afsharpour *et al.*, 2012) and modulated electron radiation therapy (Alexander *et al.*, 2011). Uncertainties quoted in clinical patient-specific Monte Carlo simulations are usually of type-A (number of particles simulated). However, it should be kept in mind that type-B uncertainties (cross sections, geometry specification) also play an important role. Specifically, the tissue composition specification based on CT information has been investigated and shown to introduce additional uncertainties especially in low-energy applications such as brachytherapy (Landry *et al.*, 2010, 2011). For more information on the Monte Carlo technique as applied to planning

dose calculations in general we refer to reviews, task group reports and textbooks (Chetty *et al.*, 2007; Reynaert *et al.*, 2007; Seco and Verhaegen, 2013). The performance of Monte Carlo algorithms in the context of SRT is discussed in more detail in Section 4.5.

Deterministic methods (sometimes referred to as discrete ordinate methods) are another technique to solve the LBTE. For a given volumetric domain of matter, subject to a radiation source, the solution to the LBTE gives an “exact” description of the dose within the domain. However, since closed form, or analytic, solutions to the LBTE can only be obtained for a few simplified problems, the LBTE is solved in a non-analytic manner. Methods, which deterministically solve the LBTE, can be broadly referred to as grid-based Boltzmann solvers (GBBS), which explicitly solve the LBTE through discretization in space, angle and energy, and then iteratively solving the LBTE (Lewis and Miller, 1984). The LBTE is solved on a grid of computational elements and typically use a similar multi-group treatment in energy and truncated serial expansions with spherical base functions of cross sections and fluence. A commercial implementation of a GBBS is the Varian Acuros XB system. Uncertainties in the GBBS are primarily of a systematic nature (*e.g.*, cross sections, approximations made during implementation, and resolution of discretization).

4.5 Small Field Implications of Dose Calculation Algorithms

The main issue in the context of small field dose calculations is the accurate modeling of lateral electron scattering in heterogeneous situations with density significantly different from water, such as in the case of lung SBRT. Numerous studies have investigated the performance of different types of clinical dose calculation algorithms on calculation accuracy involving small fields and heterogeneities, most importantly in lung. In general, type-a dose calculation algorithms overestimate the absorbed dose inside lung and tumor tissues under the conditions of lateral electron disequilibrium (LED) (Aarup *et al.*, 2009; Carrasco *et al.*, 2004; Engelsman *et al.*, 2001; Jones and Das, 2005; Knoos *et al.*, 2006; Mackie *et al.*, 1985). For example, Engelsman *et al.* (2001) compared the dose calculation accuracy of pencil beam, modified Batho, and equivalent path length (EPL) algorithms with film and ionization chamber measurements. Beam energies of 6 MV, 8 MV, 15 MV, and 18 MV were used to irradiate a 50 mm polystyrene target centrally positioned in a lung slab, simulated by cork. Their results show that the three algorithms predict up to 20 % higher dose levels in the lung and tumor compared with the

actual delivered dose values. As expected, the error in dose calculation increased with photon beam energy.

Tillikainen *et al.* (2008) showed that the AAA algorithm, earlier classified as an intermediate between type-a and type-b algorithms, produced errors up to 8 % in lung tissue for small field 18 MV x-ray irradiation of a phantom. Kroon *et al.* (2013) investigated the performance of the AAA dose calculation algorithm against the Acurus XB (AXB, the deterministic solver which can be considered an advanced type-b algorithm). Figure 4.3 shows a comparison of absorbed dose using AAA, AXB, and film measurements in a heterogeneous slab with low density in small fields ($1\text{ cm}^2 \times 1\text{ cm}^2$ and $4\text{ cm}^2 \times 4\text{ cm}^2$). It should be noted that although the density of the slab in the phantom is unrealistically low (0.03 g cm^{-3}) and emphasizes the trend of the differences, it shows the inherent limitations of algorithms that might be manifested in situations of clinical relevance (e.g., dose distributions in lungs compromised by radiation-induced lung disease).

For stereotactic and conventional lung volumetric modulated arc therapy plans, Kroon *et al.* (2013) showed that the dosimetric impact on near-minimum PTV dose ($D_{98\%}$) using AAA instead of AXB was large (*i.e.*, underdose up to 12.3 %) for stage I and very small (*i.e.*, underdose up to 0.8 %) for stage III lung treatments. The accuracy of the deterministic Acurus AXB algorithm under different conditions including small fields has been established by

comparison with Monte Carlo algorithms as well as by comparison with measurements (Bush *et al.*, 2011; Fogliata *et al.*, 2011a, 2011b, 2011c; Han *et al.*, 2011).

Type-b algorithms for dose calculations in lung tissue (e.g., CCC) have been investigated by numerous authors, generally, by comparison against detailed measurements or by comparison to advanced type-b algorithms, such as Monte Carlo methods. The general conclusion is that these algorithms are superior to type-a methods for calculating dose in electron disequilibrium regions and adequate for conventional clinical application (Aarup *et al.*, 2009; Carrasco *et al.*, 2004; Haedinger *et al.*, 2005; Hasenbalg *et al.*, 2007; Jones and Das, 2005; Panettieri *et al.*, 2007). A comparison of CCC and Monte Carlo by Chow *et al.* (2009) suggested that the CCC algorithm performed adequately in a $4\text{ cm}^2 \times 4\text{ cm}^2$ with a lung heterogeneity for lung densities equal to or exceeding 0.3 g cm^{-3} but that an increased dose calculation uncertainty is obtained for small fields and when the lung density ranges from 0.1 g cm^{-3} to 0.3 g cm^{-3} —the usual conditions that compromise electron equilibrium (Papanikolaou *et al.*, 2004). The significance of the deviation depends on the energy and field size of the beam.

Disher *et al.* (2012) performed a systematic Monte Carlo investigation of the combination of beam and lung density parameters that cause significant LED within and near a tumor embedded in lung and they quantified dose reduction due to density and disequilibrium.

For a 6 MV ($3\text{ cm}^2 \times 3\text{ cm}^2$) field irradiating a 1 cm^3 tumor embedded in lung with ultra-low density of 0.001 g cm^{-3} the dose in upstream lung and tumor center were reduced by 80 % with respect to the water density calculation (Fig. 4.4). The sensitivity of the dose calculation algorithm accuracy to energy supports the recommendation made in Section 2 that lower energy photon beams ($\leq 10\text{ MV}$) are the energies to be used for the clinical implementation of SRT programs.

Some of the general clinical implications of the advanced type-b dose calculation algorithms, such as Monte Carlo algorithms, have been discussed in reviews and task group reports (Chetty *et al.*, 2007; Reynaert *et al.*, 2006, 2007). The clinical dose differences found between MC-based and conventional algorithms are highly dependent on beam arrangements, field sizes, beam energies, tumor size, and location especially for anatomical sites where the target is situated near tissues with widely varying densities, such as the lung and head/neck (Chetty *et al.*, 2007). Similarly, in small fields, with a penumbra region that occupies most of the field area,

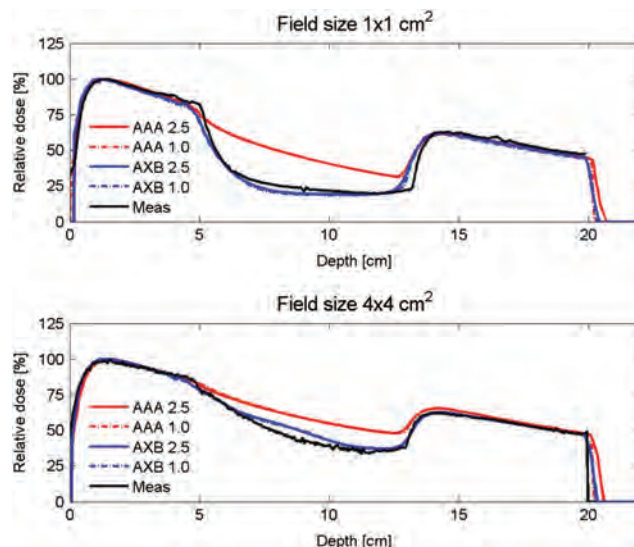


Figure 4.3. Comparison of the intermediate type-a-type-b algorithm AAA and the advanced type-b Acurus XB (AXB, Varian) calculations with measured percentage depth doses for field sizes of $1\text{ cm}^2 \times 1\text{ cm}^2$ and $4\text{ cm}^2 \times 4\text{ cm}^2$. The phantom consists of foam, with a low-density $\rho = 0.03\text{ g cm}^{-3}$ and a thickness of 8 cm sandwiched between two layers of polystyrene with a density of $\rho = 1.05\text{ g cm}^{-3}$. From Kroon *et al.* (2013) with permission.

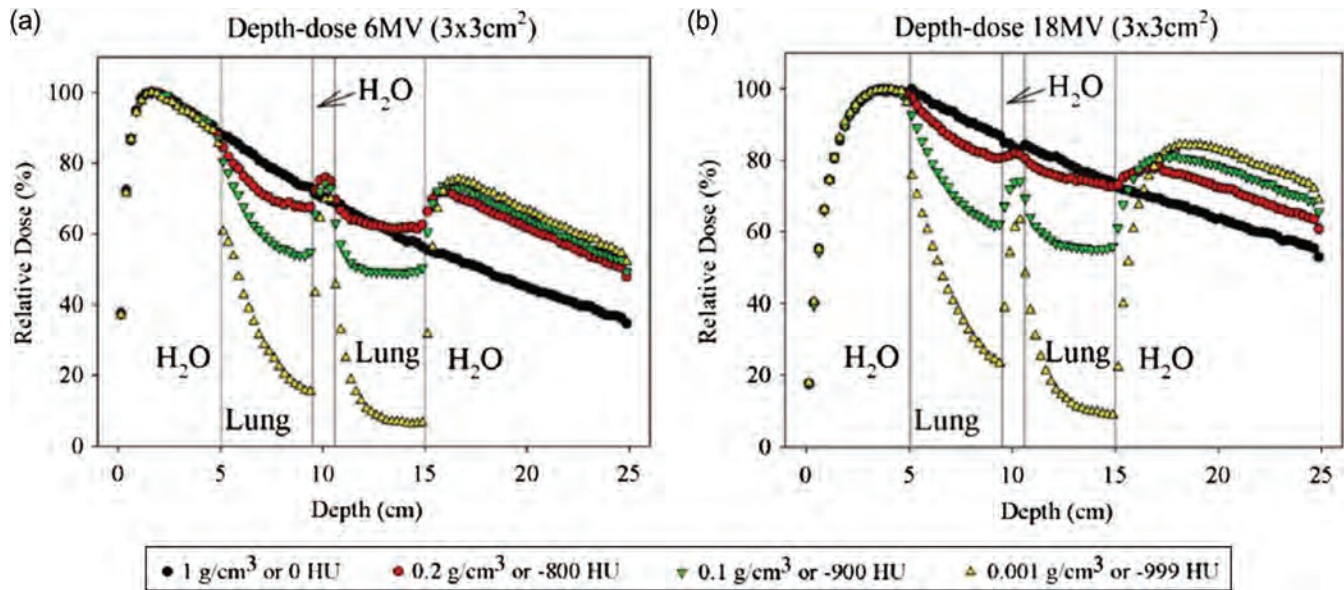


Figure 4.4. Monte Carlo-calculated central-axis depth-dose profiles for a lung slab phantom geometry irradiated by a 6 MV and a 18 MV beam ($3\text{ cm}^2 \times 3\text{ cm}^2$ field size) with a $1\text{ cm}^2 \times 1\text{ cm}^2 \times 1\text{ cm}^3$ tumor embedded in the lung, with decreasing lung slab density. Adapted from Disher *et al.* (2012) with permission.

the differences between type-a and type-b algorithms depend on many factors, such as lung density, field size, and the position and size of the target. However, in addition to this, due to electron transport, differences found in a lung conformal radiation therapy treatment plan using small fields and 15 MV photons are much larger than those found with a standard field AP/PA lung plan, using large field sizes and 6 MV photon beams (Chetty *et al.*, 2007). Numerous lung planning studies have shown sometimes substantial differences (10–20 %) between pencil beam and Monte Carlo algorithms (Chen *et al.*, 2010; Fogliata *et al.*, 2007; Knoos *et al.*, 1995, 2006; Ma, 1998; Pawlicki and Ma, 2001; Vanderstraeten *et al.*, 2006; Wang *et al.*, 2002).

Figure 4.5, from Lacornerie *et al.* (2014), is an example of the difference in absorbed dose between Monte Carlo and an EPL correction algorithm in the case of a 3.6 cm^3 pulmonary tumor surrounded by lung tissue (CyberKnife 6 MV plan). With a prescribed dose of 60 Gy, the lateral extent of the region outside of the gross tumor volume (GTV), where the dose difference exceeds 15 Gy, is shown in red and is much larger than the GTV (contoured in red) to planning target volume (PTV) margin (in blue). Since clinical outcomes based on prescription using the EPL algorithm are significant, the clinical implications of these types of differences merit consideration (Section 4.6).

In summary, of the type-b model-based dose calculation algorithms, point kernel superposition-convolution models are expected to be clinically acceptable for calculations in tissues involving lung

densities of around 0.3 g cm^{-3} , for field sizes of $4\text{ cm}^2 \times 4\text{ cm}^2$ and larger, as the model is expected to handle lateral scaling of the electron transport due to locally varying heterogeneities. Type-a model-based pencil beam kernel-based convolution algorithms (e.g., EPL and others) contain lateral scaling approximations that are inaccurate and not clinically acceptable for heterogeneous configurations involving low-density media. Model-based algorithms intermediate between type-a and type-b such as the AAA model that contains a more detailed handling of the lateral electron scatter, perform in a reasonable fashion for conventional fields but break down for small fields in extracranial applications in regions involving significant density variation (e.g., lung). The impact of lateral electron scatter becomes more significant with increasing energy as the lateral range of the secondary electrons increases. It has been demonstrated that advanced type-b model-based dose calculation algorithms such as Monte Carlo techniques and deterministic solvers (currently Acuros AXB, Varian) are accurate for small field dose calculation for treatment planning for situations involving small fields and tissue heterogeneity and this Report recommends these for SRT treatment planning dose calculations.

4.6 Considerations for Clinical Prescription Using Type-b Dose Calculation Algorithms in Small Fields

Data-based algorithms without heterogeneity corrections and model-based algorithms of type-a have

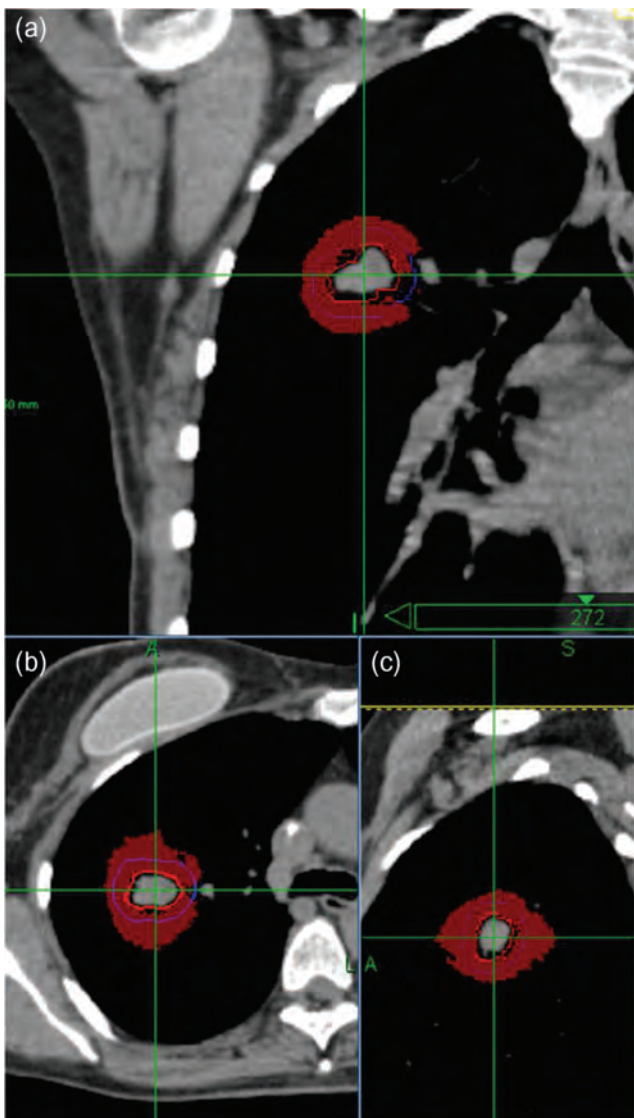


Figure 4.5. Region of dose difference exceeding 15 Gy outside the GTV (shown in red), between equivalent path length correction (EPL) and Monte Carlo for CyberKnife (6 MV) treatments of a tumor with size 3.6 cm^3 . The GTV (contoured in red) to PTV margin is shown in blue. A: coronal view, B: axial view, C: sagittal view. Dose prescribed 60 Gy. Adapted from Lacornerie *et al.* (2014) with permission.

been used for a long time to guide and record dose prescription in clinical protocols. With the present general availability of type-b algorithms (*i.e.*, AAA, CCC, Monte Carlo, or deterministic), prescription and recording of dose distributions has led to discussions on how to best transfer the clinical experience with the former to modern dose calculation algorithms. The dose differences between the former algorithms and the newer type-b algorithms observed in clinical treatment planning with small fields are substantial, especially in pulmonary SRT applications where, due to electron disequilibrium

and re-buildup effects the degree of PTV coverage is strongly affected by low-density tissues surrounding the tumor. This is a situation in which the physical conditions for use of PTV coverage to represent CTV coverage (ICRU, 2010) are not fulfilled. For these reasons, the transfer of the relation between absorbed dose and clinical effect from former algorithms to state-of-the-art dose calculation algorithms is still a matter of discussion. For example, in the context of RTOG trial 0236 (Timmerman *et al.*, 2004), Xiao *et al.* (2009) stated that the results of their study about heterogeneity corrections will be used for future protocols. However, the same group (Li *et al.*, 2012) reported in the context of heterogeneities and the RTOG trial 0813 (Bezjak *et al.*, 2009) that further studies are expected to establish protocol criteria for MC dose calculations. Hurkmans *et al.* (2009), in the ROSEL trial, proposed a variable dose conformity requirement depending on the size of the PTV and the type of algorithm used. The prescription dose was the same for all lesions but the heterogeneity in PTV and the dose constraints for the lung varied depending on the size of the PTV. Van der Voort van Zyp *et al.* (2010b) studied the prescription dose for non-small cell lung cancer according to tumor location and size for EPL based and Monte Carlo based algorithms for CyberKnife. Figure 4.6 shows the ratio of Monte Carlo dose to the EPL dose reported as $D_{95\%}$, $D_{99\%}$, and mean dose for different tumor sizes. Based on a separate accuracy validation against measurements, it was concluded that the dose calculated by EPL underestimates the real dose, especially for small and peripheral tumors. Given the clinical experience using historical EPL prescription, the authors provide a conversion in dose prescription based on tumor size. Since the EPL dose underestimates the real dose, an EPL prescription scenario of $3 \text{ Gy} \times 20 \text{ Gy}$ for peripheral tumors required the following MC dose schedules to achieve the same delivery: $3 \text{ Gy} \times 16 \text{ Gy}$ for tumors $< 3 \text{ cm}$, $3 \text{ Gy} \times 17 \text{ Gy}$ for tumors of 3 cm to 5 cm and $3 \text{ Gy} \times 18 \text{ Gy}$ for tumors $> 5 \text{ cm}$ (van der Voort van Zyp *et al.*, 2010b).

Lacornerie *et al.* (2014) discussed three different prescription scenarios and the impact of dose calculation algorithm accuracy: (1) prescription dose to PTV $D_{95\%}$ using a type-a algorithm (*i.e.*, EPL) followed by reevaluation of the delivered dose using a type-b algorithm (*i.e.*, MC); (2) prescription dose to PTV $D_{95\%}$ using a type-b algorithm, and (3) prescription to GTV $D_{50\%}$ using type-b algorithm (optimization for homogeneity over the PTV performed using type-a algorithm). The authors showed that the correlation between dose prescribed to the PTV using a type-b and GTV median dose is weak and

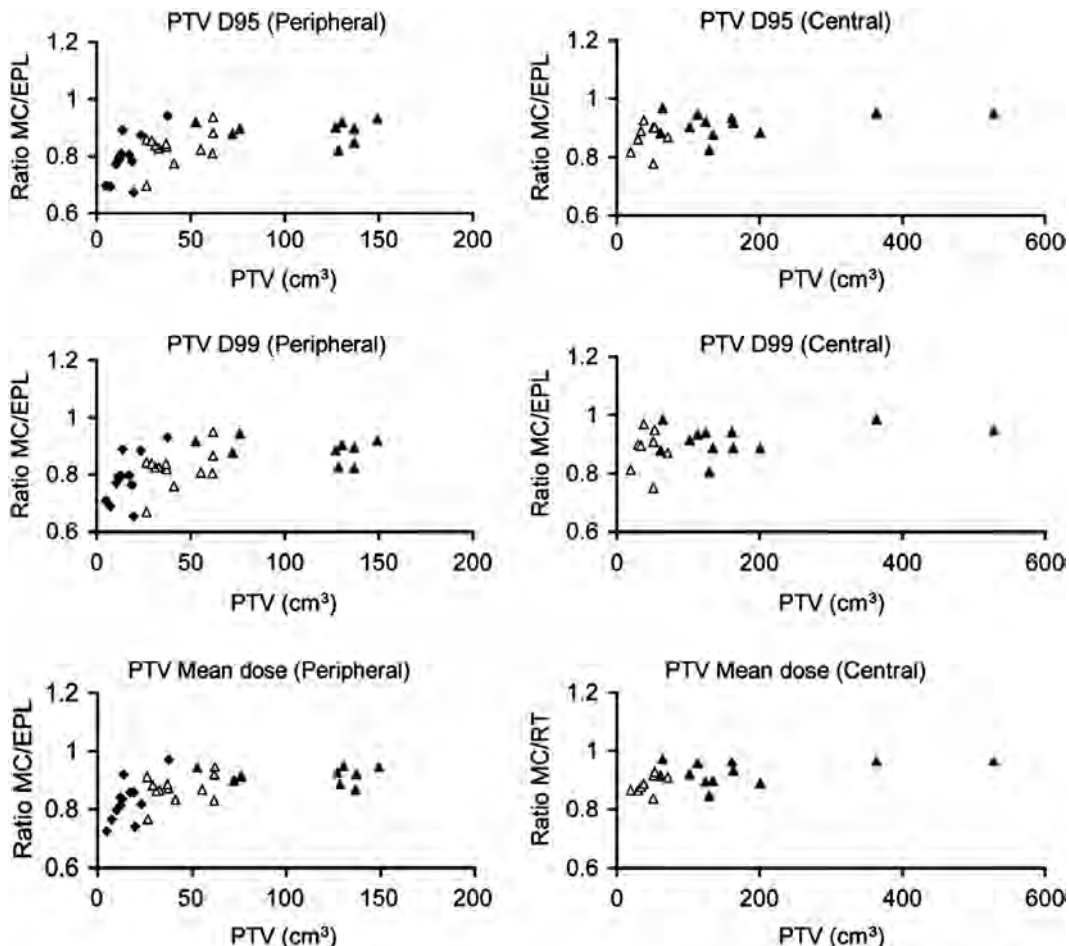


Figure 4.6. Ratio of MC and EPL calculated PTV $D_{95\%}$, $D_{99\%}$ and mean dose for peripheral and central pulmonary tumors. Bold diamonds represent tumors <3 cm, open triangles represent tumors of 3 cm to 5 cm and bold triangles represent tumors >5 cm. Data is for the CyberKnife 6 MV beam. Adapted from van der Voort van Zyp *et al.* (2010b) with permission.

large, tumor size-dependent variations occurred. They suggested using type-a algorithms to optimize the PTV dose (not unlike, *e.g.*, RTOG 0236), to recalculate dose with type-b algorithm and rescale the prescription to the GTV median dose ($D_{50\%}$). The GTV median dose, rather than near-minimum dose, $D_{98\%}$ (ICRU, 2010) is chosen since it is the least dependent on small low-density regions within the GTV (Bibault *et al.*, 2015). Optimization using a type-b algorithm based on a PTV $D_{95\%}$ prescribed dose may lead to overdosing of the GTV. The reason for this is that the optimizer will attempt to boost the fluence in the low-density areas around the GTV so as to achieve the prescription. A GTV that moves into this region of high fluence will hence be overdosed. An alternative is the use of a robust planning approach (*e.g.*, RaySearch, Inc) where, in the case of pulmonary targets, the optimization goal is CTV coverage on all phases of the breathing cycle. Robust optimization using TPSs (*e.g.*, RaySearch, Inc.), that utilize probability distributions for a GTV

to be in a certain location, allow for a more consistent prescription scenarios.

4.7 Implementation Considerations

Besides approximations of the physical processes involved in dose depositions, discretization effects depending on the numerical implementation in TPS will impact dose accuracy. The collapsed cone implementation of point kernel convolution-superposition limits the number of directions in which dose is spread from a primary point of interaction.⁸ This may also limit the spatial resolution which may be problematic when fluence gradients become very sharp and require sub-millimeter pixels in fluence

⁸The same type of restriction applies also to deterministic Boltzmann equation solvers, sometimes referred to as the discrete ordinate method. In this case direction angles are discretized (or collapsed) although serial expansions of fluence and cross sections are used to filter the effects of the discretization.

maps for full resolution. Although the electron transport significantly blurs the dose deposition distribution, resolving small targets and organs at risk may still require a high resolution of the dose.

The calculation grid size affects the accuracy of the dose calculation. It has been reported in the literature that a 2.5 mm isotropic grid produces an accuracy of about 1 % in the high-dose region of an IMRT plan consisting of multiple fields (Dempsey *et al.*, 2005). Kroon *et al.* (2013) found that the use of grid size of 2.5 mm was comparable in terms of accuracy with 1.0 mm for clinical VMAT lung treatments planned with the Acurus XB TPS. However, the calculation time increases drastically when grid size 1 mm was used. Chung *et al.* (2006) found a dose difference of 2.3 % of the prescribed dose for 2 mm calculation grids as compared to 1.5 mm grids, rising to 5.6 % for 4 mm grids. Their conclusion is that 2 mm grids are required for high-dose gradient areas. Consistent with these studies, the AAPM TG-101 report recommends the use of an isotropic grid size of 2 mm or finer (Benedict *et al.*, 2010). The AAPM TG-105 report (Chetty *et al.*, 2007) recommends for Monte Carlo algorithms typical values of voxel sides of 2 mm to 5 mm for field sizes greater than $3\text{ cm}^2 \times 3\text{ cm}^2$ and 1 mm to 2 mm for field sizes less than $3\text{ cm}^2 \times 3\text{ cm}^2$, again consistent with the above recommendations.

A side effect of Monte Carlo dose calculations is statistical uncertainty in the dose distributions. Reducing the voxel size will increase the relative uncertainty for a fixed number of source particles because fewer particles deposit dose in the smaller volume. Increasing the voxel volume will reduce the relative uncertainty but may introduce errors due to reduced spatial resolution. For clinical interpretation and optimization, DVHs are used and while they are relatively insensitive to noise, DVH blurring will occur. Variance reduction techniques and smoothing algorithms have been implemented that may reduce the impact of statistical uncertainty. Most TPSs allow the user to run the calculation to a prerequisite statistical uncertainty.

Advanced type-b algorithms (*i.e.*, Monte Carlo and deterministic solvers) have the capability to express the absorbed dose in tissue, D_t^t . In Monte Carlo simulations, assuming that the exact atomic composition of the tissue of a specific patient is available, dose-to-tissue specification is perhaps the most natural one. Historically, however, radiotherapy dose

⁹Some collapsed cone implementations (*e.g.*, Oncentra) intrinsically calculate dose to medium for conditions of electronic equilibrium. Other implementations effectively calculate a quantity close to dose to medium because of approximations (*e.g.*, the CT Hounsfield unit lookup table).

measurements and calculations have been performed in, or specified in terms of the absorbed dose to water. Hence, clinical expertise on dose-outcome relation is based on the latter. The fact that the differences between the two have been found significant for MV beams (Chetty *et al.*, 2007; Dogan *et al.*, 2006; Keall, 2002; Knoos *et al.*, 2006; Liu, 2002; Ma and Li, 2011; Siebers *et al.*, 2000), has triggered discussions on the appropriateness of one versus the other type of dose specification. Andreo (2015) discussed in detail the different scenarios for relation between dose to tissue and dose to water-like media, and discussed stopping power ratios and fluence correction factors, the latter of which are usually ignored in the conversion process (Siebers *et al.*, 2000). Figure 4.7 shows dose calculations using type-b algorithms (*i.e.*, Eclipse AAA, Varian and Monaco 5, Elekta) converted and compared to reference dose. Andreo (2015) showed that mass stopping-power ratios to water are more dependent on possible patient-to-patient differences in composition, and therefore on I -values, than on density. Likewise, electron fluence in different media is more dependent on media composition (and their I -values) than on density. Since segmentation due to patient-specific tissue composition and I -values cannot be obtained for individual patients, the differences between dose-to-tissue or dose-to-water specification are often a matter of choice on the

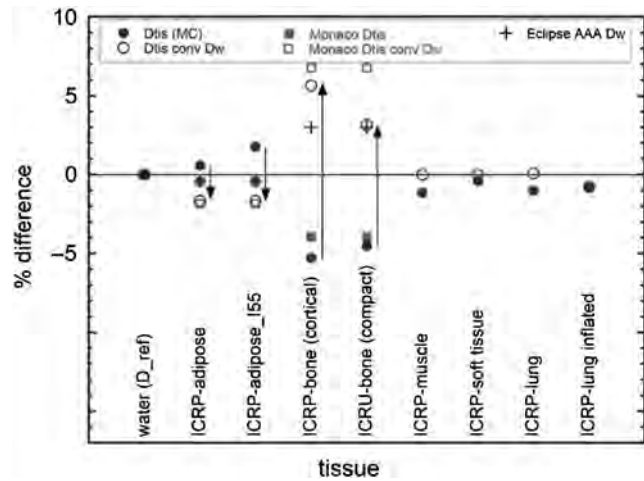


Figure 4.7. Percentage difference with a reference dose $D_{w,\text{ref}}$ (horizontal line) of converted dose-to-water $D_{\text{tissue}}^{\text{conv-}w}$ (open circles) obtained from dose-to-tissue (filled circles), and results obtained with the Varian Eclipse AAA (crosses) and Elekta Monaco 5 (squares) treatment planning systems. D_{tissue}^t are dose calculations based on the electron fluence in tissue. Eclipse AAA yields dose to water-equivalent tissue directly. Monaco calculates dose to tissue (filled squares) and, optionally, converts it into dose to water-equivalent tissue (open squares). The arrows indicate conversion from $D_{\text{tissue}}^{\text{conv-}w}$ to $D_{\text{tissue}}^{\text{conv-}w}$ using Bragg-Gray $s_{w,\text{tissue}}^{\text{BG}}$ mass stopping-power ratios, following the Siebers *et al.* (2000) approach. Adapted from Andreo (2015) with permission.

preferences of the user than on objective criteria. In this choice, an important consideration is that, for tissues such as bone or lung, the biologically relevant quantity is dose to tissue embedded in bone (e.g., osteoblasts) or the dose to the living part of lung (e.g., capillaries surrounding alveoli). Ultimately, the target may be the cell nucleus and the RNA. In such cases, it is unreasonable to specify the correction to a particular soft tissue, and hence dose is specified to water.

Although Andreo's (2015) analysis was for electron spectra obtained in broad-field radiation therapy, his conclusions are expected to stand for SRT because of the only modest spectral changes in small fields (Section 2.2).

4.8 Measurement Aspects of Treatment Planning Algorithm Commissioning

Measured beam data (*i.e.*, PDD, profiles, output factors) and geometric information on the treatment head are basic data for the implementation and commissioning of a treatment planning algorithm. The data are commonly used in an iterative tuning process to determine beam model parameters such as shape of the primary energy fluence distribution and the width of the focal spot. For model-based algorithms the basic subset of dosimetric data is usually smaller than for correction-based algorithms but the extended commissioning dataset is used to provide inherent validation of the beam model. For small field commissioning the suitability of the detector used in the data acquisition is essential. In principle, the correction factors to convert the detector signal to absorbed dose need to be taken into consideration when matching the model to the data (see, *e.g.*, Ralston *et al.*, 2012). For more discussion on this topic, see Section 2.

The accuracy of a clinical dose calculation algorithm depends on the accuracy of the beam model and the accuracy of the patient dose calculation model. To optimize the performance of the treatment planning algorithm specifically for small field applications the user should pay special attention to the following aspects:

- Source (or focal spot) size and verification of small field output for central and off-axis fields.
- Jaw and leaf-end field edge positioning and MLC transmission at different off axis positions.
- Backup jaw and MLC leaf-edge interaction (*i.e.*, position of jaw with respect to MLC).
- MLC interleaf leakage and leaf-side modeling.
- Multileaf intraleaf leakage modeling.
- Penumbra and full profile when penumbra overlap for small field sizes.

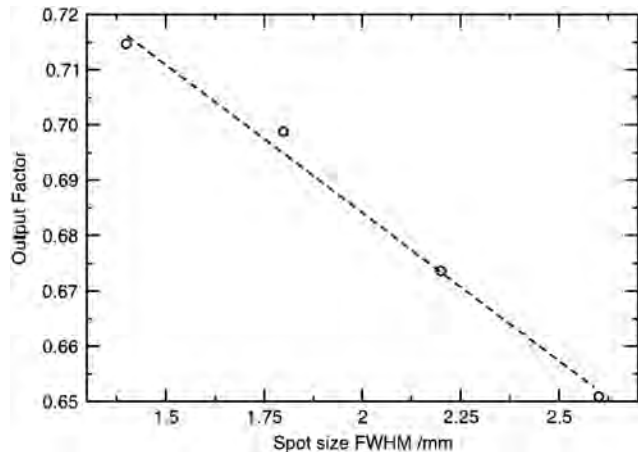


Figure 4.8. Sensitivity of output factor on accelerator electron source size for CyberKnife (Accuray, Inc). Adapted from Francescon *et al.* (2008) with permission.

- In low-density media, widening of penumbra, buildup, and re-buildup for beam traversing low-density regions.

The focal spot size in particular is of primary importance for beam commissioning in small fields (Francescon *et al.*, 2008; Sterpin *et al.*, 2007, 2011). A chosen value for this may lead to the algorithm to performing adequately in broad beams, but not in narrow beams. Figure 4.8, from a study by Francescon *et al.* (2008) shows the sensitivity of the output factor of a CyberKnife to the spot size. However, it is likely that the sensitivity is not unique to the CyberKnife. The spot (or source) size is a parameter in the TPS and it is recommended that it be tuned appropriately before the TPS is used for treatment planning calculations involving small fields.

Since heterogeneities such as air cavities, lung, high density bone or metal fillings are in the treatment field, such as in, for example for lung or head-and-neck sites, dose calculations with heterogeneity corrections are part of the TPS validation task. With the conditions of LED for small fields and the large variation in dose with field size and depth that creates steep dose gradients, validation with measurements is essential. This could involve carrying out measurements (*e.g.*, depth dose, profiles, output factors, and isodose distributions) in solid phantoms, which contain low-density material. Low-density medium may be simulated by lung-equivalent plastic (*e.g.*, RMI), Styrofoam, cork or balsa wood (density approximately 0.16 g cm^{-3}). For more information on TPS validation AAPM TG 53 (Fraass *et al.*, 1998) and IAEA TRS 430 (IAEA, 2004) can be consulted. For specific discussions on validation of TPS dose calculations in heterogeneous phantoms see AAPM TG 65 (Papanikolaou *et al.*, 2004).

5. Image-Guided Beam Delivery

5.1 Introduction

Daily setup variations and internal organ motion and deformation are a concern for external beam radiation therapy because they can modify the actual dose distribution in the patient, and consequently alter the clinical outcome and have effects on organs at risk different from the expectations of the planned dose distribution. To take these uncertainties into account, appropriate margins around the CTV are used to ensure adequate target coverage. This can result in a significant increase of the irradiated volume and, therefore, a significant additional exposure of healthy tissue. To reduce daily treatment variations, image-guided radiation therapy (IGRT) technology has been widely adopted to provide real-time geometric and anatomic information with the patient in the treatment position. The assumption behind the implementation of IGRT is that when the precision of radiation treatment is improved, it should increase survival and decrease complications. The concurrent clinical benefit of IGRT for the patient is the ability to monitor the changes in position and status of the tumor (*i.e.*, shrinkage or expansion) and/or patient that can occur during the course of radiation treatment and to adjust the beam delivery accordingly.

5.2 Purpose of IGRT in SRT

In SRT treatments, positional variations have an even greater impact on the dose distribution compared to conformal radiation therapy, due to the high gradients present in the dose distribution obtained with small fields. Moreover, a hypofractuated scheme is usually employed in SRT and, therefore, the need for daily correction to match the original plan is greater because there is less averaging of the dose delivery over many fractions.

SRT is particularly demanding of precision (*i.e.*, reproducibility) as well as accuracy (*i.e.*, how close the determination of a quantity is to the true value) of the dose delivered to the target. These are essential in the delivery of high doses per fraction in very few fractions. Therefore, in SRT treatments, the verification of target location in all treatment positions during all fractions for the entire procedure should

ideally be achieved at sub-millimeter precision. This is achievable in tests with phantoms, but in patients it is more problematic, due to the uncertainties discussed below. Nevertheless, IGRT helps to keep the total positional uncertainty within a few millimeters.

AAPM Task Group Report 104 (AAPM, 2009) discusses three different roles in which IGRT is used:

- Prior to the dose delivery as a check of the positioning of the patient and localization of the target and surrounding structures. In this way, both systematic and random errors can be corrected prior to the delivery.
- During delivery, correction can be performed by monitoring the target or its surrogate (*e.g.*, implanted fiducial or anatomical landmark). This is important for the quantification of intrafraction organ or tumor motion.
- At the end of the treatment, for quality assurance purposes or to evaluate the amount of intrafraction motion after the correction has been applied.

Research into techniques for online plan adaptation (Thongphiew *et al.*, 2009; Yan *et al.*, 1997) is ongoing, but such approaches require real-time quality assurance (QA), an area that needs considerable development. The information given by image guidance can be used online or offline for adaptation purposes (*e.g.*, modifying the plan and delivery for the next fraction). The best strategy would be an online correction technique based on treatment plan adaptation, but this may require re-contouring and re-optimization.

The deviation in position of the CTV triggering corrective action should be consistent with the PTV margin selected for the clinical situation at hand. When the shifts from the original position of the target, and/or of the organs at risk, exceed the margins used in planning, the risk of underdosing the target and overdosing the OAR becomes significant.

In SRT treatments, both the shifts of the target prior to delivery and the changes in the target volume or internal organ variations during delivery should be evaluated and recorded.

Clinical implementation of IGRT has been described in the literature (Bissonnette *et al.*, 2009; Chung *et al.*, 2004; Gill *et al.*, 2011; Guckenberger *et al.*, 2007a; Hawkins *et al.*, 2006; Kupelian *et al.*, 2008; Li *et al.*, 2010; Meyer *et al.*, 2007; Sandhu *et al.*, 2008; Sonke *et al.*, 2009; Zeidan *et al.*, 2007).

An example of the clinical impact of the application of IGRT is reported in the paper of de Crevoisier *et al.* (2005) on prostate cancer. They showed that the biochemical control was significantly influenced by the degree of distension of the rectum as shown in Fig. 5.1 (de Crevoisier *et al.*, 2005). This not only emphasizes the need for daily prostate localization with IGRT, but also speaks to the potential impact on local-regional control of positional uncertainty in all radiotherapy sites. Cui *et al.* (2002) showed that incorporation of IGRT with repositioning reduces the risk of geometric miss and results in good biochemical control (PSA) that is independent of rectal volume/distension while maintaining very low rates of chronic GI toxicity. The clinical evidence supports the conclusion that higher quality dose delivery resulting from IGRT can result in higher clinical control rates, reduced toxicity (e.g., lung and liver SBRT), and new treatment options (Bujold *et al.*, 2012).

5.3 IGRT Technology

5.3.1 Immobilization Systems

Reproducible patient positioning is essential in order to deliver dose to the target accurately. An

immobilization system is useful to reduce interfraction setup errors, and to reduce intrafraction movement of the patient. Stereotactic head frames have been employed for decades in SRS despite their invasiveness. Various systems, such as masks, shoulder fixators, arm positioning devices, vacuum cushions, *etc.*, are presently employed to help place the patient in the same position as during planning. To minimize respiratory motion, some body-frame systems include abdominal compression (Fuss *et al.*, 2004; Wang *et al.*, 2004; 2006). A list of immobilization systems adopted for stereotactic treatments, with information on their accuracy, is presented in Table IV of the AAPM TG-101 report (Benedict *et al.*, 2010).

The accuracy and reproducibility of positioning are very much dependent on the anatomic region involved and on the immobilization system used. Sub-millimeter accuracy has been achieved using invasive and noninvasive localization frames for SRS (Gill *et al.*, 1991; Ramakrishna *et al.*, 2010). Thermoplastic masks have been demonstrated to yield setup errors on the order of 1 mm or less, for a fixed target, such as a brain lesion (Gevaert *et al.*, 2012; Guckenberger *et al.*, 2007b; Masi *et al.*, 2008; Tryggestad *et al.*, 2011). Cerviño *et al.* (2010) reported a frameless maskless technique using only a head mold with video surface monitoring and CBCT. They reported average shifts after setup for 23 patients of 1.85 mm (Cerviño *et al.*, 2010).

However, for moving targets such as lung tumors or abdominal organs, the shifts, even after an accurate positioning of the patient, can be of the order of 2–3 mm for translations and several degrees for

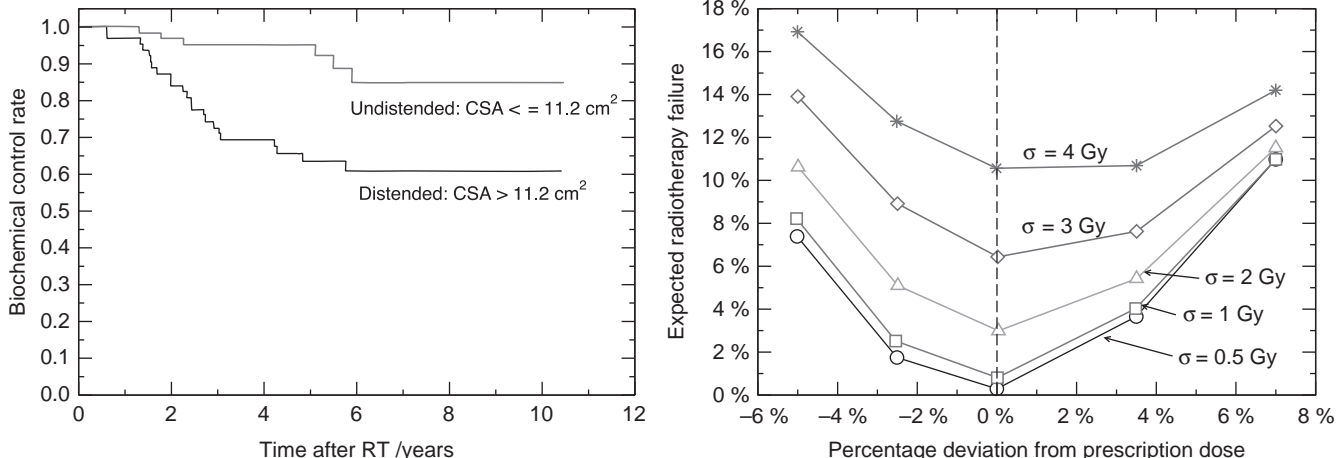


Figure 5.1. Left panel: Impact of rectal distension during CT-simulation on outcome of prostate patients. Distension, quantified as the average cross-sectional rectal area (CSA), resulted in poorer biochemical (PSA) control (de Crevoisier *et al.*, 2005). Right panel: the impact of random errors in target dose delivery reproducibility (with σ 0.5 Gy to 4 Gy) compared to percentage deviation from prescription dose (systematic errors), on expected radiotherapy failure (de Crevoisier, personal communication). At doses higher than the prescription dose, failures include complications. It can be observed that, as random errors are reduced (lower σ) as is the case with SRT, the impact of delivery accuracy (lower percentage deviation from prescription dose) becomes more significant.

rotations (Guckenberger *et al.*, 2007b; Soete *et al.*, 2006). For lung tumors, for example, a day-to-day baseline shift of the tumor of several millimeters relative to the vertebral bodies has been shown (Masi *et al.*, 2008; Sonke *et al.*, 2008; 2009; Sweeney *et al.*, 2012). For such tumors, bony structures have limitations as surrogates for target alignment and image guidance based on direct tumor visualization or by means of implanted fiducials is desirable for alignment.

The ability of immobilization devices to maintain patient positioning will be strained during prolonged treatments. Monitoring of patient and tumor position is particularly important during the long treatment times associated with hypofractionated schedules using small treatment fields, typical of SRT treatments.

5.3.2 Overview of Current IGRT Technologies

The currently available technologies to perform IGRT can be divided, according to their operation, into planar systems, volumetric systems, and non-radiographic systems. In Benedict *et al.* (2010), a detailed description of the different modalities for IGRT imaging is reported. In this report, only the IGRT technologies currently clinically implemented are described. New technologies are under development and may become potentially available after the publication of this report.

5.3.2.1 Planar systems. Electronic portal imaging devices (EPIDs) and stereoscopic x-ray imaging belong to this category. These systems allow matching of planar, kilovoltage (kV) radiographs, fluoroscopy, or megavoltage (MV) images with digitally reconstructed radiographs (DRRs) from the planning CT.

The EPID was the first system used for IGRT both online and offline (Boyer *et al.*, 1992). It can be used for calculation of the shifts between planned isocenter and imaged isocenter by comparing the portal images of the beams with the DRR obtained by the treatment planning system (TPS). The accuracy of the localization with this technique is of the order of 2 mm for fixed organs like spinal sites (Lovelock *et al.*, 2005). The disadvantages of this technique lie in the fact that it provides only 2D information (unless several gantry angles are used for imaging). In addition, EPID-based imaging has low contrast, and therefore it is possible to distinguish only bony anatomy, lung density difference or implanted fiducial markers. Furthermore, the technique is relatively time-consuming and mostly

limited to reduce 2D setup errors. Therefore, the use of EPID-based IGRT in SRT is limited to the treatment of spinal sites or fixed lesions.

Stereoscopic devices are kV-based: they use angled x-ray tubes, usually orthogonal, with corresponding opposed flat panels. These devices are used by the CyberKnife (Accuray) system (Fig. 5.2) (Adler *et al.*, 1997) by the ExacTrac X-ray (Brainlab) system (Fig. 5.3) (Jin *et al.*, 2008a), and by the Vero (Brainlab/MHI) system (Fig. 5.4) (Burghelea *et al.*, 2014). They can provide 3D information and they are used for real-time tracking of moving target with synchronized single imaging and fluoroscopy. The disadvantages of this technique are lack of volumetric tissue information, the need for a surrogate to localize the target; the lack of information on the spatial relationship between PTV and PRVs; its fixed spatial orientation does not allow use of different imaging angles for optimal target imaging.

5.3.2.2 Volumetric systems. This category includes in-room CT, kV–MV cone-beam CT, MV fan-beam CT, digital tomosynthesis, 3D ultrasound, and in-room MRI. In-room CT has a short scanning time to produce images of diagnostic quality and can be used for IGRT re-planning strategies (Kuriyama *et al.*, 2003). A limitation is that the patient or the couch has to be moved, with the introduction of an uncertainty on setup. It does not allow for detection of intrafractional patient and organ motion.

Kilovoltage cone-beam CT (kV-CBCT) is performed with Linac-integrated hardware (Jaffray *et al.*, 1999) by using a kV x-ray tube with an opposed flat panel detector, at 90° with respect to the direction of the beam (Fig. 5.5). This type of IGRT technique is also suitable for detecting organ motion. Due to the relatively low doses required, it allows for more frequent image acquisitions to check the patient position during long SBRT sessions thereby reducing the effect of intrafraction positioning uncertainties (Higgins *et al.*, 2011). It can also be used for intrafraction motion monitoring of lung tumors by using either a long acquisition time (60 s) (Guckenberger *et al.*, 2006; Hugo *et al.*, 2007; Wang *et al.*, 2007) or with a 4D feature, using a respiration-correlated approach (Sonke *et al.*, 2005). This technique allows for a more accurate representation of the motion of the tumor with respect to the average 4D CT scan and it reduces the inter-observer variability in the detection of tumor position (Sweeney *et al.*, 2012). Sometimes, implanted fiducials must be used as surrogates of the organ, such as in the prostate when it is not

PRESCRIBING, RECORDING, AND REPORTING SMALL BEAM SRT

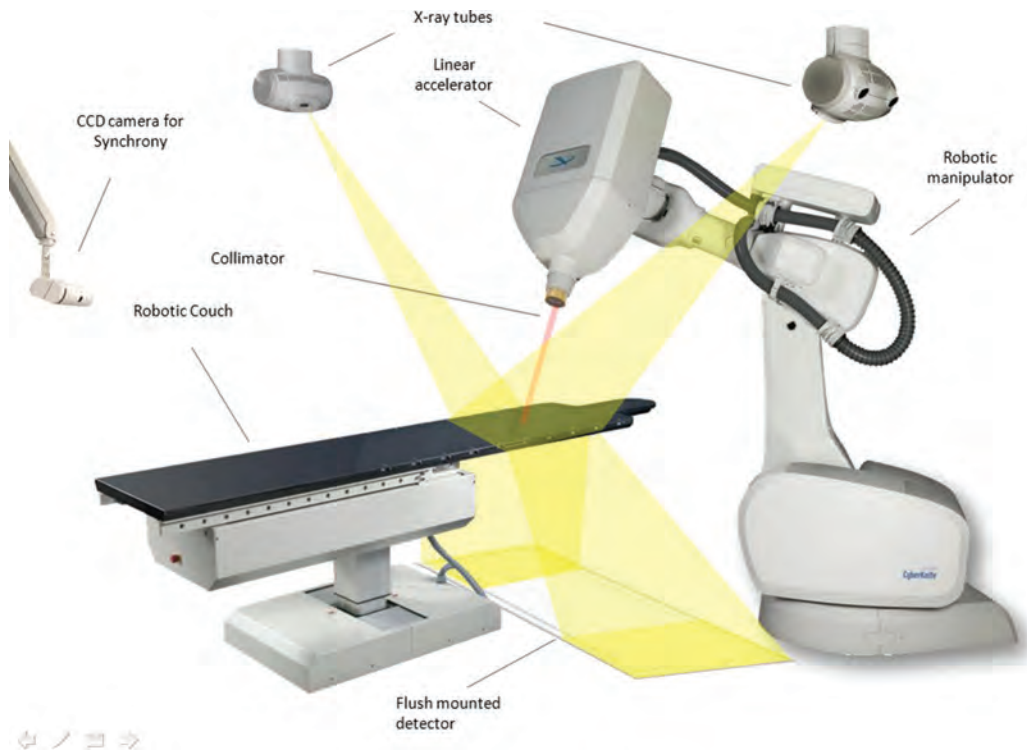


Figure 5.2. The CyberKnife™ system with its main components including IGRT systems. The stereotactic x-ray systems have ceiling-mounted x-ray tubes and floor-mounted detectors. The x-ray systems are supplemented with a ceiling-mounted camera to determine the patient surface contour.



Figure 5.3. The ExacTrac™ system with floor-mounted x-ray tubes and ceiling-mounted flat panel detectors.

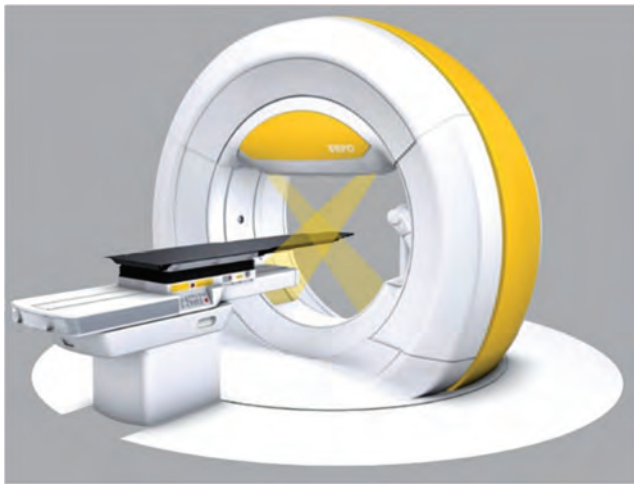


Figure 5.4. The Vero™ system, which consists of ring gantry-mounted stereotactic x-ray systems.



Figure 5.5. A kV-CBCT integrated into a C-arm linac gantry.

clearly distinguishable on the image. This technique has been implemented on all the modern Linacs (Varian Trilogy, Varian Truebeam, Elekta Synergy, Siemens Artiste, Brainlab/MHI Vero).

An MV-CBCT system is the MVision™ (Siemens). It generates a 3D image of the patient anatomy from the same x-ray beam (6 MV) used for treatment, by using the EPID as a detector. Image and x-ray beam share the same isocenter. Patient 3D anatomy in treatment position can be checked at any moment before dose delivery (Morin *et al.*, 2006). Another type of MV-CBCT is used on the Artiste Linac (Siemens) (Fast *et al.*, 2012), coupled with an in-line kV system (kView™, Siemens) (Fig. 5.6). It has the advantage that the imaging beam and the treatment beam have the same

isocenter and the disadvantage that the kV system cannot be used during the treatment.

MV fan-beam CT is an IGRT system included in all TomoTherapy systems (Fig. 5.7) (Accuray Inc., Sunnyvale). MV fan-beam CT uses an energy reduced (about 3.5 MV) treatment beam for imaging and these images can be used for adaptive treatment planning (Schubert *et al.*, 2009; Welsh *et al.*, 2006). The images do not suffer from high-Z artifacts. The disadvantage is a lower soft-tissue contrast compared to kV imaging, and it is difficult to use for intrafraction motion management.

Digital Tomosynthesis is an intermediate solution between fluoroscopy and CBCT based on limited gantry rotation with multiple radiographs. It has the advantage that it reduces the imaging dose



Figure 5.6. In-line kV-CBCT integrated in a C-arm linac.



Figure 5.7. The TomoTherapy HD (Accuray) system that has a fan-beam CT detector and generates low megavoltage x-rays with its linac.

to the patient compared to other systems. It has a reduced acquisition time and a higher image quality for anatomy moving with respiratory motion, since it can be acquired in a single breath-hold (Wu *et al.*, 2011).

5.3.2.3 Nonradiographic systems. For IGRT, other types of imaging solutions have been adopted such as ultrasound, surface detection systems, electromagnetic systems, radioactive source-based systems, and MRI-based systems.

Ultrasound (US) systems: US imaging has the advantage of being nonionizing radiation. Ultrasound has typically had the disadvantages of requiring significant operator intervention, providing images of variable quality and being at risk of systematic error from probe pressure on the patient. In the case of prostate SRT, intrafraction transperineal 3D ultrasound might address these limitations. A probe is left in contact with the perineum during treatment with automatic scanning of a 45 degree field of view every 2.5 s (Lachaine and Falco, 2013; Wallace *et al.*, 2012). Used in conjunction with implanted fiducial markers, US systems are able to detect the position of soft-tissue tumors in the abdominal/pelvic region (*e.g.*, Clarity System, Fig. 5.8). Another example of the application of ultrasound to IGRT is the BAT™ technology (Best Medical) for a frameless SBRT of liver using an ABC device. Target localization using US in combination with ABC reduced the target positioning error to <5 mm (Boda-Heggemann *et al.*, 2008). The disadvantages of US are poor image quality, inter-user variability, and differences between CT-contours and US structures.

Surface detection systems can be optically guided or video-based systems. Examples include the Catalyst HD™ system (C-Rad AB, Sweden) or the AlignRT® system (Li *et al.*, 2011) (VisionRT). The first system consists of three cameras mounted at optimal angles for maximum patient coverage. An integrated couch tracking is possible with 360°



Figure 5.8. Ultrasound Clarity™ system (Elekta AB, Sweden).

automatic reference rotation for noncoplanar treatments. The second system makes use of a pseudo-random speckle pattern projected on the patient's skin. The cameras use stereovision techniques and a triangulation process to create a high-resolution 3D surface of the patient (displayed on monitor). These systems have the advantage of being real-time imaging systems and images can be acquired with respiratory gating; the positioning process is fully automated. The disadvantage is that they can position the skin with high precision but not the internal organs (*i.e.*, the correlation between skin and internal organ position is poor). Their role lies more in the realm of patient setup, collision detection and prevention during dynamic radiation therapy.

Electromagnetic radiofrequency-based systems have been developed (*e.g.*, Calypso system, Varian, Fig. 5.9), which continuously report the 3D position of the target during the entire treatment. It is based on RF tracking of implanted beacon transponders. It has been used in prostate and lung tumor tracking. With this system, it is possible to have a real-time monitoring of intrafraction motion. It has the advantage of not delivering extra-dose to the patient. A system using an implantable electromagnetic transmitter inserted into a catheter has been developed (Raypilot, Micropos, Sweden) for real-time tracking of prostate position. It has the advantage that a micro-MOSFET dosimeter can be mounted near the sensor for *in vivo* dosimetry. The disadvantages of these systems are that no images are available; therefore, they are not usable for replanning and adaptation.

A radioactive source-based tracking system (RealEye, Navotek, Israel) has been developed. A low activity marker (*i.e.*, 1 marker for 4D localization) is implanted in the patient and a rotating collimated "sensor", mounted on the gantry, can detect the position of the marker and its positional changes inside

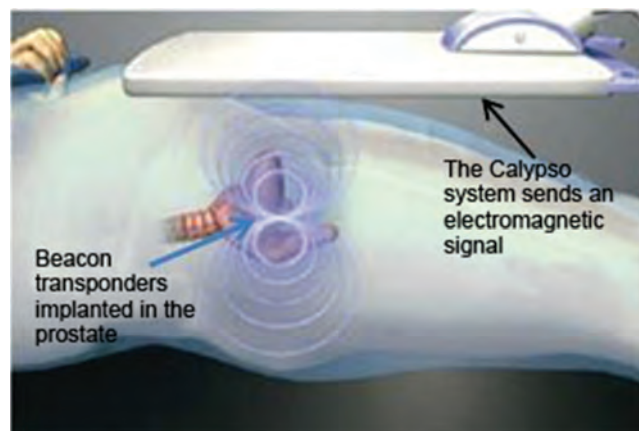


Figure 5.9. Radiofrequency-based Calypso™ system.

the patient. The advantages are that the markers are very small and 4D localization in real time is possible. A minor disadvantage is that they are not usable with energies of 10 MV or greater, due to the interference from neutron-induced activation of short-lived isotopes in the linac and other materials. The absorbed dose received by the patient from radiation emitted by the radioactive source (3700 kBq ^{192}Ir) is lower than the dose from a weekly CBCT.

In-room MRI guidance is an emerging imaging technique based on the use of a magnetic resonance imager to create the image of the patient, with the advantages of better soft-tissue contrast and no additional dose to the patient, opening the possibility of continuously imaging the patient during treatment delivery. There are different systems on the market or currently under development: the ViewRay (ViewRay, Cleveland, Ohio) "MRIdian™" system is currently the only one available clinically (Dempsey *et al.*, 2005; Mutic and Dempsey, 2014). It employs three Cobalt-60 sources and a 0.35 T MR scanner (Fig. 5.10). Other systems that are integrating MRI with a linear accelerator are under development (Hybrid MR-Linac, UMC, Utrecht, The Netherlands). One system implements a rotating MR (0.2 T)/Linac (Edmonton, Canada). The use of online magnetic resonance in the clinic has not yet been explored in depth, since it has been introduced in the clinic only recently (Mutic and Dempsey, 2014). Nevertheless, its potential capabilities as image guidance system are well-known: better soft-tissue contrast which will allow: (1) more accurate patient positioning of the anatomy to be irradiated, (2) online treatment plan adaptation to account for geometrical changes after the planning stage, and (3) fast planar imaging that

allows real time direct tumor and organ at risk tracking without need for surrogates or correlation models.

5.4 Radiation Dose from Image Guidance and Tracking

Repeated x-ray image guidance procedures have raised concerns over the additional radiation exposure to radiosensitive organs of radiotherapy patients, especially from kV-CBCT (Ding, 2010; Ding and Coffey, 2008; Jeng *et al.*, 2009; Perks *et al.*, 2008; Walters *et al.*, 2009). However, recent studies have shown that daily doses to soft tissues resulting from a modern kV-CBCT procedures (Ding, *et al.*, 2010) are now less than the dose resulting from conventional MV setup field imaging using an EPID (Ding, 2010; Ding *et al.*, 2008a; Murphy *et al.*, 2007; Vetterli *et al.*, 2004). The variation of organ dose among different patients can be predicted based on the patient geometry and the image procedure used. For head imaging, the results showed that the conventional EPID doses are 10 to 20 times higher than those for kV-CBCT. Doses from a pair of orthogonal MV images are 3 cGy to 4 cGy to the eyes, brain, and cord, while for a comparable or better image quality, the doses to these anatomic structures from a kV-CBCT Standard Head scan using a Varian On-Board Imager Version 1.4 are only 1 mGy to 2 mGy. For radiographic images, due to the low penetration of kV beams, the dose to the eyes is 0.01 mGy for a PA image where the eyes are near the beam exit and 1 mGy for an AP image where the eyes are near the beam entry.

The organ dose resulting from MV imaging can be calculated and accounted for in a current commercial radiotherapy TPS while more complicated methods like Monte Carlo techniques are necessary for patient dose calculations resulting from kV imaging. For a treatment regime of 30 fractions, daily MV portal imaging doses can amount to 0.2 Gy to 0.5 Gy to a patient. In situations, where the dose to organs from therapeutic beams has reached dose tolerance, ignoring these additional imaging doses can present significant risks, especially for pediatric patients. For kV image acquisitions including kV-CBCT and kV radiographs, it might be feasible to account for the imaging dose with an acceptable accuracy using tabulated values of organ dose based on the imaging acquisition parameters, imaged geometry and patient geometry.

5.5 IGRT and Management of Respiratory Motion

Lesions in the thorax and abdomen are affected by respiratory motion, and therefore special strategies have been adopted to take this into account (*i.e.*, tumor tracking, gating techniques, and breath-holding). The

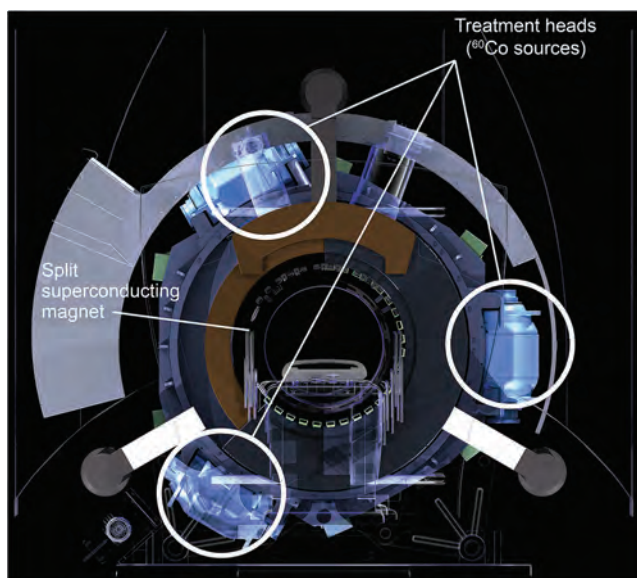


Figure 5.10. MRI-based ViewRay™ system (ViewRay, Inc.).

large movements involved for these types of lesions (Hof *et al.*, 2009) require the determination of the tumor position (in terms of both translations and rotations) at the time of planning and delivery. For every method employed, the respiratory motion management involves: (1) the capability of delineating the tumor on the image modality chosen (CT, CT-PET, and MR), by taking into account the entire respiration-induced motion of the tumor and eliminating the artifacts due to the motion; (2) the addition of appropriate margins to the CTV during planning, in order to take into account the intrafractional motion of the target and inter-fractional changes and setup errors; (3) delivery of the treatment according to the method assumed for the determination of the tumor position in the planning CT and other imaging modalities co-registered to the planning CT; and (4) monitoring of the tumor position and motion during the treatment. As described in AAPM TG-76 (AAPM, 2006), if the respiratory motion is not properly taken into account, it causes artifacts during image acquisition, leading to distortion of the target volume and incorrect positional and volumetric information. A blurred image of the target makes it difficult to delineate the boundaries and small mobile targets can be difficult to detect on the image. In the planning process, the addition of margins to account for the target motion, that are not based on the individual breathing pattern of the patient, can increase the volume of healthy tissues exposed to high doses. On the other hand, if the margins used are too small, the CTV might not receive adequate coverage. Radiation delivery in the presence of intrafraction organ motion causes an averaging or blurring of the dose distribution over the path of the motion. This displacement results in a difference between the intended and delivered dose distributions.

The assessment of respiratory motion should be performed for each patient prior to treatment, because general breathing patterns cannot be assumed for every patient. The tumor itself can be difficult, if not impossible, to observe on the image, and a surrogate such as external or internal markers, or an organ such as the diaphragm or the chest, must be used. In this case, the correlation between the displacement and phase of the surrogate and of the tumor cannot be assumed *a priori*.

5.5.1 Management of Respiratory Motion

The methods that have been developed to manage respiratory motion in radiotherapy are described in great detail in AAPM TG 76 (AAPM, 2006). They can be broadly separated into five major categories: motion-encompassing methods, breath-hold techniques, forced shallow-breathing techniques, respiratory-gating techniques, and respiration-synchronized techniques.

5.5.1.1 Motion-encompassing methods. These methods are recommended for radiotherapy facilities that do not have any system (*i.e.*, equipment) to manage respiratory motion and are helpful in defining an ITV. Since respiratory-induced tumor motion will be present during radiation delivery, it is important to estimate the mean position and range of motion during CT imaging. CT imaging techniques that can include the entire range of tumor motion for respiration (at the time of CT acquisition) are: slow CT, inhale and exhale breath-hold CT, and 4D or respiration-correlated CT. In the last-named method, since the tumor position is determined just before the treatment delivery, margins must be added to account for intrafraction variations of the mean target position as well as of patient setup. These margins must be evaluated individually by using, for example, a slow CBCT (Shah *et al.*, 2012). Moreover, since respiratory-induced tumor motion is affected by changes in the amplitude of breathing, hysteresis and baseline shifts (*i.e.*, variations in the mean position of the tumor relative to the vertebral bodies, from day to day), the margins determined before the treatment might be insufficient to adequately cover the CTV.

5.5.1.2 Breath-hold and forced shallow-breathing techniques. There are several methods of respiratory motion immobilization described in AAPM TG 76 (AAPM, 2006) based on breath-hold. Breath-hold can be achieved using deep-inspiration breath-hold (DIBH) based on spirometer-monitoring, or active breathing control (ABC) at moderate (*i.e.*, deep) inhale breath-hold (mDIBH). The latter is based on digital spirometry to measure the respiratory trace, which is in turn connected to a valve, and the mDIBH threshold is then set to approximately 75 % of the average inspiration capacity. Other types of breath-holding are the so-called “self-held breath-hold techniques”, where the patient voluntarily holds his/her breath at some point in the breathing cycle. The patient is given a hand-held switch that is connected to an interlock circuit, and depending on the state of the switch the therapist at the console is allowed to activate/deactivate the beam. Usually, a deep inhale phase is used for the beam on. This technique can be used in conjunction with a commercially available device (*e.g.*, Varian RPM), to monitor patient respiration and to control dose delivery. The patients have to voluntarily hold their breath during a specific part of the respiratory cycle while the radiation is continuously delivered during the breath-hold. The advantage of this technique is that the treatment time of the delivery is approximately half compared to a free-breathing (FB) respiratory-gating technique. Forced shallow breathing (FSB) makes

use of abdominal compression devices. The applied pressure to the abdomen reduces diaphragmatic excursions, while still permitting limited normal respiration.

The main drawbacks of breath-hold techniques are the reproducibility of the breath-hold, the ability of the patient to perform the type of breath-hold required (*i.e.*, deep or moderate inhale or exhale) and the use of equipment provided to control breathing. The selection of margins should take into account the variability and reproducibility of the breath-hold. Image guidance is recommended, to check the tumor excursion within the breath-hold period at each treatment fraction.

5.5.1.3 Respiratory-gating techniques. Respiratory gating involves the administration of radiation (during both imaging and treatment delivery) within a particular portion of the patient's breathing cycle, commonly referred to as the "gate". In principle, since imaging and treatment are synchronized with the patient's respiration cycle, there is potential for CTV–PTV margin reduction. In summary, gating can be achieved with external markers (*e.g.*, Varian RPM respiratory-gating system) or internal markers as surrogates of tumor motion. In the first case, the correlation with the internal position of the tumor must be verified and specified quality controls of the system must be performed. In the second case, the magnitude of marker motion detected by the system needs to be verified, and the automated tracking of the internal fiducial markers must be ensured to be robust (AAPM, 2006). Disadvantages of the technique are that they require a long duration both during acquisition of CT-gated images and gated treatment. These increase the potential to exacerbate breathing irregularity, and there is a possibility that the time-dependent internal target position will not correlate well with the tracked surrogate marker. Additionally, patients selected for gating are frequently those that have the most trouble with breathing, thereby complicating the implementation of the technique.

5.5.1.4 Respiration-synchronized free-breathing techniques. These techniques represent real-time tumor-tracking systems, such as the Synchrony™ tracking system of the CyberKnife®. There are different ways to locate the tumor during treatment: (1) real-time imaging of the tumor itself *via* (*e.g.*, fluoroscopy); (2) real-time imaging of artificial fiducial markers implanted in the tumor; (3) inference of the tumor position from surrogate breathing motion signals; and (4) nonradiographic tracking of an active or passive signaling device implanted in the tumor. This last-named modality of

tracking is based on implantable radiofrequency coils that can be tracked electromagnetically outside the patient (Balter *et al.*, 2003; 2005; Seiler *et al.*, 2000).

The first modality is useful only for lung tumors, which present well-defined boundaries in the images. More often, fiducial markers implanted in or nearby the tumor are needed. To obtain information about translations and rotations of the tumor, at least three fiducial markers must be implanted. This increases the risk of inducing a pneumothorax, compared to the implantation of only one fiducial.

To determine the motion of the tumor, continuous monitoring of fiducial position can be achieved by using dual fluoroscopes mounted orthogonally in the treatment room. This increases the dose to the patient from imaging. Therefore, to reduce the frequency of radiation images, some systems use a combination of radiographic imaging and continuous monitoring of an external signal associated with the breathing. In this case, the validity of the correlation between the external signal and the internal motion of the tumor must also be assessed. This is particularly true for case (3) above, when only external signals of breathing are used to infer the tumor position. It has been shown that a simple and fixed correlation between the external breathing and the internal tumor position is not a safe assumption (Ramsey *et al.*, 2000). Therefore, it is not enough to measure the correlation just at the beginning of the treatment, without further monitoring. On the contrary, a continuous monitoring of the correlation must be performed and updated during the entire treatment.

A common problem, which applies to both beam gating and real-time tracking systems, is the presence of a time delay in the adaptive response of a radiotherapy system to a tumor position signal. This requires that the tumor position be predicted, so that the beam can be synchronized to arrive at the actual position of the tumor once the adjustment has been made. Time series prediction by adaptive filters (Murphy *et al.*, 2002) have been used to correct for this system delay. The accuracy of these prediction algorithms must be verified, especially for patients who show very irregular breathing patterns. In this case, the nominal cyclic breathing can show significant fluctuations in displacement and frequency, and the prediction error can increase (Hoogeman *et al.*, 2009).

5.5.2 Image Guidance with Respiratory Motion

The delivery of a treatment to a tumor that moves with respiration is strongly dependent on how the respiratory motion is managed. The

techniques have been described extensively in AAPM TG 76 (AAPM, 2006) and briefly reported in AAPM TG 101 (Benedict *et al.*, 2010). They are essentially based on image and optical systems, or a combination of the two. They can be summarized as: (1) image-guided techniques, (2) optical tracking systems, and (3) hybrid systems, with in-room optical systems and kV imaging.

5.5.2.1 Image-guided techniques. The use of fluoroscopy-gated images for the specific issue of respiration-induced tumor motion has been described in Sections 5.5.1.3 and 5.5.1.4 as well as emerging technologies based on online MR (Section 5.3.2.3). For SBRT with traditional linear accelerators, image guidance of tumor motion can be achieved also with cone-beam imaging of soft tissue. With CBCT, it is possible to verify whether the target motion amplitude coincides with planned limits, just before the treatment. Cone-beam CT can have a long acquisition time (*i.e.*, 60 s or more), which allows for acquisition of the average position of the tumor over the breathing cycle. However, since respiratory organ motion often leads to artifacts in the reconstructed 3D images, 4D CBCT acquisition for a phase-correlated image reconstruction has been developed (Sonke *et al.*, 2005). This image guidance technique allows a more accurate representation of the motion of the tumor with respect to the average 4D CT scan and it reduces the inter-observer variability in the detection of tumor position (Sweeney *et al.*, 2012). Correction for artifacts generated by 4D images by motion compensation algorithms are currently under investigation. These corrections should improve the capability to visualize tumor margins and reduce blurring due to motion.

Improved image quality during treatment delivery is expected through the use of an online MR image system (Section 5.3.2.3) (Green *et al.*, 2013; Parikh *et al.*, 2012). Its better soft-tissue contrast allows for a more accurate patient positioning based on the true anatomy without the need of surrogates. Moreover, online treatment plan adaptation to account for geometrical changes relative to the planning stage will likely lead to better accuracy. Fast planar imaging allows real-time, direct tumor and organ at risk tracking without need for surrogates or correlation models.

5.5.2.2 Optical tracking systems. Optical tracking systems use stereoscopic infrared cameras (Bova *et al.*, 1997; Kubo *et al.*, 2000; Meeks *et al.*, 2005; Menke *et al.*, 1994; Rogus *et al.*, 1999; Wang *et al.*,

2001) or video photogrammetry (Bert *et al.*, 2005). These technologies are used to track 3D coordinates of points on the patient's skin. This is accomplished by using either active infrared light emitting diodes (IR-LEDs) or passive markers, attached to the patient's skin, reflecting the infrared light emitted from an external source, which is then detected by two stereoscopic infrared cameras. Alternatively, this tracking can be accomplished using video photogrammetry systems, which do not need markers attached to the skin. Both of these techniques can track patient breathing and positioning during the treatment, but they assume that the internal motion of the lesion is well-correlated with the external motion of the body (*i.e.*, thorax) of the patient.

5.5.2.3 Hybrid systems. These systems represent a combination of in-room optical systems and kV imaging. They detect changes in external markers that are correlated with internal tumor movements. An example is the CyberKnife® Synchrony (Accuray) system. It allows the tracking of the tumor during the entire delivery, with continuous adaptation of the beam during the delivery to the target coordinates (CyberKnife®) and adjustment of the robotic couch (ExacTrac). The latter approach has some limitations since the couch rotations do not cover all the possible degrees of rotation of the target. The assumption on which these techniques are based is that the correlation between external markers and internal fiducial movement is constant, which should be evaluated according to the type of breathing of the patient. The Vero (Brainlab/Mitsubishi) system has also been clinically installed to perform SBRT with image guidance (Depuydt *et al.*, 2011) and it can perform real-time tumor tracking (RTTT) of lesions moving with respiration. Clinical validation of the system has been reported (Depuydt *et al.*, 2013).

5.5.2.4 Delivery adaptation based on acquired information. Final considerations are about how the information obtained with the image guidance can be used to track the motion of the tumor. This can be performed with different technologies, some of which are still under development and are not yet available clinically. Without entering in the details of the technology, we can mention four types of tracking: (1) MLC tracking (Keall *et al.*, 2014), where the treatment beam is shifted dynamically to follow the tumor motion by continuously reshaping the MLC aperture, (2) couch tracking such as that used by ExacTrack, (3) beam tracking like CyberKnife and Vero, and (4) gating to turn beam on/off based when target is inside/outside predefined thresholds.

5.6 Uncertainties in Image Guidance of Radiation Therapy Using Small Fields

3D image guidance techniques provide the highest precision and accuracy in the localization of target and organs at risk prior to the irradiation. A real 3D correction of the patient positioning should be associated with 6 degrees of freedom of the couch or of the gantry to take into account all possible rotations of the patient/tumor. The approximations introduced by the system to reposition the patient and to verify the target localization should be evaluated in terms of uncertainties generated during the whole process.

Uncertainties in image-guided SBRT are of both geometrical and dosimetric nature. The components that contribute to the overall geometric error are: inter- and intra-observer variations in GTV-CTV delineation (Steenbakkers *et al.*, 2005); motion artifacts (*i.e.*, respiration and cardiac) in the CT scan, which are random in nature but cause systematic errors during delivery (Keall *et al.*, 2002; Rietzel *et al.*, 2005); respiratory motion and heartbeat during delivery, which are periodic functions of time; daily variations of respiratory motion; variations caused by changing organ volumes; tumor growth and shrinkage; treatment-related anatomical changes; patient setup error: typical overall uncertainties of 3–5 mm (1 SD) have been reported. This list of sources of uncertainty has been suggested in AAPM TG 76 (AAPM, 2006), which is mainly focused on management of respiratory motion in radiotherapy, but is applicable to all types of tumors that are susceptible to position changes that occur both interfraction and intrafraction.

It is important to understand the nature of potential errors in order to adopt the right strategy to correct for them. Methods have been proposed as to how to calculate appropriate margins (McKenzie *et al.*, 2002; Stroom and Heijmen, 2002; Stroom *et al.*, 1999; van Herk, 2004; van Herk, *et al.*, 2000) based on a separation between systematic and random errors. For example, pre-treatment imaging can lead to systematic errors, as described in AAPM TG 76 (AAPM, 2006), which cannot be eliminated by image guidance, and therefore the error must be included in the margin estimate. It is known that the choice of the margins is fundamental since an overly restrictive margin around the CTV can lead to a geographic miss and under-dosage; conversely, excessive margins can increase the toxicity of normal tissues, particularly in SRT where the goal is to deliver high doses to the target in few fractions.

The evaluation of the optimal margin is not trivial, but IGRT can help the physician in this estimation, since it provides a way to evaluate the potential

errors (both systematic and random) before the treatment. Moreover, if imaging is repeated at the end of the treatment, an evaluation of the residual error can be made. The latter evaluation confirms whether the adopted margins were sufficient to cover all the displacements of the patient and tumor position during the treatment. This procedure, however, increases the dose to the patient and should be used with caution. Moreover, imaging at the end of the treatment is representative of the last position of the tumor but not of random and sudden displacements during the treatment that can be quite prolonged in SRT.

Tumor volume changes during a course of radiotherapy can give rise to systematic delivery errors, which can be accounted for by adapting the plan, based on the information acquired with image guidance. Random errors (due, for example, to organ motion) cause blurring in the dose distribution. In conventional radiotherapy, the random nature of these errors result in a natural averaging over the many fractions. However, in SRT, where treatment is normally delivered in few fractions, the variation of the delivered dose compared to the planned dose results in an error that is unlikely to be recovered in the subsequent fractions by this averaging process. Therefore, in SRT it is recommended that random errors, as well as systematic errors, be taken into account at every fraction.

Evaluation of the geometrical errors for different anatomical sites has been performed, and several papers have been published on this topic (Astreinidou *et al.*, 2005; Burridge *et al.*, 2006; Maleike *et al.*, 2006; McGarry *et al.*, 2009; Meijer *et al.*, 2003; Murphy, 2009, *etc.*). These data are of interest to understand the best methodology to employ for the evaluation of these errors. However, it should be kept in mind that geometrical errors are patient and planning specific and thus margins cannot be automatically adopted from other centers. Moreover, in the assessment of these errors, one should also include the potential errors introduced by the IGRT technique implementation itself. It follows that the errors, and thus the margins, determined with a specific technique cannot be automatically extended to other patients for which another IGRT technique is used.

5.6.1 Examples of IGRT Accuracy and Uncertainties

5.6.1.1 Intra-observer variability.

Uncertainties due to intra-observer variability occur as a result of the registration step between reference image and images acquired with in-room IGRT systems. For example, random and systematic uncertainties have

been estimated in the use of an ultrasound probe since the pressure of the probe causes prostate displacement (Artignan *et al.*, 2004; Serago *et al.*, 2002). A second example is the result of the matching between CBCT and planning CT which depends on the observer and on the type of registration used (Masi *et al.*, 2008), (e.g., auto match on bony anatomy or manual match on soft tissue) or fiducial markers manual registration vs automatic gray-value alignment (Shi *et al.*, 2011).

5.6.1.2 Image-registration uncertainties.

Image fusion uncertainty can be due to potential patient body deformation between simulation and treatment and to the choice of type of image registration. The spine, for example, is a somewhat flexible structure and its curvature can be different at the time of simulation and treatment. The accuracy of the algorithm used for registering the planning-reference image to the live image should be determined (Jin *et al.*, 2008b). Moreover, the choice of the region of interest (ROI) for image registration and fusion has an impact on the final uncertainty. During spine image guidance the choice of the area around the involved vertebra influences the result of the fusion (Kim *et al.*, 2009) and the uncertainty increases when spinal curvature differences are more pronounced, *i.e.*, it is larger for cervical-upper thoracic lesions (e.g., T2) than for other anatomic parts (e.g., L3 lesions) (Jin *et al.*, 2008b). An example of a poor image fusion method is the use of bony landmarks for a soft-tissue target (e.g., due to the respiration or to organ filling, see Fig. 5.11).

Baseline shifts of a tumor in the lung are not taken into account by doing an alignment on bony anatomy. As illustrated in Fig. 5.12, mean tumor position errors from 3 mm to 7 mm relative to bony anatomy have been observed (Guckenberger *et al.*, 2006; Masi *et al.*, 2008; Purdie *et al.*, 2007; Sonke *et al.*, 2008; 2009; Sweeney *et al.*, 2012).

Automated image registration may potentially fuse the wrong vertebral bodies together in regions of the spine, where the bodies are similar in shape

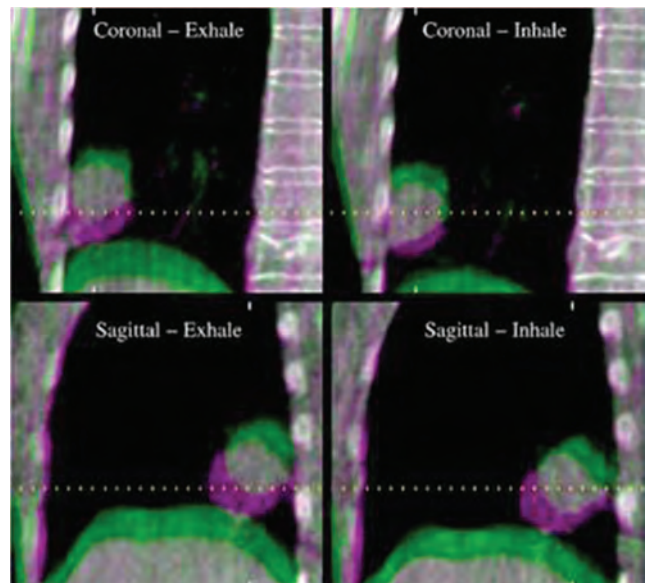


Figure 5.11. 4D CBCT acquired on different days, two phases are shown (left side: exhale; right side: inhale). Alignment was performed on the bony anatomy: the differences of tumor positions relative to the vertebral bodies are appreciable and consistent between the different respiratory phases (Sonke *et al.*, 2008).

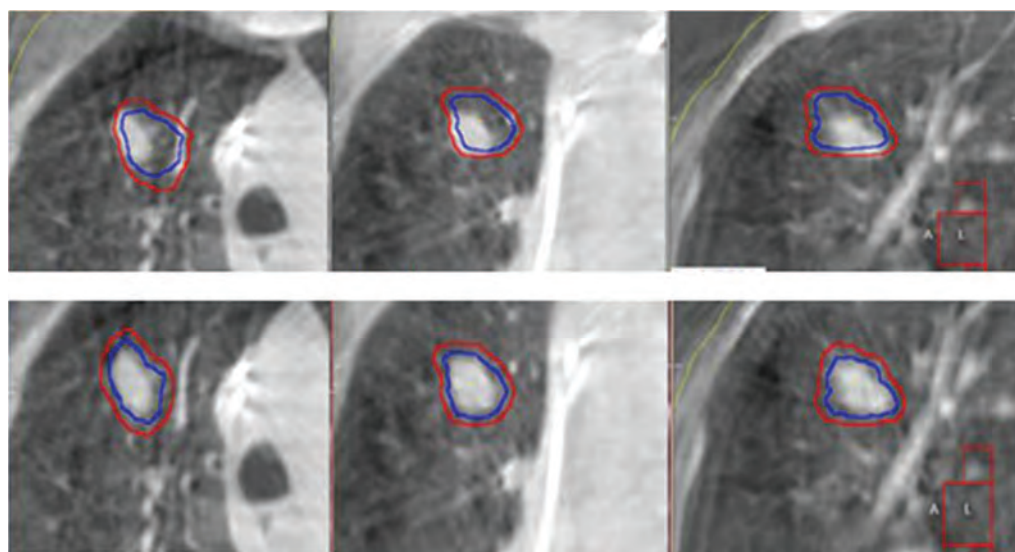


Figure 5.12. Planning ITV contours on a 3D CBCT after alignment on the bony anatomy (upper row), and after tumor alignment on the CBCT (Masi *et al.*, 2008).

(Boswell *et al.*, 2006). This would result in a suspiciously large longitudinal shift that a therapist should be alert for. Automated image registration should always be followed by close inspection of the results by the therapist and manual shifts applied if necessary.

5.6.1.3 Inadequacy of surrogates for tumor position. Examples of uncertainties are: the use of external markers on the chest of the patient, which are not always representative of the internal motion of the tumor; implanted fiducial markers affected by migration or displacement (due to migration and tumor volume changes), nonsynchronous tumor and marker motion, some difficulty in detecting the fiducial markers during planning and during treatment; the use of a surrogate, such as diaphragm as a surrogate of a tumor in the lung or of the whole liver for liver lesions. As an example, migration of markers has been extensively studied. Van der Voort van Zyp *et al.* (2011) recorded the migration of 111 markers in 42 patients with 44 pulmonary tumors. A median marker displacement of 1.3 mm (0.1 mm to 53.6 mm) was found (see Fig. 5.13).

Marker displacement exceeded 5 mm in 12 % of markers and 10 mm in 5 % of markers. Causes of marker displacement >5 mm were marker migration (2/13) and target volume changes (5/13). Nonsynchronous tumor and marker movement during breathing can be responsible for displacements >5 mm in the other 6/13 markers. Imura *et al.* (2005) reported the fixation rate of 1.5 mm gold markers after bronchoscopic placement in 57 patients with peripheral lung cancer. Only 122 of the 154 implanted markers (79 %) could be detected at treatment planning. The rate of marker fixation was higher for peripheral tumors than for central tumors. Imura *et al.* (2005) also studied the

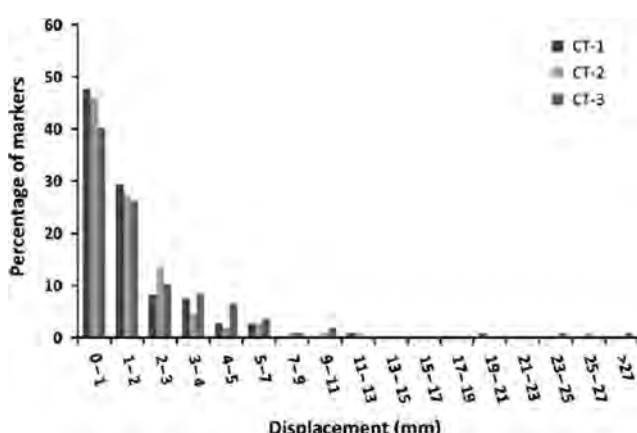
displacement of markers during treatment in 11 of the 57 patients. The change in distance between markers was ≤ 2.0 mm in 95 % of cases. However, the analysis did not include those patients in whom a marker migrated after treatment planning (7/122 markers, 6 %). Kupelian *et al.* (2007) used a 2.0 cm-long marker placed in lung tumors *via* the percutaneous intrapulmonary approach ($n = 15$ markers) or the bronchoscopic approach ($n = 8$ markers). The average displacement of the 2.0 cm-long marker was 2.6 mm. The maximum displacement was 5.4 mm. The authors stated that marker displacements >5.4 mm were probably not observed because the 2.0 cm-long marker is more likely than smaller markers to get wedged in the lung.

With regard to the correlation between internal and external markers, for RTTT systems, such as CyberKnife®, Vero, and ExacTrac™, errors can be generated due to the correlation model, which relates the internal target motion with the external breathing motion. Hoogeman *et al.* (2009) quantified the errors in the correlation model and the uncertainty in the prediction method of the CyberKnife®. Data on 44 lung cancer patients treated with tumor tracking were analyzed. Figure 5.14 (Hoogeman *et al.*, 2009) shows the different capability of three prediction methods to the changing in the breathing pattern of patients. The prediction error is found to increase with respiratory motion amplitude. Moreover, the correlation between external and internal markers can be jeopardized by phase changes in the two signals and by baseline shifts. For all the patients studied, the mean correlation model errors were <0.3 mm demonstrating that a reasonable correlation between external and internal markers can be achieved when frequent checks and update of the correlation model is performed during the treatment.

Another type of uncertainty is the deformation of the body and the organs relative to the center of implanted fiducial markers. To account for this type of error, an additional margin should be considered (Lu *et al.*, 2008).

5.6.2 Evaluation of the Total System Accuracy and Uncertainty

In order to evaluate the overall accuracy of the system, end-to-end tests are performed on phantoms (Muacevic *et al.*, 2006; Yu *et al.*, 2004). These tests are used to evaluate the total system uncertainty (*i.e.*, mechanical, imaging and registration or fusion uncertainty). Several papers have been published that report the geometrical total system uncertainty for equipment capable of image guidance (Antypas and Pantelis, 2008; Boswell *et al.*,



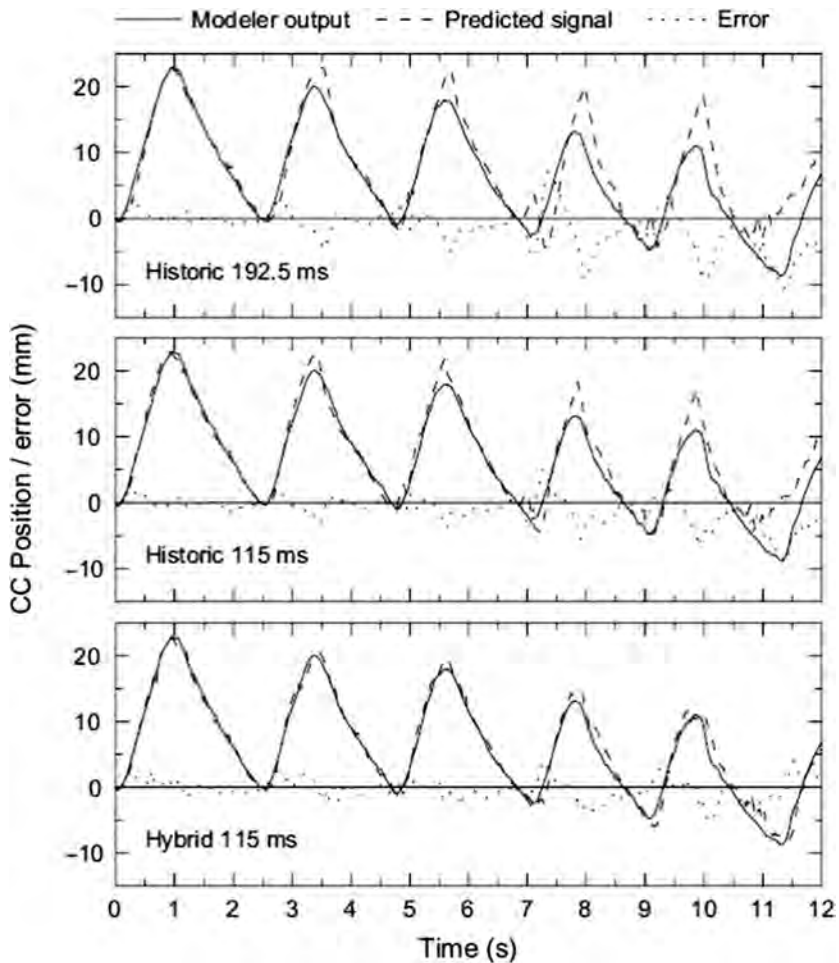


Figure 5.14. Breathing signal (solid line), predicted breathing signal (dashed line), and error of prediction (dotted line) for three prediction methods. The first cycle is predicted accurately by the three methods, but as soon as the amplitude, period and baseline change, the three models give different results: the first model (Historic with 192.5 ms time lag) fails to predict the pattern, the second with a shorter time lag (Historic with 115 ms) is slightly better and the third hybrid method (115 ms) was able to account accurately for the changing breathing pattern (Hoogeman *et al.*, 2009).

2006; Depuydt *et al.*, 2011; Desai *et al.*, 2006; Hacker *et al.*, 2006; Hyde *et al.*, 2012; Jin *et al.*, 2008b; Kilby *et al.*, 2010; Sharpe *et al.*, 2006; Verellen *et al.*, 2003). The values vary between about 0.5 mm and 2 mm (with their associated SDs) for a 3D vector. Rotation errors are usually $<1^\circ$.

In Table 5.1, the geometric residual errors on phantom tests values for some of the systems featuring image guidance are reported.

The geometric accuracy of the VERO system has been reported to be of the order of 0.54 mm calculated as the 90 % percentile with an SD of 0.2 mm in the pan direction and 0.22 mm in the tilt direction of the gimbals (Depuydt *et al.*, 2011) by simulating a 1D and 2D breathing movement.

As underlined in the AAPM TG 101 report, the geometrical errors measured on phantom tests are related to ideal conditions, where the experiment is under a controlled and reproducible situation. The

actual patient targeting accuracy is affected by unexpected changes due to patient movement, anatomical variations and decreased image quality resulting from patient anatomy.

A post-treatment analysis of the correspondence between the actual (*i.e.*, mean) position of the target during treatment and the position defined with the IGRT system can be a useful tool to measure the real accuracy of the geometrical localization of the system. It has been shown (Hoogeman *et al.*, 2009) that the intrafraction standard uncertainty of the prediction and correlation model increases as a function of the respiration motion amplitude for the CyberKnife® Synchrony® RTTT system, and varies between 0.2 mm and 2.5 mm, even if the total geometrical accuracy of the system obtained with end-to-end tests is much better (Kilby *et al.*, 2010).

Image-guided radiation therapy devices introduce hardware and software uncertainties in the process

Table 5.1. Geometric residual errors of current commercial IGRT systems

IGRT system	IGRT geometric residual errors on phantom tests
Novalis	Total residual average error: $\leq 1.5 \text{ mm} \pm 0.7 \text{ mm}$ (Hacker <i>et al.</i> , 2006)
ExacTrac	$0.56 \text{ mm} \pm 0.7 \text{ mm}$ (Jin <i>et al.</i> , 2008b) $0.6 \text{ mm} \pm 0.9 \text{ mm}$ (Verellen <i>et al.</i> , 2003)
CyberKnife	Maximum error: $0.56 \text{ mm} \pm 0.7 \text{ mm}$ (Antypas and Pantelis, 2008) $0.8 \text{ mm} \pm 0.05 \text{ mm}$ (Desai <i>et al.</i> , 2006) $0.4 \text{ mm} \pm 0.1 \text{ mm}$ Skull tracking; $0.5 \text{ mm} \pm 0.2 \text{ mm}$ Spine tracking; $0.3 \text{ mm} \pm 0.1 \text{ mm}$ Fiducial tracking; (Kilby <i>et al.</i> , 2010).
CBCT	$<1.4 \text{ mm}$ translations and $< 0.7^\circ$ rotations at 95 % confidence interval level (Hyde <i>et al.</i> , 2012) $1-1.5 \text{ mm}$ 95 % confidence interval level (Sharpe <i>et al.</i> , 2006)
TomoTherapy	$\pm 1 \text{ mm}$ (Fenwick <i>et al.</i> , 2004) 1 mm (Boswell <i>et al.</i> , 2006)
VERO	$0.54 \text{ mm} \pm 0.2 \text{ mm}$ (Depuydt <i>et al.</i> , 2011)

of localization of the target (Letourneau *et al.*, 2005). Therefore, it would be important to assess the accuracy of such systems before using them to make corrective actions in the patient treatment.

Unfortunately, there are some types of uncertainty that are difficult to quantify. In fact, while the geometrical accuracy of a system can be assessed with appropriate tests made on phantoms (see Section 5.7) and its stability can be checked with an established quality assurance program, software uncertainties are not easily quantifiable. It is difficult to evaluate the accuracy of the registration (*i.e.*, fusion) algorithms between planning-reference image and live image, due to the fact that the images of a patient obtained with these systems are usually of poor quality and subject to artifacts. Therefore, tests on phantoms only provide a partial evaluation of the accuracy of the image-registration procedure.

5.7 Quality Assurance for Image Guidance for SRT

In SRT, the need for high accuracy requires special considerations in the design of the QA program. In particular, since image guidance has a great impact on the accuracy of target localization both at the pre-treatment step and during treatment for moving targets, a continuous and dedicated QA program must be established to avoid systematic errors. In IGRT systems, these arise from: (1) misalignment between imaging isocenter and delivery isocenter and (2) differences in the procedure of localization (*i.e.*, delineation) of the target in the planning CT and in the treatment rooms (tumor is visible or surrogates are used). For tumors moving with respiratory

motion, QA procedures must address two fundamental sources of potential error in dose delivery: (1) determination of the tumor position as a function of time and (2) calibration of the spatial relationship between the tracking coordinate system and the beam-delivery coordinate system.

Several task group reports have been published that provide useful recommendations and guidelines for QA procedures in IGRT systems. For SRT, useful recommendations and references can be found in AAPM TG 101 (AAPM, 1993; Benedict *et al.* 2010; Kutcher *et al.*, 1994; Och *et al.*, 1992) for imaging equipment and in the supplement published in the *International Journal of Radiation Oncology Biology Physics* (vol. 71, S1–S214, 2008), which suggests a set of annual, monthly, and daily QA activities and tolerances for various IGRT systems (summarized in Table V of AAPM TG 101, Benedict *et al.* 2010). For kV x-ray imaging employed for patient setup and target localization, the AAPM TG 104 report was published in 2009 (AAPM, 2009), while for CT-based IGRT technologies, a report (AAPM TG 179) was published in 2012 (Bissonnette *et al.*, 2012).

AAPM TG 104 reports on in-room kV imaging systems that belong to the following categories: rail-tracked-mounted systems, ceiling/floor-mounted systems and gantry-mounted systems. For these systems, general guidance for appropriate acceptance testing and QA is provided. The AAPM Report TG 179 provides recommendations for quality assurance protocols for CT-based imaging systems including MV beams employed for imaging. The IGRT systems described there are: kilovolt and megavolt cone-beam CT, fan-beam MVCT, and CT on rails. For fan-beam MVCT, the specific report of AAPM TG 148 (Langen *et al.*, 2010) remains a reference source of information. In the report of AAPM TG 179, it is recommended that for technologies where the isocenter of the system does not coincide with the isocenter of the linac (*i.e.*, kV-CBCT, MV-CBCT, and CT on rails), the spatial relationship between the two isocenters (*i.e.*, geometric calibration of the system) must be considered carefully, together with a periodic assessment of this calibration. A daily check of the geometric calibration is suggested. The tolerance specification of the spatial calibration is within $\pm 2 \text{ mm}$ for kV-CBCT, which is considered acceptable also for SRT. CT-on rails has shown to give a better agreement between CT isocenter and treatment isocenter, within $\pm 1 \text{ mm}$ (Bissonnette *et al.*, 2012). For MV-CBCT, EPID positioning errors with respect to the linac isocenter should not exceed 1 mm in the horizontal plane. Also in this case, a daily check is recommended, while residual alignments must be recalibrated and

checked every 6 months. Image quality is an important feature of an IGRT system and quality control should be performed to assess the stability of the parameters used to quantify image quality. Compared to conventional multi-slice CT scanners, the image quality of CT-based IGRT systems is lower. Therefore, it is not possible to apply the same evaluation criteria. Nevertheless, the same types of parameters are used to evaluate image quality: scale and distance accuracy, low contrast resolution, spatial resolution, uniformity and noise, accuracy of Hounsfield Units. This last-named parameter becomes important only if IGRT scans are used for dose calculations (Bissonnette *et al.*, 2012). In general, image quality should be measured during the commissioning process and baselines should be built at the acceptance tests, which should be used subsequently to detect any deterioration of the image system. The parameters that define image quality can affect image-registration accuracy, and therefore the performance of the system must be controlled. However, these parameters have been shown to remain relatively unchanged with time (Bissonnette *et al.*, 2008; Gayou *et al.*, 2007; Saw *et al.*, 2007; Yoo *et al.*, 2006). AAPM TG 179 emphasizes that image-registration methods have an impact on IGRT systems in a way that is currently difficult to assess (Bissonnette *et al.*, 2012). In fact, protocols for patient-specific image registration and fusion software acceptance testing and quality assurance are not currently established. Nevertheless, there are several factors in the image-registration process that should be taken into account in the evaluation of the accuracy of this step: from the

compromise made in deciding what structures will be better aligned (*i.e.*, bony anatomy versus soft-tissue or vice-versa) to the selection of the method of correction after a registration result (often only translational movements of the couch are allowed and not rotations). Moreover, soft-tissue contrast is often poor in CT-based images and the selection of the image-registration algorithm must be evaluated according to the clinical case. A visual inspection of the final registration and manual adjustment by a qualified expert is always recommended. Another important issue, which will become increasingly important, is the use of nonrigid registration algorithms, which should better take into account moving or deforming anatomy. For these types of algorithms, tests should be developed to determine their accuracy. The AAPM report on clinical implementation of deformable registration algorithms (AAPM TG 132, Brock *et al.*, 2017), provides useful guidelines and recommendations on how to perform quantitative validation and commissioning of this type of software.

It has been mentioned before that portal imaging has been widely used for verification of patient setup and position of target and organs at risk. AAPM TG 58 (Herman *et al.*, 2001) provides guidelines for quality assurance of EPIDs. For SRT, the use of 2D portal image systems is not recommended, unless it is combined with software or with a stereoscopic method that provides some level of 3D information on the target coordinates.

For the nonisocentric CyberKnife system, AAPM TG 135 provides a set of quality controls specific to this system.

6. Quality Assurance

6.1 Introduction

A comprehensive quality assurance (QA) program should aim to ensure the safest and highest achievable accuracy of radiation treatment by establishing a systematic approach in setting up and in maintaining the program. The goal of QA is to reduce the uncertainty in SRT treatment and to set an error tolerance limit for SRT treatment.

The overall uncertainty of an SRT system is the combination of uncertainties resulting from several components, which mainly consist of uncertainties in the:

- target location;
- dosimetry in the treatment-planning system (TPS);
- radiation treatment delivery system;
- image-guidance system.

Uncertainties associated with the target location are contributed by image quality, system resolution, patient-dependent motion artifacts, contrast concentration and uptake, contouring subjectivity as well as image registration accuracy between different images acquired with different image modalities, such as computed tomography (CT), magnetic resonance imaging (MRI), and Positron emission tomography (PET).

Uncertainties associated with the dosimetry in the TPS consist of absorbed dose calculation algorithm uncertainties, planning system commissioning uncertainties resulting from absorbed dose calibration and relative dose measurement uncertainties, DVH calculation algorithm uncertainty, *etc.*

Uncertainties in the radiation dose delivery system consist of machine therapeutic dose delivery-related uncertainties, which depend on the accuracy of beam radiation output stability, mechanical radiation isocenter, and how well it delivers the radiation based on the treatment plan when the radiation beams are intensity modulated.

Uncertainties in the image-guidance system are related to patient positioning uncertainties, which are contributed by the uncertainties in the imaging system isocenter calibration and patient immobilization.

Inaccuracy in any of the components will lead to inaccuracy of the SRT treatment. An institution embarking on radiation medicine using small beams should establish a comprehensive QA program to minimize the uncertainties in each of the components. The QA program ensures that the prescribed dose distribution is delivered to the intended target within the stated uncertainties and its success requires the involvement of the entire radiation therapy professional team. For SRT treatments, execution of this mandate requires an extraordinary amount of vigilance. To establish such a complex and delicate procedure at a new site, it is advisable to form a specialized and dedicated team. This team, consisting of radiation oncologists, physicists and therapists, should have an open line of communication with the manufacturer, whose role as partner is to provide technical expertise to the customer and to put the new site in contact with expertise gained from introducing the technology at other sites.

Clinical implementation of a QA program depends on the details of the treatment unit, additional beam defining accessories, the selected beam-delivery technique, beam dosimetry, treatment planning, image-guidance devices, etc. In general, QA procedures will be specific to the particular equipment and to the implemented technology. It is important that an institution that starts a new small beam therapy program has access, through the manufacturer, to dosimetric data of users of the same equipment. The institution should also obtain independent checks of the beam output from other established institutions or, preferably, perform end-to-end checks through independent available external audit services, before the first patient treatment begins.

Commissioning and validation of small beam delivery and TPSs include machine-specific beam-data acquisition, data entry into the TPS, configuration of each beam, validation of the calculations, development of operational procedures and constancy checks, as well as training of all staff concerned with the operation of the treatment system. The measurements described below follow the QA requirements for different classes of radiation equipment.

6.2 QA of SRT Machines

Due to the differences in the radiation delivery devices, as well as how beams are shaped, the QA procedures are tailored to fit different SRT machine types which are addressed in the following.

6.2.1 QA of Linear Accelerators Adapted for SRT

Linear accelerators adapted for SRT are non-dedicated systems consisting of a conventional radiation therapy linear accelerator adapted for stereotactic procedures by using beam limiting devices introduced as additional tertiary accessories such as specialized add-on circular collimators attached to an accessory tray as well as a micro-multileaf collimator (Ding *et al.*, 2006, 2008b, Solberg *et al.*, 2001).

Cones define divergent circular fields with diameters typically varying from 4 mm to 30 mm. It has been reported (Bogdanich and Rebelo, 2010; IAEA Report Series 17, 2000b) that there are significant (possibly catastrophic) radiation leakages when the secondary collimator jaw field sizes extend outside the shielded area of the SRS cone accessory device. Any implementation of new equipment or technique must be subjected to a complete closed-loop validation. This can be achieved by using radiographs that cover a large enough area to detect any potential leakage radiation.

In addition to general QA recommendations for medical accelerators, which have been described in AAPM TG-142 (Klein *et al.*, 2009), there are added requirements on the performance of linear accelerators in terms of accuracy and precision when these systems are adapted to perform SRT procedures. These requirements include tighter tolerance on accelerator mechanical accuracy and the accuracy of image-guidance devices. The dosimetric uncertainty and spatial uncertainty of small fields should be tested. An end-to-end closed-loop system test is recommended to avoid the systematic errors that may exist in the beam calibration, beam configuration in planning system, and dose calculation algorithm used in the planning system. Daily accuracy tests for the consistency between the beam isocenter and imaging isocenter of an image-guidance device should be performed.

Since SRS is delivered with only a few fractions, it is beneficial to develop a checklist to be used for each SRS treatment before a patient is treated. The checklist should include different check boxes for a therapist, a physicist, and a physician. These check boxes might include: isocenter selection, cone size and jaw size if a cone is used, the contour of the maximum MLC leaf opening for a modulated treatment

field, etc. The checklist is usually appropriate only to the specific treatment equipment. Developing a checklist requires input and team effort of dedicated, trained professionals.

Patient-specific QA checks typically include validation of the planned dose distributions in a phantom, validation of modulated photon fluence using a portal imaging system, point-dose measurement, and independent monitor unit (MU) validations using MU check software.

Since image guidance is commonly used for patient positioning, it is essential that the spatial accuracy of the image-guidance device be verified on a daily basis (or before the treatment) and documented. The spatial tolerance of the patient position before each beam delivery, based on the result of image registration between planned image and acquired image, should be specified depending on the treatment target and location (typically <1 mm and <1 degree of rotation). When the couch position is modified as a result of the image-guidance procedure, it is essential that the patient position be re-verified before the radiation is delivered. Figure 6.1 shows an example of a checklist that should be completed before delivery of each target treatment. It has been shown that with an appropriate QA program (for both dosimetry and image-guidance device) in place, accurate dose delivery is achievable with high precision when a linear accelerator-based frameless system is used (see Section 5).

6.2.2 QA of Gamma Stereotactic Radiosurgery System

Quality assurance for Gamma Stereotactic units has been discussed by a number of authors since the installation of the first commercial Gamma Knife™ in 1987 (Drzymala *et al.*, 1994; Goetsch, 2008; Larson *et al.*, 1993; Maitz *et al.*, 1995; Schell and Wu, 1995). AAPM Report 54 (Schell *et al.*, 1995) gave guidance for the Leksell Gamma Knife™ Model U, which was in widespread use at that time. Subsequent publications have dealt with innovations that have increased the complexity and capability of static GSR units (Goetsch, 2002b; Yu *et al.*, 2000). Rotating GSR units were first described in 1999 by Goetsch and by Kubo and Araki (Goetsch *et al.*, 1999; Kubo and Araki, 2002). AAPM Task Group 178 was formed in 2008 and charged with writing a protocol on GSR dosimetry and QA.

Elekta Instruments has added the Extend™ system for relocatable treatments of Gamma Knife™ Perfexion patients. The system utilizes a vacuum-stabilized biteblock system for repeated placement with submillimeter accuracy. A cone beam CT

QUALITY ASSURANCE

Center for Radiation Oncology Frameless Radiosurgery Checklist	Patient Name: MR#: xxxxxxxx DOB: dd/mm/YYYY																																																																																																			
<table border="1" style="width: 100%; border-collapse: collapse;"> <tr> <td style="width: 10%; padding: 2px;">Date of Service</td> <td style="width: 15%; padding: 2px;">8/13/2014</td> <td style="width: 10%; padding: 2px;">Treatment Site:</td> <td style="width: 10%; padding: 2px;">Choose</td> <td style="width: 10%; padding: 2px;">Isocenter:</td> <td style="width: 10%; padding: 2px;"></td> <td style="width: 10%; padding: 2px;"></td> <td style="width: 10%; padding: 2px;">Fraction# :</td> <td style="width: 10%; padding: 2px;">of</td> </tr> </table>		Date of Service	8/13/2014	Treatment Site:	Choose	Isocenter:			Fraction# :	of																																																																																										
Date of Service	8/13/2014	Treatment Site:	Choose	Isocenter:			Fraction# :	of																																																																																												
<table border="1" style="width: 100%; border-collapse: collapse;"> <tr> <td colspan="9" style="padding: 2px;">Therapist: Initials of person verifying checklist contents</td> </tr> <tr> <td colspan="9" style="padding: 2px; text-align: center;">1. Signed patient consent</td> <td style="width: 10%; text-align: center;">Pick Drop Down</td> </tr> <tr> <td colspan="9" style="padding: 2px; text-align: center;">2. Signature on prescription form</td> <td style="width: 10%; text-align: center;">Pick Drop Down</td> </tr> <tr> <td colspan="9" style="padding: 2px; text-align: center;">3. Before Setup PT: Cone Size Choose</td> <td style="width: 10%; text-align: center;">Pick Drop Down</td> </tr> <tr> <td colspan="9" style="padding: 2px; text-align: center;">4. Seat belts</td> <td style="width: 10%; text-align: center;">Pick Drop Down</td> </tr> <tr> <td colspan="9" style="padding: 2px; text-align: center;">5. Validation of patient placement in treatment position</td> <td style="width: 10%; text-align: center;">Pick Drop Down</td> </tr> <tr> <td colspan="9" style="padding: 2px; text-align: center;">6. Confirm isocenter between ExacTrac and Varian RT</td> <td style="width: 10%; text-align: center;">Pick Drop Down</td> </tr> <tr> <td colspan="9" style="padding: 2px; text-align: center;">7. Verify isocenter coordinates in ExacTrac</td> <td style="width: 10%; text-align: center;">Pick Drop Down</td> </tr> <tr> <td colspan="9" style="padding: 2px; text-align: center;">8. Medication Prior to treatment</td> <td style="width: 10%; text-align: center;">Pick Drop Down</td> </tr> <tr> <td colspan="9" style="padding: 2px; text-align: center;">9. Comments:</td> <td style="width: 10%; text-align: center;"></td> </tr> </table>		Therapist: Initials of person verifying checklist contents									1. Signed patient consent									Pick Drop Down	2. Signature on prescription form									Pick Drop Down	3. Before Setup PT: Cone Size Choose									Pick Drop Down	4. Seat belts									Pick Drop Down	5. Validation of patient placement in treatment position									Pick Drop Down	6. Confirm isocenter between ExacTrac and Varian RT									Pick Drop Down	7. Verify isocenter coordinates in ExacTrac									Pick Drop Down	8. Medication Prior to treatment									Pick Drop Down	9. Comments:									
Therapist: Initials of person verifying checklist contents																																																																																																				
1. Signed patient consent									Pick Drop Down																																																																																											
2. Signature on prescription form									Pick Drop Down																																																																																											
3. Before Setup PT: Cone Size Choose									Pick Drop Down																																																																																											
4. Seat belts									Pick Drop Down																																																																																											
5. Validation of patient placement in treatment position									Pick Drop Down																																																																																											
6. Confirm isocenter between ExacTrac and Varian RT									Pick Drop Down																																																																																											
7. Verify isocenter coordinates in ExacTrac									Pick Drop Down																																																																																											
8. Medication Prior to treatment									Pick Drop Down																																																																																											
9. Comments:																																																																																																				
<table border="1" style="width: 100%; border-collapse: collapse;"> <tr> <td colspan="9" style="padding: 2px;">Physicist: Initials of person verifying checklist contents</td> </tr> <tr> <td colspan="9" style="padding: 2px; text-align: center;">1. Before setup PT: Collisions and CIA O's for MLC</td> <td style="width: 10%; text-align: center;">Pick Drop Down</td> </tr> <tr> <td colspan="9" style="padding: 2px; text-align: center;">2. Cone mount and Gantry Field Size ($5 \times 5 \text{ cm}^2$)</td> <td style="width: 10%; text-align: center;">Pick Drop Down</td> </tr> <tr> <td colspan="9" style="padding: 2px; text-align: center;">3. Isocenter selection</td> <td style="width: 10%; text-align: center;">Pick Drop Down</td> </tr> <tr> <td colspan="9" style="padding: 2px; text-align: center;">4. Cone size Choose</td> <td style="width: 10%; text-align: center;">Pick Drop Down</td> </tr> <tr> <td colspan="9" style="padding: 2px; text-align: center;">5. Dynamic Conformal Arc</td> <td style="width: 10%; text-align: center;">Pick Drop Down</td> </tr> <tr> <td colspan="9" style="padding: 2px; text-align: center;">6. IMRT</td> <td style="width: 10%; text-align: center;">Pick Drop Down</td> </tr> <tr> <td colspan="9" style="padding: 2px; text-align: center;">7. Isocenter position on positioning BOX</td> <td style="width: 10%; text-align: center;">Pick Drop Down</td> </tr> <tr> <td colspan="9" style="padding: 2px; text-align: center;">8. Comments:</td> <td style="width: 10%; text-align: center;"></td> </tr> </table>		Physicist: Initials of person verifying checklist contents									1. Before setup PT: Collisions and CIA O's for MLC									Pick Drop Down	2. Cone mount and Gantry Field Size ($5 \times 5 \text{ cm}^2$)									Pick Drop Down	3. Isocenter selection									Pick Drop Down	4. Cone size Choose									Pick Drop Down	5. Dynamic Conformal Arc									Pick Drop Down	6. IMRT									Pick Drop Down	7. Isocenter position on positioning BOX									Pick Drop Down	8. Comments:																			
Physicist: Initials of person verifying checklist contents																																																																																																				
1. Before setup PT: Collisions and CIA O's for MLC									Pick Drop Down																																																																																											
2. Cone mount and Gantry Field Size ($5 \times 5 \text{ cm}^2$)									Pick Drop Down																																																																																											
3. Isocenter selection									Pick Drop Down																																																																																											
4. Cone size Choose									Pick Drop Down																																																																																											
5. Dynamic Conformal Arc									Pick Drop Down																																																																																											
6. IMRT									Pick Drop Down																																																																																											
7. Isocenter position on positioning BOX									Pick Drop Down																																																																																											
8. Comments:																																																																																																				
<table border="1" style="width: 100%; border-collapse: collapse;"> <tr> <td colspan="9" style="padding: 2px;">Physician: Initials of person verifying checklist contents</td> </tr> <tr> <td colspan="9" style="padding: 2px; text-align: center;">1. Signature on forms and printout</td> <td style="width: 10%; text-align: center;">Pick Drop Down</td> </tr> <tr> <td colspan="9" style="padding: 2px; text-align: center;">2. Cone Size Choose and Gantry Field Size ($5 \times 5 \text{ cm}^2$) checks</td> <td style="width: 10%; text-align: center;">Pick Drop Down</td> </tr> <tr> <td colspan="9" style="padding: 2px; text-align: center;">3. Isocenter selection and position</td> <td style="width: 10%; text-align: center;">Pick Drop Down</td> </tr> <tr> <td colspan="9" style="padding: 2px; text-align: center;">4. Review Physics QA</td> <td style="width: 10%; text-align: center;">Pick Drop Down</td> </tr> <tr> <td colspan="9" style="padding: 2px; text-align: center;">5. Medication Prior to treatment</td> <td style="width: 10%; text-align: center;">Pick Drop Down</td> </tr> <tr> <td colspan="9" style="padding: 2px; text-align: center;">6. Comments:</td> <td style="width: 10%; text-align: center;"></td> </tr> </table>		Physician: Initials of person verifying checklist contents									1. Signature on forms and printout									Pick Drop Down	2. Cone Size Choose and Gantry Field Size ($5 \times 5 \text{ cm}^2$) checks									Pick Drop Down	3. Isocenter selection and position									Pick Drop Down	4. Review Physics QA									Pick Drop Down	5. Medication Prior to treatment									Pick Drop Down	6. Comments:																																							
Physician: Initials of person verifying checklist contents																																																																																																				
1. Signature on forms and printout									Pick Drop Down																																																																																											
2. Cone Size Choose and Gantry Field Size ($5 \times 5 \text{ cm}^2$) checks									Pick Drop Down																																																																																											
3. Isocenter selection and position									Pick Drop Down																																																																																											
4. Review Physics QA									Pick Drop Down																																																																																											
5. Medication Prior to treatment									Pick Drop Down																																																																																											
6. Comments:																																																																																																				
Physicist: <Signed By> Date: <Signed date/time>		Physician: <Approved By> Date: <Approved date/time>																																																																																																		

Figure 6.1. Sample SRT delivery process checklist emphasizing the involvement and responsibility of different professionals in the steps toward safe SRT delivery.

accessory is available commercially. The Gamma Knife, in common with similar rotating gamma stereotactic radiosurgery (GSR) systems, has changed greatly over the years. The manual treatment mode, with the treatment staff responsible for setting and checking coordinates to the nearest tenth of a millimeter, has now been almost entirely replaced by automated treatments with record and verify capabilities.

Initial acceptance testing and commissioning is somewhat dependent on the sophistication of the treatment center. Gamma stereotactic radiosurgery systems always include a unique, custom TPS, which is provided with all the physical factors necessary to treat patients, except for measurement of the output of the machine at the unit center point under reference conditions. This absorbed dose rate is dependent on the activity of ^{60}Co loaded into the device. For

a given manufacturer, the ratio of the reference absorbed dose rate to the activity of the radioactive sources is constant. It is impossible for a clinical user to experimentally verify the single source profile tables contained in the TPS. This can only be done in an experimental setting with a single source and collimator assembly. Until recently, the relative output measurements (also known as "helmet factors") were exceedingly difficult to measure by clinical users (Mack *et al.*, 2002). The use of radiochromic film, with two exposures on the same film, has been reported to yield good estimates of the output of this extremely small field size (Ma *et al.*, 2009).

Gamma Knife or GSR centers must create and maintain their own daily, weekly, monthly, and annual set of QA protocols. These protocols must typically be submitted to a regulatory agency at the

time of submission of an application for a radioactive materials license to possess a gamma SRS device. Daily checks typically include testing the functionality of the unit on a short test run and also checking the daily decayed estimate of standard absorbed dose rate computed by the TPS. The Elekta Gamma Knife Perfexion is supplied with a diode test tool (consisting of four diodes) that measures output during a 4-min exposure for comparison against pre-computed profiles. The emergency alarms and interlocks should be checked on a weekly basis. On a monthly basis, regulatory agencies require an output measurement be performed by a “spot check.” Measurements should be within 1 % to 2 % of that predicted by the last annual measurement.

On an annual basis, the physicist should perform every test required in the site radioactive material license. It should include performance of all the manufacturer’s recommended tests, rigorous checking of all interlocks and emergency warning systems, and a full calibration of the output of the unit (Bhatnagar *et al.*, 2012).

6.2.3 QA of the Tomotherapy System

Helical tomotherapy is an intensity modulated radiation therapy delivery technique developed at the University of Wisconsin-Madison and introduced into clinical use in 2003 by TomoTherapy, Inc. The system is now distributed by Accuray Inc. (Sunnyvale). A linear accelerator is mounted on a slip ring gantry in the helical tomotherapy system. The tomotherapy system has megavoltage fan-beam computed tomography (MVCT) imaging capabilities. During treatment delivery, the accelerator rotates while the treatment table is translated simultaneously.

Although a number of general QA procedures and recommendations for conventional linear accelerators are adopted for helical tomotherapy units, some are not directly applied to helical tomotherapy. In the context of SRS, Soisson *et al.* (2010) described procedures for testing the dose delivery accuracy of the tomotherapy system. They determined the accuracy of stereotactic localization and treatment for tomotherapy to be $0.45 \text{ mm} \pm 0.17 \text{ mm}$, indicating a localization precision of 0.3 mm within a 95 % confidence interval. These tolerances are well within conventional SRS tolerances and compare favorably to other linear accelerator-based techniques.

More generally, QA procedures specific to tomotherapy units have been reported in AAPM TG-148 (Langen *et al.*, 2010). These QA procedures include treatment planning, radiation delivery, image guidance (using MVCT), and dosimetric verification

techniques that are specific and unique to tomotherapy. For example, unlike traditional machine commissioning tasks, the tomotherapy system uses a common beam model in its planning system and the beams from each treatment unit are adjusted so that the beam parameters match the common beam model. During onsite acceptance testing procedure, the matching of the machine parameters to the common beam model is verified. Because of the special nature of the tomotherapy machine, some aspects of traditional machine commissioning tasks do not apply. Daily QA should include the beam output and MVCT image quality consistency. The monthly, quarterly, and annual test should also be performed to cover beam parameter consistency, couch mechanical movement, gantry rotation, and TPS end-loop tests.

With regard to the application of tomotherapy to SRT, the AAPM TG-148 (Langen *et al.*, 2010) report states that specific attention should be the accuracy of laser localization, geometric distortions and the concordance of imaging, treatment delivery, and laser position.

6.2.3.1 Laser localization. There are two independent laser systems used for patient setup, a movable, red laser and fixed, green laser. The accurate longitudinal spacing between the stationary, green laser plane and the treatment isocenter should be tested annually using a small radiation beam and a film that is marked at the virtual isocenter according to the stationary laser. The center of the radiation field should agree with the laser position to within 1 mm. The accurate movement of the movable laser with respect to the stationary laser should be tested monthly using a predefined plan with known red-to-green laser offsets and the red laser movements with respect to the green laser should be within 1 mm of the planned movement. At initialization, the green and red lasers should coincide to within 1 mm when the machine is used for SRT treatments. This should be tested daily. The laser systems are independent of each other and if it is found that the two systems do not coincide upon system initialization, the physicist must investigate which of the two laser systems has changed. This test inherently tests the stability of both laser systems.

6.2.3.2 Geometric distortions. Megavoltage fan-beam computed tomography is an integral part of the IGRT capabilities of the tomotherapy unit. The accurate reconstruction of an object in the MVCT image in terms of dimension and orientation can be tested monthly with a rigid plastic phantom of known dimensions and orientation. Distances

between small embedded objects (or fiducials) in the x , y , and z directions, and the orientation of the phantom as they appear in the MVCT image can be compared with the physical distances and orientation of the phantom. When the machine is used for SRT, the dimension of the embedded objects or distances between fiducial markers as measured in the MVCT image should be within 1 mm of the physical distances. The recommended test frequency and tolerances are in accord with those recommended in TG-142.

6.2.3.3 Imaging/treatment/laser coordinate coincidence. In the tomotherapy system, the delivery geometry and the imaging geometry should be coincident. Even so, the coincidence between the treatment and imaging coordinate system should be verified. This is done typically in an end-to-end test where a phantom is imaged, a plan is generated in the TPS, MVCT imaging is used to check the phantom alignment, the phantom is treated and the dose distribution within the phantom is tested for accuracy to establish image and treatment coordinate coincidence. The tolerance of this test is based on the combined uncertainty of the image registration and the dose calculation. The recommended tolerance for the treatment and imaging coordinate coincidence is 1 mm when the machine is used for SRT. The imaging parameters and dose calculation grids may need to be chosen accordingly.

6.2.4 QA of CyberKnife®

The Accuray CyberKnife system is a 6 MV, flattening filter-free linear X-band accelerator mounted on a robotic arm. The beam is collimated using circular cones of fixed dimensions of diameters ranging from 5 mm to 60 mm or with an iris variable collimator that uses two offset banks of six prismatic tungsten segments to form a polygon with 12 sides and 12 angles (*i.e.*, dodecagon), which results in a nearly perfectly circular irradiation pattern. The iris collimator generates the same range of field sizes as the fixed collimators. The largest (60 mm) fixed cone is used for reference dosimetry. The AAPM published a report on Quality Assurance for Robotic Radiosurgery (Dieterich *et al.*, 2011). The CyberKnife is a complex system consisting of several subsystems. Therefore, a QA program for each individual subsystem should be established and documented (*e.g.*, a specific QA program for the linear accelerator, another for the robotic manipulator, another for the image system) as well as an end-to-end tests that check the overall delivery quality. A detailed description of the quality controls and frequency to be performed on the robotic accelerator is

provided in the report of AAPM TG 135 (Dieterich *et al.*, 2011). The linear accelerator is very compact and light and has some constructional differences compared with linear accelerators used for conventional radiotherapy. Nevertheless, most of the QA procedures that are described for standard linear accelerators can also be applied to the compact flattening filter-free robotic accelerator.

Dosimetrically, as described in Section 2, the main differences are related to the absence of a flattening filter (FFF beam), the non-isocentric and non-coplanar delivery, and the use of in-room imaging for all aspects of treatment alignment. The CyberKnife users should be aware of the dosimetric implications when they apply protocols for clinical reference dosimetry, as described in Section 2 and in other reports and papers on reference dosimetry (Alfonso *et al.*, 2008; Almond *et al.*, 1999; Kawachi *et al.*, 2008; Kilby *et al.*, 2010; McEwen *et al.*, 2014).

Since the core of the robotic accelerator system is its ability to perform image guidance during the treatment by tracking the tumor, it is essential that this part is controlled and the accuracy of the image and tracking system is verified. Specific QA image-guidance tests are reported in TG 135 (Dieterich *et al.*, 2011), with the aim of verifying the accuracy of the imaging algorithm calculation, the effect of changes of imaging parameters on image quality and the targeting accuracy (*i.e.*, the capability of the system to adjust the beam to the new position of the target, taking into account both translations and rotations). This type of verification is performed with an end-to-end test, by using anthropomorphic phantoms. As pointed out in TG 135, the limitations of these tests and phantoms are that they represent an idealized condition that deviates from the real patient situation. It is suggested to develop tests and phantoms closely resembling the real patient treatment condition, so as to detect loss of accuracy when the imaging system is degrading or the conditions are not so ideal (*e.g.*, large patients).

Another important check is the accuracy of the radiation delivery. This involves both the accuracy of the robot and the linear accelerator motion in space. In the CyberKnife system, the robot positions the nominal source of the linear accelerator at specific points in space termed “nodes,” distributed on a surface centered around the x-ray targeting system (Fig. 6.2). A group of these nodes is called a path or trajectory. During the treatment, the linear accelerator is moved along these nodes and the radiation is delivered from the directions pointing toward the target. An important process in the accuracy of the system is the path calibration that is usually performed by the vendor at the acceptance test or after a failure of a second-level QA. (A second-level QA is a QA test

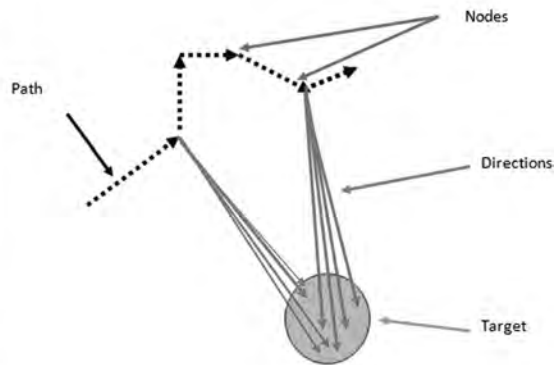
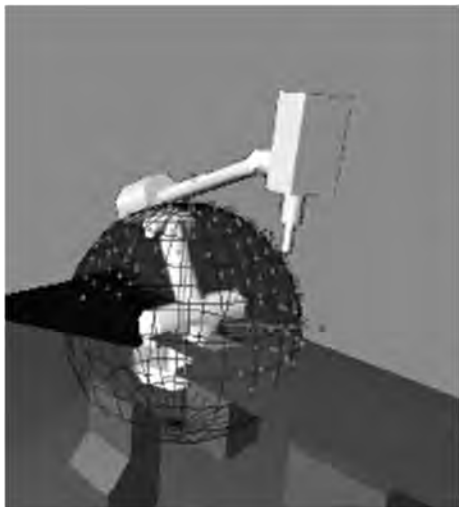


Figure 6.2. Conceptual diagram of the node locations and trajectory around the patient.

on the robotic manipulator performed by running a simulation in “BB-test mode” to visually evaluate the individual beam pointing accuracy to a level of approximately ± 1.5 mm; Dieterich *et al.*, 2011).

Nevertheless, as recommended by TG 135 (Dieterich *et al.*, 2011), there should be an easier procedure available for the physicist to check quantitatively the geometric accuracy of individual node pointing, since the current QA tests [“auto” QA (AQA) and end-to-end (E2E) tests] are insufficiently sensitive. The E2E test and AQA tests are used to check the overall accuracy of the system (including x-ray imaging, couch and robot mechanical alignments and algorithms, for isocentric alignment) for the different tracking modalities (see AAPM TG 135 for a detailed description). Task Group 135 raises a very important point about the check on the delivered dose as a patient-specific plan QA. In fact, the current overall clinical delivery accuracy tests (*i.e.*, E2E and AQA tests) are not suitable to verify the non-isocentric delivery accuracy, nor to verify the delivered dose. Therefore, ideally, patient-specific plan QA should be performed to verify the dosimetric and geometric accuracy of the delivered dose. Since this is a very time-consuming QA procedure, the frequency with which patient-specific QA should be performed is under debate (Dieterich *et al.*, 2011).

Other important aspects in patient-specific QA are related to the type of phantoms and detectors currently available on the market that are not always suitable to measure the steep gradients present in CyberKnife treatment plans. A patient-specific plan QA procedure consists in overlaying a treatment plan onto a phantom containing a dosimeter, modifying the beam target points and prescription dose according to the characteristics of the detector, and then

delivering one treatment fraction. The system provides capabilities to generate these QA plans, to move the beam arrangement relative to the dosimeter, and to rescale the MUs, after which the radiation can be delivered. The most common technique is to use a point detector (usually a small-volume ionization chamber) inside a phantom (see Fig. 6.3) although care has to be taken to position the sensitive volume of the detector in a region where the absorbed dose is relatively homogeneous.

This type of measurement provides only a 1D check of the plan and should be accompanied by 2D/3D measurements. The conversion of the small ionization chamber reading to absorbed dose in this composite delivery should take into account the correction factors, as discussed in several papers (Bouchard and Seuntjens, 2004; Capote *et al.*, 2004; Dong *et al.*, 2002; Ezzell *et al.*, 2009; Laub and Nusslin, 2003; Leybovich *et al.*, 2003; Low *et al.*, 2003; 2011; Martens *et al.*, 2000). Low *et al.* (2011) suggested the use of a Farmer-like ion chamber with a large volume instead of a microchamber for patient-specific point-dose measurements. This is to reduce the impact of positioning errors and other issues such as leakage or polarity effects related to the operation of small-volume microchambers (Le Roy *et al.*, 2011).

To validate dose distributions for small fields, measurement devices are required to have high resolution. Radiochromic film such as EBTTM or MDTM is most commonly used although film dosimetry requires the development of local expertise. Other devices such as detector arrays for these measurements have limitations that are linked to the very steep dose gradients found in CyberKnife treatment plans combined with the relatively low spatial resolution of many array detectors and the non-coplanar

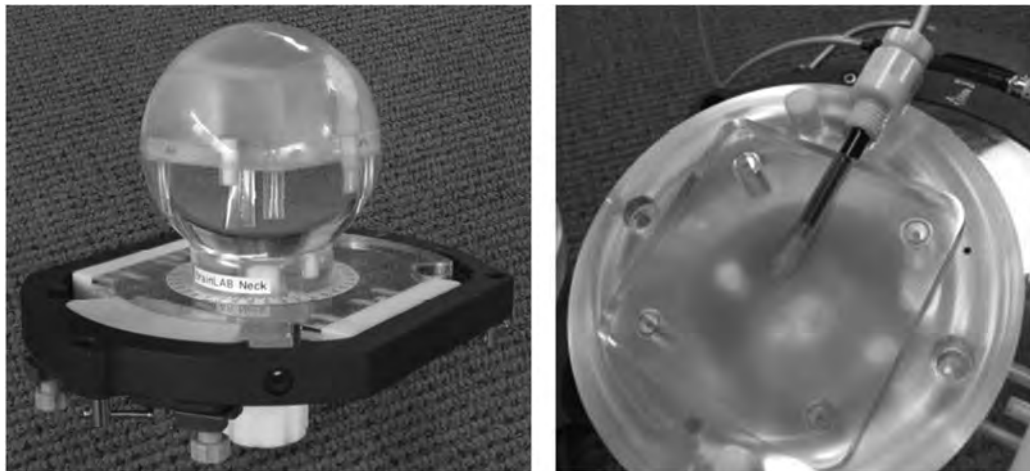


Figure 6.3. Lucy 3D QA phantomTM.

workspace combined with the response anisotropy of the detectors used in the arrays. Along these lines, more recently, some promising devices have come on the market (e.g., PTW OctaviusTM 1000 SRS device).

6.2.5 QA for Dedicated SRT Accelerators

As mentioned in Section 1, in recent years, several dedicated SRT accelerators have come on the market such as the Varian Truebeam STX and Varian Edge. The general principles of a QA program discussed for the previous devices are also applicable to these devices, such as the role of the manufacturer in providing complete dosimetric and mechanical information needed to establish an appropriate QA program. Given the specific properties and radiation geometries there will be specific QA requirements for each device. It is expected that various professional and scientific societies will publish reports detailing these specific QA procedures.

6.3 Uncertainties

The overall uncertainty of an SRT system is composed of (i) uncertainties associated with the imaging equipment used for planning (CT); (ii) uncertainties in the dosimetry (Section 2) and TPS (Section 4); (iii) uncertainties in the machine delivery system; and (iv) uncertainties in the image-guidance system (Section 5). In a comprehensive QA program, the individual uncertainties contributing to each step of the delivery must be evaluated

(Mackie and Palta, 2011). In addition, an end-to-end test will provide an estimate of the overall uncertainty. However, it should be realized that the end-to-end test is only valid for that specific situation. There may be scenarios that lead to errors/uncertainties that are not captured by the end-to-end test. For example, Hounsfield units wrongly generated on large patients that are not captured by the usual normally-sized QA phantom. Also, treatment of a large patient may give rise to couch flex not covered by an end-to-end test on a normal QA phantom. Hence, QA of the individual subsystems as mentioned above is important.

In summary, progress in radiation delivery devices, in TPSs and in image-guidance devices is constantly being made. This progress will continue to reduce the tolerance limit of SRT treatments. The goals of a QA program should be adapted and tailored to each specific system.

Techniques and methods should be developed to minimize the uncertainties in each component in order to reduce the overall uncertainty. A QA program dedicated to these specific components must evaluate the individual uncertainties and establish the tolerance limit of the system before the clinical use of any radiation treatment device. The QA program should have regular QA procedures in place to verify and to confirm the established tolerance limits are maintained and documented. A clinically acceptable uncertainty should consider the target dose, target size, and target location relative to the critical organs.

7. Prescribing, Recording, and Reporting

7.1 ICRU Reporting Levels

ICRU (ICRU, 1993; 1999; 2004; 2007; 2010) stated three levels of prescribing, recording, and reporting. The definitions of the three levels have been extensively described in the previous report (ICRU, 2010), but are summarized here for completeness:

- Level 1 recommendations are the minimum standards for prescribing and reporting. Below these standards radiotherapy should not be performed and these standards apply for simple treatments such as 2D planned treatments.
- Level 2 recommendations apply for the prescribing and reporting state-of-the-art techniques using computational dosimetry and 3D imaging. Treating at Level 2, all volumes of interest [e.g., gross tumor volume (GTV), clinical target volume (CTV), planning target volume (PTV), organs at risk (OARs), and planning organ-at-risk volume (PRV) (Section 3)] are delineated and 3D absorbed-dose distributions are available and they include heterogeneity corrections (Section 4). Dose–volume histograms (DVHs) for all volumes of interest are computed. A complete QA program is used to ensure that the prescribed treatment is accurately delivered (Section 6).
- Level 3 recommendations are recommendations for optional reporting of research and novel developments. They are used for the development of new techniques and/or approaches for which reporting criteria are not yet standardized by the ICRU (ICRU, 2010).

The definitions and recommendations in ICRU Reports 50 and 62 (ICRU, 1993; 1999) encouraged the delineation of the tumor or target and OAR volumes on 3D image sets such as a CT scan. With the introduction of intensity modulated radiation therapy (IMRT), prescriptions were based on DVH. The coverage of the PTV by a specific dose was specified by a DVH, and with the inverse planning the coverage was optimized with the use of the constraints, not only the constraints of the PTV were used but also the constraints on the critical structures or OARs. ICRU Report 83 (ICRU, 2010) recommended that users of commercial treatment planning

systems ensure that these systems have the ability to compute the dose accurately for small fields, inhomogeneous tissues, and in regions of electron disequilibrium and the present report underlines these requirements for SRT (Section 4).

In SRT, the definitions of GTV, CTV, and PTV have been largely ignored in the past, using isodose coverage instead of DVH information. Isodose coverage is a qualitative metric and this report strongly recommends the use of the dose–volume information in the evaluation of the SRT dose distributions. Level 1 reporting, including the reporting of absorbed dose at a point, cannot be used for SRT. The reasons for this are multiple:

- The absorbed-dose distribution within a PTV for SRT is less homogeneous than in conventional radiation therapy. Due to the heterogeneous dose distribution, a selected dose-reporting point can be positioned within a region of high or low absorbed dose, and therefore can mislead the mean absorbed dose within a structure. A point on the central axis is not a representative point because it can be positioned outside the PTV.
- The point of the maximum absorbed dose is unlikely to be representative.
- With the use of Monte Carlo calculations, it is proven that the dose in small volumes fluctuates; therefore, it is difficult and uncertain to determine absorbed dose at a point, whereas this is reasonably achieved in a larger volume.
- The absorbed-dose gradient at the boundary of a PTV in single or multiple SRT beams can be more than 10 %/mm, and a small shift in the field delivery can affect the reliability of using a single point to report the absorbed dose.
- Sufficient evaluation tools for Level 2 reporting are provided within the modern treatment planning systems and are the standard for use in SRT.
- An SRT program is commissioned as a special technique in clinical setups that already have the capabilities to deliver Level 2 IMRT and 3D-CRT programs.

It is essential to use a consistent methodology for the prescribing, reporting, and recording of

dose–volume metrics for SRT in order to evaluate the efficacy of SRT compared with conventional radiation therapy. Relative to IMRT (ICRU, 2010), where there have been only few studies comparing the efficacy of IMRT with older established methods, there are currently even less comparative studies in the field of SRT.

7.2 Dose Prescription in SRT

The process of developing a treatment plan consists of three major components as illustrated in Fig. 7.1:

- The planning aims, also known as the treatment goals, must be described and defined. These planning aims consist of the delineated volumes of interest (PTV, PRV) and the desired absorbed-dose levels in these volumes of interest. Usually, the planning aims are specified by the treating physician.
- An optimization process of the (complex) beam delivery. This process is performed by the computer but often the initial planning aims must be adjusted. This process is performed by the physicist/dosimetrist in collaboration with the treating physician.
- A complete set of finally accepted values, which becomes the “prescription” and, together with the required “technical data” represents the “accepted treatment plan.” The treating physician is ultimately responsible for this entire process.

Historically, dose prescription in SRS has been using the so-called “coverage isodose” to represent some form of minimum target dose, as it was related to techniques using fixed circular collimators. The type of prescription was validated throughout clinical results published since the late 1970s (see Fig. 7.2).

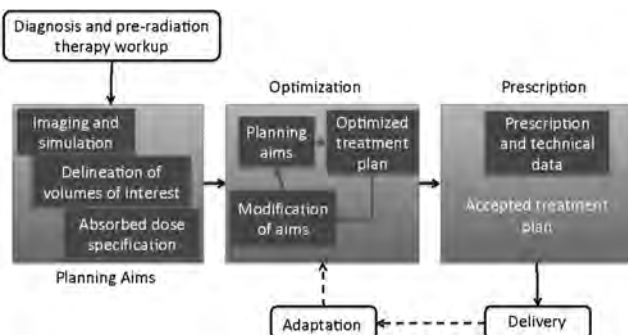


Figure 7.1. Flowchart of a typical SRT course. Note that the delivery step contains patient-specific quality assurance, if necessary, patient setup with immobilization, image verification, setup adjustment, if necessary, and treatment. The dashed lines represent a possible inter-fraction adaptation of the plan.

There is a large amount of prospective data demonstrating the local control for benign and malignant tumors together with low toxicity in targets of smaller than 3 cm treated with single fraction radiotherapy treatments. However, large variations in prescription methods were demonstrated in the published data. No strict recommendations for dose prescription and recording have been made until the present time. New SRT techniques have been applied in the last decade, including non-isocentric and non-coplanar configurations. Dose prescription in SRT has been generally defined as a dose delivered to the outer border of the PTV or on an isodose surface that most optimally conforms to the outline (surface) of the PTV as a percentage of the maximum dose together with optimally restricted dose to the OAR. No strict recommendations were available for this type of dose prescription and no recommendations have been available on how to record the treatment prescription and plan. In 2010, the ICRU Report 83 was published on Prescribing, Recording, and Reporting photon-beam IMRT. The present section adapts ICRU Report 83 and provides guidelines for Prescribing, Recording, and Reporting photon-beam SRT.

In ICRU Report 83, emphasis was placed on prescribed dose to a typical point in the target tissues. The median absorbed dose, $D_{50\%}$, is considered a more reliable measure of a typical absorbed dose even in a relatively heterogeneously irradiated tumor. Often in IMRT, for a target volume, the median absorbed dose is close to the mean absorbed dose (and should be as close as possible to the near-minimum dose $D_{98\%}$ so as to achieve dose homogeneity). However in SRT, with the exception of small lung lesions, there is generally much less normal tissue within the PTV and there may be critical normal tissues very close to the target volume. Hence, the treatment of these spatially limited volumes with multiple small photon beams may imply dose heterogeneity to maintain optimal conformity and acceptably steep dose gradients. There are also technical considerations that affect the uncertainty on the value and the location of the maximum dose. These are associated with the type of dose-calculation algorithm, whether Monte Carlo based, deterministic, or convolution-superposition based, the dose-calculation grid, and parameters of the beam model (*i.e.*, spot size) and beam modifiers (*i.e.*, MLC and leakage). For a more complete discussion, see Section 4.

7.2.1 Recommendation for Prescription in SRT

The recommendation for SRT prescription follows the schematic shown in Fig. 7.1:

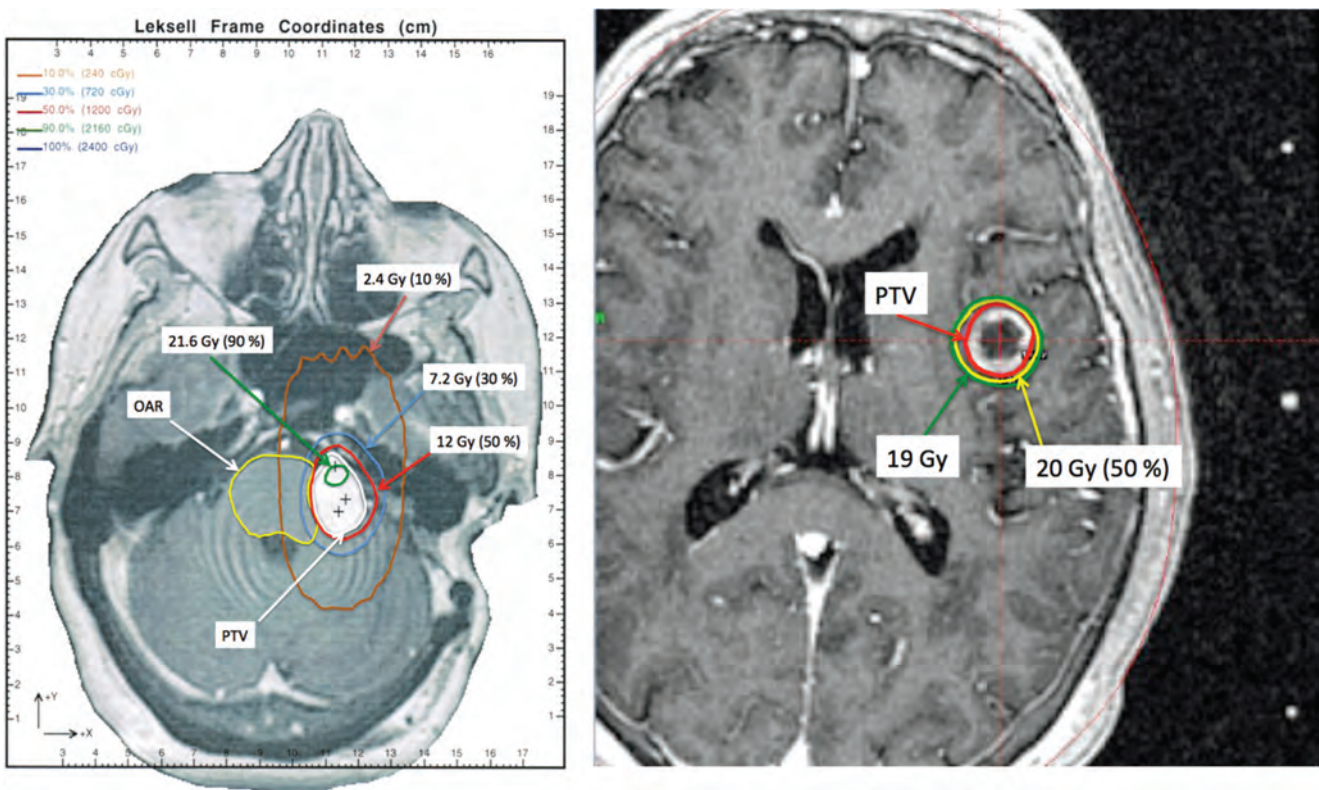


Figure 7.2. Example of radiosurgery coverage isodose. (a) A sporadic acoustic neuroma is partially resected. Six years later—with significant progression of residual tumor—a now 52-year-old woman is treated with single fraction radiosurgery. A total of 12 Gy is prescribed to the 50 % isodose surface and delivered using frame-based localization and three isocenters on a modified linear accelerator. Conical cones (1.0, 1.5, and 2.0 cm) are used in a dynamic delivery technique (concurrent couch and gantry motion) with 10 MV photons. (b) A left parietal metastasis: 69-year-old male, non-small cell lung brain metastasis, 2.17 cm^3 , treated with 20 Gy to the 50 % isodose.

- Define the Planning Aims: as part of the prescription process, constraints on the OARs should be well described and available as a departmental policy in order to make clinical evaluation possible over time.
- Plan and Optimize: this can be an iterative process where planning aims are prioritized and a compromise achieved.
- Prescribe a complete set of finally accepted values, which becomes the prescription and, together with the required technical data represent the accepted treatment plan. Absorbed dose is prescribed to the isodose surface D_V that covers an optimal percentage volume of the PTV while optimally restricting dose to the PRV. Optimal in this context means the best possible coverage of the PTV according to the clinical situation (e.g., brain metastases, spine).

For example, in a 1.5 cm^3 brain metastasis, the prescription could be close to 100 % of the PTV, while for a vertebral metastasis, prescription over 85 % of the PTV could present challenges with regard to homogeneity and the dose to the spinal cord (OAR, Fig. 7.3). Currently, some treatment

planning systems provide methods limited to prescription as a percentage of maximum dose. This report strongly recommends that manufacturers provide the software tools that allow the ICRU recommended prescription method to be applied.

7.3 Reporting in SRT

Recommendations for reporting are based on dose and volume information obtained from DVHs. DVHs are routinely used in radiotherapy to evaluate and report 3D conformal radiation therapy, IMRT, electron and ion beam therapies (ICRU, 1985; 2004; 2007; Yanagi *et al.*, 2010). As will be discussed in Section 7.3.2, a DVH represents, in a concise although simplified way, the dose–volume relationship within a volume of interest. Visual inspection of DVHs can lead to identification of clinically important characteristics of a dose distribution, such as the presence (but not the location) of regions of high or low dose or other dose heterogeneities, which are often difficult to assess rapidly and consistently from conventional isodose or color-wash presentations. Cumulative DVHs are histograms of the volume elements that receive at least a

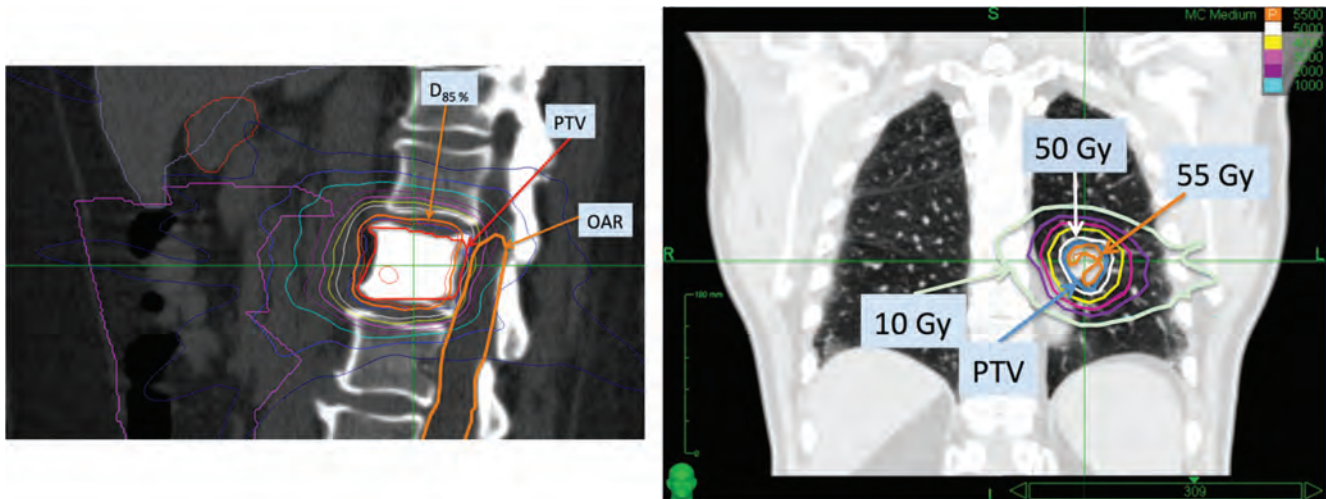


Figure 7.3. Examples of spine (left panel) and lung (right panel) metastasis treatment plans. The spine treatment achieves the prescription dose to only 85 % of the PTV, $D_{85\%}$, because of the nearby cord (OAR). The lung metastasis receives prescription dose to 98 % of the PTV, $D_{98\%}$.

given dose and they are usually expressed as either the absolute volume, or the volume relative to the total structure volume, receiving at least a given dose D . Cumulative DVHs are the dose integral of a differential DVH defined by $dV(D)/dD$ which is the increment of volume per unit dose at dose D (ICRU, 2010). DVHs can be used to determine values such as D_{median} , which is the dose received by at least 50 % of the volume making it often a good choice for a representative dose prescription value for the PTV, even though it does not indicate the location in the volume where the median dose value lies and may be less appropriate if the dose distribution in the structure is highly heterogeneous. In science, the usual specification for a value in which there can be some variation is the mean (ICRU, 2010).

7.3.1 Recommendation for Reporting at Level 2

In order to have a common language and ability to compare clinical results, reporting rules are recommended in this Report. As discussed in Section 7.1, SRT reporting should only be done at Level 2 or 3 as defined by ICRU (ICRU, 1993; 1999; 2010). Level 2 reporting represents state-of-the-art radiation therapy techniques whereas Level 3 reports research and developmental procedures.

Level 2 reporting should include the following items:

- Brief clinical history including description of the clinical examination, location, diagnostic technique used, histopathological evaluation if any, staging, prior treatment, performance status.

- Treatment intent (*i.e.*, palliative, curative)
- Patient simulation (*i.e.*, immobilization devices, accessories, planning image acquisition, and protocols)
- Target volumes and OAR selection and delineation
 - (1) Target volumes
 - (i) GTV (cm^3)
 - (ii) CTV (cm^3)
 - (iii) ITV, PTV (cm^3)
 - (2) Normal tissues
 - (i) OAR (cm^3)
 - (ii) PRV (cm^3)
 - (iii) RVR (cm^3)
- Planning aims and dose–volume constraints
- Description of treatment planning system (*i.e.*, algorithm, voxel size, calculation dose grid, type-A uncertainty for MC-based systems)
- Prescription
- Patient-specific QA
- Delivery (*i.e.*, treatment unit and energy, image verification device, and data set)
- Dose reporting
 - (1) Dose in PTV and, if applicable in CTV and/or GTV
 - (2) Dose in OAR and PRV.

For dose reporting (Item 10), the present report recommends the following metrics:

- PTV median absorbed dose, $D_{50\%}$: As this report recommends a CTV be defined for each case, the $D_{50\%}$ can be also reported for CTV. In the specific case of peripheral lung lesions, where the dose distribution is strongly affected by tissue density

- variations, a dose to a target, which does not include uninvolved lung parenchyma ($D_{50\%}$ (GTV/CTV)), should be systematically reported.
- The SRT near-maximum dose, $D_{\text{near-max}}$: For PTV V larger than or equal to 2 cm^3 , the volume near-max represents 2 % of the PTV, as recommended in ICRU Report 83 ($D_{2\%}$). For PTV V of less than 2 cm^3 , near-max is an absolute volume of 35 mm^3 , in which case $D_{35\text{mm}^3}$ is reported.
 - The SRT near-minimum dose, $D_{\text{near-min}}$: For PTV V larger or equal than 2 cm^3 , the volume near-min represents 98 % of the PTV, as recommended in ICRU Report 83 ($D_{98\%}$). For PTV V of less than 2 cm^3 , near-min is an absolute volume of 35 mm^3 , in which case $D_{V-35\text{mm}^3}$ is reported.

7.3.2 Discussion and Rationale of Level 2 Reporting

7.3.2.1 Dose-volume specification. It is recommended that dose-volume specification be used for reporting the treatment plan. This information can be found on a cumulative DVH as the dose value specified at a percent volume V. Cumulative DVHs are histograms of the volume elements that receive at least a given absorbed dose, and they are usually expressed as either the absolute volume or the volume relative to the total structure volume, receiving at least a given absorbed dose, D. Each point on the line of a relative cumulative DVH is described by the following equation:

$$\text{DVH}(D) = 1 - \frac{1}{V} \int_0^D \frac{dV(D')}{dD'} dD' \quad (7.1)$$

where V is volume of the structure and D the dose in the structure represented by the DVH (Fig. 7.4). The differential DVH is defined by $dV(D)/dD$, which is the increment of volume per absorbed dose at absorbed dose, D.

In ICRU Report 83 (ICRU, 2010), a recommendation was made to report the near-maximum absorbed dose (e.g., $D_{2\%}$) as an alternative for the maximum absorbed dose. These recommendations were made to ensure that an absorbed dose is reported that is not reliant on a single computation point and suffers less from sampling errors and calculation uncertainties (Das *et al.*, 2008c). In the present report, for small PTV (*i.e.*, less than 2 cm^3) it is recommended to specify the SRT near-maximum dose as D_V , where V represents a minimal absolute volume element within which the absorbed dose can be calculated to sufficient accuracy. The volume element needs to be chosen taking into account the calculation grid size and considerations that pertain to dose-calculation accuracies in a single voxel. Studies (Benedict *et al.*,

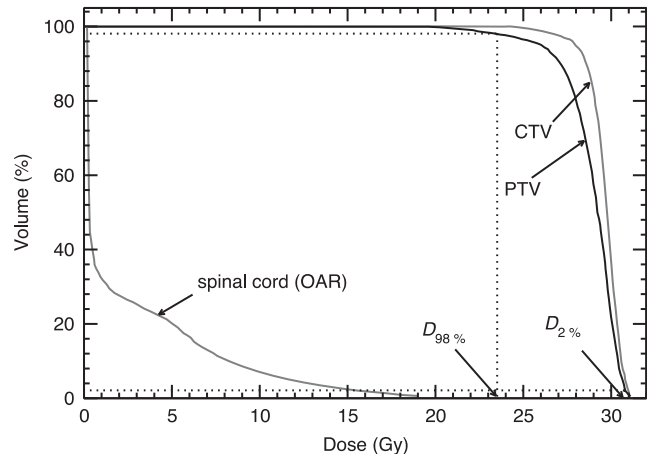


Figure 7.4. DVH for the SRT spine metastasis case with dose distribution displayed in Fig. 7.3 (left panel). Median dose ($D_{50\%}$) to the CTV 29.7 Gy, median dose ($D_{50\%}$) to the PTV: 29.2 Gy, SRT near-maximum dose to the PTV $D_{2\%}$ 30.8 Gy. Since the PTV $286 \text{ cm}^3 > 2 \text{ cm}^3$, the SRT near-maximum dose to the PTV is equal to the near-maximum dose to the PTV, $D_{2\%}$.

2010; Roberge *et al.*, 2015) have reported absolute volumes of 30 mm^3 to 35 mm^3 as being adequate minimal volumes. The reason that a percentage volume element (e.g., 2 % for the specification of near-maximum dose in IMRT) may, in certain conditions, be an inadequate volume is when the structure is small and a percentage specification may lead to volumes that are below the resolution of the dose-calculation grid. For example, a 100 mm^3 volume may be suitable for extracranial SRT (*i.e.*, 100 cubic voxels measuring 1 mm on a side) whereas a 15 mm^3 volume may be more suitable for cranial radiosurgery.

With respect to the reporting of minimum dose, ICRU Report 83 (ICRU, 2010) introduced the near-minimum dose, $D_{98\%}$, which is the minimum dose that covers 98 % of the volume of the PTV. The percent volume V that D_V is based on should be reported textually or as a subscript value (e.g., $D_{98\%} = 50 \text{ Gy}$, $D_{\text{median}} = 55 \text{ Gy}$). The dose-volume metric, $D_{100\%}$, would be commonly called the minimum dose. Since, the $D_{100\%}$ value is the dose in a single voxel, the minimum dose may not be accurately determined because it is often located in a high-gradient region at the edge of the PTV, making it highly sensitive to the resolution of the calculation and the accuracy of delineating the CTV and determining the PTV. Therefore, reporting of $D_{100\%}$ is not recommended.

In the present report, the concept of the SRT near-minimum dose $D_{\text{near-min}}$ analogously to the concept of SRT near-maximum dose is introduced to ensure that the volume element in which the low dose is calculated is sufficiently large to maintain dose-calculation accuracy. The volume that received

at least this minimal dose thus becomes $V - 35 \text{ mm}^3$. Other dose–volume values, such as $D_{95\%}$, may also be reported but should not replace the reporting of $D_{V-35\text{mm}^3}$. The clinical relevance of the lowest PTV dose points may depend on their position within the PTV. In SRT planning, because of the manner in which the prescription is made and because of the steep dose gradients, low-dose regions (*i.e.*, cold spots) within the PTV are more unlikely than in IMRT. The location of low-dose regions within the GTV, CTV, and PTV boundaries may be of concern but the DVH will not provide that information. Such regions might, however, be identifiable using isodose contours. Hence, it is important that the radiation oncologist not rely solely on the DVH for treatment evaluation but also carefully inspect the dose distributions slice-by-slice (or in three dimensions) to make sure that the PTV is being adequately irradiated and that any regions of low dose are those required to avoid complications.

The PTV is defined largely to accommodate alignment and motion uncertainties and the treatment plan is frequently designed such that the PTV receives a lower dose at its boundaries than in its body. Since it is unlikely that the CTV is always located near the edge of the PTV, the dose actually delivered to the CTV is likely to be closer to the desired distribution than the DVH of the PTV would suggest. Thus, the DVH of the PTV will tend to exaggerate the inhomogeneity of dose to the CTV due to setup error or motion. Similarly, the DVH of the CTV will tend to indicate more homogeneity than is actually the case. It is therefore useful to show the PTV and the CTV DVHs on the same graph as these approximate the confidence envelope of the DVH of the CTV, assuming a correct dose distribution and accurate contouring of volume. The dose–volume values for the PTV and CTV thus represent the lower bound and upper bound on dose to the CTV, respectively (ICRU, 2010).

This report does not recommend any particular value of D_V for a prescription. However, the median dose, $D_{50\%}$, is likely to be a good measure for a typical dose in a relatively homogeneously irradiated tumor, has been shown to be computed accurately by many commercial treatment planning systems (Das *et al.*, 2008c), and its value is easy to determine from a cumulative DVH. Wherever the CTV lies within the PTV envelope, the CTV median dose is almost constant. The original rationale for reporting the dose at the ICRU reference point and reporting of $D_{50\%}$ are very similar (*i.e.*, reporting an absorbed dose that is largely representative of the absorbed dose to the PTV). However, numerically the values will likely differ significantly depending on the dose distribution in the PTV, particularly for SRT treatments.

The PTV is a concept designed to ensure that the CTV receives an adequate dose. The CTV $D_{50\%}$ and $D_{2\%}$ should be very similar to these metrics for the PTV. However, near $D_{98\%}$ the DVHs for the CTV and PTV may diverge considerably. If it were possible to obtain the “true” DVH for the CTV, where motion and setup uncertainties were accounted for in detail, it would typically be contained within the DVHs of the CTV and PTV. Often a compromise must be made between achieving a high dose to the PTV and protecting sensitive normal structures. This is less important in SRT than in IMRT because of the more limited amount of irradiated volume in SRT compared with IMRT. The clinician must be the judge of the degree of compromise taking into account that regions of low dose in the target volume may lead to a reduced probability of tumor control. With a prescription using, for example, $D_{98\%}$, there will be, by definition, 2 % of the defined PTV with a dose lower than the prescription.

7.3.2.2 Dose–volume reporting specific to OAR and PRV. Organs have been defined as serial or parallel depending on their functional arrangement of normal tissue cells (ICRU, 2010; Withers, 1986; Withers *et al.*, 1988). This distinction is important to determine the absorbed-dose limits in normal tissues (*i.e.*, OAR) because the irradiation of a small volume of serial-like tissues, such as the esophagus or spinal cord, can result in high toxicity. Parallel-like tissues, such as liver and kidneys, may have sufficient reserve capacity such that inactivation of a substantial portion of the organ will not lead to clinically detectable complication. In Table 7.1, recommended parameters to be reported specific to the OAR and PRV are summarized. For parallel structures, the mean dose to these organs or, more commonly, V_D , the proportion of the organ volume receiving absorbed dose above a given threshold dose (expressed in absolute terms) have been the metrics felt to best correlate with risk of complication. Typically, V_D would be reported using the value of D and V as a percentage of the volume of the organ.

For “serial” structures, metrics are the maximum point dose or the dose to a small volume. As indicated during the introduction of the concepts “SRT

Table 7.1. Parameters quantifying OAR effects

Parameter
1. Volume V_D of tissue receiving a clinically relevant dose D depending on the type of organ or clinical situation
2. SRT near-maximum dose $D_{2\%}$ or $D_{35\text{mm}^3}$
3. D_{mean} and/or D_{median} depending on the type of organ or clinical situation

near-maximum" and "SRT near-minimum" absorbed dose, because of the small volumes irradiated in SRT, absolute volumes (irradiated for serial structures or spared for parallel structures) are of more significance than relative volumes.

At the same time, quantities such as mean doses and/or proportion of the organ volume above (or below) a threshold dose will continue to play a role in evaluating the risk to parallel organs. It should be noted that since in SRT, dose distributions near normal tissue structures are highly non-homogeneous, the mean dose and median dose for normal tissue structures are not similar in value and so the median dose cannot be used as an accurate substitute for the mean. It is also recommended for parallel-like organs that the entire organ be contoured so that accurate values of D_{mean} and V_D can be determined. The maximum dose as specified by a single calculation point (D_{max} or $D_{0\%}$) has often been reported for serial-like organs or structures.

In all cases, it is recommended to report more than one dose–volume point. For serial-like structures, this will be the near-maximum point dose in addition to the dose to a small clinically relevant volume. For parallel-like structures, at least two dose–volume points should be reported. For example, liver dose could be reported in terms of absolute volume below a specific threshold dose (the threshold could be 21 Gy for a five-fraction scheme) and mean dose to the organ.

If an OAR, such as the brain or heart, is not clearly a serial-like or parallel-like structure then at least three dose–volume specifications should be reported. This would include D_{mean} , $D_{2\%}$, and a third specification of V_D that correlates well with a dose D , which if exceeded within some volume, has a known high probability of causing a serious complication. If an OAR has features of both serial-like and parallel-like structures, it is preferable to break it down into its components and report the dose to these areas separately rather than relying on total organ metrics (e.g., the main bronchi can be contoured separately from the lung parenchyma).

7.3.2.3 Dose homogeneity. In IMRT and in 3D conformal radiotherapy, dose homogeneity and dose conformity are independent specifications of the quality of the dose distribution. Dose homogeneity characterizes the uniformity of the dose distribution within the target volume. Dose conformity characterizes the degree to which the high-dose region conforms to the target volume, usually the PTV. Figure 7.5 adapted from ICRU Report 83 (ICRU, 2010) illustrates examples of dose homogeneity and dose conformity.

Several definitions of homogeneity index have been proposed and some individuals favor one over another often depending on the radiotherapy modality. In SRT where dose homogeneity is characteristic-ally low, the ratio of the maximum dose to the prescription dose has been used (Khoo *et al.*, 1999; Murphy *et al.*, 2001). This definition only indicates the magnitude of overdosing but, perhaps more importantly, does not indicate the magnitude of underdosage as compared with the prescription. ICRU previously recommended that the dose values in the PTV be confined within 95 % to 107 % of the prescribed dose (ICRU, 1999). With SRT, these constraints are not in use as some clinicians prefer a high dose in the middle of the target. The clinical use of this principle led to excellent local control of the tumor and significant experience, especially in the treatment of brain metastasis which is based on this principle. Therefore, the dose is currently often pre-scribed to the 60 % to 80 % isodose (relative to maximum dose) line that is located on the outerline of the PTV. The disadvantage of this principle is the loss of a guideline for the minimum or maximum dose to the target or PTV. Therefore, it is recommended, as in ICRU Report 83 (ICRU, 2010), that the extent of high and low dose be specified using dose–volume quantities such as SRT near-maximum dose (or $D_{2\%}$) and the SRT near-minimum dose (or $D_{98\%}$) for regions of high and low dose, respectively.

Dose homogeneity and uniformity of the dose distribution are synonymous terms (ICRU, 2010). In the best circumstances, both the mean dose to the PTV and the standard deviation of the mean would be reported. However, many treatment planning systems do not report the mean, and many do not report the standard deviation of the mean. The provision of tools to report both the mean dose to the PTV and the standard deviation of the mean is recommended to treatment planning system vendors.

7.3.2.4 Dose conformity. Dose conformity is another parameter for the quality of the dose distribution. It characterizes the degree to which the high dose region conforms to the target volume (usually the PTV) and is different from the dose homogeneity.

One of the hallmarks of 3D conformal radiotherapy and IMRT is the conformity that can be achieved between the high dose volume and the PTV. This is not the case in SRT. One measure to describe the degree of dose conformity is the conformity index (CI) although there has been some confusion over its definition. It was defined as the "quotient of the Treated Volume and the volume of the PTV" with the caveat that the PTV must lie entirely within the

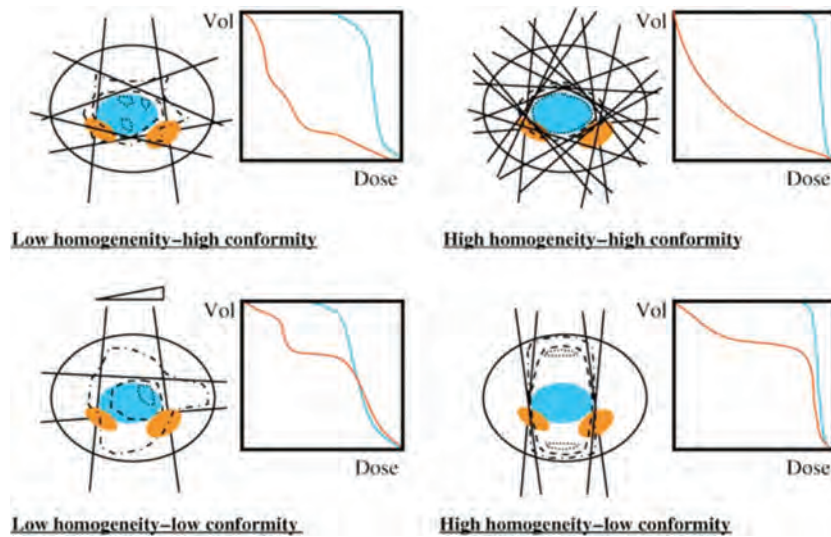


Figure 7.5. Pictographic representation of the concepts of dose conformity and dose homogeneity. The PTV is in blue and the PRV is in orange. Dashed lines indicate isodose lines. Homogeneity is a measure of the uniformity of absorbed dose in the PTV indicated by the “squareness” of the DVH. Conformity is a measure of the overlap between the isodose surface defining a significantly large absorbed dose and the surface of the PTV. Upper left panel shows the effect of unequal beam weighting to protect OARs. Lower left panel shows the effect of unequal beam weighting and use of a wedge. Upper right panel shows the effect of many beam portal angles with variable weighting. Lower right panel indicates the effect of AP/PA beam setup and lack of avoidance of the OARs. Reprinted from Fig. 3.4 in ICRU Report 83 (ICRU, 2010).

target volume (TV) (ICRU, 1999). ICRU Report 62 (ICRU, 1999) defined TV as “the volume enclosed within a specific isodose envelope.”

Although it may be biologically more rational to report a volume of tissue receiving a specific dose (e.g., the volume of tissue treated to 12 Gy or more, $V_{12\text{ Gy}}$), it has been tradition to report conformity as a ratio of the prescription isodose volume to the target volume. In its first iteration, the CI PITV (i.e., the ratio of prescription isodose volume, or PIV, to target volume) did not account for possible under-treatment of the target. For example, a PITV ratio of 2 from a treatment which irradiates 10 cm^3 of tissue to 14 Gy in order to treat a 5 cm^3 target could mean that 3 cm^3 of the target receives 14 Gy and 7 cm^3 of normal tissue receives 14 Gy just as well as it can mean that 5 cm^3 of each will receive the prescribed dose. To compensate for this potential ambiguity, a new CI has been proposed, also known as the Paddick Conformity Index (Paddick, 2000):

$$\text{Paddick Conformity Index} = \frac{TV_{PIV}^2}{TV \times PIV} \quad (7.2)$$

where TV is the target volume and TV_{PIV} the target volume within the prescription isodose volume, which compels the dose to be in the right location. This index has been subsequently modified to its reciprocal so that it has the same scale as the PITV ratio (when the PITV is > 1 , which it almost always is).

$$\text{Conformity Index} = \frac{TV \times PIV}{TV_{PIV}^2} \quad (7.3)$$

Conformity offers only a snapshot of the normal tissue treated to the prescription isodose but complications likely occur because of the dose delivered in the falloff region beyond the prescription isodose. This could be represented again by the volume of a specified isodose (e.g., $V_{12\text{ Gy}}$ —volume receiving dose larger than or equal to 12 Gy) but, despite the simplicity and biologic rationale, this has not gained widespread acceptance because it does not lend itself to comparing or summarizing plan quality between targets of different sizes treated to different doses. A simple proposed gradient index divides the volume of the isodose, which is half of the prescription by the prescription isodose (for example, the V_{10}/V_{20}).

When a plan contains multiple targets, vendors of planning systems should be expected to provide software that can calculate the new CI (Eq. 7.3) for each lesion treated. This may not be realistic for the gradient index, where lower isodose surfaces will more commonly blend into each other. In these cases, reporting of a global V_D of an isodose lower than the lowest prescription dose may be helpful (e.g., $V_{12\text{ Gy}}$).

The gradient index and CIs were designed with the assumption that no margin is added from GTV to PTV. As any margin from GTV to PTV will contain mainly (if not only) normal tissue, these indices

should be reported relative to the GTV (and this should be explicitly stated for clarity). However, in the planning process it may be useful to calculate them relative to the PTV. Only through more rigorous and uniform reporting of these parameters will it be possible to better associate these parameters with treatment complication.

For radiosurgery in the brain, extra parameters may be considered such as the dose gradient index, GI, defined as:

$$GI = \frac{PIV_{\text{half}}}{PIV} \quad (7.4)$$

where PIV_{half} represents the prescription isodose volume at half the prescription isodose (e.g., at 25 %), and PIV , the full prescription isodose volume (e.g., at 50 %).

7.3.3 Reporting at Level 3

Reporting of developmental techniques and concepts is about concepts and techniques that have not yet reached a stage when they have been deemed sufficiently established to recommend in routine practice. However, their continued investigation is encouraged and some such concepts and developments are described below. With Level 3 reporting one should consider integral dose, clinical and biological evaluation metrics (i.e., TCP and NTCP, and dose coverage histogram) as well as equivalent uniform dose-based optimization or reporting of probability coverage.

7.3.3.1 Reporting integral dose. The concept of integral dose in radiation therapy has gained interest in the context of second cancer induction or complication as a result of the irradiation of large body volumes and the extensive exposure at the time of diagnostic/planning and image guidance. In SRT, the treated volumes are typically small and the number of fractions limited. Nevertheless, strong consideration should be given to the recording of integral dose especially for patient treated for benign lesions. We refer to the definition of integral dose on page 30 of ICRU Report 83 (ICRU, 2010).

7.3.3.2 Biology-based evaluation metrics.

Caution must be taken when biological-based evaluation metrics are used clinically, but they are very

interesting research quantities. They account for not only dose and volume, both of which can be physically defined, but also to some extent on clinical observations and/or biological models. In principle, biological models are an important addition to a purely physical quantity because they relate to the aims of radiation therapy to provide improved tumor control and/or to reduce the probability of damaging healthy tissue (ICRU, 2010). For a complete description, see ICRU Report 83 (ICRU, 2010).

7.4 Reporting of Software Versions for Treatment Planning and Delivery

Dose-calculation algorithms have evolved dramatically since the beginning of this century. Monte Carlo as well as deterministic dose-calculation algorithms are now in clinical use. These model-based systems rely on accurate beam characterization and use algorithms to account for collimator leaf shape and extrafocal radiation (i.e., scatter from the head of the treatment unit), either from parameterized measurements or by direct modeling of the accelerator components. Hence, the performance is affected by tunable parameters such as grid size, algorithm, heterogeneity correction, and specification of dose to water versus dose to tissue (see Section 4 for more details). It is thus very important to report these details of the treatment delivery software in addition to the treatment planning system.

7.5 Reporting of Confidence Intervals

It is difficult to assess the estimations of uncertainty, but, confidence intervals should be reported if possible. Confidence intervals are presently considered to be part of Level 2 or Level 3 reporting. For example, rather than simply reporting $D_{50\%}$ for an individual or the average value of $D_{50\%}$ for patients in a trial, it would be useful to report the confidence intervals for those values. If quality-assurance measurements were conducted to verify the doses delivered to patients in the trial, the population-averaged deviation of the measurements from the planned dose, normalized to the planned dose, would be a useful measure as would the confidence interval of the deviation.

Appendix A: Clinical Examples

A.1 Lung Cancer

A.1.1 Patient History

A 79 year old male presented with increased shortness of breath and mass on a chest x-ray in February 2015. The mass was located in the left middle lobe and had a diameter of 12 mm on a CT-scan. Bronchoscopy revealed a squamous cell carcinoma and the PET(CT) scan showed a solitary PET-positive nodule in the lung. The patient had a history of COPD GOLD class III with a FEV1 (forced expiratory volume) of 1130 ml (46 % of the predicted value) and a history of cerebrovascular accidents and transient ischemic attack. The ventilation/perfusion scan showed that the right lung contributed 48 % of the ventilation/perfusion capacity while the left lung contributed 42 %. As the patient had mediocre lung function, he was considered inoperable. This patient was referred for curative stereotactic treatment with the CyberKnife.

A.1.2 Treatment Intent

The intent of the treatment was to cure the patient.

A.1.3 Simulation

The patient assumed the prone treatment position on a vacuum mattress used for the planning CT-scan. The treatment planning CT scan was made with intravenous contrast during exhalation with our wide-bore multi-slice CT simulator. The patient was scanned from the teeth to the middle of his abdomen. The trans-axial imaging had a slice thickness of 1.5 mm.

A.1.4 Target volume and OAR selection and Delineation

The planning CT was transferred to the treatment planning system (Accuray, Sunnyvale, CA). The tumor and organs at risk (OAR) were then contoured. The gross tumor volume (GTV, 1.5 cm^3) was contoured using the lung window. The planning target volume (PTV, 6.7 cm^3) was obtained by adding a

5 mm margin to the GTV. The OARs were the lungs, the heart, the esophagus and the spinal cord.

A.1.5 Planning Aims and DVH Constraints

The total dose was prescribed to the outer border of the PTV, and 95 % of the volume of the PTV had to receive the prescription dose. The dose constraints for the organs at risk for a peripheral lung tumor are shown in Table A.1.

A.1.6 Description of Treatment Planning System

The treatment planning was made with Multiplan version 2.2.0, the treatment planning system of the Cyberknife (Accuray, Sunnyvale, CA). Multiplan has implemented both equivalent path length (EPL) and Monte Carlo (MC) dose calculation algorithms. The MC dose calculation algorithm was validated (Grofsmid *et al.*, 2010). The treatment plans in Multiplan were first recalculated with EPL, and then with MC. This was done to eliminate subtle differences between the OnTarget and Multiplan treatment planning systems. A high-resolution grid (256×256) was used for the EPL and MC calculations and the type-A uncertainty in the MC calculation was set to 2 %. MC computation time was approximately 5–10 minutes.

A.1.7 Prescription

The PTV (outer border) was treated with a dose of 51 Gy in 3 fractions and the dose was prescribed to the 74 % isodose line (Fig. A.1).

A.1.8 Patient-specific QA

QA of stereotactic lung treatments is part of an overall QA program for this stereotactic unit. The QA is performed weekly. The end-to-end tests are performed alternating such that the end-to-end test for Xsight lung tracking occurs every 8 weeks. The end-to-end test for fiducial tracking is performed every 4 weeks.

Patient-specific QA did not include pre-treatment QA; instead, it consists of a semi-automated check of the treatment plan according to a check list.

These checks include treatment parameters, tracking alignment, plan details, Monte Carlo checks and an independent MU calculation.

A.1.9 Delivery

The dose was delivered with the CyberKnife using an iris collimator. In total, 97 non-coplanar beams were used with a total of 11 302 monitor units per fraction. The tumor was treated with the fiducial tracking system of the CyberKnife.

A.1.10 Dose Reporting

The PTV was 6.7 cm^3 . The median absorbed dose to the PTV ($D_{50\%}$) was 56.0 Gy, the near minimum dose $D_{98\%}$ was 50.4 Gy and the near maximum dose

Table A.1. Dose constraints for a peripheral tumor, treated with 51 Gy in 3 fractions

Organ	D_{\max} (Gy)
Spinal Cord	18 Gy
Esophagus	21 Gy
Trachea and main bronchus	33 Gy
Plexus brachialis	21 Gy
Liver*	17 Gy
Organ	Volume & dose
Lung minus GTV	<31 % should receive 13 Gy

was $D_{2\%} = 63.4 \text{ Gy}$. The median absorbed dose to the GTV ($D_{50\%}$) was 60.6 Gy, the near minimum dose $D_{98\%}$ was 56.6 Gy and the near maximum dose was $D_{2\%} = 64.5 \text{ Gy}$. Doses to normal tissues (lungs, heart, spinal cord, etc.) were within the constraints (see Table A.1).

A.2 Prostate

A.2.1 Patient History

A 73 year-old male was diagnosed with low-risk prostate cancer (Gleason 3 + 3, AJCC Stage T_{1C}) based on a PSA of 8.03 ng ml⁻¹. In 2012, he enrolled in an RTOG randomized phase II trial of hypofractionated radiotherapy for favorable risk prostate cancer (RTOG 0938).

A.2.2 Treatment Intent

The intent of the treatment was to cure the patient.

A.2.3 Simulation

The patient was implanted with 4 intra-prostatic gold fiducials.

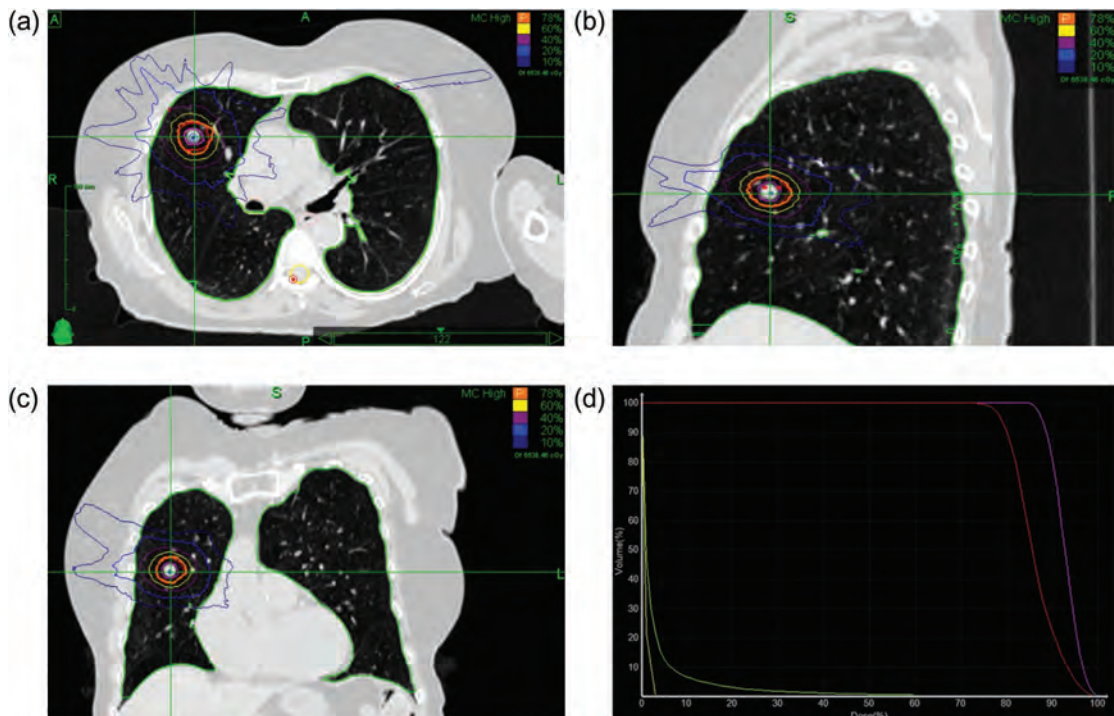


Figure A.1. Lung cancer SBRT treatment with Cyberknife. The dose distribution is in the axial (a), sagittal (b) and coronal (c) planes and the dose volume histogram is shown in (d). The PTV is shown in red, the GTV in purple, the “lungs minus GTV” in green and the spinal cord in yellow. The dose is prescribed to the 78 % isodose line (blue).

A.2.4 Target Volume and OAR Selection and Delineation

The prostate and organs at risk were contoured on the planning CT. The rectum was contoured from the anus to a length of 15 cm. The planning target volume was defined as the prostate plus a 3 mm margin posteriorly, and 5 mm in all other dimensions.

A.2.5 Planning Aims and DVH Constraints

The planning aims and DVH constraints are summarized in Table A.2.

A.2.6 Description of Treatment Planning System

Treatment was planned with Eclipse 10.0 (Varian Medical Systems, Palo Alto, CA) using an analytical anisotropic dose calculation algorithm.

A.2.7 Prescription

Treatment was in five fractions treated over 13 days to a total of 36.25 Gy (Fig. A.2).

Table A.2. Planning aims and DVH constraints used in the prostate case

Structure	Volume	Dose
PTV	Maximum dose (1 cm ³)	≤107 % of prescription
	Minimum dose to 95 % of PTV	100 % of prescription
Rectum	Maximum dose (1 cm ³)	≤105 % of prescription
	Maximum dose (3 cm ³)	≤95 % of prescription
	Dose to 50 %	≤50 % of prescription
Bladder	Maximum dose (1 cm ³)	≤105 % of prescription
	Dose to 10 %	≤90 % of prescription
	Dose to 50 %	≤50 % of prescription
Penile bulb	Maximum dose (voxel)	100 % of prescription
	Maximum dose (3 cm ³)	≤54 % of prescription
Femoral heads	Maximum dose (voxel)	≤81 % of prescription
	Maximum dose (10 cm ³)	≤54 % of prescription
Urethra	Maximum dose (voxel)	≤107 % of prescription

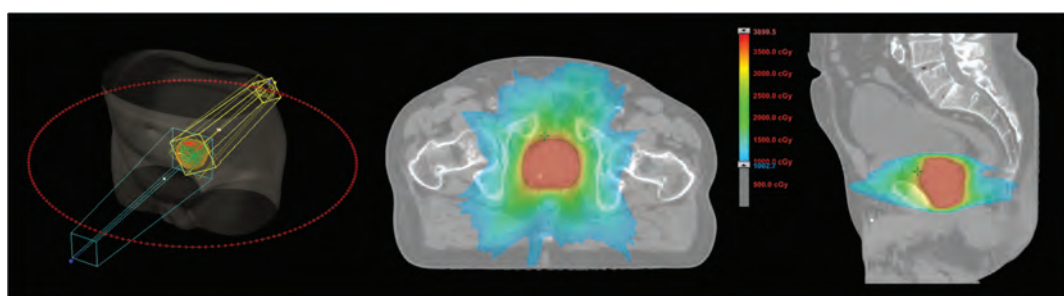


Figure A.2. Volumetric arc plan for prostate SBRT. From Left: arc trajectory, prostate target. Middle and right, axial and sagittal view.

A.2.8 Patient-specific QA

Independent monitor unit verification was performed using independent QA software (RadCalc 6, Lifeline Software Inc., Austin, TX). The point dose verified was specified to be within 3 % of the calculation from the original TPS. In addition, for each fraction, files logging MLC positions and monitor units (“dynalogs”, Varian Medical Systems, Palo Alto, CA) were analyzed using an in-house software.

A.2.9 Delivery

The treatment was planned and delivered using volumetric IMRT. Two co-planar arcs were used with perpendicular collimator angles. Daily orthogonal x-ray images were used for image guidance.

A.2.10 Dose Reporting

Target volumes. The CTV volume was 71.3 cm³ and the PTV 126.7 cm³. Median absorbed dose to the CTV and PTV was 37.5 Gy. $D_{2\%}$ was 38.1 Gy and $D_{98\%}$ was 36.4 Gy. The near maximum target dose to 1 cm³ was 105 % of the prescription dose.

Organs at Risk. The near maximum dose to the rectum (1 cm³) was 97 % of the prescription dose. The dose to 50 % of the rectum was 25 % of the prescription dose. The near maximum dose (1 cm³) to the bladder was 101 % of the prescription dose. The dose to 50 % of the bladder was 2.5 % of the prescription dose. The near maximum dose to the penile bulb (1 cm³) was 14 % of the prescription. The near maximum (1 cm³) dose to the urethra was 101 % of the prescription. The maximum point dose to the femoral head was 17.6 Gy (Fig. A.2).

Two years post-treatment, the patient’s PSA was 0.55 ng/ml and the patient experienced no bowel or bladder toxicity (he was not sexually active prior or after treatment).

A.3 Reirradiation with Stereotactic Radiotherapy

A.3.1 Patient History

A 48 year old male was diagnosed 4 years prior with a T3N1M1 sigmoid carcinoma. He had 1 liver metastasis and 1 lung nodule at the time of the diagnosis. On FDG-PET/CT scan the liver metastasis and the primary tumor were PET-positive, the lung nodule was not. The patient was first treated with a sigmoid resection followed by 6 cycles of FOLFOX. He had stable disease after chemotherapy and was treated with a wedge resection of segment 4. Thereafter, the long nodule was progressive and a biopsy revealed an adenocarcinoma. The lung metastasis was treated with stereotactic radiotherapy to a total dose of 60 Gy in 3 fractions. The GTV was contoured using the lung window. The PTV was derived by adding a 5 mm margin to the GTV. The OAR consisted of lungs, heart, and spinal cord. Inverse treatment planning was done. The outer line of the PTV was treated with a dose of 60 Gy in 3 fractions and the dose was prescribed to the 80 % isodose line (Fig. A.1). Two years later, the diagnosis was made of 3 liver metastases that were treated with radiofrequency ablation. Three months thereafter, a new lung metastasis was diagnosed, located one cm distal from the previous one.

A.3.2 Treatment Intent

The intent of the treatment was to cure the patient.

A.3.3 Simulation

The patient assumed the prone treatment position on a vacuum mattress used for the planning CT-scan. The treatment planning CT scan was made with intravenous contrast during exhalation with our wide-bore multi-slice CT simulator. The patient was scanned from his teeth to the middle of his abdomen. The trans-axial imaging had a slice thickness of 1.5 mm.

A.3.4 Target Volume and OAR Selection and Delineation

The planning CT was transferred to the treatment planning system (Accuray, Sunnyvale, CA). The tumor and organs at risk (OAR) were then contoured. The gross tumor volume (GTV, 3.28 cm^3) was contoured using the lung window. The planning target volume (PTV, 14.0 cm^3) was derived by adding a 5 mm margin to the GTV. The OAR consisted of both lungs, the heart, and the spinal cord. In the current and previous treatment plan, the lungs and the heart were contoured completely. The esophagus, spinal

cord, and trachea were contoured in each treatment plan in such a way that the length of the contoured organ was equal on both CT scans. The length of the contoured organ was based on anatomical structures such as the carina and vertebra and was based on the extents of radiation fields of both plans.

A.3.5 Planning Aims and DVH Constraints

The total dose was prescribed to the outer border of the PTV, and 95 % of the volume of the PTV had to receive the prescribed dose. The dose constraints for the organs at risk for a lung metastases are shown in Table A.1.

A.3.6 Description of Treatment Planning System

The treatment planning was made with Multiplan version 2.2.0, the treatment planning system of the Cyberknife (Accuray, Sunnyvale, CA). Multiplan has implemented both EPL and Monte Carlo (MC) dose calculation algorithms. The MC dose calculation algorithm was validated at our institution (Grofsmid *et al.*, 2010). The treatment plans in Multiplan were first recalculated with EPL and then with MC. This was done to eliminate subtle differences between the On Target and Multiplan treatment planning systems. A high-resolution grid (256^2) was used for the EPL and MC calculations and the variance in MC calculation was set to 2 %. The MC computation time was approximately 5–10 minutes.

For the dose summation, the treatment plans were recalculated with the Monte Carlo algorithm. The CT scans, dose distributions and structure sets were sent to a (in-house developed) software platform for analysis. First, two CT scans were aligned rigidly by using an automatic bone match (translation and rotation). Then, for each organ individually, a non-rigid registration was applied based on the contours of the organs at risk. Using the obtained transformation, the dose distribution of the re-irradiation was mapped to the dose grid of the first treatment and the dose values were summed after having converted both dose distributions to an equieffective dose in 2 Gy fractions with $\alpha/\beta = 3 \text{ Gy}$ ($\text{EQD}_{2.3}$) (Bentzen *et al.*, 2012). Finally, dose volume histograms (DVHs) of the organs at risk were calculated using the summed dose distribution.

The percentage volume of the lung receiving $\text{EQD}_{2.3} = 20 \text{ Gy}$ or more (V_{20}) and mean lung dose (MLD) were calculated *without* subtraction of the GTV, CTV, or PTV. The reason for this is that the target of the first irradiation was not always at the same location in the lung as the target of the second irradiation. Therefore, dose addition of the lung with subtraction of the target would have resulted in a

dose addition in a deformed lung. This deformed lung was not present at the time of the treatment, and would therefore result in a wrong calculation.

A.3.7 Prescription

The outer line of the PTV was treated with a dose of 60 Gy in 3 fractions and the dose was prescribed to the 80 % isodose line.

A.3.8 Patient-specific QA

No specific patient QA was performed.

A.3.9 Delivery

The dose was delivered with the CyberKnife. In total, non-coplanar beams were used with kV tracking.

A.3.10 Dose Reporting

The PTV was 14.0 cm^3 . The median absorbed dose to the PTV ($D_{50\%}$) was 66.9 Gy, the near minimum dose $D_{98\%}$ was 57.6 Gy and the near maximum dose

was $D_{2\%} = 73.3 \text{ Gy}$. The median absorbed dose to the GTV ($D_{50\%}$) was 71.4 Gy, the near minimum dose $D_{98\%}$ was 64.5 Gy and the near maximum dose was $D_{2\%} = 73.2 \text{ Gy}$. Doses to normal tissues (e.g., lungs, heart, spinal cord) were within the constraints (see Table A.1). As a result of the dose summation, the maximum EQD_{2,3} in the left lung was 589 Gy, and 29 cm^3 received an EQD_{2,3} of 250 Gy or more.

Figure A.3 shows the dose distribution of the first irradiation, second irradiation, and the accumulated dose distribution in the patient. Figure A.4 shows the DVH of the left lung and the PTV. The patient is now 2 years out of the re-irradiation and had no toxicity from the radiation treatments.

A.4 Spine Case using Helical TomoTherapy

A.4.1 Patient History

A 73 year old male known for metastatic clear cell renal cancer had progressive disease at the L3 vertebral body. He had previously been treated with Sunitinib following a palliative nephrectomy.

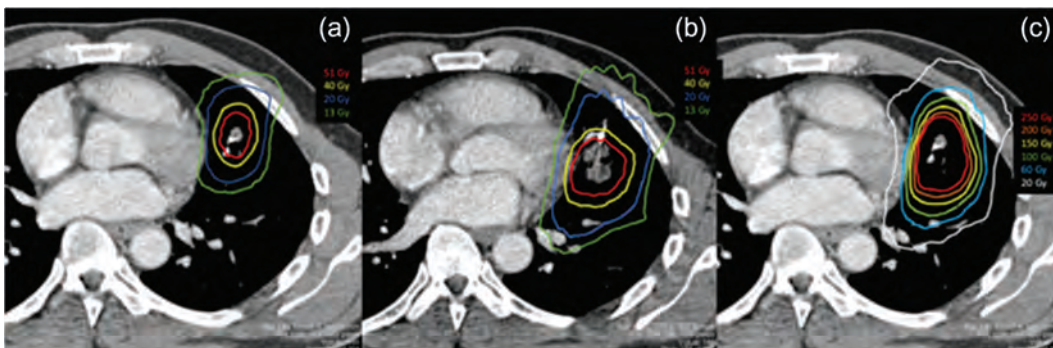


Figure A.3. (a) the dose distribution of the first irradiation in absolute dose; (b) the dose distribution of the re-irradiation in absolute physical dose; (c) accumulated dose distribution in EQD_{2,3}.

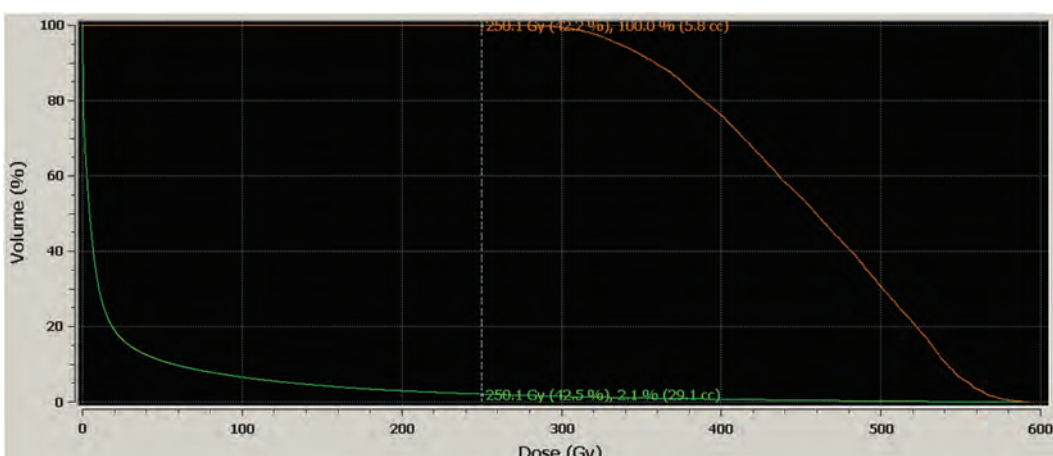


Figure A.4. DVH of a re-irradiation showing accumulated dose in the left lung (green line) and the PTV (orange line).

In 2012, the mass effect of the vertebral metastases was relieved by a decompressive laminectomy.

A.4.2 Treatment Intent

Post-operative palliative treatment.

A.4.3 Simulation

The patient was immobilized with a double vacuum cushion system and imaged with a CT simulator using 2 mm thick slices acquired every 1 mm.

A.4.4 Target Volume and OAR Selection and Delineation

To better define tumor and organs at risk, the images were co-registered to a 3D T2 simulation MRI. The clinical target volume included the gross tumor and an anatomically defined segment of the residual bony structures.

A.4.5 Planning Aims and DVH Constraints

The treatment was planned using helical TomoTherapy. A 2.5 cm jaw setting was used with a modulation factor of 2.1 and a pitch of 0.11. Each fraction was delivered with two helical arcs of 6 Gy each. Volumetric megavoltage imaging was obtained prior to each arc.

A.4.6 Description of Treatment Planning System

The treatment planning system used was TomoTherapy (Accuray, Sunnyvale, CA) with a 'fine' calculation grid (0.234 cm × 0.234 cm × 0.3 cm). TomoTherapy uses a convolution/superposition algorithm based on the collapsed cone approach.

A.4.7 Prescription

24 Gy in 2 fractions. The treatment was specified in the planning system so that 98 % of the target would receive the prescription dose of 24 Gy (Fig. A.5).

A.4.8 Patient-specific QA

The patient specific QA was performed on a ScandiDos Delta4 (ScandiDos, Uppsala, Sweden) which consists of two arrays of diodes. A gamma analysis (Low *et al.*, 1998) with pass rate of 97 % was measured using criteria of 3 % dose difference and 3 mm distance to agreement.

A.4.9 Delivery

At delivery two helical megavoltage CTs were acquired, one prior to treatment and one at mid-treatment. When necessary, the patient's position

Table A.3. Dose-volume parameters reported for the spine case with TomoTherapy

Quantity	CTV	PTV	OAR thecal sac
$D_{50\%}$ (median dose)	28.8 Gy	28.6 Gy	
Average dose	27.0 Gy	26.9 Gy	
Volume	137 cm ³	183 cm ³	
$D_{2\%}$		31.3 Gy	
$D_{98\%}$		12.9 Gy	
$D_{0.1\text{ cm}^3}$ (SRT near max)	32 Gy	13.2 Gy	
$D_{PTV-1\text{ cm}^3}$ (SRT near min)	22 Gy		
D_{\max} (maximum point dose)			14.7 Gy

was corrected after each image through the required couch translations (the gantry start angle was also adjusted as necessary).

A.4.10 Dose Reporting

The dose-volume parameters are summarized in Table A.3.

The patient had no acute or delayed toxicity of treatment but unfortunately required a second surgery and a second course of radiation (30 Gy in 4 fractions) 3 years later to treat progression of his L3 metastasis with compression of the thecal sac.

A.5 Spine Case with CyberKnife

A.5.1 Patient History

A 56 year old female presented with a solitary LI bone metastasis at the time of the diagnosis of a localized advanced breast cancer. She received front line chemotherapy but after 2 months, due to increase in local pain without neurological symptoms, stereotactic radiotherapy was considered. MRI demonstrated a solitary metastasis of the full vertebra without collapse. Treatment was considered on a G4 CyberKnife (Accuray Inc.)

A.5.2 Treatment Intent

The intent of the treatment was to palliate the patient.

A.5.3 Simulation

The patient was positioned supine on a vacuum mattress used for the planning CT-scan. The treatment planning CT scan was made with intravenous contrast in a large-bore multi-slice CT simulator. The trans-axial imaging had a slice thickness of 1.5 mm.

A.5.4 Target Volume and OAR Selection and Delineation

The tumor and OAR were then contoured. The CTV was contoured as the whole vertebra and had a volume

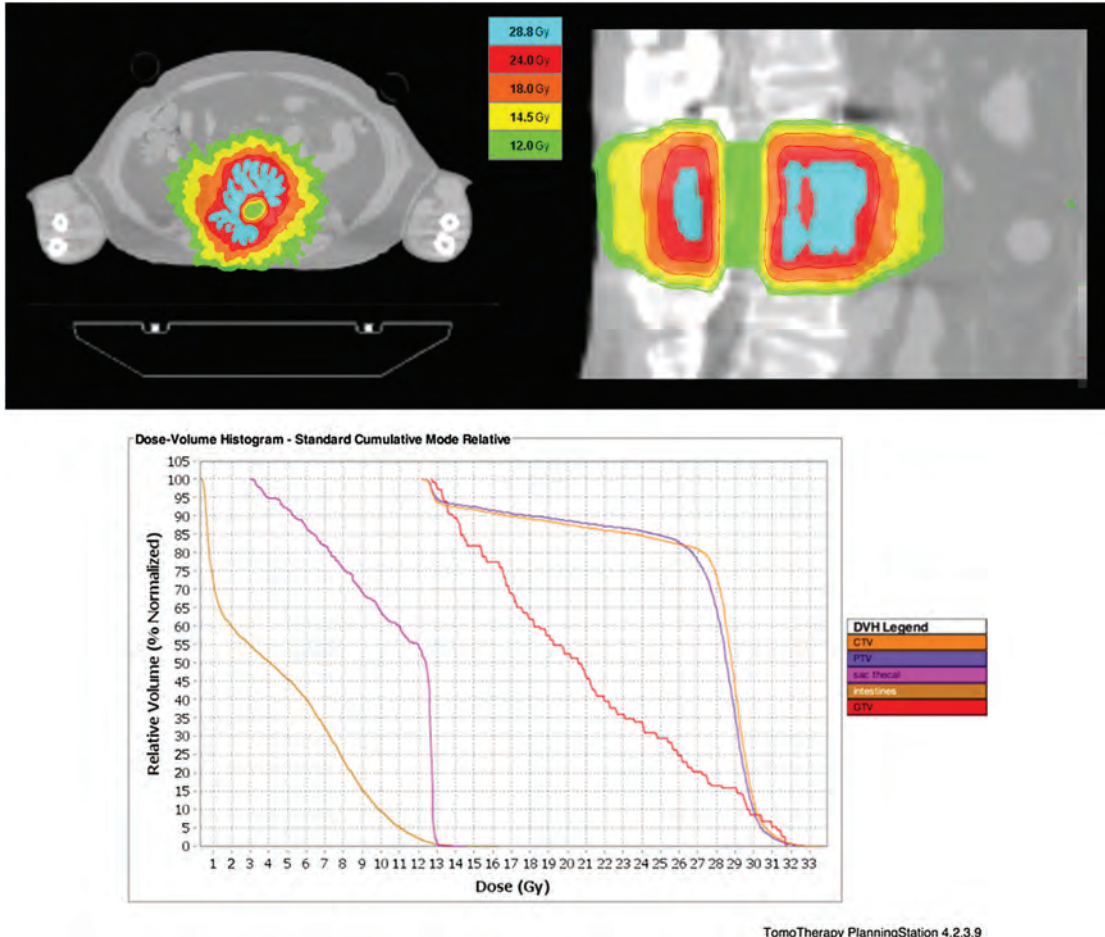


Figure A.5. Dose distribution (upper panel) and DVHs (lower panel) for the spine case using helical TomoTherapy. DVHs shown are for GTV, CTV, PTV and OARs (thecal sac, intestines).

of 161 cm^3 . The PTV (286 cm^3) was the CTV plus 3 mm margin. No GTV was contoured. The PTV was derived by adding a 5 mm margin to the GTV. The OAR consisted of liver, bowel kidney and spinal cord.

A.5.5 Planning Aims and DVH Constraints

The planning CT was transferred to the treatment planning system (Accuray, Sunnyvale, CA). Inverse treatment planning was done. Two opposite orthogonal (45 degrees) digitally reconstructed radiographs (DRRs) were generated for the tumor tracking with X-sight spine used.

A.5.6 Description of Treatment Planning System

The treatment planning was made with Multiplan version 5.1, the treatment planning system of the CyberKnife (Accuray, Sunnyvale, CA). The EPL algorithm (Ray-Tracing) was used for prescription and Monte Carlo dose calculation as a check.

A.5.7 Prescription

The PTV (outer line) was treated with a dose of 27 Gy in 3 fractions of 9 Gy and the dose was prescribed to the 85 % isodose line (Fig. A.6).

A.5.8 Patient Specific QA

No patient specific QA was performed. QA on a treatment, chosen randomly, is performed once a month.

A.5.9 Delivery

The final plan consisted of 188 non-coplanar beams.

A.5.10 Dose Reporting

The PTV was 286 cm^3 . The median absorbed dose to the PTV ($D_{50\%}$) was 29.2 Gy, the near minimum dose $D_{98\%}$ was 23.5 Gy and the near maximum dose $D_{2\%}$ was 30.8 Gy. The median absorbed dose to the CTV ($D_{50\%}$) was 29.7 Gy.

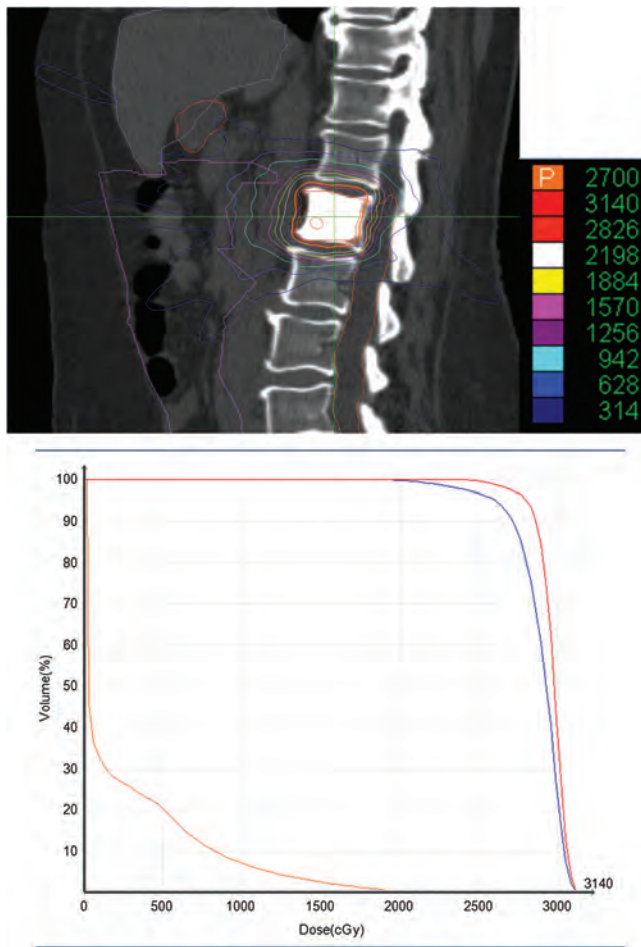


Figure A.6. Dose distribution and DVH (PTV in blue, CTV in red, OAR in orange).

A.6 Brain Metastasis

A.6.1 Patient History

A 67 year old female patient presented with brain metastasis from a breast carcinoma. No other metastatic localization.

A.6.2 Treatment Intent

Long-term palliation

A.6.3 Simulation

CT and MR were performed with the Leksell Frame on day of treatment.

A.6.4 Target Volume and OAR Selection and Delineation

The tumor was contoured on a Leksell GammaPlan (Elekta) with 1 mm thickness slices of MRI. CT and MRI were co-registered on frame fiducials. The external contour was auto segmented on

CT. No margin was used. $GTV = 1.12 \text{ cm}^3$. The OAR consisted of the entire brain.

A.6.5 Planning Aims and DVH Constraints

The volume $V_{12 \text{ Gy}}(\text{brain}) < 5 \text{ cm}^3$

A.6.6 Description of Treatment Planning System

The treatment planning was made with GammaPlan v10.1.1. The algorithm, TMR 10, is based on depth of point prescription (maximum dose) only.

A.6.7 Prescription

The GTV was treated with a dose of 24 Gy at the periphery of the volume in one fraction and the dose was prescribed to 50 % of maximum dose (Fig. A.7).

A.6.8 Patient-specific QA

No patient specific QA was performed.

A.6.9 Delivery

The dose was delivered with the GammaKnife C with the 8 mm collimator, using 7 shots (different positions of isocenter in the target, moving the frame in the machine with the auto positioning system), with different times. The dose rate was 3.1 Gy min^{-1}

A.6.10 Dose Reporting

The median absorbed dose to the GTV ($D_{50\%}$) was 31.2 Gy, the near minimum dose $D_{98\%}$ was 24.0 Gy and the near maximum dose $D_{2\%}$ was 44.7 Gy. The volume $V_{12 \text{ Gy}}(\text{brain}) = 2.9 \text{ cm}^3$

A.7 Acoustic Neuroma

A.7.1 Patient History

A 45 year old patient presented with a history of hearing loss. He has a radiological diagnosis of a 2.2 cm left acoustic neuroma as determined by MRI.

A.7.2 Treatment Intent

The intent of the treatment was to cure the patient.

A.7.3 Simulation

The patient was simulated in a thermoplastic mask. The simulation CT scan was acquired with intravenous contrast and 2 mm thick slices and 1 mm spacing. The CT images were co-registered to two thin-slice MRI image sets: a contrast-enhanced

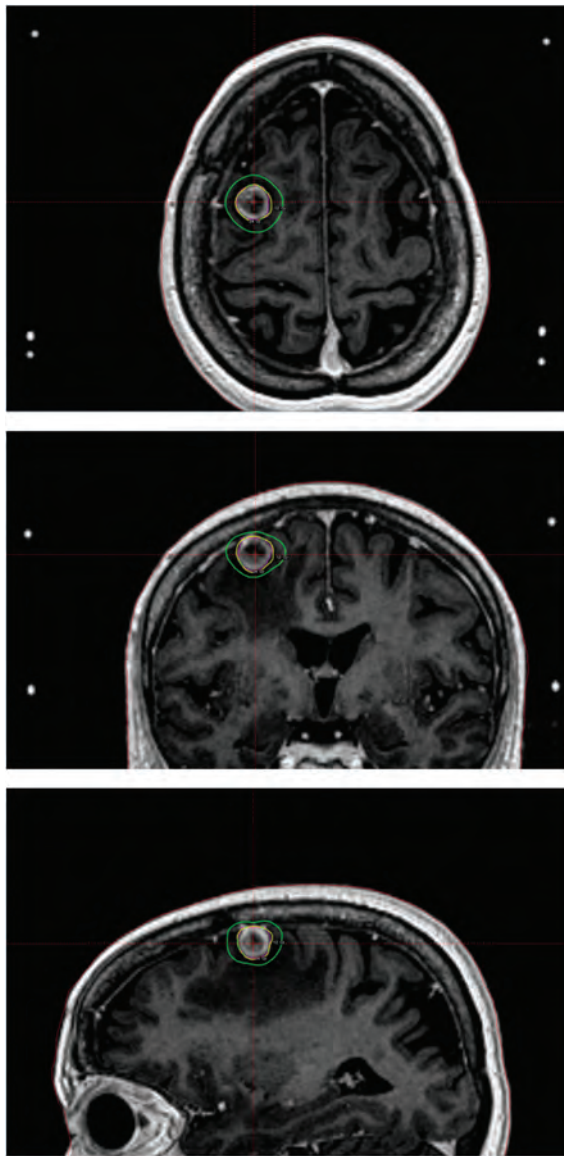


Figure A.7. 24 Gy (prescription) and 12 Gy isodoses are indicated in yellow and green lines, respectively.

3D T1 image set (1 mm slices) and a focal gradient echo series (constructive interference in steady state (CISS), 0.6 mm slices).

A.7.4 Target Volume and OAR Selection and Delineation

The GTV was 4.58 cm^3 in volume. The GTV equaled the CTV and PTV. Eyes, oral cavity and brainstem were defined as organs at risk (in more recent practice, the cochlea is also routinely defined as an OAR).

A.7.5 Planning Aims and DVH Constraints

Beams were blocked from entering through the eyes or oral cavity. Conformity and gradient were optimized using concentric planning structures

defined around the PTV. The volume of brainstem receiving more than 18 Gy was minimized (as was the maximum dose to the brainstem). Improved gradient and cochlear sparing was achieved while allowing greater dose inhomogeneity within the target.

A.7.6 Description of Treatment Planning System

The treatment planning was made with Multiplan version 3.5.2, the treatment planning system of the Cyberknife (Accuray, Sunnyvale, CA). The EPL algorithm (Ray-Tracing) was used for calculation in a high-resolution grid (Fig. A.8).

A.7.7 Prescription

18 Gy in 3 fractions on non-consecutive days specified to the 83 % isodose surface.

A.7.8 Patient-specific QA

Independent monitor unit verification was performed using independent QA software (RadCalc 6, Lifeline Software Inc., Austin, TX). The point dose verified was specified to be within 2 % of the calculation from the original Accuray TPS.

A.7.9 Delivery

The non-isocentric plan was delivered with stereoscopic image guidance. A single fixed 15 mm collimator was used to deliver a total of 10 151 monitor units through 60 beams (*i.e.*, 50 nodes).

A.7.10 Dose Reporting

The GTV volume was 4.29 cm^3 . The median absorbed dose to the GTV ($D_{50\%}$) was 20.4 Gy, the SRT near minimum dose for a volume of 100 mm^3 was 18.5 Gy and the SRT near maximum dose for a volume of 100 mm^3 was 20.6 Gy. The near minimum dose $D_{98\%}$ was 18.4 Gy and the near maximum dose $D_{2\%}$, was 20.7 Gy. The conformity index (CI) was 1.4. The gradient index (GI) was 4.7.

A.8 Hepatocarcinoma

A.8.1 Patient History

A 67 year old male with past medical history of diabetes and child A6 common cirrhosis (alcohol) was referred for a nodule of the right liver (2 cm in February 2014). Biopsies confirm an hepatocarcinoma (grade 2). Due to hepatic failure at that time, no specific treatment was proposed outside best supportive care. In June 2014, new staging demonstrated better liver function with a stable liver mass (2.5 cm). SBRT was recommended by a multidisciplinary board.

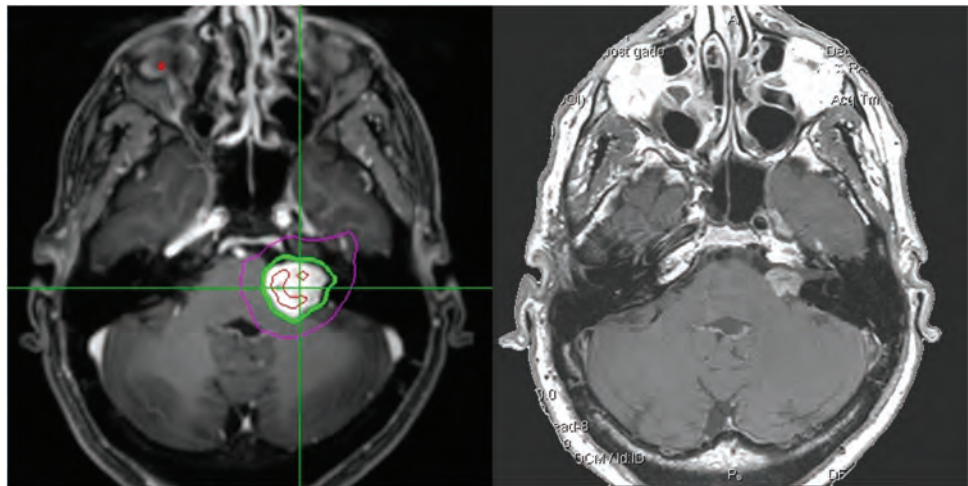


Figure A.8. Left panel: Dose distribution for the treatment of an acoustic neuroma (green: 18 Gy prescription, red: 21 Gy, pink: 9 Gy). Right panel: follow-up MRI.

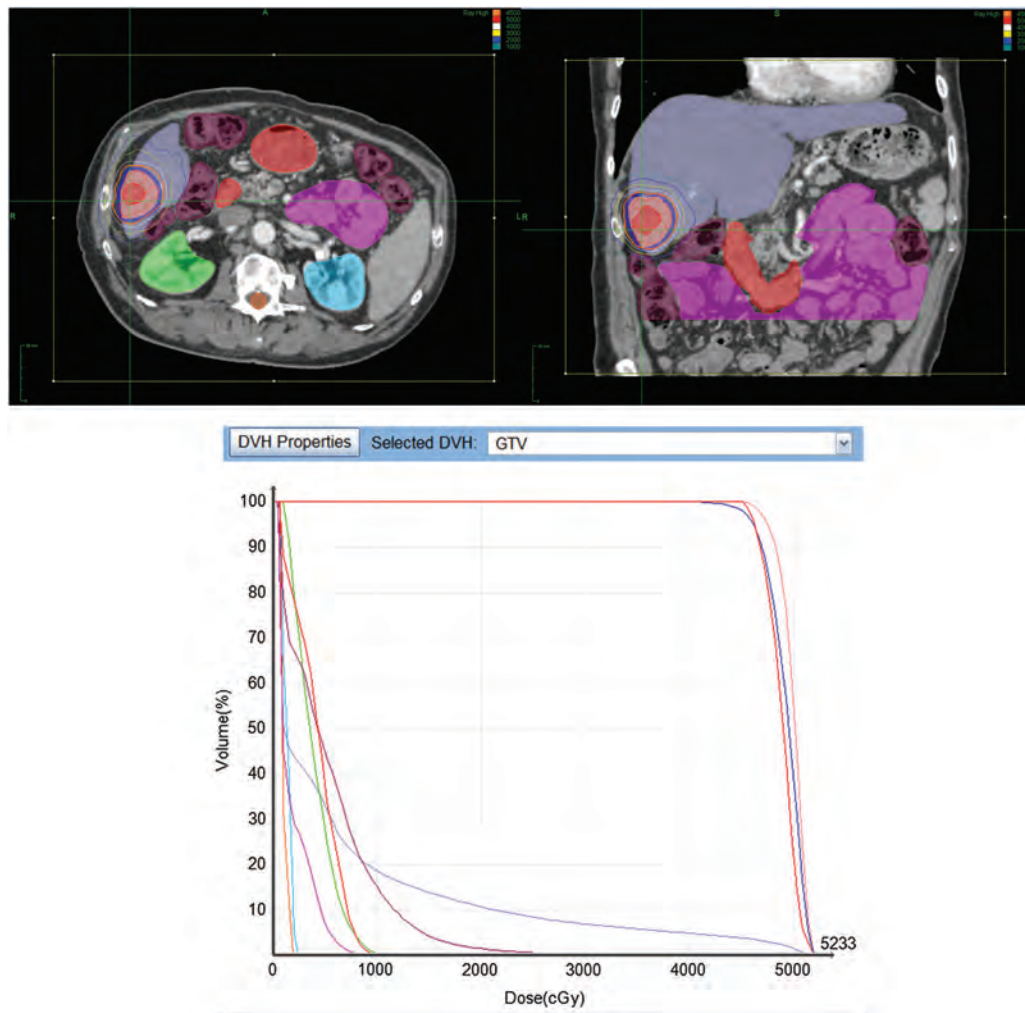


Figure A.9. Coronal (upper panel, right) and axial slices (upper panel left) of the liver treatment plan. Lower panel shows the DVHs with color curves matched to the colorwash used in the organs shown in the upper panel.

A.8.2 Treatment Intent

The intent of the treatment was to cure the patient.

A.8.3 Simulation

Gold seeds (fiducials) were implanted around the lesion. 7 days after placement of the fiducial markers the patient was in supine position on a mattress used at the planning CT-scan. The treatment planning CT scan was made with intravenous contrast during exhalation with a wide-bore CT. The patient was scanned from the carina to the hips. The axial imaging had a slice thickness of 3 mm to have a better contrast for contouring; same acquisition was used to create slices of 1 mm thickness to define fiducial positions with the highest resolution.

A.8.4 Target Volume and OAR Selection and Delineation

The tumor and OAR were contoured on a Masterplan workstation (Elekta, Veenendaal, Netherlands) with 3 mm thickness slices and copied to 1 mm thickness slices. The contouring was performed on the planning CT with contrast. The patient had previously undergone MRI to rule out additional hepatic lesions; the MRI was used as a visual reference for contouring without registration. The GTV included contrast-enhanced disease visible on CT scan or MRI with contrast. The CTV included the GTV and a 1-cm margin of liver to account for possible microscopic disease (today only 5 mm is used for the GTV-CTV margin for primary liver tumor), and the PTV encompassed the CTV with 3 mm expansion. (GTV = 97.9 cm³; CTV = 454 cm³; PTV = 681 cm³).

The OAR consisted of right kidney, the large bowel, the ribs and the liver itself. The planning CT and the ROI were transferred to the treatment planning system (Accuray, Sunnyvale, CA).

A.8.5 Planning Aims and DVH Constraints

The planning aims and DVH constraints are summarized in Tables A.4 and A.5.

A.8.6 Description of Treatment Planning System

The treatment planning was made with Multiplan version 5.1, the treatment planning system of the CyberKnife (Accuray, Sunnyvale, CA). The EPL algorithm (Ray-Tracing) was used for prescription and Monte Carlo dose calculation only as a check (Fig. A.9).

Table A.4. The dose constraints for the organs at risk for treatment of a liver tumor with 3 fractions

Liver	$V_{15} < 50\%$ $V_{21} < 33\%$ $V_{\text{total}} - V_{17} > 700\text{ cm}^3$
Stomach	$V_{19} < 10\text{ cm}^3$ $V_{21} < 5\text{ cm}^3$ $V_{25} < 0.5\text{ cm}^3$
Duodenum	$V_{15} < 5\text{ cm}^3$ $V_{24} < 0.5\text{ cm}^3$
Small bowel	$V_{16} < 5\text{ cm}^3$ $V_{27} < 0.5\text{ cm}^3$
Large bowel	$V_{20} < 20\text{ cm}^3$ $V_{30} < 1\text{ cm}^3$
Kidneys	$V_{10} < 50\%$ $V_{\text{total}} - V_{15} > 200\text{ cm}^3$
Ribs	$V_{22} < 10\text{ cm}^3$ $V_{29} < 1\text{ cm}^3$ $V_{37} < 0.035\text{ cm}^3$

Table A.5. Dose-volume parameters for target and OARs of the liver treatment

Liver	$V_{15} = 13.7\%$ $V_{21} = 10\%$ $V_{\text{total}} - V_{17} > 1237\text{ cm}^3$
Large bowel	$V_{20} = 6.9\text{ cm}^3$ $V_{30} = 0.3\text{ cm}^3$
Right Kidney	$V_{10} = 10\%$
Ribs	$V_{22} = 3.7\text{ cm}^3$ $V_{29} = 0.98\text{ cm}^3$ $V_{37} = 0.03\text{ cm}^3$

A.8.7 Prescription

The PTV was treated with a dose of 45 Gy in 3 fractions and the dose was prescribed to the 86 % of maximum dose.

A.8.8 Patient-specific QA

No patient specific QA was performed. A specific QA, chosen randomly, was performed once a month.

A.8.9 Delivery

The dose was delivered with the CyberKnife, using Synchrony (*i.e.*, real-time respiratory tracking system that builds a correlation model between external markers and fiducials). In total, 92 non-coplanar beams were used (*i.e.*, 44 nodes) with a total of 8444 monitor units per fraction.

A.8.10 Dose Reporting

The median absorbed dose to the PTV ($D_{50\%}$) was 49.5 Gy, the near minimum dose $D_{98\%}$ was

44.9 Gy and the near maximum dose was $D_{2\%} = 51.6$ Gy.

The median absorbed dose to the CTV ($D_{50\%}$) was 50.0 Gy, the near minimum dose $D_{98\%}$ was 46.5 Gy and the near maximum dose was $D_{2\%} = 51.7$ Gy.

The median absorbed dose to the GTV ($D_{50\%}$) was 48.9 Gy, the near minimum dose $D_{98\%}$ was 45.6 Gy and the near maximum dose was $D_{2\%} = 51.4$ Gy.

Doses to normal tissues (e.g., liver, large bowel, kidney, ribs) were within the constraints (Table A.5).

References

- AAPM (1983). American Association of Physicists in Medicine. "A protocol for determination of absorbed dose from high-energy photon and electron beam," *Med. Phys.* **10**(6): 741–771.
- AAPM (2006). American Association of Physicists in Medicine. *The Management of Respiratory Motion in Radiation Oncology*, AAPM Report No. 91 (American Association of Physicists in Medicine, Alexandria, VA).
- AAPM (2009). American Association of Physicists in Medicine. *The Role of In-Room kV X-Ray Imaging for Patient Setup and Target Localization*, AAPM Report No. 104 (American Association of Physicists in Medicine, Alexandria, VA).
- Arup, L.R., Nahum, A.E., Zacharatou, C., Juhler-Nottrup, T., Knoos, T., Nystrom, H., Specht, L., Wieslander, E., and Korreman, S.S. (2009). "The effect of different lung densities on the accuracy of various radiotherapy dose calculation methods: Implications for tumour coverage," *Radiother. Oncol.* **91**, 405–414.
- Adler, J.R. Jr, Chang, S.D., Murphy, M.J., Doty, J., Geis, P., and Hancock, S.L. (1997). "The Cyberknife: A frameless robotic system for radiosurgery," *Stereotact. Funct. Neurosurg.* **69**, 124–128.
- Adler, J.R. Jr, Murphy, M.J., Chang, S.D., and Hancock, S.L. (1999). "Image-guided robotic radiosurgery," *Neurosurgery* **44**, 1299–1306; discussion 1306–1307.
- Afsharpour, H., Landry, G., D'Amours, M., Enger, S., Reniers, B., Poon, E., Carrier, J.F., Verhaegen, F., and Beaulieu, L. (2012). "ALGEBRA: Algorithm for the heterogeneous dosimetry based on GEANT4 for brachytherapy," *Phys. Med. Biol.* **57**, 3273–3280.
- Ahnesjö, A. (1989). "Collapsed cone convolution of radiant energy for photon dose calculation in heterogeneous media," *Med. Phys.* **16**, 577–592.
- Ahnesjö, A., and Aspradakis, M.M. (1999). "Dose calculations for external photon beams in radiotherapy," *Phys. Med. Biol.* **44**, R99–155.
- Ahnesjö, A., Andreo, P., and Brahme, A. (1987). "Calculation and application of point spread functions for treatment planning with high energy photon beams," *Acta Oncol.* **26**, 49–56.
- Ahnesjö, A., Weber, L., Murman, A., Saxner, M., Thorslund, I., and Traneus, E. (2005) Beam modeling and verification of a photon beam multisource model. *Med. Phys.* **32**, 1722–1737.
- AJCC (2010). American Joint Committee on Cancer. *Cancer Staging Handbook*, 7th ed. (Springer, New York).
- Alaei, P., Ding, G., and Guan, H. (2010). "Inclusion of the dose from kilovoltage cone beam CT in the radiation therapy treatment plans," *Med. Phys.* **37**, 244–248.
- Alexander, A., Soisson, E., Hijal, T., Sarfehnia, A., and Seuntjens, J. (2011). "Comparison of modulated electron radiotherapy to conventional electron boost irradiation and volumetric modulated photon arc therapy for treatment of tumour bed boost in breast cancer," *Radiother. Oncol.* **100**, 253–258.
- Alfonso, R., Andreo, P., Capote, R., Huq, M.S., Kilby, W., Kjall, P., Mackie, T.R., Palmans, H., Rosser, K., Seuntjens, J., Ullrich, W., and Vatnitsky, S. (2008). "A new formalism for reference dosimetry of small and nonstandard fields," *Med. Phys.* **35**, 5179–5186.
- Almond, P.R., Biggs, P.J., Coursey, B.M., Hanson, W.F., Huq, M.S., Nath, R., and Rogers, D.W. (1999). "AAPM's TG-51 protocol for clinical reference dosimetry of high-energy photon and electron beams," *Med. Phys.* **26**, 1847–1870.
- Alongi, F., Arcangeli, S., Filippi, A.R., Ricardi, U., and Scorsetti, M. (2012). "Review and uses of stereotactic body radiation therapy for oligometastases," *Oncologist* **17**, 1100–1107.
- Aluwini, S., van Rooij, P., Hoogeman, M., Bangma, C., Kirkels, W.J., Incrocci, L., and Kolkman-Deurloo, I.K. (2010). "CyberKnife stereotactic radiotherapy as monotherapy for low- to intermediate-stage prostate cancer: Early experience, feasibility, and tolerance," *J. Endourol.* **24**, 865–869.
- Andreo, P. (1991). "Monte Carlo techniques in medical radiation physics," *Phys. Med. Biol.* **36**, 861–920.
- Andreo, P. (2000). "On the beam quality specification of high-energy photons for radiotherapy dosimetry," *Med. Phys.* **27**, 434–440.
- Andreo, P. (2015). "Dose to 'water-like' media or dose to tissue in MV photons radiotherapy treatment planning: still a matter of debate," *Phys. Med. Biol.* **60**, 309–337.
- Antypas, C., and Pantelis, E. (2008). "Performance evaluation of a CyberKnife G4 image-guided robotic stereotactic radiosurgery system," *Phys. Med. Biol.* **53**, 4697–4718.
- Aoyama, H., Shirato, H., Tago, M., Nakagawa, K., Toyoda, T., Hattano, K., Kenjyo, M., Oya, N., Hirota, S., Shioura, H., Kunieda, E., Inomata, T., Hayakawa, K., Katoh, N., and Kobashi, G. (2006). "Stereotactic radiosurgery plus whole-brain radiation therapy vs stereotactic radiosurgery alone for treatment of brain metastases: a randomized controlled trial," *JAMA* **295**, 2483–2491.

PRESCRIBING, RECORDING, AND REPORTING SMALL BEAM SRT

- Araki, F. (2006). "Monte Carlo study of a Cyberknife stereotactic radiosurgery system," *Med. Phys.* **33**, 2955–2963.
- Archambault, L., Beddar, A.S., Gingras, L., Roy, R. and Beaulieu, L. (2006). "Measurement accuracy and cerenkov removal for high performance, high spatial resolution scintillation dosimetry," *Med. Phys.* **33**, 128–135.
- Archambault, L., Beddar, A.S., Gingras, L., Lacroix, F., Roy, R., and Beaulieu, L. (2007). "Water-equivalent dosimeter array for small-field external beam radiotherapy," *Med. Phys.* **34**, 1583–1592.
- Arndt, J (1999) Gamma Knife Dosimetry and Treatment Planning. MO-B1. *41st Annual Meeting of the American Association of Physicists in Medicine*. Nashville. (<https://www.aapm.org/meetings/99AM/handouts.html> (December 2016, last date accessed) (American Association of Physicists in Medicine, Arlington, VA).
- Artignan, X., Smitsmans, M.H., Lebesque, J.V., Jaffray, D.A., van Her, M., and Bartelink, H. (2004). "Online ultrasound image guidance for radiotherapy of prostate cancer: impact of image acquisition on prostate displacement," *Int. J. Radiat. Oncol. Biol. Phys.* **59**, 595–601.
- Aspradakis, M.M., Morrison, R.H., Richmond, N.D., and Steele, A. (2003). "Experimental verification of convolution/superposition photon dose calculations for radiotherapy treatment planning," *Phys. Med. Biol.* **48**, 2873–2893.
- Aspradakis, M.M., Byrne, P.J., Palmans, H., Conway, J., Warrington, A.P., Rosser, K., and Duane, S. (2010). *Standards, Applications and Quality Assurance in Medical Radiation Dosimetry (IDOS), Small Field MV Photon Dosimetry*, IPEM Report 103 (International Atomic Energy Agency, Vienna).
- Astreinidou, E., Bel, A., Raaijmakers, C.P., Terhaard, C. H., and Lagendijk, J.J. (2005). "Adequate margins for random setup uncertainties in head-and-neck IMRT," *Int. J. Radiat. Oncol. Biol. Phys.* **61**, 938–944.
- Attix, F.H. (1986). *Introduction to Radiological Physics and Radiation Dosimetry* (Willey-VCH, Weinheim).
- Austin-Seymour, M., Kalet, I., McDonald, J., KromhoutSchiro, S., Jacky, J., Hummel, S., and Unger, J. (1995). "Three dimensional planning target volumes: A model and a software tool," *Int. J. Radiat. Oncol. Biol. Phys.* **33**, 1073–1080.
- Balter, J.M., TenHaken, R.K., Lawrence, T.S., Lam, K.L., and Robertson, J.M. (1996). "Uncertainties in CT-based radiation therapy treatment planning associated with patient breathing," *Int. J. Radiat. Oncol. Biol. Phys.* **36**, 167–174.
- Balter, J.M., Wright, N., Dimmer, S., Friemel, B., Newell, J., Cheng, Y., and Mate, T. (2003). "Demonstration of accurate localization and continuous tracking of implantable wireless electromagnetic transponders," *Int. J. Radiat. Oncol. Biol. Phys.* **57**, S264–S265.
- Balter, J.M., Wright, J.N., Newell, L.J., Friemel, B., Dimmer, S., Cheng, Y., Wong, J., Vertatschitsch, E., and Mate, T.P. (2005). "Accuracy of a wireless localization system for radiotherapy," *Int. J. Radiat. Oncol. Biol. Phys.* **61**, 933–937.
- Barcia-Salorio, J.L., Hernandez, G., Broseta, J., Gonzalez-Darder, J., and Ciudad, J. (1982). "Radiosurgical treatment of carotid-cavernous fistula," *Appl. Neurophysiol.* **45**, 520–522.
- Baron, R.L. (1994). "Understanding and optimizing use of contrast material for CT of the liver," *AJR Am. J. Roentgenol.* **163**, 323–331.
- Bassinet, C., Huet, C., Derreumaux, S., Brunet, G., Chea, M., Baumann, M., Lacornerie, T., Gaudaire-Josset, S., Trompier, F., Roch, P., Boisserie, G., and Clairand, I. (2013). "Small fields output factors measurements and correction factors determination for several detectors for a CyberKnife(R) and linear accelerators equipped with microMLC and circular cones," *Med. Phys.* **40**, 071725.
- Batho, H.F. (1964). "Lung corrections in Cobalt 60 beam therapy," *J. Can. Assoc. Radiol.* **15**, 79–83.
- Baum, C., Alber, M., and Nusslin, F. (2006). "Dosimetric consequences of the application of a rectum hull-planning volume for treatment planning of intensity modulated radiotherapy of prostate cancer," *Med. Phys.* **16**, 208–216.
- Beddar, S., and Briere, T.M. (2009). "Plastic scintillation detectors," pp. 978–1082 in *Clinical Dosimetry Measurements in Radiotherapy*, Rogers, D.W., and Cygler, J.E., Eds. (American Association of Physicists in Medicine Summer School, Madison, WI).
- Beddar, A.S., Briere, T.M., Balter, P., Pan, T., Tolani, N., Ng, C., Szklaruk, J., and Krishnan, S. (2008). "4D-CT imaging with synchronized intravenous contrast injection to improve delineation of liver tumors for treatment planning," *Radiother. Oncol.* **87**, 445–448.
- Benedict, S.H., Yenice, K.M., Followill, D., Galvin, J.M., Hinson, W., Kavanagh, B., Keall, P., Lovelock, M., Meeks, S., Papiez, L., Purdie, T., Sadagopan, R., Schell, M.C., Salter, B., Schlesinger, D.J., Shiu, A.S., Solberg, T., Song, D.Y., Stieber, V., Timmerman, R., Tome, W.A., Verellen, D., Wang, L., and Yin, F.F. (2010). "Stereotactic body radiation therapy: The report of AAPM Task Group 101," *Med. Phys.* **37**, 4078–4101.
- Benmakhoul, H., Sempau, J., and Andreo, P. (2014). "Output correction factors for nine small field detectors in 6 MV radiation therapy photon beams: A PENELOPE Monte Carlo study," *Med. Phys.* **41**, 041711.
- Bentzen, S.M., and Gregoire, V. (2011). "Molecular imaging-based dose painting: A novel paradigm for radiation therapy prescription," *Semin. Radiat. Oncol.* **21**, 101–110.
- Bentzen, S.M., Dorr, W., Gahbauer, R., Howell, R.W., Joiner, M.C., Jones, B., Jones, D.T., van der Kogel, A.J., Wambersie, A., and Whitmore, G. (2012). "Bioeffect modeling and equieffective dose concepts in radiation oncology – Terminology, quantities and units," *Radiother. Oncol.* **105**, 266–268.
- Bert, C., Methane, K.G., Doppke, K., and Chen, G.T. (2005). "A phantom evaluation of a stereo-vision surface imaging system for radiotherapy patient setup," *Med. Phys.* **32**, 2753–2762.
- Betti, O., and Derechinsky, V. (1982). "Multilayer stereotaxic irradiation," *Neurochirurgie* **28**, 55–56.
- Bezjak, A., Papiez, L., Bradley, J., Gore, E., Gaspar, L., Kong, F.M., Timmerman, R., Hu, C., and Normolle, D.

References

- (2009). *Seamless Phase I/II Study of Stereotactic Lung Radiotherapy (SBRT) for Early Stage, Centrally Located, Non-Small Cell Lung Cancer (NSCLC) in Medically Inoperable Patients*, RTOG 0813 (American College of Radiology, Reston, VA).
- Bhatnagar, J.P., Novotny, J. Jr, and Huq, M.S. (2012). “Dosimetric characteristics and quality control tests for the collimator sectors of the Leksell Gamma Knife® Perfexion™,” *Med. Phys.* **39**, 231–236.
- Bibault, J.E., Mirabell, X., Lacornerie, T., Tresch, E., Reynaert, N. and Lartigau, E. (2015). “Adapted prescription dose for Monte Carlo algorithm in lung SBRT: Clinical outcome on 205 patients,” *PLoS One* **10**(7), e0133617, doi:10.1371/journal.pone.0133617.
- BIR (1996). British Institute of Radiology. *Central Axis Depth Dose Data for Use in Radiotherapy, 1996: A Survey of Depth Doses and Related Data Measured in Water or Equivalent Media*, BJR Suppl. 25 (British Institute of Radiology, London).
- Bissonnette, J.P., Moseley, D.J., and Jaffray, D.A. (2008). “A quality assurance program for image quality of cone-beam CT guidance in radiation therapy,” *Med. Phys.* **35**, 1807–1815.
- Bissonnette, J.P., Purdie, T.G., Higgins, J.A., Li, W., and Bezjak, A. (2009). “Cone-beam computed tomographic image guidance for lung cancer radiation therapy,” *Int. J. Radiat. Oncol. Biol. Phys.* **73**, 927–934.
- Bissonnette, J.P., Balter, P.A., Dong, L., Langen, K.M., Lovelock, D.M., Miften, M., Moseley, D.J., Pouliot, J., Sonke, J.J., and Yoo, S. (2012). “Quality assurance for image-guided radiation therapy utilizing CT-based technologies: A report of the AAPM TG-179,” *Med. Phys.* **39**, 1946–1963.
- Bjarnsgard, B.E., and Kase, K.R. (1985). “Replacement correction factors for photon and electron dose measurements,” *Med. Phys.* **12**, 785–787.
- Bjarnsgard, B.E., Zhu, T.C., and Ceberg, C. (1996). “Tissue-phantom ratios from percentage depth doses,” *Med. Phys.* **23**, 629–634.
- Boda-Heggemann, J., Kohler, F.M., Kupper, B., Wolff, D., Wertz, H., Mai, S., Hesser, J., Lohr, F., and Wenz, F. (2008). “Accuracy of ultrasound-based (BAT) prostate-repositioning: a three-dimensional on-line fiducial-based assessment with cone-beam computed tomography,” *Int. J. Radiat. Oncol. Biol. Phys.* **70**, 1247–1255.
- Boehling, N.S., Grosshans, D.R., Allen, P.K., McAleer, M.F., Burton, A.W., Azeem, S., Rhines, L.D., and Chang, E.L. (2012). “Vertebral compression fracture risk after stereotactic body radiotherapy for spinal metastases,” *J. Neurosurg. Spine* **16**, 379–386.
- Bogdanich, W., and Rebelo, K. (2010). “A pinpoint beam strays invisibly, harming instead of healing,” *NY Times* (December 28)
- Bolzicco, G., Favretto, M.S., Scremin, E., Tambone, C., Tasca, A., and Guglielmi, R. (2010). “Image-guided stereotactic body radiation therapy for clinically localized prostate cancer: Preliminary clinical results,” *Technol. Cancer Res. Treat.* **9**, 473–477.
- Bondiau, P.Y., Courdi, A., Bahadoran, P., Chamorey, E., Queille-Roussel, C., Lallement, M., Birtwistle-Peyrottes, I., Chapellier, C., Pacquelet-Cheli, S., and Ferrero, J.M. (2013). “Phase 1 clinical trial of stereotactic body radiation therapy concomitant with neoadjuvant chemotherapy for breast cancer,” *Int. J. Radiat. Oncol. Biol. Phys.* **85**, 1193–1199.
- Bouchard, H., and Seuntjens, J. (2004). “Ionization chamber-based reference dosimetry of intensity modulated radiation beams,” *Med. Phys.* **31**, 2454–2465.
- Bouchard, H., and Seuntjens, J. (2013). “Application of Monte Carlo techniques in radiation therapy,” pp. 43–64 in *Monte Carlo Techniques in Radiation Therapy*, Seco, J. and Verhaegen, F. (Taylor and Francis Books, Inc, Florence, KY).
- Bouchard, H., Seuntjens, J., and Palmans, H. (2012). “On charged particle equilibrium violation in external photon fields,” *Med. Phys.* **39**, 1473–1480.
- Boswell, S., Tome, W., Jeraj, R., Jaradat, H., and Mackie, T.R. (2006). “Automatic registration of megavoltage to kilovoltage CT images in helical tomotherapy: An evaluation of the setup verification process for the special case of a rigid head phantom,” *Med. Phys.* **33**, 4395–4404.
- Bova, F.J., Buatti, J.M., Friedman, W.A., Mendenhall, W.M., Yang, C.C., and Liu, C. (1997). “The University of Florida frameless high-precision stereotactic radiotherapy system,” *Int. J. Radiat. Oncol. Biol. Phys.* **38**, 875–882.
- Boyer, A., and Mok, E. (1985). “A photon dose distribution model employing convolution calculations,” *Med. Phys.* **12**, 169–177.
- Boyer, A.L., Antonuk, L., Fenster, A., Van Herk, M., Meertens, H., Munro, P., Reinstein, L.E., and Wong, J. (1992). “A review of electronic portal imaging devices (EPIDs),” *Med. Phys.* **19**, 1–16.
- Bradbury, M., and Hricak, H. (2005). “Molecular MR imaging in oncology,” *Magn. Reson. Imaging Clin. N. Am.* **13**, 225–240.
- Brahme, A. (1988). “Optimal setting of multileaf collimators in stationary beam radiation therapy,” *Strahlenther. Onkol.* **164**, 343–350.
- Bral, S., Gevaert, T., Linthout, N., Versmessen, H., Collen, C., Engels, B., Verdries, D., Everaert, H., Christian, N., De Ridder, M., and Storme, G. (2011). “Prospective, risk-adapted strategy of stereotactic body radiotherapy for early-stage non-small-cell lung cancer: Results of a Phase II trial,” *Int. J. Radiat. Oncol. Biol. Phys.* **80**, 1343–1349.
- Brenner, D.J. (2008). “The linear-quadratic model is an appropriate methodology for determining isoeffective doses at large doses per fraction,” *Semin. Radiat. Oncol.* **18**, 234–239.
- Brock, K.K., Mutic, S., McNutt, T.R., Li, H., Kessler, M.L. (2017). “Use of image registration and fusion algorithms and techniques in radiotherapy: Report of the AAPM Radiation Therapy Committee Task Group No. 132,” *Med. Phys.* (DOI:10.1002/mp.12256).
- Brown, J.M., Brenner, D.J., and Carlson, D.J. (2013). “Dose escalation, not ‘new biology,’ can account for the efficacy of stereotactic body radiation therapy with non-small cell lung cancer,” *Int. J. Radiat. Oncol. Biol. Phys.* **85**, 1159–1160.
- Brown, J.M., Carlson, D.J., and Brenner, D.J. (2014). “The tumor radiobiology of SRS and SBRT: Are more

- than the 5 Rs involved?," *Int. J. Radiat. Oncol. Biol. Phys.* **88**, 254–262.
- Bujold, A., Craig, T., Jaffray, D., and Dawson, L.A. (2012). "Image-guided radiotherapy: Has it influenced patient outcomes?," *Semin. Radiat. Oncol.* **22**, 50–61.
- Bunge, H., Guevara, J., and Chinela, A. (1987). "Stereotactic brain radiosurgery with Gamma Unit III RBS 5000," in *Proceedings of the 8th European Congress of Neurosurgery Barcelona*, Isamat, F., Jefferson, A., Loew, F., and Symon, L., Eds., *Acta Neurochirurgica Suppl.* **42** (Springer, Vienna).
- Burghlela, M., Verellen, D., Gevaert, T., Depuydt, T., Poels, K., Simon, V., and De Ridder, M. (2014). "Feasibility of using the Vero SBRT system for intra-cranial SRS," *J. Appl. Clin. Med. Phys.* **15**, 4437.
- Burns, D.T. (2012). "An analysis of existing data for Wair, Ic and the product Wairsc, air," *Metrologia* **49**, 507–512.
- Burns, D.T., Picard, S., Kessler, C., and Roger, P. (2014). "Use of the BIPM calorimetric and ionometric standards in megavoltage photon beams to determine Wair and Ic," *Phys. Med. Biol.* **59**, 1353–1365.
- Burridge, N., Amer, A., Marchant, T., Sykes, J., Stratford, J., Henry, A., McBain, C., Price, P., and Moore, C. (2006). "Online adaptive radiotherapy of the bladder: Small bowel irradiated-volume reduction," *Int. J. Radiat. Oncol. Biol. Phys.* **66**, 892–897.
- Bush, K., Gagne, I.M., Zavgorodni, S., Ansbacher, W., and Beckham, W. (2011). "Dosimetric validation of Acuros XB with Monte Carlo methods for photon dose calculations," *Med. Phys.* **38**, 2208–2221.
- Buttar, C.M., Conway, J., Meyfarth, R., Scarsbrook, G., Sellin, P.J., and Whitehead, A. (1997). "CVD diamond detectors as dosimeters for radiotherapy," *Nucl. Instr. Meth. Phys. Res. A* **392**, 281–284.
- Capote, R., Sanchez-Doblado, F., Leal, A., Lagares, J.I., Arrans, R., and Hartmann, G.H. (2004). "An EGSnrc Monte Carlo study of the microionization chamber for reference dosimetry of narrow irregular IMRT beamlets," *Med. Phys.* **31**, 2416–2422.
- Carrasco, P., Jornet, N., Duch, M.A., Weber, L., Ginjaume, M., Eudaldo, T., Jurado, D., Ruiz, A., and Ribas, M. (2004). "Comparison of dose calculation algorithms in phantoms with lung equivalent heterogeneities under conditions of lateral electronic disequilibrium," *Med. Phys.* **31**, 2899–2911.
- Cengiz, M., Ozyigit, G., Yazici, G., Dogan, A., Yildiz, F., Zorlu, F., Gurkaynak, M., Gullu, I.H., Hosal, S., and Akyol, F. (2011). "Salvage reirradiation with stereotactic body radiotherapy for locally recurrent head-and-neck tumors," *Int. J. Radiat. Oncol. Biol. Phys.* **81**, 104–109.
- Cervino, L.I., Pawlicki, T., Lawson, J.D., and Jiang, S.B. (2010). "Frame-less and mask-less cranial stereotactic radiosurgery: A feasibility study," *Phys. Med. Biol.* **55**, 1863–1873.
- Chan, R., He, Y., Haque, A., and Zwischenberger, J. (2001). "Computed tomographic-pathologic correlation of gross tumor volume and clinical target volume in non-small cell lung cancer: A pilot experience," *Arch. Pathol. Lab. Med.* **125**, 1469–1472.
- Chang, J.Y., Balter, P.A., Dong, L., Yang, Q., Liao, Z., Jeter, M., Bucci, M.K., McAleer, M.F., Mehran, R.J., Roth, J.A., and Komaki, R. (2008). "Stereotactic body radiation therapy in centrally and superiorly located Stage I or isolated recurrent non-small-cell lung cancer," *Int. J. Radiat. Oncol. Biol. Phys.* **72**, 967–971.
- Chang, D.T., Swaminath, A., Kozak, M., Weintraub, J., Koong, A.C., Kim, J., Dinniwell, R., Brierley, J., Kavanagh, B.D., Dawson, L.A., and Schefter, T.E. (2011). "Stereotactic body radiotherapy for colorectal liver metastases," *Cancer* **117**, 4060–4069.
- Charles, P.H., Crowe, S.B., Kairn, T., Knight, R.T., Hill, B., Kenny, J., Langton, C.M., and Trapp, J.V. (2013). "Monte Carlo-based diode design for correction-less small field dosimetry," *Phys. Med. Biol.* **58**, 4501–4512.
- Chen, H., Lohr, F., Fritz, P., Wenz, F., Dobler, B., Lorenz, F., and Muhlnickel, W. (2010). "Stereotactic, single-dose irradiation of lung tumors: A comparison of absolute dose and dose distribution between pencil beam and Monte Carlo algorithms based on actual patient CT scans," *Int. J. Radiat. Oncol. Biol. Phys.* **78**, 955–963.
- Chen, Q., Chen, Y., Chen, M., Chao, E., Sterpin, E., and Lu, W. (2011). "A slit method to determine the focal spot size and shape of TomoTherapy system," *Med. Phys.* **38**, 2841–2849.
- Cheng, C.W., Cho, S.H., Taylor, M., and Das, I.J. (2007). "Determination of zero-field size percent depth doses and tissue maximum ratios for stereotactic radiosurgery and IMRT dosimetry: Comparison between experimental measurements and Monte Carlo simulation," *Med. Phys.* **34**, 3149–3157.
- Chetty, I.J., Curran, B., Cygler, J.E., DeMarco, J.J., Ezzell, G., Faddegon, B.A., Kawrakow, I., Keall, P.J., Liu, H., Ma, C.M., Rogers, D.W.O., Seuntjens, J., Sheikh-Bagheri, D., and Siebers, J.V. (2007). "Report of the AAPM Task Group No. 105: Issues associated with clinical implementation of Monte Carlo-based photon and electron external beam treatment planning," *Med. Phys.* **34**, 4818–4853.
- Cheung, J.Y., Yu, K.N., Ho, R.T., and Yu, C.P. (1999). "Monte Carlo calculated output factors of a Leksell Gamma Knife unit," *Phys. Med. Biol.* **44**, N247–N49.
- Chi, A., Liao, Z., Nguyen, N.P., Xu, J., Stea, B., and Komaki, R. (2010). "Systemic review of the patterns of failure following stereotactic body radiation therapy in early-stage non-small-cell lung cancer: Clinical implications," *Radiother. Oncol.* **94**, 1–11.
- Chi, A., Wen, S., Liao, Z., Fowler, J., Xu, J., Nguyen, N.P., Welsh, J.S., and Komaki, R. (2013). "What would be the most appropriate alpha/beta ratio in the setting of stereotactic body radiation therapy for early stage non-small cell lung cancer," *Biomed. Res. Int.* **2013**, 391021.
- Chow, J.C., Leung, M.K., and Van Dyk, J. (2009). "Variations of lung density and geometry on inhomogeneity correction algorithms: A Monte Carlo dosimetric evaluation," *Med. Phys.* **36**, 3619–3630.
- Chu, M., Zinchenko, Y., Henderson, S.G., and Sharpe, M.B. (2005). "Robust optimization for intensity

References

- modulated radiation therapy treatment planning under uncertainty," *Phys. Med. Biol.* **50**, 5463–5477.
- Chung, P.W., Haycocks, T., Brown, T., Cambridge, Z., Kelly, V., Alasti, H., Jaffray, D.A., and Catton, C.N. (2004). "On-line aSi portal imaging of implanted fiducial markers for the reduction of interfraction error during conformal radiotherapy of prostate carcinoma," *Int. J. Radiat. Oncol. Biol. Phys.* **60**, 329–334.
- Chung, H., Jin, H., Palta, J., Suh, T.S., and Kim, S. (2006). "Dose variations with varying calculation grid size in head and neck IMRT," *Phys. Med. Biol.* **51**, 4841–4856.
- Chung, E., Davis, S., and Seuntjens, J. (2013). "Experimental analysis of general ion recombination in a liquid-filled ionization chamber in high-energy photon beams," *Med. Phys.* **40**, 062104.
- Clarke, R.H., and Horsley, V. (1906). "On a method of investigating the deep ganglia and tracts of the central nervous system (cerebellum)," *Br. Med. J.* **2**, 1799–1800.
- Collins, B.T., Erickson, K., Reichner, C.A., Collins, S.P., Gagnon, G.J., Dieterich, S., McRae, D.A., Zhang, Y., Yousefi, S., Levy, E., Chang, T., Jamis-Dow, C., Banovac, F., and Anderson, E.D. (2007). "Radical stereotactic radiosurgery with real-time tumor motion tracking in the treatment of small peripheral lung tumors," *Radiat. Oncol.* **2**, 39.
- Colombo, F., Benedetti, A., Pozza, F., Avanzo, R.C., Marchetti, C., Chierego, G., and Zanardo, A. (1985). "External stereotactic irradiation by linear accelerator," *Neurosurgery* **16**, 154–160.
- Comet, B., Kramar, A., Faivre-Pierret, M., Dewas, S., Coche-Dequeant, B., Degardin, M., Lefebvre, J.L., Lacornerie, T., and Lartigau, E.F. (2012). "Salvage stereotactic reirradiation with or without cetuximab for locally recurrent head-and-neck cancer: a feasibility study," *Int. J. Radiat. Oncol. Biol. Phys.* **84**, 203–209.
- Cox, B.W., Spratt, D.E., Lovelock, M., Bilsky, M.H., Lis, E., Ryu, S., Sheehan, J., Gerszten, P.C., Chang, E., Gibbs, I., Soltys, S., Sahgal, A., Deasy, J., Flickinger, J., Quader, M., Mindea, S., and Yamada, Y. (2012). "International Spine Radiosurgery Consortium consensus guidelines for target volume definition in spinal stereotactic radiosurgery," *Int. J. Radiat. Oncol. Biol. Phys.* **83**, e597–e605.
- Cranmer-Sargison, G., Weston, S., Evans, J.A., Sidhu, N.P., and Thwaites, D.I. (2012). "Monte Carlo modelling of diode detectors for small field MV photon dosimetry: Detector model simplification and the sensitivity of correction factors to source parameterization," *Phys. Med. Biol.* **57**, 5141–5153.
- Cranmer-Sargison, G., Charles, P.H., Trapp, J.V., and Thwaites, D.I. (2013). "A methodological approach to reporting corrected small field relative outputs," *Radiat. Oncol.* **109**, 350–355.
- Crop, F., Van Rompaye, B., Paelinck, L., Vakaet, L., Thierens, H., and De Wagter, C. (2008). "On the calibration process of film dosimetry: OLS inverse regression versus WLS inverse prediction," *Phys. Med. Biol.* **53**, 3971–84.
- Cui, Q., Dong, X., Wang, D., Hao, X., Wang, J., Li, Q., Kong, D., and Liu, N. (2002). "Diagnosis and treatment of primary gastric non-Hodgkin's lymphoma: Analysis of 157 patients," *Zhonghua Yu Fang Yi Xue Za Zhi* **36**, 502–504.
- Curran, B. (2003). "IMRT delivery using serial tomotherapy," pp. 221–245 in *Intensity Modulated Radiation Therapy: The State of the Art*, Palta, J., and Mackie, T. R., Eds. (American Association of Physicists in Medicine, Alexandria, VA).
- Curtis, S.B. (1986). "Lethal and potentially lethal lesions induced by radiation – a unified repair model," *Radiat. Res.* **106**, 252–270.
- Cygler, J.E., and Yukihara, E.G. (2009). "Optically stimulated luminescence (OSL) dosimetry in radiotherapy," pp. 841–846 in *Clinical Dosimetry Measurements in Radiotherapy*, Rogers, D.W., and Cygler, J.E., Eds. (American Association of Physicists in Medicine Summer School, Madison, WI).
- Czarnecki, D., and Zink, K. (2013). "Monte Carlo calculated correction factors for diodes and ion chambers in small photon fields," *Phys. Med. Biol.* **58**, 2431–2444.
- Das, I.J., Cheng, C.W., Watts, R.J., Ahnesjo, A., Gibbons, J., Li, X.A., Lowenstein, J., Mitra, R.K., Simon, W.E., and Zhu, T.C. (2008a). "Accelerator beam data commissioning equipment and procedures: Report of the TG-106 of the Therapy Physics Committee of the AAPM," *Med. Phys.* **35**, 4186–4215.
- Das, I.J., Ding, G.X., and Ahnesjo, A. (2008b). "Small fields: Nonequilibrium radiation dosimetry," *Med. Phys.* **35**, 206–215.
- Das, I.J., Cheng, C.W., Chopra, K.L., Mitra, R.K., Srivastava, S.P., and Glatstein, E. (2008c). "Intensity-modulated radiation therapy dose prescription, recording, and delivery: Patterns of variability among institutions and treatment planning systems," *J. Natl. Cancer Inst.* **100**, 300–307.
- Dasu, A., Lofroth, P.O., and Wickman, G. (1998). "Liquid ionization chamber measurements of dose distributions in small 6 MV photon beams," *Phys. Med. Biol.* **43**, 21–36.
- Debois, M., Oyen, R., Maes, F., Verswijvel, G., Gatti, G., Bosmans, H., Feron, M., Bellon, E., Kutcher, G., Van Poppel, H., and Vanuytsel, L. (1999). "The contribution of magnetic resonance imaging to the three-dimensional treatment planning of localized prostate cancer," *Int. J. Radiat. Oncol. Biol. Phys.* **45**, 857–865.
- de Crevoisier, R., Tucker, S.L., Dong, L., Mohan, R., Cheung, R., Cox, J.D., and Kuban, D.A. (2005). "Increased risk of biochemical and local failure in patients with distended rectum on the planning CT for prostate cancer radiotherapy," *Int. J. Radiat. Oncol. Biol. Phys.* **62**, 965–973.
- Demaria S., Golden E.B., and Formenti, S.C. (2015). "Role of local radiation therapy in cancer immunotherapy," *JAMA Oncol.* **1**, 1325–1332.
- Dempsey, J.F., Romeijn, H.E., Li, J.G., Low, D.A., and Palta, J.R. (2005a). "A fourier analysis of the dose grid resolution required for accurate IMRT fluence map optimization," *Med. Phys.* **32**, 380–388.

PRESCRIBING, RECORDING, AND REPORTING SMALL BEAM SRT

- Dempsey, J.F., Benoit, D., Fitzsimmons, J.R., Haghightat, A., Li, J.G., Low, D.A., Mutic, S., Palta, J.R., Romeijn, H.E., and Sjoden, G.E. (2005b). "A device for real time 3D Image-Guided IMRT," *Int. J. Radiat. Oncol. Biol. Phys.* **63**, S202.
- Deng, J., Guerrero, T., Ma, C.M., and Nath, R. (2004). "Modelling 6 MV photon beams of a stereotactic radiosurgery system for Monte Carlo treatment planning," *Phys. Med. Biol.* **49**, 1689–1704.
- Depuydt, T., Verellen, D., Haas, O., Gevaert, T., Linthout, N., Duchateau, M., Tournel, K., Reynders, T., Leysen, K., Hoogeman, M., Storme, G., and De Ridder, M. (2011). "Geometric accuracy of a novel gimbals based radiation therapy tumor tracking system," *Radiother. Oncol.* **98**, 365–372.
- Depuydt, T., Poels, K., Verellen, D., Engels, B., Collen, C., Haverbeke, C., Gevaert, T., Buls, N., Van Gompel, G., Reynders, T., Duchateau, M., Tournel, K., Boussaer, M., Steenbeke, F., Vandebroucke, F., and De Ridder, M. (2013). "Initial assessment of tumor tracking with a gimbaled linac system in clinical circumstances: A patient simulation study," *Radiother. Oncol.* **106**, 236–240.
- Derechinsky, V.E., and Betti, O.O. (1986). "Convergent multibeam unit for radiation," U.S. Patent: 4,583,537, April 22, 1986 (U.S. Patent and Trademark Office, Alexandria, VA).
- Desai, P., Parry, C., D'Souza, M., and Medbery, C. (2006). "Comprehensive Cyberknife QA-A 2 year experience," *Med. Phys.* **33**, 2082.
- Devic, S. (2011). "Radiochromic film dosimetry: Past, present, and future," *Eur. J. Med. Phys.* **27**, 122–134.
- Dewas, S., Bibault, J.E., Mirabel, X., Fumagalli, I., Kramar, A., Jarraya, H., Lacornerie, T., Dewas-Vautravers, C., and Lartigau, E. (2012). "Prognostic factors affecting local control of hepatic tumors treated by stereotactic body radiation therapy," *Radiat. Oncol.* **7**, 166.
- DeWerd, L.A., and Bartol, L.J. (2009). "Thermoluminescent dosimetry," pp. 815–840 in *Clinical Dosimetry Measurements in Radiotherapy*, Rogers, D.W., and Cygler, J.E., Eds. (American Association of Physicists in Medicine Summer School, Madison, WI).
- Dhakal, S., Corbin, K.S., Milano, M.T., Philip, A., Sahasrabudhe, D., Jones, C., and Constine, L.S. (2012). "Stereotactic body radiotherapy for pulmonary metastases from soft-tissue sarcomas: Excellent local lesion control and improved patient survival," *Int. J. Radiat. Oncol. Biol. Phys.* **82**, 940–945.
- Dieterich, S., Cavedon, C., Chuang, C.F., Cohen, A.B., Garrett, J.A., Lee, C.L., Lowenstein, J.R., d'Souza, M.F., Taylor, D.D. Jr, Wu, X., and Yu, C. (2011). "Report of AAPM TG 135: Quality assurance for robotic radiosurgery," *Med. Phys.* **38**, 2914–2936.
- Ding, G.X. (2010). "X-ray imaging dose from IGRT," *Med. Phys.* **37**, 3409.
- Ding, G.X., and Coffey, C.W. (2008). "Is it time to include imaging doses in the reportable total radiation doses of radiotherapy patients?," *Int. J. Radiat. Oncol. Biol. Phys.* **72**, S145–S146.
- Ding, G.X., and Krauss, R. (2013). "An empirical formula to obtain tissue-phantom ratios from percentage depth-dose curves for small fields," *Phys. Med. Biol.* **58**, 4781–4789.
- Ding, G.X., Duggan, D.M., and Coffey, C.W. (2006). "Commissioning stereotactic radiosurgery beams using both experimental and theoretical methods," *Phys. Med. Biol.* **51** 2549–2566.
- Ding, G.X., Price, R., and Coffey, C. (2008a). "X-ray imaging dose to patients in the era of image-guided radiation therapy," *Med. Phys.* **35**, 2966.
- Ding, G.X., Duggan, D.M., and Coffey, C.W. (2008b). "A theoretical approach for non-equilibrium radiation dosimetry," *Phys. Med. Biol.* **53** 3493–3499.
- Ding, G.X., Munro, P., Pawlowski, J., Malcolm, A., and Coffey, C.W. (2010). "Reducing radiation exposure to patients from kV-CBCT imaging," *Radiother. Oncol.* **97**, 585–592.
- Disher, B., Hajdok, G., Gaede, S., and Battista, J.J. (2012). "An in-depth Monte Carlo study of lateral electron disequilibrium for small fields in ultra-low density lung: Implications for modern radiation therapy," *Phys. Med. Biol.* **57**, 1543–1559.
- Dogan, N., Siebers, J.V., and Keall, P.J. (2006). "Clinical comparison of head and neck and prostate IMRT plans using absorbed dose to medium and absorbed dose to water," *Phys. Med. Biol.* **51**, 4967–4980.
- Dong, S.L., Chu, T.C., Lee, J.S., Lan, G.Y., Wu, T.H., Yeh, Y.H., and Hwang, J.J. (2002). "Estimation of mean-glandular dose from monitoring breast entrance skin air kerma using a high sensitivity metal oxide semiconductor field effect transistor (MOSFET) dosimeter system in mammography," *Appl. Radiat. Isot.* **57**, 791–799.
- Dorr, W. (1997). "Three A's of repopulation during fractionated irradiation of squamous epithelia: Asymmetry loss, acceleration of stem-cell divisions and abortive divisions," *Int. J. Radiat. Biol.* **72**, 635–643.
- Drzymala, R.E., Mohan, R., Brewster, L., Chu, J., Goitein, M., Harms, W., and Urie, M. (1991). "Dose-volume histograms," *Int. J. Radiat. Oncol. Biol. Phys.* **21**, 71–78.
- Drzymala, R.E., Klein, E.E., Simpson, J.R., Rich, K.M., Wasserman, T.H., and Purdy, J.A. (1994). "Assurance of high quality linac-based stereotactic radiosurgery," *Int. J. Radiat. Oncol. Biol. Phys.* **30**, 459–472.
- Eklund, K., and Ahnesjo, A. (2008). "Fast modelling of spectra and stopping-power ratios using differentiated fluence pencil kernels," *Phys. Med. Biol.* **53**, 4231–4247.
- Elia, A.E., Shih, H.A., and Loeffler, J.S. (2007). "Stereotactic radiation treatment for benign meningiomas," *Neurosurg. Focus* **23**, E5.
- El Naqa, I. (2013). "Outcomes modeling," pp. 257–75 in *Informatics in Radiation Oncology*, Starkschall, G., and Siochi, C., Eds. (CRC Press, Boca Raton, FL).
- El Naqa, I., Pater, P., and Seuntjens, J. (2012). "Monte Carlo role in radiobiological modelling of radiotherapy outcomes," *Phys. Med. Biol.* **57**, R75–R97.
- Emami, B., Lyman, J., Brown, A., Coia, L., Goitein, M., Munzenrider, J.E., Shank, B., Solin, L.J., and Wesson, M. (1991). "Tolerance of normal tissue to therapeutic

References

- irradiation," *Int. J. Radiat. Oncol. Biol. Phys.* **21**, 109–122.
- Engelsman, M., Damen, E.M., Koken, P.W., van't Veld, A. A., van Ingen, K.M., and Mijnheer, B.J. (2001). "Impact of simple tissue inhomogeneity correction algorithms on conformal radiotherapy of lung tumours," *Radiother. Oncol.* **60**, 299–309.
- Ezzell, G.A., Burmeister, J.W., Dogan, N., LoSasso, T.J., Mechalakos, J.G., Mihailidis, D., Molineu, A., Palta, J. R., Ramsey, C.R., Salter, B.J., Shi, J., Xia, P., Yue, N.J., and Xiao, Y. (2009). "IMRT commissioning: Multiple institution planning and dosimetry comparisons, a report from AAPM Task Group 119," *Med. Phys.* **36**, 5359–5373.
- Failla, G.A., Wareing, T., Archambault, Y., and Thompson, S. (2011). *Acuros XB Advanced Dose Calculation for the Eclipse Treatment Planning System RAD 10156* (Varian Medical Systems, Palo Alto, CA).
- Fakiris, A.J., McGarry, R.C., Yiannoutsos, C.T., Papiez, L., Williams, M., Henderson, M.A., and Timmerman, R. (2009). "Stereotactic body radiation therapy for early-stage non-small-cell lung carcinoma: Four-year results of a prospective phase II study," *Int. J. Radiat. Oncol. Biol. Phys.* **75**, 677–682.
- Fallone, B.G., Murray, B., Rathee, S., Stanescu, T., Steciw, S., Vidakovic, S., Blosser, E., and Tymofichuk, D. (2009). "First MR images obtained during megavoltage photon irradiation from a prototype integrated linac-MR system," *Med. Phys.* **36**, 2084–2088.
- Fano, U. (1954). "Note on the Bragg-Gray cavity principle for measuring energy dissipation," *Radiat. Res.* **1**, 237–240.
- Fast, M.F., Koenig, T., Oelfke, U., and Nill, S. (2012). "Performance characteristics of a novel megavoltage cone-beam-computed tomography device," *Phys. Med. Biol.* **57**, N15–N24.
- Fenwick, J.D., Tome, W.A., Jaradat, H.A., Hui, S.K., James, J.A., Balog, J.P., DeSouza, C.N., Lucas, D.B., Olivera, G.H., Mackie, T.R., and Paliwal, B.R. (2004). "Quality assurance of a helical tomotherapy machine," *Phys. Med. Biol.* **49**, 2933–2953.
- Fippel, M., Haryanto, F., Dohm, O., Nusslin, F., and Kriesen, S. (2003). "A virtual photon energy fluence model for Monte Carlo dose calculation," *Med. Phys.* **30**, 301–311.
- Flickinger, J.C., Pollock, B.E., Kondziolka, D., and Lunsford, L.D. (1996). "A dose-response analysis of arteriovenous malformation obliteration after radiosurgery," *Int. J. Radiat. Oncol. Biol. Phys.* **36**, 873–879.
- Flickinger, J.C., Kondziolka, D., Lunsford, L.D., Kassam, A., Phuong, L.K., Liscak, R., and Pollock, B. (2000). "Development of a model to predict permanent symptomatic postradiosurgery injury for arteriovenous malformation patients," *Int. J. Radiat. Oncol. Biol. Phys.* **46**, 1143–1148.
- Fogliata, A., Vanetti, E., Albers, D., Brink, C., Clivio, A., Knoos, T., Nicolini, G., and Cozzi, L. (2007). "On the dosimetric behaviour of photon dose calculation algorithms in the presence of simple geometric heterogeneities: Comparison with Monte Carlo calculations," *Phys. Med. Biol.* **52**, 1363–1385.
- Fogliata, A., Nicolini, G., Clivio, A., Vanetti, E., and Cozzi, L. (2011a). "Dosimetric evaluation of Acuros XB Advanced Dose Calculation algorithm in heterogeneous media," *Radiat. Oncol.* **6**, 82.
- Fogliata, A., Nicolini, G., Clivio, A., Vanetti, E., and Cozzi, L. (2011b). "Accuracy of Acuros XB and AAA dose calculation for small fields with reference to RapidArc® stereotactic treatments," *Med. Phys.* **38**, 6228–6237.
- Fogliata, A., Nicolini, G., Clivio, A., Vanetti, E., Mancosu, P., and Cozzi, L. (2011c). "Dosimetric validation of the Acuros XB Advanced Dose Calculation algorithm: Fundamental characterization in water," *Phys. Med. Biol.* **56**, 1879–1904.
- Ford, E., and Evans, S. (2014). "RO ILS launch offers secure incident reporting system to track errors and near-misses," *ASTRO News (Summer)*, 14–12.
- Formenti, S.C., and Demaria, S. (2009). "Systemic effects of local radiotherapy," *Lancet Oncol.* **10**, 718–726.
- Forrest, L.J., Mackie, T.R., Ruchala, K., Turek, M., Kapatoes, J., Jaradat, H., Hui, S., Balog, J., Vail, D.M., and Mehta, M.P. (2004). "The utility of megavoltage computed tomography images from a helical tomotherapy system for setup verification purposes," *Int. J. Radiat. Oncol. Biol. Phys.* **60**, 1639–1644.
- Fowler, J.F., Welsh, J.S., and Howard, S.P. (2004). "Loss of biological effect in prolonged fraction delivery," *Int. J. Radiat. Oncol. Biol. Phys.* **59**, 242–249.
- Fowler, J.F. (2006). "Development of radiobiology for oncology – a personal view," *Phys. Med. Biol.* **51**, R263–R286.
- Fraass, B., Doppke, K., Hunt, M., Kutcher, G., Starkschall, G., Stern, R., and Van Dyke, J. (1998). "American Association of Physicists in Medicine Radiation Therapy Committee Task Group 53: Quality assurance for clinical radiotherapy treatment planning," *Med. Phys.* **25**, 1773–1829.
- Francescon, P., Cora, S., and Cavedon, C. (2008). "Total scatter factors of small beams: A multidetector and Monte Carlo study," *Med. Phys.* **35**, 504–513.
- Francescon, P., Cora, S., and Satariano, N. (2011). "Calculation of $k(Q(\text{clin}), Q(\text{msr}))$ ($f(\text{clin}), f(\text{msr})$) for several small detectors and for two linear accelerators using Monte Carlo simulations," *Med. Phys.* **38**, 6513–6527.
- Francescon, P., Kilby, W., Satariano, N., and Cora, S. (2012). "Monte Carlo simulated correction factors for machine specific reference field dose calibration and output factor measurement using fixed and iris collimators on the CyberKnife system," *Phys. Med. Biol.* **57**, 3741–3758.
- Francescon, P., Beddar, S., Satariano, N., and Das, I.J. (2014). "Variation of $k(Q(\text{clin}), Q(\text{msr}))$ ($f(\text{clin}), f(\text{msr})$) for the small-field dosimetric parameters percentage depth dose, tissue-maximum ratio, and off-axis ratio," *Med. Phys.* **41**, 101708.
- Friedman, W.A., and Bova, F.J. (1989). "The University-of-Florida Radiosurgery System," *Surg. Neurol.* **32**, 334–342.
- Fuss, M., Salter, B.J., Rassiah, P., Cheek, D., Cavanaugh, S.X., and Herman, T.S. (2004). "Repositioning accuracy

- of a commercially available double-vacuum whole body immobilization system for stereotactic body radiation therapy," *Technol. Cancer Res. Treat.* **3**, 59–67.
- Gayou, O., Parda, D.S., Johnson, M., and Miften, M. (2007). "Patient dose and image quality from megavoltage cone beam computed tomography imaging," *Med. Phys.* **34**, 499–506.
- Gevaert, T., Verellen, D., Tournel, K., Linthout, N., Bral, S., Engels, B., Collen, C., Depuydt, T., Duchateau, M., Reynders, T., Storme, G., and De Ridder, M. (2012). "Setup accuracy of the Novalis ExacTrac 6DOF system for frameless radiosurgery," *Int. J. Radiat. Oncol. Biol. Phys.* **82**, 1627–1635.
- Gill, S.S., Thomas, D.G.T., Warrington, A.P., and Brada, M. (1991). "Relocatable frame for stereotactic external beam radiotherapy," *Int. J. Radiat. Oncol. Biol. Phys.* **20**, 599–603.
- Gill, S., Thomas, J., Fox, C., Kron, T., Rolfo, A., Leahy, M., Chander, S., Williams, S., Tai, K.H., Duchesne, G.M., and Foroudi, F. (2011). "Acute toxicity in prostate cancer patients treated with and without image-guided radiotherapy," *Radiat. Oncol.* **6**, 145.
- Giraud, P., Antoine, M., Larrouy, A., Milleron, B., Callard, P., De Rycke, Y., Carette, M.F., Rosenwald, J.C., Cosset, J.M., Housset, M., and Touboul, E. (2000). "Evaluation of microscopic tumor extension in non-small-cell lung cancer for three-dimensional conformal radiotherapy planning," *Int. J. Radiat. Oncol. Biol. Phys.* **48**, 1015–1024.
- Goetsch, S.J. (2002a). "Risk analysis of Leksell Gamma Knife Model C with automatic positioning system," *Int. J. Radiat. Oncol. Biol. Phys.* **52**, 869–877.
- Goetsch, S. (2002b). "4-mm gamma knife helmet factor," *Int. J. Radiat. Oncol. Biol. Phys.* **54**, 300; author reply 301.
- Goetsch, S.J. (2008). "Linear accelerator and gamma knife-based stereotactic cranial radiosurgery: Challenges and successes of existing quality assurance guidelines and paradigms," *Int. J. Radiat. Oncol. Biol. Phys.* **71**, S118–S121.
- Goetsch, S.J., Murphy, B.D., Schmidt, R., Micka, J., De Werd, L., Chen, Y., and Shockley, S. (1999). "Physics of rotating gamma systems for stereotactic radiosurgery," *Int. J. Radiat. Oncol. Biol. Phys.* **43**, 689–696.
- Goitein, M., and Schultheiss, T.E. (1985). "Strategies for treating possible tumor extension – some theoretical considerations," *Int. J. Radiat. Oncol. Biol. Phys.* **11**, 1519–1528.
- Green, O.L., Hu, Y., Zeng, Q., Nana, R., Patrick, J.L., Shvartsman, S., Eagan, T., Mutic, S., and Dempsey, J.F. (2013). "Realizing the QUANTEC vision by applying weighted hybrid iterative spiral K-space encoding estimation (WHISKEE) to actuated dose (DA) accumulation via image deformation (DAAvID)," *Int. J. Radiat. Oncol. Biol. Phys.* **87**, 14.
- Greene, F.L. (2002). "The American Joint Committee on Cancer: Updating the strategies in cancer staging," *Bull. Am. Coll. Surg.* **87**, 13–15.
- Grills, I.S., Fitch, D.L., Goldstein, N.S., Yan, D., Chmielewski, G.W., Welsh, R.J., and Kestin, L.L. (2007). "Clinicopathologic analysis of microscopic extension in lung adenocarcinoma: Defining clinical target volume for radiotherapy," *Int. J. Radiat. Oncol. Biol. Phys.* **69**, 334–341.
- Grimm, J., LaCouture, T., Croce, R., Yeo, I., Zhu, Y., and Xue, J. (2011). "Dose tolerance limits and dose volume histogram evaluation for stereotactic body radiotherapy," *J. Appl. Clin. Med. Phys.* **12**, 267–292.
- Grofsmid, D., Dirkx, M., Marijnissen, H., Woudstra, E., and Heijmen, B. (2010). "Dosimetric validation of a commercial Monte Carlo based IMRT planning system," *Med. Phys.* **37**, 540–549.
- Guckenberger, M., Meyer, J., Wilbert, J., Baier, K., Mueller, G., Wulf, J., and Flentje, M. (2006). "Cone-beam CT based image-guidance for extracranial stereotactic radiotherapy of intrapulmonary tumors," *Acta Oncol.* **45**, 897–906.
- Guckenberger, M., Meyer, J., Wilbert, J., Richter, A., Baier, K., Mueller, G., and Flentje, M. (2007a). "Intra-fractional uncertainties in cone-beam CT based image-guided radiotherapy (IGRT) of pulmonary tumors," *Radiother. Oncol.* **83**, 57–64.
- Guckenberger, M., Meyer, J., Wilbert, J., Baier, K., Sauer, O., and Flentje, M. (2007b). "Precision of image-guided radiotherapy (IGRT) in six degrees of freedom and limitations in clinical practice," *Strahlenther. Onkol.* **183**, 307–313.
- Guckenberger, M., Bachmann, J., Wulf, J., Mueller, G., Krieger, T., Baier, K., Richter, A., Wilbert, J., and Flentje, M. (2010). "Stereotactic body radiotherapy for local boost irradiation in unfavourable locally recurrent gynaecological cancer," *Radiother. Oncol.* **94**, 53–59.
- Guckenberger, M., Klement, R.J., Kestin, L.L., Hope, A.J., Belderbos, J., Werner-Wasik, M., Yan, D., Sonke, J.J., Bissonnette, J.P., Xiao, Y., and Grills, I.S. (2013). "Lack of a dose-effect relationship for pulmonary function changes after stereotactic body radiation therapy for early-stage non-small cell lung cancer," *Int. J. Radiat. Oncol. Biol. Phys.* **85**, 1074–1081.
- Guerrero, M., and Carbone, M. (2010). "Mechanistic formulation of a lineal-quadratic-linear (LQL) model: Split-dose experiments and exponentially decaying sources," *Med. Phys.* **37**, 4173–4181.
- Guerrero, M., and Li, X.A. (2004). "Extending the linear-quadratic model for large fraction doses pertinent to stereotactic radiotherapy," *Phys. Med. Biol.* **49**, 4825–4835.
- Hacker, F., Rosca, F., Friesen, S., Zygmanski, P., and Ramakrishna, N. (2006). "Accuracy assessment of a non-invasive image guided system for intracranial linac based stereotactic radiosurgery," *Med. Phys.* **33**, 2066.
- Haedinger, U., Krieger, T., Flentje, M., and Wulf, J. (2005). "Influence of calculation model on dose distribution in stereotactic radiotherapy for pulmonary targets," *Int. J. Radiat. Oncol. Biol. Phys.* **61**, 239–249.
- Hall, E.J., and Giaccia, A.J. (2006). *Radiobiology for the Radiologist*, 6th ed. (Lippincott Williams, and Wilkins, Philadelphia).
- Han, T., Mikell, J.K., Salehpour, M., and Mourtada, F. (2011). "Dosimetric comparison of Acuros XB deterministic radiation transport method with Monte Carlo and

References

- model-based convolution methods in heterogeneous media," *Med. Phys.* **38**, 2651–2664.
- Hara, R., Itami, J., Kondo, T., Aruga, T., Uno, T., Sasano, N., Ohnishi, K., Kiyozuka, M., Fuse, M., Ito, M., Naoi, K., and Kohno, Y. (2006). "Clinical outcomes of single-fraction stereotactic radiation therapy of lung tumors," *Cancer* **106**, 1347–1352.
- Hartmann, G.H., Schlegel, W., Sturm, V., Kober, B., Pasty, O., and Lorenz, W.J. (1985). "Cerebral radiation surgery using moving field irradiation at a linear accelerator facility," *Int. J. Radiat. Oncol. Biol. Phys.* **11**, 1185–1192.
- Hasenbalg, F., Neuenschwander, H., Mini, R., and Born, E.J. (2007). "Collapsed cone convolution and analytical anisotropic algorithm dose calculations compared to VMC++ Monte Carlo simulations in clinical cases," *Phys. Med. Biol.* **52**, 3679–3691.
- Hawkins, M.A., Brock, K.K., Eccles, C., Moseley, D., Jaffray, D., and Dawson, L.A. (2006). "Assessment of residual error in liver position using kV cone-beam computed tomography for liver cancer high-precision radiation therapy," *Int. J. Radiat. Oncol. Biol. Phys.* **66**, 610–619.
- Hazard, L.J., Jensen, R.L., and Shrieve, D.C. (2005). "Role of stereotactic radiosurgery in the treatment of brain metastases," *Am. J. Clin. Oncol.* **28**, 403–410.
- Heath, E., and Seuntjens, J. (2006). "A direct voxel tracking method for four-dimensional Monte Carlo dose calculations in deforming anatomy," *Med. Phys.* **33**, 434–445.
- Herfarth, K.K., Debus, J., Lohr, F., Bahner, M.L., Rhein, B., Fritz, P., Hoss, A., Schlegel, W., and Wannenmacher, M.F. (2001). "Stereotactic single-dose radiation therapy of liver tumors: Results of a phase I/II trial," *J. Clin. Oncol.* **19**, 164–170.
- Herman, M.G., Balter, J.M., Jaffray, D.A., McGee, K.P., Munro, P., Shalev, S., Van Herk, M., and Wong, J.W. (2001). "Clinical use of electronic portal imaging: Report of AAPM Radiation Therapy Committee Task Group 58," *Med. Phys.* **28**, 712–737.
- Heron, D.E., Rwigema, J.C., Gibson, M.K., Burton, S.A., Quinn, A.E., and Ferris, R.L. (2011). "Concurrent cetuximab with stereotactic body radiotherapy for recurrent squamous cell carcinoma of the head and neck: A single institution matched case-control study," *Am. J. Clin. Oncol.* **34**, 165–172.
- Heron, D.E., Rajagopalan, M.S., Stone, B., Burton, S., Gerszten, P.C., Dong, X., Gagnon, G.J., Quinn, A., and Henderson, F. (2012). "Single-session and multisession CyberKnife radiosurgery for spine metastases—University of Pittsburgh and Georgetown University experience," *J. Neurosurg. Spine* **17**, 11–18.
- Higgins, J., Bezjak, A., Hope, A., Panzarella, T., Li, W., Cho, J.B., Craig, T., Brade, A., Sun, A., and Bissonnette, J.P. (2011). "Effect of image-guidance frequency on geometric accuracy and setup margins in radiotherapy for locally advanced lung cancer," *Int. J. Radiat. Oncol. Biol. Phys.* **80**, 1330–1337.
- Hof, H., Hoess, A., Oetzel, D., Debus, J., and Herfarth, K. (2007). "Stereotactic single-dose radiotherapy of lung metastases," *Strahlenther. Onkol.* **183**, 673–678.
- Hof, H., Rhein, B., Haering, P., Kopp-Schneider, A., Debus, J., and Herfarth, K. (2009). "4D-CT-based target volume definition in stereotactic radiotherapy of lung tumours: Comparison with a conventional technique using individual margins," *Radiother. Oncol.* **93**, 419–423.
- Hoogeman, M., Prevost, J.B., Nuyttens, J., Poll, J., Levendag, P., and Heijmen, B. (2009). "Clinical accuracy of the respiratory tumor tracking system of the cyberknife: Assessment by analysis of log files," *Int. J. Radiat. Oncol. Biol. Phys.* **74**, 297–303.
- Horst, J., Czarnecki, D., and Zink, K. (2015). "The influence of neutron contamination on dosimetry in external photon beam radiotherapy" *Med. Phys.* **42**, 6529–6536.
- Houdek, P.V., Fayos, J.V., Van Buren, J.M., and Ginsberg, M.S. (1985). "Stereotactic radiotherapy technique for small intracranial lesions," *Med. Phys.* **12**, 469–472.
- Hristov, D., Liu, L., Adler, J.R., Gibbs, I.C., Moore, T., Sarmiento, M., Chang, S.D., Dodd, R., Marks, M., and Do, H.M. (2011). "Technique for targeting arteriovenous malformations using frameless image-guided robotic radiosurgery," *Int. J. Radiat. Oncol. Biol. Phys.* **79**, 1232–1240.
- Hugo, G.D., Liang, J., Campbell, J., and Yan, D. (2007). "On-line target position localization in the presence of respiration: A comparison of two methods," *Int. J. Radiat. Oncol. Biol. Phys.* **69**, 1634–1641.
- Hurkmans, C.W., Cuijpers, J.P., Lagerwaard, F.J., Widder, J., van der Heide, U.A., Schuring, D., and Senan, S. (2009). "Recommendations for implementing stereotactic radiotherapy in peripheral stage IA non-small cell lung cancer: Report from the Quality Assurance Working Party of the randomised phase III ROSEL study," *Radiat. Oncol.* **4**, 1.
- Hyde, D., Lochray, F., Korol, R., Davidson, M., Wong, C.S., Ma, L., and Sahgal, A. (2012). "Spine stereotactic body radiotherapy utilizing cone-beam CT image-guidance with a robotic couch: Intrafraction motion analysis accounting for all six degrees of freedom," *Int. J. Radiat. Oncol. Biol. Phys.* **82**, e555–e562.
- IAEA (1987). International Atomic Energy Agency. *Absorbed Dose Determination in Photon and Electron Beams: An International Code of Practice*, IAEA Technical Reports Series No. 277 (International Atomic Energy Agency, Vienna).
- IAEA (2000a). International Atomic Energy Agency. *Absorbed Dose Determination in External Beam Radiotherapy*, IAEA Technical Reports Series No. 398 (International Atomic Energy Agency, Vienna).
- IAEA (2000b). International Atomic Energy Agency. *Lessons Learned from Accidental Exposures in Radiation Therapy*, IAEA Safety Report Series 17 (International Atomic Energy Agency, Vienna).
- IAEA (2004). International Atomic Energy Agency. *Commissioning and Quality Assurance of Computerized Planning Systems for Radiation Treatment of Cancer*, IAEA Technical Reports Series No. 430 (International Atomic Energy Agency, Vienna).
- IAEA (2014). International Atomic Energy Agency. *Radiation Protection of Patients (RPOP): Short Case*

- Histories of Major Accidental Exposure Events in Radiotherapy* (International Atomic Energy Agency, Vienna).
- IAEA-AAPM (2017). International Atomic Energy Agency-American Association of Physicists in Medicine. *Dosimetry of Small Static Fields Used in External Beam Radiotherapy: An IAEA-AAPM International Code of Practice for Reference and Relative Dose Determination*. Technical Reports Series No. 483 (International Atomic Energy Agency, Vienna).
- ICRU (1978). International Commission on Radiation Units and Measurements. *Dose Specification for Reporting External Beam Therapy with Photons and Electrons*, ICRU Report 29 (International Commission on Radiation Units and Measurements, Bethesda, MD).
- ICRU (1985). International Commission on Radiation Units and Measurements, *Determination of Dose Equivalents Resulting from External Radiation Sources*, ICRU Report 39 (International Commission on Radiation Units and Measurements, Bethesda, MD).
- ICRU (1993). International Commission on Radiation Units and Measurements, *Prescribing, Recording and Reporting Photon Beam Therapy*, ICRU Report 50 (International Commission on Radiation Units and Measurements, Bethesda, MD).
- ICRU (1999). International Commission on Radiation Units and Measurements, *Recording and Reporting Photon Beam Therapy (Supplement to ICRU Report 50)*, ICRU Report 62 (International Commission on Radiation Units and Measurements, Bethesda, MD).
- ICRU (2004). International Commission on Radiation Units and Measurements, *Prescribing, Recording and Reporting Electron Beam Therapy* ICRU Report 71, *J. ICRU* **4** (Oxford University Press, Oxford).
- ICRU (2007). International Commission on Radiation Units and Measurements, *Prescribing, Recording and Reporting Electron Beam Therapy*, ICRU Report 78, *J. ICRU* **7** (Oxford University Press, Oxford).
- ICRU (2010). International Commission on Radiation Units and Measurements, *Prescribing, Recording and Reporting Electron Beam Therapy*, ICRU Report 83, *J. ICRU* **10** (Oxford University Press, Oxford).
- Imura, M., Yamazaki, K., Shirato, H., Onimaru, R., Fujino, M., Shimizu, S., Harada, T., Ogura, S., Dosaka-Akita, H., Miyasaka, K., and Nishimura, M. (2005). "Insertion and fixation of fiducial markers for setup and tracking of lung tumors in radiotherapy," *Int. J. Radiat. Oncol. Biol. Phys.* **63**, 1442–1447.
- Ishigaki, T., Sakuma, S., and Watanabe, M. (1988). "Computer-assisted rotation and multiple stationary irradiation technique – newly designed overrunning multi-leaf collimators for conformation radiotherapy," *Eur. J. Radiol.* **8**, 76–81.
- Jaffray, D.A., Battista, J.J., Fenster, A., and Munro, P. (1993). "X-ray sources of medical linear accelerators: Focal and extra-focal radiation," *Med. Phys.* **20**, 1417–1427.
- Jaffray, D.A., Drake, D.G., Moreau, M., Martinez, A.A., and Wong, J.W. (1999). "A radiographic and tomographic imaging system integrated into a medical linear accelerator for localization of bone and soft-tissue targets," *Int. J. Radiat. Oncol. Biol. Phys.* **45**, 773–789.
- Jager, P.L., de Korte, M.A., Lub-de Hooge, M.N., van Waarde, A., Koopmans, K.P., Perik, P.J., and de Vries, E.G. (2005). "Molecular imaging: What can be used today," *Cancer Imaging* **5**, S27–S32.
- Jeng, S.C., Tsai, C.L., Chan, W.T., Tung, C.J., Wu, J.K., and Cheng, J.C. (2009). "Mathematical estimation and in vivo dose measurement for cone-beam computed tomography on prostate cancer patients," *Radiother. Oncol.* **92**, 57–61.
- Jensen, M.D., Abdellatif, A., Chen, J., and Wong, E. (2012). "Study of the IMRT interplay effect using a 4DCT Monte Carlo dose calculation," *Phys. Med. Biol.* **57**, N89–N99.
- Jeraj, R., and Keall, P. (1999). "Monte Carlo-based inverse treatment planning," *Phys. Med. Biol.* **44**, 1885–1896.
- Jereczek-Fossa, B.A., Piperno, G., Ronchi, S., Catalano, G., Fodor, C., Cambria, R., Fossati Ing, P., Gherardi, F., Alterio, D., Zerini, D., Garibaldi, C., Baroni, G., De Cobelli, O., and Orechia, R. (2014). "Linac-based stereotactic body radiotherapy for oligometastatic patients with single abdominal lymph node recurrent cancer," *Am. J. Clin. Oncol.* **37**, 227–233.
- Jia, X., Gu, X., Graves, Y.J., Folkerts, M., and Jiang, S.B. (2011). "GPU-based fast Monte Carlo simulation for radiotherapy dose calculation," *Phys. Med. Biol.* **56**, 7017–7031.
- Jin, J.Y., Yin, F.F., Tenn, S.E., Medin, P.M., and Solberg, T.D. (2008a). "Use of the BrainLAB ExacTrac X-Ray 6D system in image-guided radiotherapy," *Med. Dosim.* **33**, 124–134.
- Jin, J.Y., Ryu, S., Rock, J., Faber, K., Chen, Q., Ajlouni, M., and Movsas, B. (2008b). "Evaluation of residual patient position variation for spinal radiosurgery using the Novalis image guided system," *Med. Phys.* **35**, 1087–1093.
- Joiner, M., and Kogel, A.V.D. (2009). *Basic Clinical Radiobiology*, 4th ed. (Hodder Arnold, London).
- Joiner, M.C., Marples, B., Lambin, P., Short, S.C., and Turesson, I. (2001). "Low-dose hypersensitivity: Current status and possible mechanisms," *Int. J. Radiat. Oncol. Biol. Phys.* **49**, 379–389.
- Jones, A.O., and Das, I.J. (2005). "Comparison of inhomogeneity correction algorithms in small photon fields," *Med. Phys.* **32**, 766–776.
- Jorcano, S., Molla, M., Escude, L., Sanz, S., Hidalgo, A., Toscas, J.I., Linero, D., and Miralbell, R. (2010). "Hypofractionated extracranial stereotactic radiotherapy boost for gynecologic tumors: A promising alternative to high-dose rate brachytherapy," *Technol. Cancer Res. Treat.* **9**, 509–514.
- Kano, H., Kondziolka, D., Flickinger, J.C., Park, K.J., Parry, P.V., Yang, H.C., Sirin, S., Niranjan, A., Novotny, J. Jr, and Lunsford, L.D. (2012). "Stereotactic radiosurgery for arteriovenous malformations, Part 6: Multistaged volumetric management of large arteriovenous malformations," *J. Neurosurg.* **116**, 54–65.

References

- Katz, A.J., Santoro, M., Ashley, R., Diblasio, F., and Witten, M. (2010). "Stereotactic body radiotherapy for organ-confined prostate cancer," *BMC Urol.* **10**, 1.
- Kawachi, T., Saitoh, H., Inoue, M., Katayose, T., Myojoyama, A., and Hatano, K. (2008). "Reference dosimetry condition and beam quality correction factor for CyberKnife beam," *Med. Phys.* **35**, 4591–4598.
- Kawaguchi, K., Sato, K., Horie, A., Iketani, S., Yamada, H., Nakatani, Y., Sato, J., and Hamada, Y. (2010). "Stereotactic radiosurgery may contribute to overall survival for patients with recurrent head and neck carcinoma," *Radiat. Oncol.* **5**, 51.
- Kawrakow, I., and Fippel, M. (2000). "Investigation of variance reduction techniques for Monte Carlo photon dose calculation using XVMC," *Phys. Med. Biol.* **45**, 2163–2183.
- Keall, P. (2002). "Dm rather than Dw should be used in Monte Carlo treatment planning. Against the proposition," *Med. Phys.* **29**, 923–924.
- Keall, P.J., Kini, V.R., Vedam, S.S., and Mohan, R. (2002). "Potential radiotherapy improvements with respiratory gating," *Australas. Phys. Eng. Sci. Med.* **25**, 1–6.
- Keall, P.J., Colvill, E., O'Brien, R., Ng, J.A., Poulsen, P.R., Eade, T., Kneebone, A., and Booth, J.T. (2014). "The first clinical implementation of electromagnetic transponder-guided MLC tracking," *Med. Phys.* **41**, 020702.
- Khoo, V.S., Padhani, A.R., Tanner, S.F., Finnigan, D.J., Leach, M.O., and Dearnaley, D.P. (1999). "Comparison of MRI with CT for the radiotherapy planning of prostate cancer: A feasibility study," *Br. J. Radiol.* **72**, 590–597.
- Kilby, W., Dooley, J.R., Kuduvalli, G., Sayeh, S., and Maurer, C.R. Jr. (2010). "The CyberKnife Robotic Radiosurgery System in 2010," *Technol. Cancer Res. Treat.* **9**, 433–452.
- Kim, S., Jin, H., Yang, H., and Amdur, R.J. (2009). "A study on target positioning error and its impact on dose variation in image-guided stereotactic body radiotherapy for the spine," *Int. J. Radiat. Oncol. Biol. Phys.* **73**, 1574–1579.
- King, C.R., Brooks, J.D., Gill, H., Pawlicki, T., Cotrutz, C., and Presti, J.C. Jr (2009). "Stereotactic body radiotherapy for localized prostate cancer: Interim results of a prospective phase II clinical trial," *Int. J. Radiat. Oncol. Biol. Phys.* **73**, 1043–1048.
- Kirkpatrick, J.P., Meyer, J.J., and Marks, L.B. (2008). "The linear-quadratic model is inappropriate to model high dose per fraction effects in radiosurgery," *Semin. Radiat. Oncol.* **18**, 240–243.
- Klassen, N.V., Shortt, K.R., Seuntjens, J., and Ross, C.K. (1999). "Fricke dosimetry: The difference between G (Fe3+) for ^{60}Co gamma-rays and high-energy x-rays," *Phys. Med. Biol.* **44**, 1609–1624.
- Klein, E.E., Hanley, J., Bayouth, J., Yin, F.F., Simon, W., Dresser, S., Serago, C., Aguirre, F., Ma, L., Arjomandy, B., Liu, C., Sandin, C., and Holmes, T. (2009). "Task Group 142 report: Quality assurance of medical accelerators," *Med. Phys.* **36**, 4197–4212.
- Klein, D.M., Tailor, R.C., Archambault, L., Wang, L., Therriault-Proulx, F., and Beddar, A.S. (2010). "Measuring output factors of small fields formed by collimator jaws and multileaf collimator using plastic scintillation detectors," *Med. Phys.* **37**, 5541–5549.
- Knoos, T., Ahnesjo, A., Nilsson, P., and Weber, L. (1995). "Limitations of a pencil beam approach to photon dose calculations in lung tissue," *Phys. Med. Biol.* **40**, 1411–1420.
- Knoos, T., Wieslander, E., Cozzi, L., Brink, C., Fogliata, A., Albers, D., Nystrom, H., and Lassen, S. (2006). "Comparison of dose calculation algorithms for treatment planning in external photon beam therapy for clinical situations," *Phys. Med. Biol.* **51**, 5785–7807.
- Kollova, A., Liscak, R., Novotny, J. Jr, Vladyka, V., Simonova, G., and Janouskova, L. (2007). "Gamma Knife surgery for benign meningioma," *J. Neurosurg.* **107**, 325–336.
- Kooshkabadi, A., Lunsford, L.D., Tonetti, D., Flickinger, J.C., and Kondziolka, D. (2013). "Gamma Knife thalamotomy for tremor in the magnetic resonance imaging era," *J. Neurosurg.* **118**, 713–718.
- Kooy, H.M., Dunbar, S.F., Tarbell, N.J., Mannarino, E., Ferarro, N., Shusterman, S., Bellerive, M., Finn, L., McDonough, C.V., and Loeffler, J.S. (1994). "Adaptation and verification of the relocatable Gill-Thomas-Cosman frame in stereotactic radiotherapy," *Int. J. Radiat. Oncol. Biol. Phys.* **30**, 685–691.
- Kosunen, A., and Rogers, D.W. (1993). "Beam quality specification for photon beam dosimetry," *Med. Phys.* **20**, 1181–1188.
- Krauss, A., and Kapsch, R.P. (2007). "Calorimetric determination of kQ factors for NE 2561 and NE 2571 ionization chambers in 5 cm \times 5 cm and 10 cm \times 10 cm radiotherapy beams of 8 MV and 16 MV photons," *Phys. Med. Biol.* **52**, 6243–6259.
- Kroon, P.S., Hol, S., and Essers, M. (2013). "Dosimetric accuracy and clinical quality of Acuros XB and AAA dose calculation algorithm for stereotactic and conventional lung volumetric modulated arc therapy plans," *Radiat. Oncol.* **8**, 149.
- Kry, S.F., Alvarez, P., Molineu, A., Amador, C., Galvin, J., and Followill, D.S. (2013). "Algorithms used in heterogeneous dose calculations show systematic differences as measured with the Radiological Physics Center's anthropomorphic thorax phantom used for RTOG credentialing," *Int. J. Radiat. Oncol. Biol. Phys.* **85**, e95–e100.
- Kubo, H.D., and Araki, F. (2002). "Dosimetry and mechanical accuracy of the first rotating gamma system installed in North America," *Med. Phys.* **29**, 2497–2505.
- Kubo, H.D., Len, P.M., Minohara, S., and Mostafavi, H. (2000). "Breathing-synchronized radiotherapy program at the University of California Davis Cancer Center," *Med. Phys.* **27**, 346–353.
- Kupelian, P.A., Forbes, A., Willoughby, T.R., Wallace, K., Manon, R.R., Meeks, S.L., Herrera, L., Johnston, A., and Herran, J.J. (2007). "Implantation and stability of metallic fiducials within pulmonary lesions," *Int. J. Radiat. Oncol. Biol. Phys.* **69**, 777–785.

PRESCRIBING, RECORDING, AND REPORTING SMALL BEAM SRT

- Kupelian, P.A., Lee, C., Langen, K.M., Zeidan, O.A., Manon, R.R., Willoughby, T.R., and Meeks, S.L. (2008). "Evaluation of image-guidance strategies in the treatment of localized prostate cancer," *Int. J. Radiat. Oncol. Biol. Phys.* **70**, 1151–1157.
- Kuriyama, K., Onishi, H., Sano, N., Komiyama, T., Aikawa, Y., Tateda, Y., Araki, T., and Uematsu, M. (2003). "A new irradiation unit constructed of self-moving gantry-CT and linac," *Int. J. Radiat. Oncol. Biol. Phys.* **55**, 428–435.
- Kurjewicz, L., and Berndt, A. (2007). "Measurement of Gamma Knife helmet factors using MOSFETs," *Med. Phys.* **34**, 1007–1012.
- Kutcher, G.J., Coia, L., Gillin, M., Hanson, W.F., Leibel, S., Morton, R.J., Palta, J.R., Purdy, J.A., Reinstein, L. E., Svensson, G.K., Weller, M., and Wingfield, L. (1994). "Comprehensive QA for radiation oncology: Report of AAPM Radiation Therapy Committee Task Group 40," *Med. Phys.* **21**, 581–618.
- Lachaine, M., and Falco, T. (2013). "Intrafractional prostate motion management with the Clarity autoscan system," *Med. Phys. Int.* **1**, 72–80.
- Lacornerie, T., Lisbona, A., Mirabel, X., Lartigau, E., and Reynaert, N. (2014). "GTV-based prescription in SBRT for lung lesions using advanced dose calculation algorithms," *Radiat. Oncol.* **9**, 223.
- Lagerwaard, F.J., Haasbeek, C.J., Smit, E.F., Slotman, B. J., and Senan, S. (2008). "Outcomes of risk-adapted fractionated stereotactic radiotherapy for stage I non-small-cell lung cancer," *Int. J. Radiat. Oncol. Biol. Phys.* **70**, 685–692.
- Lagerwaard, F.J., Aaronson, N.K., Gundy, C.M., Haasbeek, C.J., Slotman, B.J., and Senan, S. (2012). "Patient-reported quality of life after stereotactic ablative radiotherapy for early-stage lung cancer," *J. Thorac. Oncol.* **7**, 1148–1154.
- Landry, G., Reniers, B., Murrer, L., Lutgens, L., Gurn, E. B., Pignol, J.P., Keller, B., Beaulieu, L., and Verhaegen, F. (2010). "Sensitivity of low energy brachytherapy Monte Carlo dose calculations to uncertainties in human tissue composition," *Med. Phys.* **37**, 5188–5198.
- Landry, G., Granton, P.V., Reniers, B., Ollers, M.C., Beaulieu, L., Wildberger, J.E., and Verhaegen, F. (2011). "Simulation study on potential accuracy gains from dual energy CT tissue segmentation for low-energy brachytherapy Monte Carlo dose calculations," *Phys. Med. Biol.* **56**, 6257–6278.
- Langen, K.M., Papanikolaou, N., Balog, J., Crilly, R., Followill, D., Goddu, S.M., Grant, W. III, Olivera, G., Ramsey, C.R., and Shi, C. (2010). "QA for helical tomotherapy: Report of the AAPM Task Group 148," *Med. Phys.* **37**, 4817–4853.
- Larraga-Gutierrez, J.M., Ballesteros-Zebadua, P., Rodriguez-Ponce, M., Garcia-Garduno, O.A., and de la Cruz, O.O. (2015). "Properties of a commercial PTW-60019 synthetic diamond detector for the dosimetry of small radiotherapy beams," *Phys. Med. Biol.* **60**, 905–924.
- Larson, D.A., Flickinger, J.C., and Loeffler, J.S. (1993). "The radiobiology of radiosurgery," *Int. J. Radiat. Oncol. Biol. Phys.* **25**, 557–561.
- Larsson, B., Leksell, L., Rexed, B., Sourander, P., Mair, W., and Andersson, B. (1958). "The high-energy proton beam as a neurosurgical tool," *Nature* **182**, 1222–1223.
- Lassman, A.B., Iwamoto, F.M., Cloughesy, T.F., Aldape, K.D., Rivera, A. L., Eichler, A.F., Louis, D.N., Paleologos, N.A., Fisher, B.J., Ashby, L.S., Cairncross, J.G., Roldan, G.B., Wen, P.Y., Ligon, K.L., Schiff, D., Robins, H.I., Rocque, B.G., Chamberlain, M.C., Mason, W.P., Weaver, S.A., Green, R.M., Kamar, F.G., Abrey, L.E., DeAngelis, L.M., Jhanwar, S.C., Rosenblum, M.K., and Panageas, K.S. (2011). "International retrospective study of over 1000 adults with anaplastic oligodendroglial tumors," *Neuro. Oncol.* **13**, 649–659.
- Laub, W.U., and Nusslin, F. (2003). "Monte Carlo dose calculations in the treatment of a pelvis with implant and comparison with pencil-beam calculations," *Med. Dosim.* **28**, 229–233.
- Lawrence, Y.R., Li, X.A., el Naqa, I., Hahn, C.A., Marks, L.B., Merchant, T.E., and Dicker, A.P. (2010). "Radiation dose-volume effects in the brain," *Int. J. Radiat. Oncol. Biol. Phys.* **76**, S20–S27.
- Lee, W.J. (2009). "Neuroendocrine tumors of the liver," *Korean J. Hepatol.* **15**, 528–532.
- Leksell, L. (1951). "The stereotaxic method and radiosurgery of the brain," *Acta Chir. Scand.* **102**, 316–319.
- Leksell, L. (1968). "Cerebral radiosurgery. I. Gammathalamotomy in two cases of intractable pain," *Acta Chir. Scand.* **134**, 585–595.
- Le Roy, M., de Carlan, L., Delaunay, F., Donois, M., Fournier, P., Ostrowsky, A., Vouillame, A., and Bordy, J.M. (2011). "Assessment of small volume ionization chambers as reference dosimeters in high-energy photon beams," *Phys. Med. Biol.* **56**, 5637–5651.
- Letourneau, D., Pouliot, J., and Roy, R. (1999). "Miniature scintillating detector for small field radiation therapy," *Med. Phys.* **26**, 2555–2561.
- Letourneau, D., Martinez, A.A., Lockman, D., Yan, D., Vargas, C., Ivaldi, G., and Wong, J. (2005). "Assessment of residual error for online cone-beam CT-guided treatment of prostate cancer patients," *Int. J. Radiat. Oncol. Biol. Phys.* **62**, 1239–1246.
- Leveque, M., Carron, R., and Regis, J. (2013). "Radiosurgery for the treatment of psychiatric disorders: A review," *World Neurosurg.* **80**, S32 e1–e9.
- Lewis, E.E., and Miller, W.F. (1984). *Computational Methods of Neutron Transport* (Wiley, New York).
- Leybovich, L.B., Sethi, A., and Dogan, N. (2003). "Comparison of ionization chambers of various volumes for IMRT absolute dose verification," *Med. Phys.* **30**, 119–123.
- Li, X.A., Soubra, M., Szanto, J., and Gerig, L.H. (1995). "Lateral electron equilibrium and electron contamination in measurements of head-scatter factors using miniphantoms and brass caps," *Med. Phys.* **22**, 1167–1170.
- Li, S., Rashid, A., He, S., and Djajaputra, D. (2004). "A new approach in dose measurement and error analysis for narrow photon beams (beamlets) shaped by different multileaf collimators using a small detector," *Med. Phys.* **31**, 2020–2032.
- Li, S., Medin, P., Pillai, S., and Solberg, T. (2006). "Analysis of photon beam data from multiple institutions: An argument for reference data," *Med. Phys.* **33**, 1991.

References

- Li, W., Moseley, D.J., Bissonnette, J.P., Purdie, T.G., Bezjak, A., and Jaffray, D.A. (2010). "Setup reproducibility for thoracic and upper gastrointestinal radiation therapy: Influence of immobilization method and online cone-beam CT guidance," *Med. Dosim.* **35**, 287–296.
- Li, G., Ballangrud, A., Kuo, L.C., Kang, H., Kirov, A., Lovelock, M., Yamada, Y., Mechakos, J., and Amols, H. (2011). "Motion monitoring for cranial frameless stereotactic radiosurgery using video-based three-dimensional optical surface imaging," *Med. Phys.* **38**, 3981–3994.
- Li, J., Galvin, J., Harrison, A., Timmerman, R., Yu, Y., and Xiao, Y. (2012). "Dosimetric verification using Monte Carlo calculations for tissue heterogeneity-corrected conformal treatment plans following RTOG 0813 dosimetric criteria for lung cancer stereotactic body radiotherapy," *Int. J. Radiat. Oncol. Biol. Phys.* **84**, 508–513.
- Lightstone, A.W., Benedict, S.H., Bova, F.J., Solberg, T.D., and Stern, R.L. (2005). "Intracranial stereotactic positioning systems: Report of the American Association of Physicists in Medicine Radiation Therapy Committee Task Group No. 68," *Med. Phys.* **32**, 2380–2398.
- Ling, C.C., Humm, J., Larson, S., Amols, H., Fuks, Z., Leibel, S., and Koutcher, J.A. (2000). "Towards multidimensional radiotherapy (MD-CRT): Biological imaging and biological conformality," *Int. J. Radiat. Oncol. Biol. Phys.* **47**, 551–560.
- Linskey, M.E., Andrews, D.W., Asher, A.L., Burri, S.H., Kondziolka, D., Robinson, P.D., Ammirati, M., Cobbs, C.S., Gaspar, L.E., Loeffler, J.S., McDermott, M., Mehta, M.P., Mikkelsen, T., Olson, J.J., Paleologos, N.A., Patchell, R.A., Ryken, T.C., and Kalkanis, S.N. (2010). "The role of stereotactic radiosurgery in the management of patients with newly diagnosed brain metastases: A systematic review and evidence-based clinical practice guideline," *J. Neurooncol.* **96**, 45–68.
- Liu, H.H. (2002). "D_m rather than D_w should be used in Monte Carlo treatment planning. For the proposition," *Med. Phys.* **29**, 922–923.
- Lo, S.S., Fakiris, A.J., Teh, B.S., Cardenes, H.R., Henderson, M.A., Forquer, J.A., Papiez, L., McGarry, R.C., Wang, J.Z., Li, K., Mayr, N.A., and Timmerman, R.D. (2009). "Stereotactic body radiation therapy for oligometastases," *Expert Rev. Anticancer Ther.* **9**, 621–635.
- Lo, S.S., Fakiris, A.J., Chang, E.L., Mayr, N.A., Wang, J. Z., Papiez, L., Teh, B.S., McGarry, R.C., Cardenes, H.R., and Timmerman, R.D. (2010). "Stereotactic body radiation therapy: A novel treatment modality," *Nat. Rev. Clin. Oncol.* **7**, 44–54.
- Lobo, J., and Popescu, I.A. (2010). "Two new DOSXYZnrc sources for 4D Monte Carlo simulations of continuously variable beam configurations, with applications to RapidArc, VMAT, TomoTherapy and CyberKnife," *Phys. Med. Biol.* **55**, 4431–4443.
- Loeffler, J.S., Niemierko, A., and Chapman, P.H. (2003). "Second tumors after radiosurgery: Tip of the iceberg or a bump in the road?" *Neurosurgery* **52**, 1436–1440; discussion 1440–1442.
- LoSasso, T., Chui, C.S., and Ling, C.C. (1998). "Physical and dosimetric aspects of a multileaf collimation system used in the dynamic mode for implementing intensity modulated radiotherapy," *Med. Phys.* **25**, 1919–1927.
- Lovelock, D.M., Hua, C., Wang, P., Hunt, M., Fournier-Bidoz, N., Yenice, K., Toner, S., Lutz, W., Amols, H., Bilsky, M., Fuks, Z., and Yamada, Y. (2005). "Accurate setup of paraspinal patients using a noninvasive patient immobilization cradle and portal imaging," *Med. Phys.* **32**, 2606–2614.
- Low, D.A., Harms, W.B., Mutic, S., and Purdy, J.A. (1998). "A technique for the quantitative evaluation of dose distributions," *Med. Phys.* **25**, 656–661.
- Low, D.A., Parikh, P., Dempsey, J.F., Wahab, S., and Huq, S. (2003). "Ionization chamber volume averaging effects in dynamic intensity modulated radiation therapy beams," *Med. Phys.* **30**, 1706–1711.
- Low, D.A., Moran, J.M., Dempsey, J.F., Dong, L., and Oldham, M. (2011). "Dosimetry tools and techniques for IMRT," *Med. Phys.* **38**, 1313–1338.
- Lu, W.G., Chen, M.L., Olivera, G.H., Ruchala, K.J., and Mackie, T.R. (2004). "Fast free-form deformable registration via calculus of variations," *Phys. Med. Biol.* **49**, 3067–3087.
- Lu, X.Q., Shanmugham, L.N., Mahadevan, A., Nedea, E., Stevenson, M.A., Kaplan, I., Wong, E.T., La Rosa, S., Wang, F., and Berman, S.M. (2008). "Organ deformation and dose coverage in robotic respiratory-tracking radiotherapy," *Int. J. Radiat. Oncol. Biol. Phys.* **71**, 281–289.
- Luo, W., Li, J., Price, R.A. Jr, Chen, L., Yang, J., Fan, J., Chen, Z., McNeeley, S., Xu, X., and Ma, C.M. (2006). "Monte Carlo based IMRT dose verification using MLC log files and R/V outputs," *Med. Phys.* **33**, 2557–2564.
- Ma, C.M. (1998). "Characterization of computer simulated radiotherapy beams for Monte-Carlo treatment planning," *Radiat. Phys. Chem.* **53**, 329–344.
- Ma, C.M., and Li, J. (2011). "Dose specification for radiation therapy: Dose to water or dose to medium?" *Phys. Med. Biol.* **56**, 3073–3089.
- Ma, C.M. and Jiang, S.B. (1999). "Monte Carlo modelling of electron beams from medical accelerators," *Phys. Med. Biol.* **44**, R157–R189.
- Ma, C.M., and Paskalev, K. (2006). "In-room CT techniques for image-guided radiation therapy," *Med. Dosim.* **31**, 30–39.
- Ma, C.M., Mok, E., Kapur, A., Pawlicki, T., Findley, D., Brain, S., Forster, K., and Boyer, A.L. (1999). "Clinical implementation of a Monte Carlo treatment planning system," *Med. Phys.* **26**, 2133–2143.
- Ma, L., Kjall, P., Novotny, J., Nordstrom, H., Johansson, J., and Verhey, L. (2009). "A simple and effective method for validation and measurement of collimator output factors for Leksell Gamma Knife Perfexion," *Phys. Med. Biol.* **54**, 3897–3907.
- Mack, A., Scheib, S.G., Major, J., Gianolini, S., Pazmandi, G., Feist, H., Czempiel, H., and Kreiner, H.J. (2002). "Precision dosimetry for narrow photon beams used in radiosurgery-determination of Gamma Knife output factors," *Med. Phys.* **29**, 2080–2089.

PRESCRIBING, RECORDING, AND REPORTING SMALL BEAM SRT

- Mackie T.R., and Palta J., Eds. (2011). *Uncertainties in External Beam Radiation Therapy* (Medical Physics Publishing, Madison, WI).
- Mackie, T.R., Scrimger, J.W., and Battista, J.J. (1985). "A convolution method of calculating dose for 15-MV x rays," *Med. Phys.* **12**, 188–196.
- Mackie, T.R., Bielajew, A.F., Rogers, D.W., and Battista, J.J. (1988). "Generation of photon energy deposition kernels using the EGS Monte Carlo code," *Phys. Med. Biol.* **33**, 1–20.
- Mageras, G.S., Pevsner, A., Yorke, E.D., Rosenzweig, K.E., Ford, E.C., Hertanto, A., Larson, S.M., Lovelock, D.M., Erdi, Y.E., Nehmeh, S.A., Humm, J.L., and Ling, C.C. (2004). "Measurement of lung tumor motion using respiration-correlated CT," *Int. J. Radiat. Oncol. Biol. Phys.* **60**, 933–941.
- Maglieri, R., Licea, A., Evans, M., Seuntjens, J., and Kildea, J. (2015). "Measuring neutron spectra in radiotherapy using the nested neutron spectrometer," *Med. Phys.* **42**, 6162–6169.
- Maitz, A.H., Wu, A., Lunsford, L.D., Flickinger, J.C., Kondziolka, D., and Bloomer, W.D. (1995). "Quality assurance for gamma knife stereotactic radiosurgery," *Int. J. Radiat. Oncol. Biol. Phys.* **32**, 1465–1471.
- Maleike, D., Unkelbach, J., and Oelfke, U. (2006). "Simulation and visualization of dose uncertainties due to interfractional organ motion," *Phys. Med. Biol.* **51**, 2237–2252.
- Manning, M.A., Cardinale, R.M., Benedict, S.H., Kavanagh, B.D., Zwicker, R.D., Amir, C., and Broaddus, W.C. (2000). "Hypofractionated stereotactic radiotherapy as an alternative to radiosurgery for the treatment of patients with brain metastases," *Int. J. Radiat. Oncol. Biol. Phys.* **47**, 603–608.
- Marks, L.B., Yorke, E.D., Jackson, A., Ten Haken, R.K., Constine, L.S., Eisbruch, A., Bentzen, S.M., Nam, J., and Deasy, J.O. (2010). "Use of normal tissue complication probability models in the clinic," *Int. J. Radiat. Oncol. Biol. Phys.* **76**, S10–S19.
- Martens, C., De Wagter, C., and De Neve, W. (2000). "The value of the PinPoint ion chamber for characterization of small field segments used in intensity-modulated radiotherapy," *Phys. Med. Biol.* **45**, 2519–2530.
- Masi, L., Casamassima, F., Menichelli, C., Pasciuti, K., Doro, R., Polli, C., D'Imporzano, E., and Bonucci, I. (2008). "On-line image guidance for frameless stereotactic radiotherapy of lung malignancies by cone beam CT: Comparison between target localization and alignment on bony anatomy," *Acta Oncol.* **47**, 1422–1431.
- McEwen, M.R. (2010). "Measurement of ionization chamber absorbed dose k_Q factors in megavoltage photon beams," *Med. Phys.* **37**, 2179–2193.
- McEwen, M.R., and Ross, C.K. (2009). "Fricke and alanine dosimeters," pp. 1027–1058 in *Clinical Dosimetry Measurements in Radiotherapy*, Rogers, D.W., and Cygler, J.E., Eds., Monograph 34 (Medical Physics Publishing, Madison, WI).
- McEwen, M.R., Kawrakow, I., and Ross, C.K. (2008). "The effective point of measurement of ionization chambers and the build-up anomaly in MV x-ray beams," *Med. Phys.* **35**, 950–958.
- McEwen, M., DeWerd, L., Ibbott, G., Followill, D., Rogers, D.W., Seltzer, S., and Seuntjens, J. (2014). "Addendum to the AAPM's TG-51 protocol for clinical reference dosimetry of high-energy photon beams," *Med. Phys.* **41**, 041501, doi:10.1118/1.4866223.
- McGarry, R.C., Papiez, L., Williams, M., Whitford, T., and Timmerman, R.D. (2005). "Stereotactic body radiation therapy of early-stage non-small-cell lung carcinoma: Phase I study," *Int. J. Radiat. Oncol. Biol. Phys.* **63**, 1010–1015.
- McGarry, C.K., Cosgrove, V.P., Fleming, V.A., O'Sullivan, J.M., and Hounsell, A.R. (2009). "An analysis of geometric uncertainty calculations for prostate radiotherapy in clinical practice," *Br. J. Radiol.* **82**, 140–147.
- McKenzie, A., van Herk, M., and Mijnheer, B. (2002). "Margins for geometric uncertainty around organs at risk in radiotherapy," *Radiother. Oncol.* **62**, 299–307.
- McMahon, S.J., McGarry, C.K., Butterworth, K.T., Jain, S., O'Sullivan, J.M., Hounsell, A.R., and Prise, K.M. (2015). "Cellular signaling effects in high precision radiotherapy," *Phys. Med. Biol.* **60**, 4551–4564.
- McNulty, N.J., Francis, I.R., Platt, J.F., Cohan, R.H., Korobkin, M., and Gebremariam, A. (2001). "Multi-detector row helical CT of the pancreas: Effect of contrast-enhanced multiphasic imaging on enhancement of the pancreas, peripancreatic vasculature, and pancreatic adenocarcinoma," *Radiology* **220**, 97–102.
- Medin, P.M., Foster, R.D., van der Kogel, A.J., Sayre, J.W., McBride, W.H., and Solberg, T.D. (2013). "Spinal cord tolerance to single-session uniform irradiation in pigs: Implications for a dose-volume effect," *Radiother. Oncol.* **106**, 101–105.
- Meeks, S.L., Tome, W.A., Willoughby, T.R., Kupelian, P.A., Wagner, T.H., Buatti, J.M., and Bova, F.J. (2005). "Optically guided patient positioning techniques," *Semin. Radiat. Oncol.* **15**, 192–201.
- Mehta, N., King, C.R., Agazaryan, N., Steinberg, M., Hua, A., and Lee, P. (2012). "Stereotactic body radiation therapy and 3-dimensional conformal radiotherapy for stage I non-small cell lung cancer: A pooled analysis of biological equivalent dose and local control," *Pract. Radiat. Oncol.* **2**, 288–295.
- Meijer, G.J., Rasch, C., Remeijer, P., and Lebesque, J.V. (2003). "Three-dimensional analysis of delineation errors, setup errors, and organ motion during radiotherapy of bladder cancer," *Int. J. Radiat. Oncol. Biol. Phys.* **55**, 1277–1287.
- Méndez Romero, A., Wunderink, W., Hussain, S.M., De Pooter, J.A., Heijmen, B.J., Nowak, P.C., Nuyttens, J.J., Brandwijk, R.P., Verhoef, C., Ijzermans, J.N., and Leendag, P.C. (2006). "Stereotactic body radiation therapy for primary and metastatic liver tumors: A single institution phase i-ii study," *Acta Oncol.* **45**, 831–837.
- Menke, M., Hirschfeld, F., Mack, T., Pasty, O., Sturm, V., and Schlegel, W. (1994). "Photogrammetric accuracy measurements of head holder systems used for fractionated radiotherapy," *Int. J. Radiat. Oncol. Biol. Phys.* **29**, 1147–1155.
- Meyer, J., Wilbert, J., Baier, K., Guckenberger, M., Richter, A., Sauer, O., and Flentje, M. (2007). "ICRU 2017 -- All rights reserved.
AAPM Member Copy
Single use only, copying and networking prohibited

References

- "Positioning accuracy of cone-beam computed tomography in combination with a HexaPOD robot treatment table," *Int. J. Radiat. Oncol. Biol. Phys.* **67**, 1220–1228.
- Mitchell, C.R., Folkard, M., and Joiner, M.C. (2002). "Effects of exposure to low-dose-rate ^{60}Co gamma rays on human tumor cells *in vitro*," *Radiat. Res.* **158**, 311–318.
- Mohan, R., Chui, C., and Lidofsky, L. (1986). "Differential pencil beam dose computation model for photons," *Med. Phys.* **13**, 64–73.
- Mohan, R., Zhang, X.D., Wang, H., Kang, Y.X., Wang, X.C., Liu, H., Ang, K.K., Kuban, D., and Dong, L. (2005). "Use of deformed intensity distributions for online modification of image-guided IMRT to account for interfractional anatomic changes," *Int. J. Radiat. Oncol. Biol. Phys.* **61**, 1258–1266.
- Mohr, J.P., Parides, M.K., Staph, C., Moquete, E., Moy, C. S., Overbey, J.R., Al-Shahi Salman, R., Vicaut, E., Young, W.L., Houdart, E., Cordonnier, C., Stefani, M.A., Hartmann, A., von Kummer, R., Biondi, A., Berkefeld, J., Klijn, C.J., Harkness, K., Libman, R., Barreau, X., and Moskowitz, A.J. (2014). "Medical management with or without interventional therapy for unruptured brain arteriovenous malformations (ARUBA): A multicentre, non-blinded, randomised trial," *Lancet* **383**, 614–621.
- Moraru, I.C., Tai, A., Erickson, B., and Li, X.A. (2014). "Radiation dose responses for chemoradiation therapy of pancreatic cancer: An analysis of compiled clinical data using biophysical models," *Pract. Radiat. Oncol.* **4**, 13–19.
- Morin, O., Gillis, A., Chen, J., Aubin, M., Bucci, M.K., Roach, M. III, and Pouliot, J. (2006). "Megavoltage cone-beam CT: System description and clinical applications," *Med. Dosim.* **31**, 51–61.
- Morin, J., Beliveau-Nadeau, D., Chung, E., Seuntjens, J., Theriault, D., Archambault, L., Beddar, S. and Beaulieu, L. (2013). "A comparative study of small field total scatter factors and dose profiles using plastic scintillation detectors and other stereotactic dosimeters: The case of the CyberKnife," *Med. Phys.* **40**, 011719, doi:10.1118/1.4772190.
- Mosleh-Shirazi, M.A., Evans, P.M., Swindell, W., Webb, S., and Partridge, M. (1998). "A cone-beam megavoltage CT scanner for treatment verification in conformal radiotherapy," *Radiother. Oncol.* **48**, 319–328.
- Muacevic, A., Staehler, M., Drexler, C., Wowra, B., Reiser, M., and Tonn, J.C. (2006). "Technical description, phantom accuracy, and clinical feasibility for fiducial-free frameless real-time image-guided spinal radiosurgery," *J. Neurosurg. Spine* **5**, 303–312.
- Muir, B.R., McEwen, M.R., and Rogers, D.W. (2011). "Measured and Monte Carlo calculated k_Q factors: Accuracy and comparison," *Med. Phys.* **38**, 4600–4609.
- Munro, P., Rawlinson, J.A., and Fenster, A. (1988). "Therapy imaging: Source sizes of radiotherapy beams," *Med. Phys.* **15**, 517–524.
- Murphy, J.A., Savage, C.M., Alpard, S.K., Deyo, D.J., Jayroe, J.B., and Zwischenberger, J.B. (2001). "Low-dose versus high-dose heparinization during arteriovenous carbon dioxide removal," *Perfusion* **16**, 460–468.
- Murphy, M.J., Jaden, J., and Isaksson, M. (2002). "Adaptive filtering to predict lung tumor breathing motion during image-guided radiation therapy," pp. 539–544 in *Proceedings of the 16th International Congress on Computer-Assisted Radiology and Surgery (CARS)* (Springer, Heidelberg).
- Murphy, M.J., Balter, S., BenComo, J.A. Jr, Das, I.J., Jiang, S.B., Ma, C.M., Olivera, G.H., Rodebaugh, R.F., Ruchala, K.J., Shirato, H., and Yin, F.F. (2007). "The management of imaging dose during image-guided radiotherapy: Report of the AAPM Task Group 75," *Med. Phys.* **34**, 4041–4063.
- Murphy, M.J. (2009). "Intrafraction geometric uncertainties in frameless image-guided radiosurgery," *Int. J. Radiat. Oncol. Biol. Phys.* **73**, 1364–1368.
- Mutic, S., and Dempsey, J.F. (2014). "The ViewRay System: Magnetic resonance-guided and controlled radiotherapy," *Semin. Radiat. Oncol.* **24**, 196–199.
- Nagata, Y., Takayama, K., Matsuo, Y., Norihisa, Y., Mizowaki, T., Sakamoto, T., Sakamoto, M., Mitsumori, M., Shibuya, K., Araki, N., Yano, S., and Hiraoka, M. (2005). "Clinical outcomes of a phase I/II study of 48 Gy of stereotactic body radiotherapy in 4 fractions for primary lung cancer using a stereotactic body frame," *Int. J. Radiat. Oncol. Biol. Phys.* **63**, 1427–1431.
- Ng, A.W., Tung, S.Y., and Wong, V.Y. (2008). "Hypofractionated stereotactic radiotherapy for medically inoperable stage I non-small cell lung cancer – report on clinical outcome and dose to critical organs," *Radiother. Oncol.* **87**, 24–28.
- Nizin, P.S. (1998). "On absorbed dose in narrow ^{60}Co gamma-ray beams and dosimetry of the gamma knife," *Med. Phys.* **25**, 2347–2351.
- Nuyttens, J.J., Prevost, J.B., Van der Voort van Zijp, N.C., Hoogeman, M., and Levendag, P.C. (2007). "Curative stereotactic robotic radiotherapy treatment for extracranial, extrapulmonary, extrahepatic, and extraspinal tumors: Technique, early results, and toxicity," *Technol. Cancer Res. Treat.* **6**, 605–610.
- Nuyttens, J.J., and van de Pol, M. (2012). "The CyberKnife radiosurgery system for lung cancer," *Exper. Rev. Med. Devices* **9**, 465–475.
- Nuyttens, J.J., van der Voort van Zyp, N.C., Verhoef, C., Maat, A., van Klaveren, R.J., van der Holt, B., Aerts, J., and Hoogeman, M. (2015). "Stereotactic body radiation therapy for oligometastases to the lung: A phase 2 study," *Int. J. Radiat. Oncol. Biol. Phys.* **91**, 337–343.
- Nyman, J., Johansson, K.A., and Hulten, U. (2006). "Stereotactic hypofractionated radiotherapy for stage I non-small cell lung cancer—mature results for medically inoperable patients," *Lung Cancer* **51**, 97–103.
- Och, J.G., Clarke, G.D., Sobol, W.T., Rosen, C.W., and Mun, S.K. (1992). "Acceptance testing of magnetic resonance imaging systems: Report of AAPM Nuclear Magnetic Resonance Task Group No. 6," *Med. Phys.* **19**, 217–229.
- O'Connor, J.E. (1957). "The variation of scattered x-rays with density in an irradiated body," *Phys. Med. Biol.* **1**, 352–369.
- O'Connor, J.K., Trotter, J., Davis, G.L., Dempster, J., Klintmalm, G.B., and Goldstein, R.M. (2012). "Long-

- term outcomes of stereotactic body radiation therapy in the treatment of hepatocellular cancer as a bridge to transplantation," *Liver Transpl.* **18**, 949–954.
- Okunieff, P., Petersen, A.L., Philip, A., Milano, M.T., Katz, A.W., Boros, L., and Schell, M.C. (2006). "Stereotactic body radiation therapy (SBRT) for lung metastases," *Acta Oncol.* **45**, 808–817.
- Onimaru, R., Shirato, H., Shimizu, S., Kitamura, K., Xu, B., Fukumoto, S., Chang, T.C., Fujita, K., Oita, M., Miyasaka, K., Nishimura, M., and Dosaka-Akita, H. (2003). "Tolerance of organs at risk in small-volume, hypofractionated, image-guided radiotherapy for primary and metastatic lung cancers," *Int. J. Radiat. Oncol. Biol. Phys.* **56**, 126–135.
- Onishi, H., Araki, T., Shirato, H., Nagata, Y., Hiraoka, M., Gomi, K., Yamashita, T., Niibe, Y., Karasawa, K., Hayakawa, K., Takai, Y., Kimura, T., Hirokawa, Y., Takeda, A., Ouchi, A., Hareyama, M., Kokubo, M., Hara, R., Itami, J., and Yamada, K. (2004). "Stereotactic hypofractionated high-dose irradiation for stage I nonsmall cell lung carcinoma: Clinical outcomes in 245 subjects in a Japanese multiinstitutional study," *Cancer* **101**, 1623–1631.
- Orton, C.G. (2012). "Fractionation: Radiobiologic principles and clinical practice," pp. 340–354 in *Khan's Treatment Planning in Radiation Oncology*, 4th ed., Khan, F., Gerbi, B., and Sperduto, P.W., Eds. (Wolters Kluwer Health/Lippincott Williams, Philadelphia).
- Paddick, I. (2000). "A simple scoring ratio to index the conformity of radiosurgical treatment plans. Technical note," *J. Neurosurg.* **93**, 219–222.
- Palmans, H. (2012). "Determination of the beam quality index of high-energy photon beams under nonstandard reference conditions," *Med. Phys.* **39**, 5513–5519.
- Palta, M., Yoo, S., Adamson, J.D., Prosnitz, L.R., and Horton, J.K. (2012). "Preoperative single fraction partial breast radiotherapy for early-stage breast cancer," *Int. J. Radiat. Oncol. Biol. Phys.* **82**, 37–42.
- Panettieri, V., Wennberg, B., Gagliardi, G., Duch, M.A., Ginjaume, M., and Lax, I. (2007). "SBRT of lung tumours: Monte Carlo simulation with PENELOPE of dose distributions including respiratory motion and comparison with different treatment planning systems," *Phys. Med. Biol.* **52**, 4265–4281.
- Pantelis, E., Moutsatsos, A., Zourari, K., Kilby, W., Antypas, C., Papagiannis, P., Karaikos, P., Georgiou, E., and Sakellou, L. (2010). "On the implementation of a recently proposed dosimetric formalism to a robotic radiosurgery system," *Med. Phys.* **37**, 2369–2379.
- Pantelis, E., Moutsatsos, A., Zourari, K., Petrokokkinos, L., Sakellou, L., Kilby, W., Antypas, C., Papagiannis, P., Karaikos, P., Georgiou, E., and Seimenis, I. (2012). "On the output factor measurements of the CyberKnife iris collimator small fields: Experimental determination of the $k(Q(\text{clin}), Q(\text{msr})) / (f(\text{clin}), f(\text{msr}))$ correction factors for microchamber and diode detectors," *Med. Phys.* **39**, 4875–4885.
- Papaconstadopoulos, P., Tessier, F., and Seuntjens, J. (2014). "On the correction, perturbation and modification of small field detectors in relative dosimetry," *Phys. Med. Biol.* **59**, 5937–5952.
- Papanikolaou, N., Mackie, T.R., Meger-Wells, C., Gehring, M., and Reckwerdt, P. (1993). "Investigation of the convolution method for polyenergetic spectra," *Med. Phys.* **20**, 1327–1336.
- Papanikolaou, N., Battista, J.J., Boyer, A.L., Kappas, C., Klein, E., Mackie, T.R., Sharpe, M., and Van Dyk, J. (2004). *Tissue Inhomogeneity Corrections for Megavoltage Photon Beams*, AAPM Report No. 85 (Medical Physics Publishing, Madison, WI).
- Parikh, P.J., Noel, C.E., Spencer, C., Green, O., Hu, Y., Mutic, S., and Olsen, J.R. (2012). "Comparison of onboard low-field MRI versus CBCT/MVCT for anatomy identification in radiation therapy," *Int. J. Radiat. Oncol. Biol. Phys.* **84**, S133.
- Park, C., Papiez, L., Zhang, S., Story, M., and Timmerman, R.D. (2008). "Universal survival curve and single fraction equivalent dose: Useful tools in understanding potency of ablative radiotherapy," *Int. J. Radiat. Oncol. Biol. Phys.* **70**, 847–852.
- Paskalev, K.A., Seuntjens, J.P., Patrocinio, H.J., and Podgorsak, E.B. (2003). "Physical aspects of dynamic stereotactic radiosurgery with very small photon beams (1.5 and 3 mm in diameter)," *Med. Phys.* **30**, 111–118.
- Pawlicki, T., and Ma, C.M. (2001). "Monte Carlo simulation for MLC-based intensity-modulated radiotherapy," *Med. Dosim.* **26**, 157–168.
- Perks, J., Gao, M., Smith, V., Skubic, S., and Goetsch, S. (2005). "Glass rod detectors for small field, stereotactic radiosurgery dosimetric audit," *Med. Phys.* **32**, 726–732.
- Perks, J.R., Lehmann, J., Chen, A.M., Yang, C.C., Stern, R.L., and Purdy, J.A. (2008). "Comparison of peripheral dose from image-guided radiation therapy (IGRT) using kV cone beam CT to intensity-modulated radiation therapy (IMRT)," *Radiother. Oncol.* **89**, 304–310.
- Persson, G.F., Nygaard, D.E., Munck Af Rosenschold, P., Richter Vogelius, I., Josipovic, M., Specht, L., and Korreman, S.S. (2011). "Artifacts in conventional computed tomography (CT) and free breathing four-dimensional CT induce uncertainty in gross tumor volume determination," *Int. J. Radiat. Oncol. Biol. Phys.* **80**, 1573–1580.
- Pike, B., Podgorsak, E.B., Peters, T.M., and Pla, C. (1987). "Dose distributions in dynamic stereotactic radiosurgery," *Med. Phys.* **14**, 780–789.
- Podgorsak, E.B., Olivier, A., Pla, M., Hazel, J., de Lotbiniere, A., and Pike, B. (1987). "Physical aspects of dynamic stereotactic radiosurgery," *Appl. Neurophysiol.* **50**, 263–268.
- Ponsky, L.E., and Vricella, G. (2012). "Radiosurgery for renal tumors," pp. 179–184 in *Robotic Radiosurgery. Treating Prostate Cancer and Related Genitourinary Applications*, Ponsky, L.E., Fuller, D.B., Meier, R.M., and Ma, C., Eds. (Springer, Heidelberg).
- Purdie, T.G., Bissonnette, J.P., Franks, K., Bezjak, A., Payne, D., Sie, F., Sharpe, M.B., and Jaffray, D.A. (2007). "Cone-beam computed tomography for on-line image guidance of lung stereotactic radiotherapy: Localization, verification, and intrafraction tumor position," *Int. J. Radiat. Oncol. Biol. Phys.* **68**, 243–252.
- Qi, X.S., Schultz, C.J., and Li, X.A. (2007). "Possible fractionated regimens for image-guided intensity-

- modulated radiation therapy of large arteriovenous malformations," *Phys. Med. Biol.* **52**, 5667–5682.
- Ralston, A., Liu, P., Warrener, K., McKenzie, D., and Suchowerska, N. (2012). "Small field diode correction factors derived using an air core fibre optic scintillation dosimeter and EBT2 film," *Phys. Med. Biol.* **57**, 2587–2602.
- Ramakrishna, N., Rosca, F., Friesen, S., Tezcanli, E., Zygmanszki, P., and Hacker, F. (2010). "A clinical comparison of patient setup and intra-fraction motion using frame-based radiosurgery versus a frameless image-guided radiosurgery system for intracranial lesions," *Radiother. Oncol.* **95**, 109–115.
- Ramsey, C.R., Scaperoth, D., and Arwood, D. (2000). "Clinical experience with a commercial respiratory gating system," *Int. J. Radiat. Oncol. Biol. Phys.* **48**, 164–165.
- Ramsey, C.R., Langen, K.M., Kupelian, P.A., Scaperoth, D.D., Meeks, S.L., Mahan, S.L., and Seibert, R.M. (2006). "A technique for adaptive image-guided helical tomotherapy for lung cancer," *Int. J. Radiat. Oncol. Biol. Phys.* **64**, 1237–1244.
- Rasch, C., Barillot, I., Remeijer, P., Touw, A., van Herk, M., and Lebesque, J.V. (1999). "Definition of the prostate in CT and MRI: A multi-observer study," *Int. J. Radiat. Oncol. Biol. Phys.* **43**, 57–66.
- Renaud, J., Marchington, D., Seuntjens, J., and Sarfehnia, A. (2013). "Development of a graphite probe calorimeter for absolute clinical dosimetry," *Med. Phys.* **40**, 020701, doi:10.1118/1.4773870.
- Reynaert, N., van der Marck, S., Schaart, D., van der Zee, A., Tomsej, M., van Vliet-Vroegindeweij, C., Jansen, J., Coghe, M., De Wagter, C., and Heijmen, B. (2006). *Monte Carlo Treatment Planning: An Introduction*, Report NCS-16 (Netherlands Commission on Radiation Dosimetry, Delft).
- Reynaert, N., van der Marck, S.C., Schaart, D.R., van der Zee, W., van Vliet-Vroegindeweij, C., Tomsej, M., Jansen, J., Heijmen, B., Coghe, M., and De Wagter, C. (2007). "Monte Carlo treatment planning for photon and electron beams," *Radiat. Phys. Chem.* **76**, 643–686.
- Rietzel, E., Pan, T., and Chen, G.T. (2005). "Four-dimensional computed tomography: Image formation and clinical protocol," *Med. Phys.* **32**, 874–889.
- Ritter, M.A., Forman, J.D., Kupelian, P.A., Petereit, D.G., Lawton, C.A., Chappell, R.J., and Tome, W.A. (2009). "A phase I/II trial of increasingly hypofractionated radiation therapy for prostate cancer," *Int. J. Radiat. Oncol. Biol. Phys.* **75**, S80–S81.
- Roach, M. III, Faillace-Akazawa, P., Malfatti, C., Holland, J., and Hricak, H. (1996). "Prostate volumes defined by magnetic resonance imaging and computerized tomographic scans for three-dimensional conformal radiotherapy," *Int. J. Radiat. Oncol. Biol. Phys.* **35**, 1011–1018.
- Roberge, D., Parney, I., and Brown, P.D. (2012). "Radiosurgery to the postoperative surgical cavity: Who needs evidence?," *Int. J. Radiat. Oncol. Biol. Phys.* **83**, 486–493.
- Roberge, D., Leclerc-Champagne, C., Doucet, R., and Seuntjens, J. (2015). "How low should you go: Choice of minimum dose prescription in cranial radiosurgery," *Cureus* **7**, e282.
- Roeske, J.C., Forman, J.D., Mesina, C.F., He, T., Pelizzari, C.A., Fontenla, E., Vijayakumar, S., and Chen, G.T.Y. (1995). "Evaluation of changes in the size and location of the prostate, seminal vesicles, bladder, and rectum during a course of external beam radiation therapy," *Int. J. Radiat. Oncol. Biol. Phys.* **33**, 1321–1329.
- Rogers, D.W.O. (2009). "General characteristics of radiation dosimeters and a terminology to describe them," pp. 137–146 in *Clinical Dosimetry Measurements in Radiotherapy*, Monograph 34 (Medical Physics Publishing, Madison, WI).
- Rogers, D.W., and Bielajew, A.F. (1990). "Monte Carlo techniques of electron and photon transport for radiation dosimetry," pp. 427–539 in *The Dosimetry of Ionization Radiation*, Vol. III, Bjarngard, B.E., Kase, K.R., and Attix, F.H., Eds. (Academic Press, New York).
- Rogers, D.W., Faddegon, B.A., Ding, G.X., Ma, C.M., We, J., and Mackie, T.R. (1995). "BEAM: A Monte Carlo code to simulate radiotherapy treatment units," *Med. Phys.* **22**, 503–524.
- Rogus, R.D., Stern, R.L., and Kubo, H.D. (1999). "Accuracy of a photogrammetry-based patient positioning and monitoring system for radiation therapy," *Med. Phys.* **26**, 721–728.
- Roh, K.W., Jang, J.S., Kim, M.S., Sun, D.I., Kim, B.S., Jung, S.L., Kang, J.H., Yoo, E.J., Yoon, S.C., Jang, H.S., Chung, S.M., and Kim, Y.S. (2009). "Fractionated stereotactic radiotherapy as reirradiation for locally recurrent head and neck cancer," *Int. J. Radiat. Oncol. Biol. Phys.* **74**, 1348–1355.
- Rolston, J.D., Quigg, M., and Barbaro, N.M. (2011). "Gamma knife radiosurgery for mesial temporal lobe epilepsy," *Epilepsy Res. Treat.* **2011**, 840616, doi:10.1155/2011/840616.
- Rusthoven, K.E., Kavanagh, B.D., Cardenes, H., Stieber, V.W., Burri, S.H., Feigenberg, S.J., Chidel, M.A., Pugh, T.J., Franklin, W., Kane, M., Gaspar, L.E., and Scheftel, T.E. (2009a). "Multi-institutional phase I/II trial of stereotactic body radiation therapy for liver metastases," *J. Clin. Oncol.* **27**, 1572–1578.
- Rusthoven, K.E., Kavanagh, B.D., Burri, S.H., Chen, C., Cardenes, H., Chidel, M.A., Pugh, T.J., Kane, M., Gaspar, L.E., and Scheftel, T.E. (2009b). "Multi-institutional phase I/II trial of stereotactic body radiation therapy for lung metastases," *J. Clin. Oncol.* **27**, 1579–1584.
- Rwigema, J.C., Heron, D.E., Ferris, R.L., Gibson, M., Quinn, A., Yang, Y., Ozhasoglu, C., and Burton, S. (2010). "Fractionated stereotactic body radiation therapy in the treatment of previously-irradiated recurrent head and neck carcinoma: Updated report of the University of Pittsburgh experience," *Am. J. Clin. Oncol.* **33**, 286–293.
- Sahgal, A., Ames, C., Chou, D., Ma, L., Huang, K., Xu, W., Chin, C., Weinberg, V., Chuang, C., Weinstein, P., and Larson, D.A. (2009). "Stereotactic body radiotherapy is effective salvage therapy for patients with prior

- radiation of spinal metastases," *Int. J. Radiat. Oncol. Biol. Phys.* **74**, 723–731.
- Sanchez-Doblado, F., Andreo, P., Capote, R., Leal, A., Perucha, M., Arrans, R., Nunez, L., Mainegra, E., Lagares, J.I., and Carrasco, E. (2003). "Ionization chamber dosimetry of small photon fields: A Monte Carlo study on stopping-power ratios for radiosurgery and IMRT beams," *Phys. Med. Biol.* **48**, 2081–2099.
- Sandhu, A., Sethi, R., Rice, R., Wang, J.Z., Marcus, L., Salem, C., Downs, T., Parsons, J.K., Millard, F., Pawlicki, T., and Mundt, A. (2008). "Prostate bed localization with image-guided approach using on-board imaging: Reporting acute toxicity and implications for radiation therapy planning following prostatectomy," *Radiother. Oncol.* **88**, 20–25.
- Sauer, O.A. (2009). "Determination of the quality index (Q) for photon beams at arbitrary field sizes," *Med. Phys.* **36**, 4168–4172.
- Saw, C.B., Yang, Y., Li, F., Yue, N.J., Ding, C., Komanduri, K., Huq, S., and Heron, D.E. (2007). "Performance characteristics and quality assurance aspects of kilovoltage cone-beam CT on medical linear accelerator," *Med. Dosim.* **32**, 80–85.
- Sawkey, D., Constantin, M., and Svatos, M. (2012). "Comparison of electron scattering algorithms in Geant4," *Phys. Med. Biol.* **57**, 3249–3258.
- Schaltenbrand, G., Wahren, W., and Walker, E.A. (1977). *Atlas for Stereotaxy of the Human Brain* (George Thieme, New York).
- Schell, M.C., and Wu, A. (1995), "External beam stereotactic radiosurgery physics," pp. 193–207 in *Radiation Therapy Physics*, Smith, A.R., Ed. (Springer, Berlin).
- Schell, M.C., Bova, F.J., Larson, D.A., Leavitt, D.D., Lutz, W.R., Podgorsak, E.B., and Wu, A. (1995). *Stereotactic Radiosurgery*, AAPM Report No. 54 (American Association of Physicists in Medicine, Alexandria, VA).
- Schlegel, W., Pasty, O., Bortfeld, T., Gademann, G., Menke, M., and Maierborst, W. (1993). "Stereotactically guided fractionated radiotherapy – technical aspects," *Radiother. Oncol.* **29**, 197–204.
- Schmuecking, M., Boltze, C., Geyer, H., Salz, H., Schilling, B., Wendt, T.G., Kloetzer, K.H., and Marx, C. (2009). "Dynamic MRI and CAD vs. choline MRS: Where is the detection level for a lesion characterisation in prostate cancer?," *Int. J. Radiat. Biol.* **85**, 814–824.
- Schubert, L.K., Westerly, D.C., Tome, W.A., Mehta, M.P., Soisson, E.T., Mackie, T.R., Ritter, M.A., Khuntia, D., Harari, P.M., and Paliwal, B.R. (2009). "A comprehensive assessment by tumor site of patient setup using daily MVCT imaging from more than 3,800 helical tomotherapy treatments," *Int. J. Radiat. Oncol. Biol. Phys.* **73**, 1260–1269.
- Seco, J., and Verhaegen, F., Eds. (2013). *Monte Carlo techniques in radiation therapy*. (CRC/Taylor and Francis, Boca Raton, FL).
- Sedrak, M., Wong, W., Wilson, P., Bruce, D., Bernstein, I., Khandhar, S., Pappas, C., Heit, G., and Sabelman, E. (2013). "Deep brain stimulation for the treatment of severe, medically refractory obsessive-compulsive disorder," *Perm. J.* **17**, 47–51.
- Seiler, P.G., Blattmann, H., Kirsch, S., Muench, R.K., and Schilling, C. (2000). "A novel tracking technique for the continuous precise measurement of tumour positions in conformal radiotherapy," *Phys. Med. Biol.* **45**, N103–N110.
- Sempau, J., Wilderman, S.J., and Bielajew, A.F. (2000). "DPM, a fast, accurate Monte Carlo code optimized for photon and electron radiotherapy treatment planning dose calculations," *Phys. Med. Biol.* **45**, 2263–2291.
- Sempau, J., Sanchez-Reyes, A., Salvat, F., ben Tahar, H. O., Jiang, S.B., and Fernandez-Varea, J.M. (2001). "Monte Carlo simulation of electron beams from an accelerator head using PENELOPE," *Phys. Med. Biol.* **46**, 1163–1186.
- Seppenwoolde, Y., Shirato, H., Kitamura, K., Shimizu, S., van Herk, M., Lebesque, J.V., and Miyasaka, K. (2002). "Precise and real-time measurement of 3D tumor motion in lung due to breathing and heartbeat, measured during radiotherapy," *Int. J. Radiat. Oncol. Biol. Phys.* **53**, 822–834.
- Serago, C.F., Chungbin, S.J., Buskirk, S.J., Ezzell, G.A., Collie, A.C., and Vora, S.A. (2002). "Initial experience with ultrasound localization for positioning prostate cancer patients for external beam radiotherapy," *Int. J. Radiat. Oncol. Biol. Phys.* **53**, 1130–1138.
- Seuntjens, J., and Duane, S. (2009). "Photon absorbed dose standards," *Metrologia* **46**, S39.
- Shah, C., Grills, I.S., Kestin, L.L., McGrath, S., Ye, H., Martin, S.K., and Yan, D. (2012). "Intrafraction variation of mean tumor position during image-guided hypofractionated stereotactic body radiotherapy for lung cancer," *Int. J. Radiat. Oncol. Biol. Phys.* **82**, 1636–1641.
- Sham, E., Seuntjens, J., Devic, S., and Podgorsak, E.B. (2008). "Influence of focal spot on characteristics of very small diameter radiosurgical beams," *Med. Phys.* **35**, 3317–3330.
- Sharpe, M.B., Moseley, D.J., Purdie, T.G., Islam, M., Siewerssen, J.H., and Jaffray, D.A. (2006). "The stability of mechanical calibration for a kV cone beam computed tomography system integrated with linear accelerator," *Med. Phys.* **33**, 136–144.
- Shaw, E., Kline, R., Gillin, M., Souhami, L., Hirschfeld, A., Dinapoli, R., and Martin, L. (1993). "Radiation Therapy Oncology Group: Radiosurgery quality assurance guidelines," *Int. J. Radiat. Oncol. Biol. Phys.* **27**, 1231–1239.
- Sheehan, J., and Steiner, L. (2005). "Trigeminal neuralgia," *J. Neurosurg.* **102**, 1173.
- Sheu, T., Molkentine, J., Transtrum, M.K., Buchholz, T. A., Withers, H.R., Thames, H.D., and Mason, K.A. (2013). "Use of the LQ model with large fraction sizes results in underestimation of isoeffect doses," *Radiother. Oncol.* **109**, 21–25.
- Shi, W., Li, J.G., Zlotecki, R.A., Yeung, A., Newlin, H., Palta, J., Liu, C., Chvetsov, A.V., and Olivier, K. (2011). "Evaluation of kV cone-beam CT performance for prostate IGRT: A comparison of automatic grey-

References

- value alignment to implanted fiducial-marker alignment," *Am. J. Clin. Oncol.* **34**, 16–21.
- Shrieve, D.C., Tarbell, N.J., Alexander, E., Kooy, H.M., Black, P.M., Dunbar, S., and Loeffler, J.S. (1994). "Stereotactic radiotherapy – a technique for dose optimization and escalation for intracranial tumors," *Adv. Radiat. Oncol.* **62**, 118–123.
- Siebers, J.V., Keall, P.J., Nahum, A.E., and Mohan, R. (2000). "Converting absorbed dose to medium to absorbed dose to water for Monte Carlo based photon beam dose calculations," *Phys. Med. Biol.* **45**, 983–995.
- Silvestri, G.A., Gould, M.K., Margolis, M.L., Tanoue, L.T., McCrory, D., Toloza, E., and Detterbeck, F. (2007). "Noninvasive staging of non-small cell lung cancer: ACCP evidenced-based clinical practice guidelines (2nd edition)," *Chest* **132**, 178S–201S.
- Smith, W.L., Lewis, C., Bauman, G., Rodrigues, G., D'Souza, D., Ash, R., Ho, D., Venkatesan, V., Downey, D., and Fenster, A. (2007). "Prostate volume contouring: A 3D analysis of segmentation using 3DTRUS, CT, and MR," *Int. J. Radiat. Oncol. Biol. Phys.* **67**, 1238–1247.
- Soares, C.G., Trichter, S., and Devic, S. (2009). "Radiochromic film," pp. 759–813 in *Clinical Dosimetry Measurements in Radiotherapy*, Rogers, D.W., and Cygler, J.E., Eds. (Medical Physics Publishing, Madison, WI).
- Sobin, L.H., Gospodarowicz, M.K., and Wittekind, C. (2010). *TNM Classification of Malignant Tumours*, 7th ed. (Wiley-Blackwell, Hoboken, NJ).
- Soete, G., Verellen, D., Tournel, K., and Storme, G. (2006). "Setup accuracy of stereoscopic x-ray positioning with automated correction for rotational errors in patients treated with conformal arc radiotherapy for prostate cancer," *Radiother. Oncol.* **80**, 371–373.
- Sofia, J.W. (1979). "Computer controlled, multileaf collimator for rotataional radiation therapy," *Am. J. Roentgenol.* **133**, 956–957.
- Soisson, E.T., Hardcastle, N., and Tome, W.A. (2010). "Quality assurance of an image guided intracranial stereotactic positioning system for radiosurgery treatment with helical tomotherapy," *J. Neurooncol.* **98**, 277–285.
- Solberg, T.D., Boedeker, K.L., Fogg, R., Selch, M.T., and DeSalles, A.A. (2001). "Dynamic arc radiosurgery field shaping: A comparison with static field conformal and noncoplanar circular arcs," *Int. J. Radiat. Oncol. Biol. Phys.* **49**, 1481–1491.
- Solberg, T.D., Medin, P.M., Mullins, J., and Li, S. (2008). "Quality assurance of immobilization and target localization systems for frameless stereotactic cranial and extracranial hypofractionated radiotherapy," *Int. J. Radiat. Oncol. Biol. Phys.* **71**, S131–S135.
- Somigliana, A., Cattaneo, G.M., Fiorino, C., Borelli, S., del Vecchio, A., Zonca, G., Pignoli, E., Loi, G., Calandrino, R., and Marchesini, R. (1999). "Dosimetry of Gamma Knife and linac-based radiosurgery using radiochromic and diode detectors," *Phys. Med. Biol.* **44**, 887–897.
- Song, C.W., Cho, L.C., Yuan, J., Dusenberry, K.E., Griffin, R.J., and Levitt, S.H. (2013). "Radiobiology of stereotactic body radiation therapy/stereotactic radiosurgery and the linear-quadratic model," *Int. J. Radiat. Oncol. Biol. Phys.* **87**, 18–19.
- Sonke, J.J., Zijp, L., Remeijer, P., and van Herk, M. (2005). "Respiratory correlated cone beam CT," *Med. Phys.* **32**, 1176–1186.
- Sonke, J.J., Lebesque, J., and van Herk, M. (2008). "Variability of four-dimensional computed tomography patient models," *Int. J. Radiat. Oncol. Biol. Phys.* **70**, 590–598.
- Sonke, J.J., Rossi, M., Wolthaus, J., van Herk, M., Damen, E., and Belderbos, J. (2009). "Frameless stereotactic body radiotherapy for lung cancer using four-dimensional cone beam CT guidance," *Int. J. Radiat. Oncol. Biol. Phys.* **74**, 567–574.
- Soriano, A., Castells, A., Ayuso, C., Ayuso, J.R., de Caralt, M.T., Gines, M.A., Real, M.I., Gilabert, R., Quinto, L., Trilla, A., Feu, F., Montanya, X., Fernandez-Cruz, L., and Navarro, S. (2004). "Preoperative staging and tumor resectability assessment of pancreatic cancer: Prospective study comparing endoscopic ultrasonography, helical computed tomography, magnetic resonance imaging, and angiography," *Am. J. Gastroenterol.* **99**, 492–501.
- Souhami, L., Olivier, A., Podgorsak, E.B., Villemure, J.G., Pla, M., and Sadikot, A.F. (1991). "Fractionated stereotactic radiation-therapy for intracranial tumors," *Cancer* **68**, 2101–2108.
- Souhami, L., Seiferheld, W., Brachman, D., Podgorsak, E.B., Werner-Wasik, M., Lustig, R., Schultz, C.J., Sause, W., Okunieff, P., Buckner, J., Zamorano, L., Mehta, M.P., and Curran, W.J. Jr (2004). "Randomized comparison of stereotactic radiosurgery followed by conventional radiotherapy with carmustine to conventional radiotherapy with carmustine for patients with glioblastoma multiforme: Report of Radiation Therapy Oncology Group 93-05 protocol," *Int. J. Radiat. Oncol. Biol. Phys.* **60**, 853–860.
- Spiegel, E.A., Wycis, H.T., Marks, M., and Lee, A.J. (1947). "Stereotaxic apparatus for operations on the human brain," *Science* **106**, 349–350.
- Stanic, S., Paulus, R., Timmerman, R.D., Michalski, J.M., Barriger, R.B., Bezjak, A., Videtic, G.M., and Bradley, J. (2014). "No clinically significant changes in pulmonary function following stereotactic body radiation therapy for early- stage peripheral non-small cell lung cancer: An analysis of RTOG 0236," *Int. J. Radiat. Oncol. Biol. Phys.* **88**, 1092–1099.
- Starke, R.M., Komotar, R.J., Hwang, B.Y., Fischer, L.E., Otten, M.L., Merkow, M.B., Garrett, M.C., Isaacson, S.R., and Connolly, E.S. Jr (2008). "A comprehensive review of radiosurgery for cerebral arteriovenous malformations: Outcomes, predictive factors, and grading scales," *Stereotact. Funct. Neurosurg.* **86**, 191–199.
- Steenbakkers, R.J., Duppen, J.C., Fitton, I., Deurloo, K.E., Zijp, L., Uitterhoeve, A.L., Rodrigus, P.T., Kramer, G.W., Bussink, J., De Jaeger, K., Belderbos, J.S., Hart, A.A., Nowak, P.J., van Herk, M., and Rasch, C.R. (2005). "Observer variation in target volume delineation of lung cancer related to radiation oncologist-computer interaction: A 'Big Brother' evaluation," *Radiother. Oncol.* **77**, 182–190.

PRESCRIBING, RECORDING, AND REPORTING SMALL BEAM SRT

- Steenbakkers, R.J., Duppen, J.C., Fitton, I., Deurloo, K.E., Zijp, L.J., Comans, E.F., Uitterhoeve, A.L., Rodrigus, P.T., Kramer, G.W., Bussink, J., De Jaeger, K., Belderbos, J.S., Nowak, P.J., van Herk, M., and Rasch, C.R. (2006). "Reduction of observer variation using matched CT-PET for lung cancer delineation: A three-dimensional analysis," *Int. J. Radiat. Oncol. Biol. Phys.* **64**, 435–448.
- Steinmann, D., Vordermark, D., Geinitz, H., Aschoff, R., Bayerl, A., Gerstein, J., Hipp, M., van Oorschot, B., Wypior, H.J., and Schaefer, C. (2013). "Proxy assessment of patients before and after radiotherapy for brain metastases. Results of a prospective study using the DEGRO brain module," *Strahlenther. Onkol.* **189**, 47–53.
- Sterpin, E., Tomsej, M., Cravens, B., Salvat, F., Ruchala, K., Olivera, G.H., and Vynckier, S. (2007). "Monte Carlo simulation of the tomotherapy treatment unit in the static mode using MC HAMMER, a Monte Carlo tool dedicated to tomotherapy," *J. Phys. Conf. Ser.* **74**, 012019, doi:10.1088/1742-6596/74/1/012019.
- Sterpin, E., Chen, Y., Lu, W., Mackie, T.R., Olivera, G.H., and Vynckier, S. (2011). "On the relationships between electron spot size, focal spot size, and virtual source position in Monte Carlo simulations," *Med. Phys.* **38**, 1579–1586.
- Sterpin, E., Mackie, T.R., and Vynckier, S. (2012). "Monte Carlo computed machine-specific correction factors for reference dosimetry of TomoTherapy static beam for several ion chambers," *Med. Phys.* **39**, 4066–4072.
- Stroom, J.C., and Heijmen, B.J. (2002). "Geometrical uncertainties, radiotherapy planning margins, and the ICRU-62 report," *Radiother. Oncol.* **64**, 75–83.
- Stroom, J.C., de Boer, H.C.J., Huizenga, H., and Visser, A.G. (1999). "Inclusion of geometrical uncertainties in radiotherapy treatment planning by means of coverage probability," *Int. J. Radiat. Oncol. Biol. Phys.* **43**, 905–919.
- Svedman, C., Sandstrom, P., Pisa, P., Blomgren, H., Lax, I., Kalkner, K.M., Nilsson, S., and Wersäll, P. (2006). "A prospective phase II trial of using extracranial stereotactic radiotherapy in primary and metastatic renal cell carcinoma," *Acta Oncol.* **45**, 870–875.
- Svedman, C., Karlsson, K., Rutkowska, E., Sandstrom, P., Blomgren, H., Lax, I., and Wersäll, P. (2008). "Stereotactic body radiotherapy of primary and metastatic renal lesions for patients with only one functioning kidney," *Acta Oncol.* **47**, 1578–1583.
- Sweeney, R.A., Seubert, B., Stark, S., Homann, V., Müller, G., Flentje, M., and Guckenberger, M. (2012). "Accuracy and inter-observer variability of 3D versus 4D cone-beam CT based image-guidance in SBRT for lung tumors," *Radiat. Oncol.* **7**, 81.
- Teh, B.S., Ishiyama, H., Mathews, T., Xu, B., Butler, E.B., Mayr, N.A., Lo, S.S., Lu, J.J., Blanco, A.I., Paulino, A.C., and Timmerman, R.D. (2010). "Stereotactic body radiation therapy (SBRT) for genitourinary malignancies," *Discov. Med.* **10**, 255–262.
- Teke, T., Bergman, A.M., Kwa, W., Gill, B., Duzenli, C., and Popescu, I.A. (2010). "Monte Carlo based, patient-specific RapidArc QA using Linac log files," *Med. Phys.* **37**, 116–123.
- Tessier, F., and Kawrakow, I. (2010). "Effective point of measurement of thimble ion chambers in megavoltage photon beams," *Med. Phys.* **37**, 96–107.
- Thomas, S.D., Mackenzie, M., Rogers, D.W., and Fallone, B.G. (2005). "A Monte Carlo derived TG-51 equivalent calibration for helical tomotherapy," *Med. Phys.* **32**, 1346–1353.
- Thomas, S.J., Aspradakis, M.M., Byrne, J.P., Chalmers, G., Duane, S., Rogers, J., Thomas, R.A., Tudor, G.S., Twyman, N., and Party, I.W. (2014). "Reference dosimetry on TomoTherapy: An addendum to the 1990 UK MV dosimetry code of practice," *Phys. Med. Biol.* **59**, 1339–1352.
- Thongphiew, D., Wu, Q.J., Lee, W.R., Chankong, V., Yoo, S., McMahon, R., and Yin, F.F. (2009). "Comparison of online IGRT techniques for prostate IMRT treatment: Adaptive vs repositioning correction," *Med. Phys.* **36**, 1651–1662.
- Thwaites, D. (2013). "Accuracy required and achievable in radiotherapy dosimetry: Have modern technology and techniques changed our views?," *J. Phys. Conf. Ser.* 012006, doi:10.1088/1742-6596/444/1/012006.
- Tillikainen, L., Helminen, H., Torsti, T., Siljamaki, S., Alakuijala, J., Pyyry, J., and Ulmer, W. (2008). "A 3D pencil-beam-based superposition algorithm for photon dose calculation in heterogeneous media," *Phys. Med. Biol.* **53**, 3821–3839.
- Timmerman, R., Michalski, J., Fowler, J., Johnstone, D., Choy, H., Galvin, J.M., and Gore, E. (2004). *A Phase II Trial of Stereotactic Body Radiation Therapy (SBRT) in the Treatment of Patients with Medically Inoperable Stage I/II Non-Small Cell Lung Cancer*, RTOG 0236 (American College of Radiology, Philadelphia).
- Timmerman, R., McGarry, R., Yiannoutsos, C., Papiez, L., Tudor, K., DeLuca, J., Ewing, M., Abdulrahman, R., DesRosiers, C., Williams, M., and Fletcher, J. (2006). "Excessive toxicity when treating central tumors in a phase II study of stereotactic body radiation therapy for medically inoperable early-stage lung cancer," *J. Clin. Oncol.* **24**, 4833–4839.
- Tree, A., Aluwini, S., Bryant, H., Hall, E., Incrocci, L., Kaplan, I., Ostler, P., Sanda, M., Thompson, A., and van As, N. (2013). "Successful patient acceptance of randomization within the Pace Study (prostate advances in comparative evidence)," *Int. J. Radiat. Oncol. Biol. Phys.* **87**, S365.
- Tryggestad, E., Christian, M., Ford, E., Kut, C., Le, Y., Sanguineti, G., Song, D.Y., and Kleinberg, L. (2011). "Inter- and intrafraction patient positioning uncertainties for intracranial radiotherapy: A study of four frameless, thermoplastic mask-based immobilization strategies using daily cone-beam CT," *Int. J. Radiat. Oncol. Biol. Phys.* **80**, 281–290.
- Tse, R.V., Hawkins, M., Lockwood, G., Kim, J.J., Cummings, B., Knox, J., Sherman, M., and Dawson, L. A. (2008). "Phase I study of individualized stereotactic body radiotherapy for hepatocellular carcinoma and intrahepatic cholangiocarcinoma," *J. Clin. Oncol.* **26**, 657–664.

References

- Underwood, T.S., Winter, H.C., Hill, M.A., and Fenwick, J.D. (2013). "Detector density and small field dosimetry: Integral versus point dose measurement schemes," *Med. Phys.* **40**, 082102, doi:10.1111/1.4812687.
- Unkelbach, J., and Oelfke, U. (2004). "Inclusion of organ movements in IMRT treatment planning via inverse planning based on probability distributions," *Phys. Med. Biol.* **49**, 4005–4029.
- Vanderstraeten, B., Reynaert, N., Paelinck, L., Madani, I., De Wagter, C., De Gersem, W., De Neve, W., and Thierens, H. (2006). "Accuracy of patient dose calculation for lung IMRT: A comparison of Monte Carlo, convolution/superposition, and pencil beam computations," *Med. Phys.* **33**, 3149–3158.
- van der Voort van Zyp, N.C., Prevost, J.B., Hoogeman, M.S., Praag, J., van der Holt, B., Levendag, P.C., van Klaveren, R.J., Pattynama, P., and Nuyttens, J.J. (2009). "Stereotactic radiotherapy with real-time tumor tracking for non-small cell lung cancer: Clinical outcome," *Radiother. Oncol.* **91**, 296–300.
- van der Voort van Zyp, N.C., Prevost, J.B., van der Holt, B., Braat, C., van Klaveren, R.J., Pattynama, P.M., Levendag, P.C., and Nuyttens, J.J. (2010a). "Quality of life after stereotactic radiotherapy for stage I non-small-cell lung cancer," *Int. J. Radiat. Oncol. Biol. Phys.* **77**, 31–37.
- van der Voort van Zyp, N.C., Hoogeman, M.S., van de Water, S., Levendag, P.C., van der Holt, B., Heijmen, B.J., and Nuyttens, J.J. (2010b). "Clinical introduction of Monte Carlo treatment planning: A different prescription dose for non-small cell lung cancer according to tumor location and size," *Radiother. Oncol.* **96**, 55–60.
- van der Voort van Zyp, N.C., Hoogeman, M.S., van de Water, S., Levendag, P.C., van der Holt, B., Heijmen, B.J., and Nuyttens, J.J. (2011). "Stability of markers used for real-time tumor tracking after percutaneous intrapulmonary placement," *Int. J. Radiat. Oncol. Biol. Phys.* **81**, e75–e81.
- van Herk, M. (2004). "Errors and margins in radiotherapy," *Semin. Radiat. Oncol.* **14**, 52–64.
- van Herk, M., Remeijer, P., Rasch, C., and Lebesque, J.V. (2000). "The probability of correct target dosage: Dose-population histograms for deriving treatment margins in radiotherapy," *Int. J. Radiat. Oncol. Biol. Phys.* **47**, 1121–1135.
- van Loon, J., Siedschlag, C., Stroom, J., Blauwgeers, H., van Suylen, R.J., Kneijens, J., Rossi, M., van Baardwijk, A., Boersma, L., Klomp, H., Vogel, W., Burgers, S., and Gilhuijs, K. (2012). "Microscopic disease extension in three dimensions for non-small-cell lung cancer: Development of a prediction model using pathology-validated positron emission tomography and computed tomography features," *Int. J. Radiat. Oncol. Biol. Phys.* **82**, 448–456.
- Vargo, J.A., Heron, D.E., Ferris, R.L., Rwigema, J.C., Wegner, R.E., Kalash, R., Ohr, J., Kubicek, G.J., and Burton, S. (2012). "Prospective evaluation of patient-reported quality-of-life outcomes following SBRT +/- cetuximab for locally-recurrent, previously-irradiated head and neck cancer," *Radiother. Oncol.* **104**, 91–5.
- Vassiliev, O.N., Wareing, T.A., McGhee, J., Failla, G., Salehpour, M.R., and Mourtada, F. (2010). "Validation of a new grid-based Boltzmann equation solver for dose calculation in radiotherapy with photon beams," *Phys. Med. Biol.* **55**, 581–598.
- Vatnitsky, S., Krhrunov, V.S., Fominych, V.I., and Schuele, E. (1993). "Diamond detector dosimetry for medical applications," *Radiat. Prot. Dosim.* **47**, 515–518.
- Vautravers-Dewas, C., Dewas, S., Bonodeau, F., Adenis, A., Lacornerie, T., Penel, N., Lartigau, E., and Mirabel, X. (2011). "Image-guided robotic stereotactic body radiation therapy for liver metastases: Is there a dose response relationship?" *Int. J. Radiat. Oncol. Biol. Phys.* **81**, e39–e47.
- Verellen, D., Soete, G., Linthout, N., Van Acker, S., De Roover, P., Vinh-Hung, V., Van de Steene, J., and Storme, G. (2003). "Quality assurance of a system for improved target localization and patient set-up that combines real-time infrared tracking and stereoscopic x-ray imaging," *Radiother. Oncol.* **67**, 129–141.
- Verhaegen, F., and Seuntjens, J. (2003). "Monte Carlo modelling of external radiotherapy photon beams," *Phys. Med. Biol.* **48**, R107–R164.
- Verhaegen, F., Das, I.J., and Palmans, H. (1998). "Monte Carlo dosimetry study of a 6 MV stereotactic radiosurgery unit," *Phys. Med. Biol.* **43**, 2755–2768.
- Vermeulen, S., Cotrutz, C., Morris, A., Meier, R., Buchanan, C., Dawson, P., and Porter, B. (2011). "Accelerated partial breast irradiation: Using the cyberknife as the radiation delivery platform in the treatment of early breast cancer," *Front Oncol.* **1**, doi:10.3389/fonc.2011.00043.
- Vetterli, D., Riem, H., Aebersold, D.M., Greiner, R.H., Manser, P., Cossmann, P., Kemmerling, L., Born, E.J., and Mini, R. (2004). "Introduction of a novel dose saving acquisition mode for the PortalVision aS500 EPID to facilitate on-line patient setup verification," *Med. Phys.* **31**, 828–831.
- Videtic, G.M., Stephans, K.L., Woody, N.M., Reddy, C.A., Zhuang, T., Magnelli, A., and Djemil, T. (2014). "30 Gy or 34 Gy? Comparing 2 single-fraction SBRT dose schedules for stage I medically inoperable non-small cell lung cancer," *Int. J. Radiat. Oncol. Biol. Phys.* **90**, 203–208.
- Wagner, A., Crop, F., Lacornerie, T., Vandevelde, F., and Reynaert, N. (2013a). "Use of a liquid ionization chamber for stereotactic radiotherapy dosimetry," *Phys. Med. Biol.* **58**, 2445–2459.
- Wagner, J.Y., Schwarz, K., Schreiber, S., Schmidt, B., Wester, H.J., Schwaiger, M., Peschel, C., von Schilling, C., Scheidhauer, K., and Keller, U. (2013b). "Myeloablative anti-CD20 radioimmunotherapy +/- high-dose chemotherapy followed by autologous stem cell support for relapsed/refractory B-cell lymphoma results in excellent long-term survival," *Oncotarget* **4**, 899–910.
- Wallace, H.J., Hard, D., Archambault, J., and van Herk, M. (2012). "Autoscan transperineal ultrasound of the

PRESCRIBING, RECORDING, AND REPORTING SMALL BEAM SRT

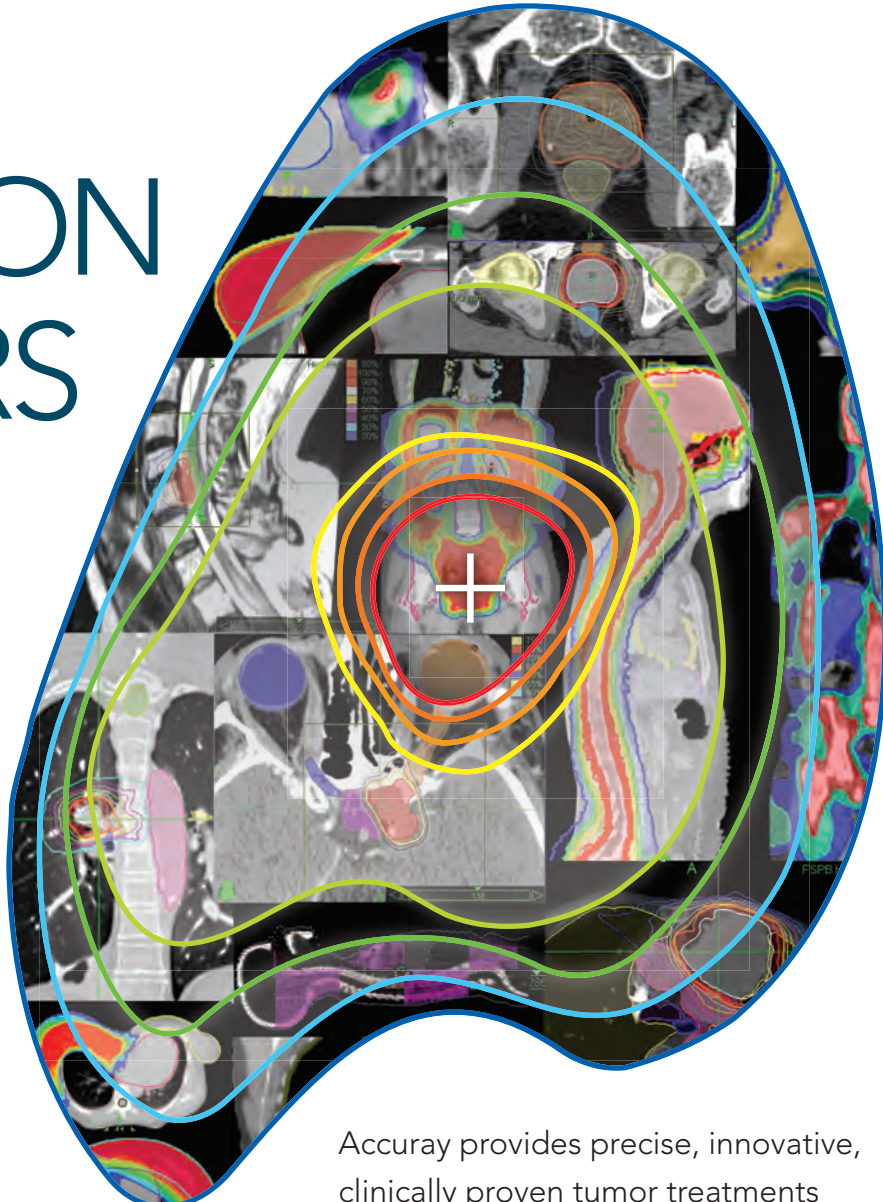
- pelvis for prostate gland localization – a feasibility study,” *Int. J. Radiat. Oncol. Biol. Phys.* **84**, S373–S374.
- Walters, B.R., Ding, G.X., Kramer, R., and Kawrakow, I. (2009). “Skeletal dosimetry in cone beam computed tomography,” *Med. Phys.* **36**, 2915–2922.
- Walton, L., Bomford, C.K., and Ramsden, D. (1987). “The Sheffield stereotactic radiosurgery unit: Physical characteristics and principles of operation,” *Br. J. Radiol.* **60**, 897–906.
- Wang, L.L., and Beddar, S. (2011). “Study of the response of plastic scintillation detectors in small-field 6 MV photon beams by Monte Carlo simulations,” *Med. Phys.* **38**, 1596–1599.
- Wang, L.T., Solberg, T.D., Medin, P.M., and Boone, R. (2001). “Infrared patient positioning for stereotactic radiosurgery of extracranial tumors,” *Comput. Biol. Med.* **31**, 101–111.
- Wang, L., Yorke, E., and Chui, C.S. (2002). “Monte Carlo evaluation of 6 MV intensity modulated radiotherapy plans for head and neck and lung treatments,” *Med. Phys.* **29**, 2705–2717.
- Wang, L., Jacob, R., Chen, L., Ma, C., Movsas, B., Feigenberg, S., and Konski, A. (2004). “Stereotactic IMRT for prostate cancer: Setup accuracy of a new stereotactic body localization system,” *J. Appl. Clin. Med. Phys.* **5**, 18–28.
- Wang, L., Feigenberg, S., Chen, L., Pasklev, K., and Ma, C.C. (2006). “Benefit of three-dimensional image-guided stereotactic localization in the hypofractionated treatment of lung cancer,” *Int. J. Radiat. Oncol. Biol. Phys.* **66**, 738–747.
- Wang, Z., Wu, Q.J., Marks, L.B., Larrier, N., and Yin, F.F. (2007). “Cone-beam CT localization of internal target volumes for stereotactic body radiotherapy of lung lesions,” *Int. J. Radiat. Oncol. Biol. Phys.* **69**, 1618–1624.
- Wang, L., Hayes, S., Paskalev, K., Jin, L., Buuyounouski, M.K., Ma, C.C., and Feigenberg, S. (2009). “Dosimetric comparison of stereotactic body radiotherapy using 4D CT and multiphase CT images for treatment planning of lung cancer: Evaluation of the impact on daily dose coverage,” *Radiother. Oncol.* **91**, 314–324.
- Wang, J.Z., Huang, Z., Lo, S.S., Yuh, W.T., and Mayr, N. A. (2010). “A generalized linear-quadratic model for radiosurgery, stereotactic body radiation therapy, and high-dose rate brachytherapy,” *Sci. Transl. Med.* **2**, 39ra48, doi: 10.1126/scitranslmed.3000864.
- Wang, X.S., Rhines, L.D., Shiu, A.S., Yang, J.N., Selek, U., Gning, I., Liu, P., Allen, P.K., Azeem, S.S., Brown, P. D., Sharp, H.J., Weksberg, D.C., Cleeland, C.S., and Chang, E.L. (2012). “Stereotactic body radiation therapy for management of spinal metastases in patients without spinal cord compression: A phase 1-2 trial,” *Lancet Oncol.* **13**, 395–402.
- Wang, H., Balter, J., and Cao, Y. (2013). “Patient-induced susceptibility effect on geometric distortion of clinical brain MRI for radiation treatment planning on a 3T scanner,” *Phys. Med. Biol.* **58**, 465–477.
- Welsh, J.S., Lock, M., Harari, P.M., Tome, W.A., Fowler, J., Mackie, T.R., Ritter, M., Kapatoes, J., Forrest, L., Chappell, R., Paliwal, B., and Mehta, M.P. (2006). “Clinical implementation of adaptive helical tomotherapy: A unique approach to image-guided intensity modulated radiotherapy,” *Technol. Cancer Res. Treat.* **5**, 465–479.
- Wersäll, P.J., Blomgren, H., Lax, I., Kalkner, K.M., Linder, C., Lundell, G., Nilsson, B., Nilsson, S., Naslund, I., Pisa, P., and Svedman, C. (2005). “Extracranial stereotactic radiotherapy for primary and metastatic renal cell carcinoma,” *Radiother. Oncol.* **77**, 88–95.
- WHO (2000). World Health Organization. *International Classification of Diseases for Oncology*, 3rd ed. (World Health Organization, Geneva).
- Wickman, G., and Holmstrom, T. (1992). “Polarity effect in plane-parallel ionization chambers using air or a dielectric liquid as ionization medium,” *Med. Phys.* **19**, 637–640.
- Wijgenraad, R., Verbeek-de Kanter, A., Kal, H.B., Taphoorn, M., Vissers, T., and Struikmans, H. (2011). “Dose-effect relation in stereotactic radiotherapy for brain metastases. A systematic review,” *Radiother. Oncol.* **98**, 292–297.
- Wijesooriya, K., Aliotta, E., Benedict, S., Read, P., Rich, T., and Larner, J. (2012). “RapidArc patient specific mechanical delivery accuracy under extreme mechanical limits using linac log files,” *Med. Phys.* **39**, 1846–1853.
- Winston, K.R., and Lutz, W. (1988). “Linear-accelerator as a neurosurgical tool for stereotactic radiosurgery,” *Neurosurgery* **22**, 454–464.
- Withers, H.R. (1986). “Predicting late normal tissue responses,” *Int. J. Radiat. Oncol. Biol. Phys.* **12**, 693–698.
- Withers, H.R., Taylor, J.M., and Maciejewski, B. (1988). “Treatment volume and tissue tolerance,” *Int. J. Radiat. Oncol. Biol. Phys.* **14**, 751–759.
- Wu, Q.J., and Bourland, J.D. (1999). “Morphology-guided radiosurgery treatment planning and optimization for multiple isocenters,” *Med. Phys.* **26**, 2151–2160.
- Wu, A., Lindner, G., Maitz, A.H., Kalend, A.M., Lunsford, L.D., Flickinger, J.C., and Bloomer, W.D. (1990). “Physics of gamma knife approach on convergent beams in stereotactic radiosurgery,” *Int. J. Radiat. Oncol. Biol. Phys.* **18**, 941–949.
- Wu, A., Zwicker, R.D., Kalend, A.M., and Zheng, Z. (1993). “Comments on dose measurements for a narrow beam in radiosurgery,” *Med. Phys.* **20**, 777–779.
- Wu, S.X., Chua, D.T., Deng, M.L., Zhao, C., Li, F.Y., Sham, J.S., Wang, H.Y., Bao, Y., Gao, Y.H., and Zeng, Z.F. (2007). “Outcome of fractionated stereotactic radiotherapy for 90 patients with locally persistent and recurrent nasopharyngeal carcinoma,” *Int. J. Radiat. Oncol. Biol. Phys.* **69**, 761–769.
- Wu, Q.J., Meyer, J., Fuller, J., Godfrey, D., Wang, Z., Zhang, J., and Yin, F.F. (2011). “Digital tomosynthesis for respiratory gated liver treatment: Clinical feasibility for daily image guidance,” *Int. J. Radiat. Oncol. Biol. Phys.* **79**, 289–296.
- Wulf, J., Hadinger, U., Oppitz, U., Thiele, W., Ness-Douroumas, R., and Flentje, M. (2001). “Stereotactic

References

- radiotherapy of targets in the lung and liver," *Strahlenther. Onkol.* **177**, 645–655.
- Wulf, J., Baier, K., Mueller, G., and Flentje, M.P. (2005). "Dose-response in stereotactic irradiation of lung tumors," *Radiother. Oncol.* **77**, 83–87.
- Wulff, J., Heverhagen, J.T., and Zink, K. (2008). "Monte Carlo-based perturbation and beam quality correction factors for thimble ionization chambers in high-energy photon beams," *Phys. Med. Biol.* **53**, 2823–2836.
- Wulff, J., Heverhagen, J.T., Zink, K., and Kawrakow, I. (2010). "Investigation of systematic uncertainties in Monte Carlo-calculated beam quality correction factors," *Phys. Med. Biol.* **55**, 4481–4493.
- Xiao, Y., Altschuler, M.D., and Bjarnegard, B.E. (1998). "Quality assurance of central axis dose data for photon beams by means of a functional representation of the tissue phantom ratio," *Phys. Med. Biol.* **43**, 2195–2206.
- Xiao, Y., Papiez, L., Paulus, R., Timmerman, R., Straube, W.L., Bosch, W.R., Michalski, J., and Galvin, J.M. (2009). "Dosimetric evaluation of heterogeneity corrections for RTOG 0236: Stereotactic body radiotherapy of inoperable stage I-II non-small-cell lung cancer," *Int. J. Radiat. Oncol. Biol. Phys.* **73**, 1235–1242.
- Xiong, G., and Rogers, D.W. (2008). "Relationship between $\%dd(10)_x$ and stopping-power ratios for flattening filter free accelerators: A Monte Carlo study," *Med. Phys.* **35**, 2104–2109.
- Yan, D., Vicini, F., Wong, J., and Martinez, A. (1997). "Adaptive radiation therapy," *Phys. Med. Biol.* **42**, 123–132.
- Yan, D., Jaffray, D.A., and Wong, J.W. (1999). "A model to accumulate fractionated dose in a deforming organ," *Int. J. Radiat. Oncol. Biol. Phys.* **44**, 665–675.
- Yanagi, T., Kamada, T., Tsuji, H., Imai, R., Serizawa, I., and Tsujii, H. (2010). "Dose-volume histogram and dose-surface histogram analysis for skin reactions to carbon ion radiotherapy for bone and soft tissue sarcoma," *Radiother. Oncol.* **95**, 60–65.
- Yeboah, C. (2011). "Characterization of linear accelerator x-ray source size using a laminated beam-spot camera," *J. Appl. Clin. Med. Phys.* **12**, 178–182.
- Yoo, S., Kim, G.Y., Hammoud, R., Elder, E., Pawlicki, T., Guan, H., Fox, T., Luxton, G., Yin, F.F., and Munro, P. (2006). "A quality assurance program for the on-board imagers," *Med. Phys.* **33**, 4431–4447.
- Young, M., Polityka, M., Hardy, T., Uhl, B., Dewitt, K., Goetsch, S., Fisher, T., Topalian, S., Zhou, J., and Papin, P. (2010). "Imaging reslicer localization for whole-body stereotaxy using TomoTherapy," *Radiosurgery* **7**, 384–396.
- Yu, X., Liu, Z., and Li, S. (2000). "Combined treatment with stereotactic intracavitary irradiation and Gamma Knife surgery for craniopharyngiomas," *Stereotact. Funct. Neurosurg.* **75**, 117–122.
- Yu, C., Main, W., Taylor, D., Kuduvalli, G., Apuzzo, M.L., Adler, J.R. Jr, and Wang, M.Y. (2004). "An anthropomorphic phantom study of the accuracy of Cyberknife spinal radiosurgery," *Neurosurgery* **55**, 1138–1149.
- Zeidan, O.A., Langen, K.M., Meeks, S.L., Manon, R.R., Wagner, T.H., Willoughby, T.R., Jenkins, D.W., and Kupelian, P.A. (2007). "Evaluation of image-guidance protocols in the treatment of head and neck cancers," *Int. J. Radiat. Oncol. Biol. Phys.* **67**, 670–677.
- Zelefsky, M.J., Greco, C., Motzer, R., Magsanoc, J.M., Pei, X., Lovelock, M., Mechakos, J., Zatcky, J., Fuks, Z., and Yamada, Y. (2012). "Tumor control outcomes after hypofractionated and single-dose stereotactic image-guided intensity-modulated radiotherapy for extracranial metastases from renal cell carcinoma," *Int. J. Radiat. Oncol. Biol. Phys.* **82**, 1744–1748.
- Zhang, B., MacFadden, D., Damyanovich, A.Z., Rieker, M., Stainsby, J., Bernstein, M., Jaffray, D.A., Mikulis, D., and Menard, C. (2010). "Development of a geometrically accurate imaging protocol at 3 Tesla MRI for stereotactic radiosurgery treatment planning," *Phys. Med. Biol.* **55**, 6601–6615.

PRECISION MATTERS

- + For your patients
- + For your practice
- + For your future



md buyline

MD Buyline verified user satisfaction supported by our 98% uptime guarantee (U.S. only).*

Accuray provides precise, innovative, clinically proven tumor treatments with outstanding reliability, service and performance.



Precise, innovative tumor treatments™

#PrecisionMatters

Visit www.Accuray.com/WhyPrecisionMatters



UTILIZE YOUR WEALTH OF KNOWLEDGE. UNLOCK A WEALTH OF POSSIBILITIES.

Introducing RapidPlan™ knowledge-based treatment planning.

Imagine a world where you can unlock the knowledge of your best plans to create the right plan. That's the power of RapidPlan. Innovative software that helps clinics leverage existing clinical knowledge to create quality plans—quickly and consistently. That means moving beyond templates to create fully customized plans to help you provide the best care for your patients.

Learn more about the benefits of RapidPlan at varian.com/RapidPlan

Radiation treatments may cause side effects that can vary depending on the part of the body being treated. The most frequent ones are typically temporary and may include, but are not limited to, irritation to the respiratory, digestive, urinary or reproductive systems, fatigue, nausea, skin irritation, and hair loss. In some patients, they can be severe. Radiation treatment is not appropriate for all cancers. See varian.com/use-and-safety for more information.

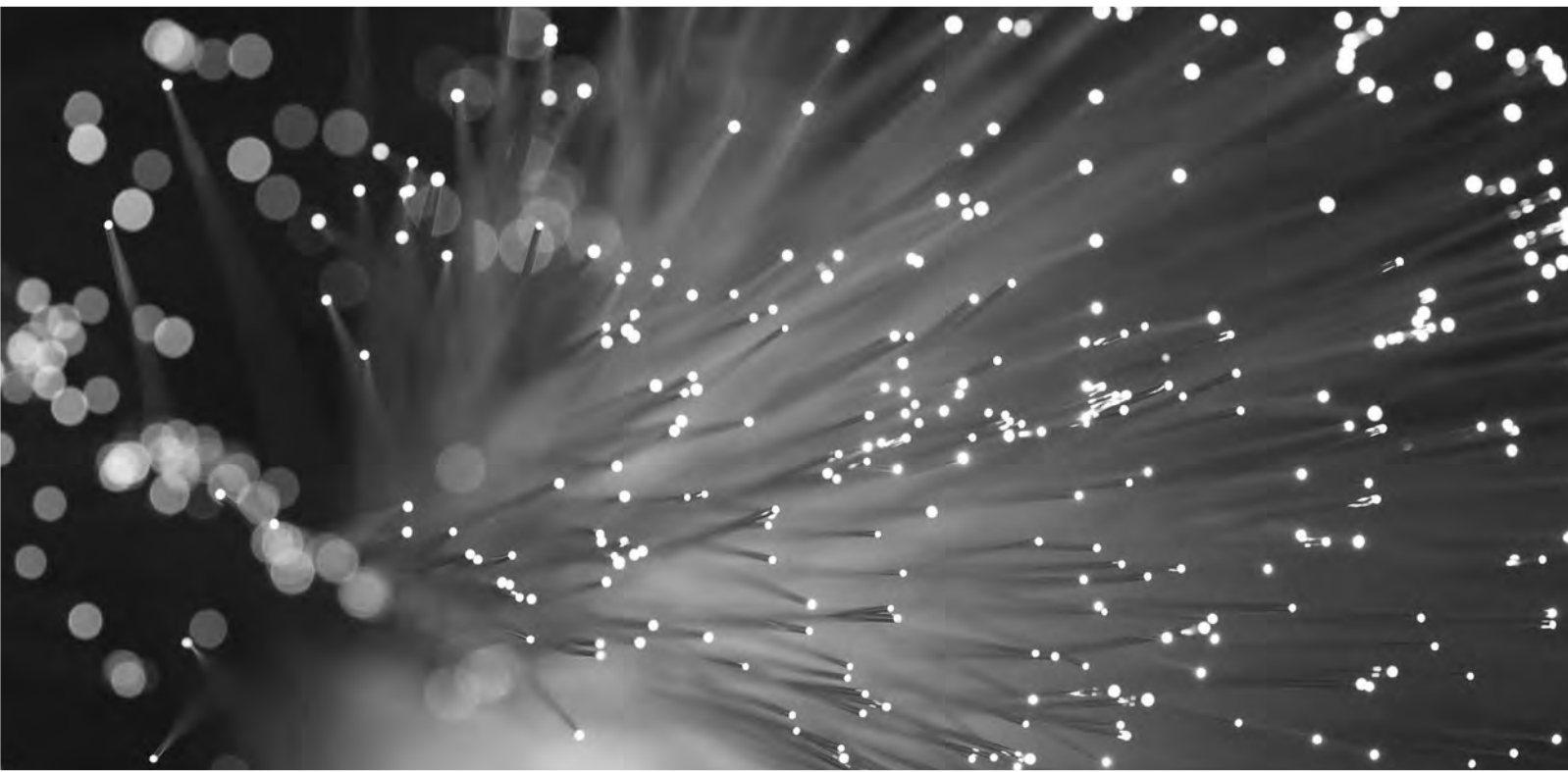
© 2015 Varian Medical Systems, Inc. Varian and Varian Medical Systems are registered trademarks, and RapidPlan is a trademark of Varian Medical Systems, Inc.

VARIAN
medical systems

A partner for **life**

Quality & speed

Advance Access publication from Oxford Journals



Articles published online ahead of print are available to read and cite with Advance Access.

academic.oup.com

OXFORD
UNIVERSITY PRESS



- Key Data for Ionizing-Radiation Dosimetry: Measurement Standards and Applications**
Report no. 90, 2014
- Prescribing, Recording, and Reporting Brachytherapy for Cancer of the Cervix**
Report no. 89, 2013
- Measurement and Reporting of Radon Exposures**
Report no. 88, 2012
- Radiation Dose and Image-Quality Assessment in Computed Tomography**
Report no. 87, 2012
- Quantification and Reporting of Low-Dose and other Heterogeneous Exposures**
Report no. 86, 2011
- Fundamental Quantities and Units for Ionizing Radiation**
Report no. 85, 2011
- Reference Data for the Validation of Doses from Cosmic-Radiation Exposure of Aircraft Crew**
Report no. 84, 2010
- Prescribing, Recording, and Reporting Photon-Beam Intensity-Modulated Radiation Therapy (IMRT)**
Report no. 83, 2010
- Mammography - Assessment of Image Quality**
Report no. 82, 2009
- Quantitative Aspects of Bone Densitometry**
Report no. 81, 2009
- Dosimetry Systems for Use in Radiation Processing**
Report no. 80, 2008
- Receiver Operating Characteristic Analysis in Medical Imaging**
Report no. 79, 2008
- Prescribing, Recording, and Reporting Proton-Beam Therapy**
Report no. 78, 2007
- Elastic Scattering of Electrons and Positrons**
Report no. 77, 2007
- Measurement Quality Assurance for Ionizing Radiation Dosimetry**
Report no. 76, 2006
- Sampling for Radionuclides in the Environment**
Report no. 75, 2006
- Patient Dosimetry of X Rays used in Medical Imaging**
Report no. 74, 2005
- Stopping of Ions Heavier Than Helium**
Report no. 73, 2005
- Dosimetry of Beta Rays and Low-Energy Photons for Brachytherapy with Sealed Sources**
Report no. 72, 2004
- Prescribing, Recording, and Reporting Electron Beam Therapy**
Report no. 71, 2004
- Image Quality in Chest Radiography**
Report no. 70, 2003
- Direct Determination of the Body Content of Radionuclides**
Report no. 69, 2003
- Retrospective Assessment of Exposures to Ionising Radiation**
Report no. 68, 2002
- Absorbed Dose Specification in Nuclear Medicine**
Report no. 67, 2002
- Determination of Operational Dose Equivalent Quantities for Neutrons**
Report no. 66, 2001
- Quantities, Units and Terms in Radioecology**
Report no. 65, 2001
- Dosimetry of High Energy Photon Beams based on Standards of Absorbed Dose to Water**
Report no. 64, 2001
- Nuclear Data for Neutron and Proton Radiotherapy and for Radiation Protection**
Report no. 63, 2000
- Prescribing, Recording and Reporting Photon Beam Therapy (Supplement to ICRU Report 50)**
Report no. 62, 1999
- Tissue Substitutes, Phantoms and Computational Modelling in Medical Ultrasound**
Report no. 61, 1998
- Fundamental Quantities and Units for Ionizing Radiation**
Report no. 60, 1998
- Clinical Proton Dosimetry—Part I: Beam Production, Beam Delivery and Measurement of Absorbed Dose**
Report no. 59, 1998
- Dose and Volume Specification for Reporting Interstitial Therapy**
Report no. 58, 1997
- Conversion Coefficients for Use in Radiological Protection Against External Radiation**
Report no. 57, 1998

- Dosimetry of External Beta Rays for Radiation Protection**
Report no. 56, 1997
- Secondary Electron Spectra from Charged Particle Interactions**
Report no. 55, 1995
- Medical Imaging—The Assessment of Image Quality**
Report no. 54, 1995
- Gamma-Ray Spectrometry in the Environment**
Report no. 53, 1994
- Particle Counting in Radioactivity Measurement**
Report no. 52, 1994
- Quantities and Units in Radiation Protection Dosimetry**
Report no. 51, 1993
- Prescribing, Recording and Reporting Photon Beam Therapy**
Report no. 50, 1993
- Stopping Powers and Ranges for Protons and Alpha Particles, with Data Disk**
Report no. 49D, 1993
- Stopping Powers and Ranges for Protons and Alpha Particles**
Report no. 49, 1993
- Phantoms and Computational Models in Therapy, Diagnosis and Protection**
Report no. 48, 1992
- Measurement of Dose Equivalents from External Photon and Electron Radiations**
Report no. 47, 1992
- Photon, Electron, Proton and Neutron Interaction Data for Body Tissues, with Data Disk**
Report no. 46D, 1992
- Photon, Electron, Proton and Neutron Interaction Data for Body Tissues**
Report no. 46, 1992
- Clinical Neutron Dosimetry—Part I: Determination of Absorbed Dose in a Patient Treated by External Beams of Fast Neutrons**
Report no. 45, 1989
- Tissue Substitutes in Radiation Dosimetry and Measurement**
Report no. 44, 1989
- Determination of Dose Equivalents from External Radiation Sources - Part 2**
Report no. 43, 1988
- Use of Computers in External Beam Radiotherapy Procedures with High-Energy Photons and Electrons**
Report no. 42, 1987
- Modulation Transfer Function of Screen-Film Systems**
Report no. 41, 1986
- The Quality Factor in Radiation Protection**
Report no. 40, 1986
- Determination of Dose Equivalents Resulting from External Radiation Sources**
Report no. 39, 1985
- Dose and Volume Specification for Reporting Intracavitary Therapy in Gynecology**
Report no. 38, 1985
- Stopping Powers for Electrons and Positrons**
Report no. 37, 1984
- Microdosimetry**
Report no. 36, 1983
- Radiation Dosimetry: Electron Beams with Energies Between 1 and 50 MeV**
Report no. 35, 1984
- The Dosimetry of Pulsed Radiation**
Report no. 34, 1982
- Radiation Quantities and Units**
Report no. 33, 1980
- Methods of Assessment of Absorbed Dose in Clinical Use of Radionuclides**
Report no. 32, 1979
- Average Energy Required to Produce an Ion Pair**
Report no. 31, 1979
- Quantitative Concepts and Dosimetry in Radiobiology**
Report no. 30, 1979
- Basic Aspects of High Energy Particle Interactions and Radiation Dosimetry**
Report no. 28, 1978
- Neutron Dosimetry for Biology and Medicine**
Report no. 26, 1977
- An International Neutron Dosimetry Intercomparison**
Report no. 27, 1978
- Conceptual Basis for the Determination of Dose Equivalent**
Report no. 25, 1976
- Determination of Absorbed Dose in a Patient Irradiated by Beams of X or Gamma Rays in Radiotherapy Procedures**
Report no. 24, 1976
- Measurement of Absorbed Dose in a Phantom Irradiated by a Single Beam of X or Gamma Rays**
Report no. 23, 1973